Christoph Peters

Grain-Size Effects in Nanoscaled Electrolyte and Cathode Thin Films for Solid Oxide Fuel Cells (SOFC)

Christoph Peters

Grain-Size Effects in Nanoscaled Electrolyte and Cathode Thin Films for Solid Oxide Fuel Cells (SOFC)

Grain-Size Effects in Nanoscaled Electrolyte and Cathode Thin Films for Solid Oxide Fuel Cells (SOFC)

by
Christoph Peters

Grain-Size Effects in
Nanoscaled Electrolyte and Cathode Thin Films
for Solid Oxide Fuel Cells (SOFC)

Zur Erlangung des akademischen Grades eines

DOKTOR-INGENIEURS (DR.-ING.)

von der Fakultät für

Elektrotechnik und Informationstechnik

der Universität Karlsruhe (TH)

genehmigte

DISSERTATION

von

Dipl.-Ing. Christoph Peters

aus Nordhorn

Tag der mündlichen Prüfung: 11.12.2008

Hauptreferentin: Prof. Dr.-Ing. Ellen Ivers-Tiffée

Korreferentin: Prof. Dr. rer. nat. Dagmar Gerthsen

Acknowledgements

Zusammenfassung

Gegenstand der vorliegenden Arbeit ist die Beantwortung der Frage, welche Vorteile keramische Dünnschichten mit nanoskaliger Morphologie für die Hochtemperaturbrennstoffzelle (solid oxide fuel cell, SOFC) bieten. Aufgrund der geringen Korngröße ist die Korngrenzdichte im Nanoskaligen so weit erhöht, dass Korngrenzeffekte möglicherweise zu einer stark verbesserten Leitfähigkeit führen. Verbesserte Ladungstransporteigenschaften wiederum senken die ohmschen Verluste im Elektrolyten und die Polarisation der Elektroden, die z.B. an der Kathode während der Sauerstoffreduktion entsteht. Beides erhöht den Wirkungsgrad von Brennstoffzellen insbesondere im Temperaturbereich 500 °C ≤ T ≤ 750 °C.

Zur systematischen Untersuchung von Korngrenzeffekten in nanoskaligen Elektrolyt- und Kathodendünnschichten wurden grundlegende experimentelle Untersuchungen durchgeführt. Dabei konzentriert sich diese Arbeit auf zwei Materialsysteme: Als Elektrolyt wird 8,3 mol% Yttrium dotiertes Zirkonoxid (YSZ) untersucht – das Standardelektrolytmaterial für die SOFC. Als Kathode wird mit Lanthanstrontiumkobaltat (LSC) ein mischleitender Perowskit gewählt, der exzellente Sauerstoffreduktionseigenschaften aufweist. Alle untersuchten Dünnschichten wurden mittels eines Sol-Gel-Prozesses hergestellt, einem Verfahren, das für Beschichtungen im industriellen Maßstab geeignet ist.

Nanoskalige Elektrolytdünnschichten

Der Ladungstransport in YSZ-Keramiken erfolgt über einen Gitterplatzwechsel von Sauerstoffionen bzw. Sauerstoffleerstellen im YSZ-Kristall. Ziel der umfassenden Experimente an den Elektrolytdünnschichten war es zu untersuchen, ob die hohe Dichte der Korngrenzen in nanoskaligen Proben zu einer hohen Konzentration von Sauerstoffleerstellen und / oder einer hohen Beweglichkeit der Ladungsträger und somit zu einer erhöhten elektrischen Leitfähigkeit führt. Dazu wurden YSZ-Dünnschichten auf isolierende Saphirsubstrate abgeschieden. Die Schichten sind homogen, rissfrei, ca. 300 nm dick und weisen eine gute Haftung zum Substrat auf. Durch anschließende Temperaturbehandlung zwischen 650 °C und 1400 °C (jeweils 24 Std.) kann die mittlere Korngröße d zwischen 5 nm und 782 nm variiert werden. Die Reinheit und Kristallinität der Korngrenzen wurde elektronenmikroskopisch nachgewiesen. Die Schichten weisen eine kubische Struktur mit tetragonalen Ausscheidungen im Nanometermaßstab auf. Diese Ausscheidungen sind homogen in den keramischen Körnern und Korngrenzen verteilt und können für die Untersuchung der Transporteigenschaften der Filme vernachlässigt werden.

Die elektrische Leitfähigkeit der YSZ-Dünnschichten wurde zwischen 200 °C und 400 °C in Luftatmosphäre untersucht: Während die Gesamtleitfähigkeit der Schichten mit Körnern im µm-Bereich mit der Leitfähigkeit polykristalliner Standardelektrolyte übereinstimmt, steigt mit

zunehmender Korngrenzdichte im Nanoskaligen der Widerstand der Proben an. Impedanz-spektroskopisch kann dieser Anstieg den Korngrenzen zugeordnet werden. Die spezifischen Leitfähigkeiten von Korn und Korngrenze für 232 nm $\leq d \leq$ 782 nm können durch Anwendung des sog. Brick-Layer-Modells berechnet werden. Dabei gibt die spezifische Leitfähigkeit den Ladungstransport bezogen auf ein einzelnes Korn bzw. eine einzelne Korngrenze mit einer äquivalenten elektrischen Korngrenzdicke δ_{gb} = 5,37 nm an. Beide Leitfähigkeiten zeigen Arrheniusverhalten, wobei die spezifische Korngrenzleitfähigkeit (E_A = 1,15 eV) zwei Deka-den unterhalb der spezifischen Kornleitfähigkeit (E_A = 1,09 eV) liegt. Die Anwendung des Brick-Layer-Modells für nanoskalige Proben mit $d \leq$ 36 nm zeigt, dass sich die Ladungs-transportvorgänge in YSZ-Dünnschichten im Nanoskaligen grundsätzlich nicht von denen in polykristallinen Materialien unterscheiden. Die Korngrenzen wirken unabhängig von der Korngröße auch im Nanoskaligen als Potenzialbarriere und behindern den Transport geladener Sauerstoffionen durch den Kristall. Durch die hohe Anzahl an Korngrenzen in na-noskaligen Materialien weisen diese Elektrolyte deshalb einen besonders hohen Gesamtwi-derstand auf.

Gegenüber herkömmlichen polykristallinen YSZ-Elektrolyten führen nanoskalige YSZ-Dünnschichten daher nicht zu einer Senkung des ohmschen Widerstandes und tragen zu keiner Verbesserung des SOFC-Wirkungsgrades bei. In dieser Arbeit wird nachgewiesen, dass nanoskalige YSZ-Dünnschichten keine günstigen Korngrenzeffekte aufweisen, die den Sauerstoffionentransport erhöhen.

Nanoskalige Kathodendünnschichten

Um den Einfluss der Mikrostruktur nanoskaliger und nanoporöser LSC-Kathoden auf die Sauerstoffreduktion zu ermitteln, wurden $(La_{1-x}Sr_x)CoO_{3-\delta}$ (x = 0,5) Dünnschichten auf YSZ-Oberflächen und auf Gadolinium dotierte Ceroxidoberflächen (GCO) mittels Sol-Gel-Verfahrens aufgebracht. Die Kristallisation der perowskitischen LSC-Phase wurde durch Thermoanalyse und röntgendiffraktometrische Experimente untersucht. Dadurch wurden folgende Kalzinierungsschritte ermittelt: 170 °C, 700° C und 900 °C (jeweils t = 5 min). Die auskristallisierten Schichten sind rissfrei und homogen und weisen eine gute Haftung zum jeweiligen Substrat auf.

Anstatt der reinen kubischen Struktur wird röntgendiffraktometrisch an beiden Probensyste-men (LSC / YSZ und LSC / GCO) eine rhomboedrische Verzerrung nachgewiesen, was auf ein leichtes Sr-Defizit und, durch die Verarmung auf dem A-Platz des ABO_3-Kristalls, auf Kobaltoxidausscheidungen im Nanometerbereich hindeutet. Aufgrund ihrer geringen Größe haben diese Zweitphasen einen vernachlässigbaren Einfluss auf die Funktion der Kathode. Allerdings führt eine Grenzflächenreaktion zwischen LSC-Kathode und YSZ-Elektrolyt zu der Bildung von Zirkonaten, die in einer massiven Schädigung der chemischen LSC-Phase re-sultiert. Diese Grenzflächenreaktion wird durch thermodynamische Simulationen für den ge-samten untersuchten Temperaturbereich von 500 °C $\leq T \leq$ 850 °C vorausgesagt – allerdings ist die Kinetik dieser Reaktion unbekannt. In der Literatur wurde die Bildung von Zirkonaten zwischen LSC und YSZ bisher für hohe Temperaturen ($T \geq$ 900 °C) und lange Zeiträume

nachgewiesen. Diese Arbeit zeigt die Kristallisation von Strontiumzirkonaten mikrostrukturell bereits bei 700 °C. Elektrische Untersuchungen über 100 Std. weisen die isolierenden Zirkonate bereits bei $T > 500$ °C zwischen der nanoskaligen LSC-Kathode und dem YSZ-Elektrolyten nach. Die Grenzfläche zwischen LSC und GCO ist hingegen über einen weiten Temperaturbereich (T_{min} = 1200 °C) stabil. Die Morphologie der Nanokathoden ändert sich mit der Temperatur: Bis 800 °C wurde selbstlimitierendes Kornwachstum festgestellt, d.h. die Größe der keramischen Körner läuft auf einen Endwert zu (d = 83 nm). Bei höheren Temperaturen unterliegt die Schicht einem nicht-parabolischen Kornwachstum, das zu einer Zerstörung der Nanokathode führt.

Die Polarisationsverluste, die während der Sauerstoffreduktion an der Kathode entstehen, sind im Fall der nanoskaligen mischleitenden LSC-Kathoden äußerst gering: In symmetrischen Zellmessungen wird bei 600 °C ein flächenspezifischer Polarisationwiderstand ASR_{pol} von 146 mΩ·cm² (LSC / YSZ) bzw. 130 mΩ·cm² (LSC / GCO) festgestellt. Diese Werte unterbieten alle veröffentlichten Polarisationswiderstände mischleitender Kathoden und zeigen somit eine ausgezeichnete elektrochemische Aktivität während der Sauerstoffreduktion. Durch ihren unterschiedlichen Stabilitätsbereich (LSC / YSZ: $T \leq 500$ °C, LSC / GCO: $T \leq 700$ °C) kommen für diese Systeme unterschiedliche Anwendungsbereiche in Frage. Mikrobrennstoffzellen (µ-SOFCs), die z.B. für den Akkuersatz in Laptops entwickelt werden, beschränken sich auf eine Temperatur von ca. 500 °C; deshalb sind dort LSC / YSZ – Kathoden vielversprechend. Hilfsaggregate für Automobile (auxiliary power units, APU) sind mit ihrer etwas höheren Betriebstemperatur eine potentielle Anwendung für die LSC / GCO – Kathoden.

Die exzellenten Eigenschaften der LSC-Nanokathoden bei der Sauerstoffreduktion beruhen neben den mischleitenden Materialeigenschaften auf der hohen Oberfläche der Elektroden. Der Sauerstoffaustausch an der Kathodenoberfläche ist im gesamten elektrochemischen Prozess der ratenbestimmende Schritt. Die Sauerstoffionendiffusion im Perowskiten und der Ladungsdurchtritt in den Elektrolyten sind bei nanoskaligen LSC-Kathoden vernachlässigbar. Das Modell von Adler, das die elektrochemische Sauerstoffreduktion an der Kathode beschreibt, wird durch den Vergleich der elektrischen Kennwerte unterschiedlicher Dünnschichtkathoden mit nanoskaliger Morphologie validiert. Das Modell sagt eine Oberflächenvergrößerung der Nanokathoden um den Faktor 8 gegenüber einer dichten Dünnschichtkathode voraus. Diese Ergebnisse motivieren zu einer weiteren Optimierung der Mikrostruktur nanoskaliger Kathoden, wobei insbesondere eine Vergrößerung der Kathodendicke zu einer weiteren Verbesserung der elektrochemischen Eigenschaften führen wird.

Die Ergebnisse dieser Arbeit und deren Diskussion zeigen, dass die Korngrenzeffekte in nanoskaligen YSZ-Dünnschichten den Gesamtwiderstand der Probe erhöhen statt ihn zu senken. Daher sollten für die Anwendung in der SOFC, Keramiken mit großen Körnern und wenigen Korngrenzen eingesetzt werden, um die ohmschen Verluste im Elektrolyten zu reduzieren. In LSC-Kathoden hingegen zeigen nanoskalige keramische Körner und eine nanoporöse Struktur exzellente Eigenschaften bei der Sauerstoffreduktion. Dabei werden die Polari-

sationswiderstände bestehender Kathodenkonzepte deutlich unterboten. Die hohe Oberfläche der Nanokathoden senkt die Polarisationsverluste entscheidend. Die Erkenntnisse zur mikrostrukturellen, chemischen und elektrischen Stabilität von nanoskaligen LSC-Dünnschichtkathoden und das Verständnis der elektrochemischen Vorgänge in der Kathode legen damit den Grundstein für den Einsatz nanoskaliger, mischleitender Kathoden im Bereich mobiler SOFC-Anwendungen.

Table of Contents

1 Introduction

1.1 Fuel Cells for Energy Supply

Ever since the beginning of industrialization, fossil fuels - coal, oil and natural gas - have been the major source of energy supply. However, it is certain that the supply of cheap, conventionally produced oil will peak and decline this century. The predictions about "peak oil" run from 2010 by ASPO (Association for the Study of Peak Oil and Gas) to a peak approximately in 2030 by DOE / AIE (US Department of Energy / International Energy Agency) [1]. Then at the latest, an energy revolution to alternative energy sources such as solar and wind will have taken place to cover the worldwide growing need for energy. Meanwhile there are fundamental environmental (*ipcc report* [2]), strategic (*ipcc report* [2]) and economic (*Stern report* [3]) interests for a responsible dealing with fossil fuels. For example, eleven of the last twelve years (1995 – 2006) rank among the twelve warmest years in the instrumental record of global surface temperature (since 1850) – the economic costs of the climate change range between 5% and 20% of the worldwide gross domestic products (several trillion Euros). Therefore, governmental and non-governmental organizations strive to solve present and future energy problems on an international level (cf. UN Climate Change Conference, Bali, Indonesia, 3-14 December 2007 [4] and its analysis by J.L. Morgan, E3G [5]).

Regardless of what the driving force may eventually be, political reason or increasing energy prices, the importance of a more efficient use of energy has been recognized as a key issue for technology development. Considerable aspirations in this context are connected with fuel cells. Interest in these alternative energy-conversion devices has increased rapidly in recent years, whereas the basic principles of fuel-cell operation are known since the early experiments of Schönbein and Grove in the first half of the 19th century. These fuel cells with high-energy conversion efficiency and low emission are promising systems for replacing combustion-based electrical generators at all sizes.

1.1.1 Working Principle of Solid Oxide Fuel Cells (SOFC)

A fuel cell can be defined as a galvanic element, in which the reactants and the products are continuously supplied and removed [6, 7]. A simplified functional principle of a solid oxide fuel cell (SOFC), a concept that is regarded as one of the most promising systems due to its high efficiency and its flexibility in terms of the fuel gas, is schematically shown in Fig. 1. The reactant gases are separated by an ionically conducting oxide membrane, which is usually made of doped zirconium oxide. The chemical potential difference between the reactant gases initiates a driving force for gas compensation through the oxygen ion-conducting

electrolyte. The electrodes facilitate the incorporation and removal of oxygen ions into and from the electrolyte.
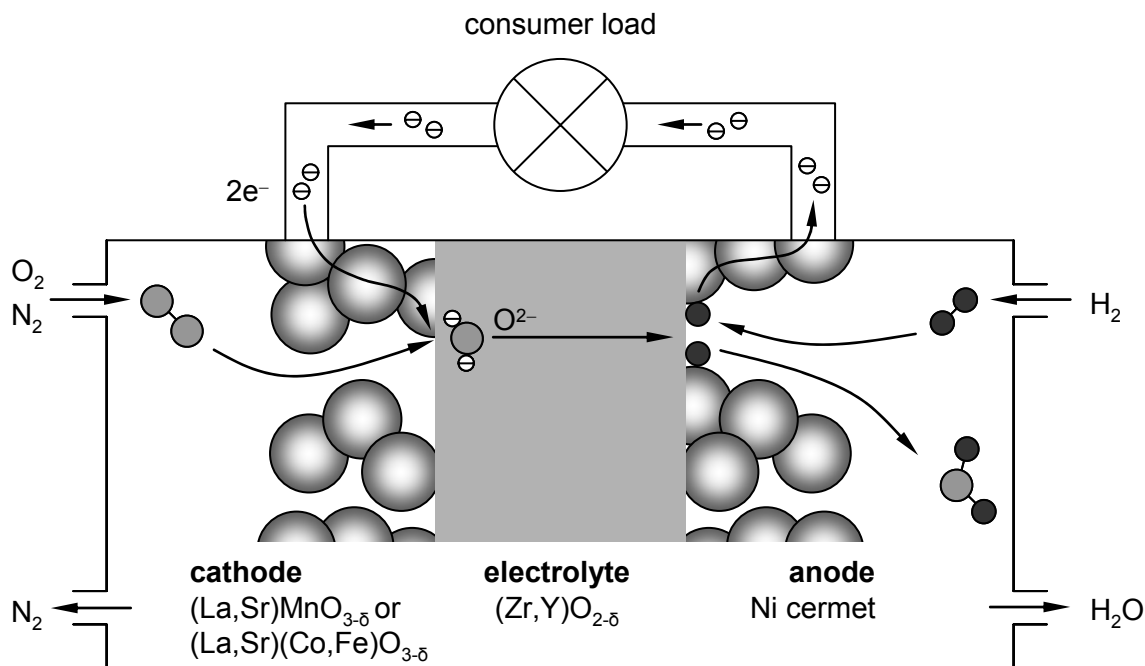
Fig. 1 Schematic SOFC concept [8]
Oxygen and fuel (here H$_2$) react via a dense, oxide ion-conducting electrolyte (e.g. yttria-doped zirconia, YSZ); the spatial separation of reduction and oxidation reaction enables the utilization of the electrons involved in the redox process.

If, for example, hydrogen is used as fuel gas, the following electrochemical reactions occur at the two electrodes:

Cathode:
$$\frac{1}{2}O_2(g) + 2e'(\text{cathode}) \rightarrow O^{2-}(\text{electrolyte})$$
Eq. 1

Anode:
$$O^{2-}(\text{electrolyte}) + H_2(g) \rightarrow H_2O(g) + 2e'(\text{anode})$$
Eq. 2

Sum:
$$\frac{1}{2}O_2(g) + H_2(g) \rightarrow H_2O(g)$$
Eq. 3
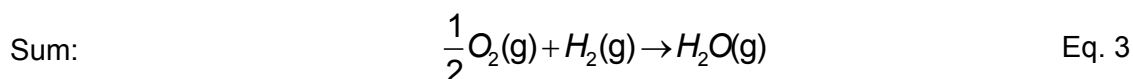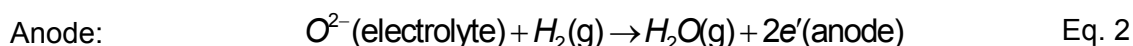
The electronically conducting SOFC cathode (typically lanthanum strontium manganite, LSM) leads the oxidant through its porous channels to the electrolyte, where the oxygen-reduction mechanism takes place (Eq. 1). The region where the electronic conducting phase (cathode), gas phase (porous cathode channels) and ionic conducting phase (electrolyte) meet, is called triple-phase boundary (tpb); the concentration of these active sites determines the electrochemical performance of the cathode. Before incorporation of the oxygen ions into the electrolyte, a variety of steps including adsorption of the molecules, dissociation into oxygen atoms and ionization take place at the cathode. Due to the chemical potential difference, the oxygen ions travel through the electrolyte towards the anode where the redox reaction occurs (Eq. 2). The electrons, which are involved in the electrochemical reaction, are forced

to flow through an outer circuit performing electrical work. In case of an open circuit, the Nernst voltage U_N arises between cathode and anode:

$$U_N = \frac{RT}{2F} \cdot \ln \sqrt{\frac{pO_2(\text{cathode})}{pO_2(\text{anode})}}$$

Eq. 4

where R is the general gas constant, T the absolute temperature, F Faraday's constant and pO_2 the respective oxygen partial pressure at cathode and anode.

In reality, however, the respective electrochemical processes in the cell are lossy. Thus, ohmic losses arise during the transport of charge carriers in the electrodes and in the electrolyte, where the latter (diffusion losses of the oxygen ions) dominate the ohmic part of the total losses. Additionally, polarization losses evolve during the conversion of electronic current into ionic current. Both the ionic transport in the electrolyte and the electrochemical reaction at the electrodes are thermally activated; thus, the ohmic and polarization losses increase with decreasing temperature. (A deeper understanding of the transport properties in the electrolyte and the electrochemical reaction in the cathode is provided in chapter 2.1.2 and chapter 2.2.1, respectively). Due to the losses, the cell voltage U_C always undercuts the Nernst voltage U_N:

$$U_C = U_N - j_L \cdot \sum_k ASR_k$$

Eq. 5

with j_L as load current and k the contributing loss portions, which are given by their respective area specific resistance (ASR).

1.1.2 Goals of SOFC Development

Efficiency and long-term stability are the two main goals of SOFC development, particularly with regard to new applications. Besides commercially available stationary systems, mobile applications like auxiliary power units (APU) [9, 10] or μ-SOFCs [11] as battery replacement are of increasing interest. In the course of that, the operating temperature of the systems need to be reduced from 800 °C ≤ T ≤ 1000 °C to T ≤ 750 °C for APU application and to T ≤ 600 °C for μ-SOFC application. In general, a reduction of the operating temperature offers advantages and bears drawbacks. The material requirements of the system and developing costs are reduced substantially for intermediate-temperature SOFCs (IT-SOFCs) at 500 °C ≤ T ≤ 750 °C. For example, the bipolar plate facilitating the electrical contacting of the fuel cells and providing the supply of the gaseous fuels can be made of highly alloyed ferritic steel as opposed to ceramic interconnects at operating temperatures below 800 °C, which makes the production of the plate suitable for a cheap mass production. Additionally, decreasing operating temperature leads to increased long-term stability and simplified thermal management of the SOFC system. On the other hand, the thermally activated transport processes in solid oxide fuel cells decrease in principle with decreasing operating temperature entailing an increase of ohmic (predominantly electrolyte based) and electrode polarization losses and thereby causing a decrease of SOFC efficiency. However, the increase of power density is a central approach in world-wide SOFC research [12] to further

the competitiveness to existing energy systems. Therefore, the development of highly efficient electrolytes and catalytically effective electrodes at 500 °C ≤ T ≤ 750 °C is of decisive relevance.

On the <u>electrolyte</u>-site the first step to meet these demands was the introduction of thin-film electrolytes (thickness $t \approx$ 10 μm) in anode-supported cells (ASC), which are able to significantly reduce the portion of ohmic losses in comparison to electrolyte-supported cells (ESC, $t \approx$ 150 μm). Besides geometrical optimization, two approaches for higher oxygen-ion conduction of the electrolyte itself are pursued: a) the development of new materials (e.g. doped lanthanum gallate, $(La,Sr)(Ga,Mg)O_{3-\delta}$, LSGM [13]) with high oxygen-diffusion properties and b) the usage of a tailored microstructure of the electrolyte taking advantage of potential grain-size effects. (However, the role of the grain boundaries on the transport properties of charge carriers is still object of controversial discussions and will be subject matter of this work).

For the development of <u>high-performance cathodes</u>, the following requirements have been stipulated [14]: beneficial chemical diffusion and oxygen-exchange properties of the cathode material (I), adjusted coefficients of thermal expansion (TEC) (II) and chemical compatibility (III) between cathode and substrate and a tailored microstructure (IV).

Some of these requirements have already been fulfilled: Mixed ionic-electronic conducting (MIEC) iron- and cobalt-containing perovskites from the $(La,Sr)(Co,Fe)O_{3-\delta}$ (LSCF) material group are already known for their high oxygen permeability (I) [15] and high electrocatalytic activity [16-18]. These MIEC materials significantly enlarge the area where the oxygen reduction can take place and thereby provide lower cathode polarization losses compared to solely electronic conducting cathode materials like $(La,Sr)(Mn)O_{3-\delta}$ (LSM). The TEC of the cathode (II) is usually adjusted by the stoichiometry on the B-site (Co, Fe) [19]; the chemical compatibility (III) is ensured by the introduction of a ceria-based interlayer between cathode and electrolyte [20, 21]. The role of the microstructure (IV), however, is still unclear.

1.1.3 Potential of Nanoscaled Thin Films

The decrease in physical dimensions down to the nanometer scale is often linked with a dramatic change of the physical and electrochemical properties of materials [22, 23]. Enhanced ionic conduction in nanocrystalline films, when it occurs, is attributed to the role of the grain boundaries. Grain boundaries are regarded as possessing high defect densities and/or enhanced mobilities [23]. Moreover, the adjoining space-charge regions may hold increased ionic defect densities. A positive space charge would be required to increase the oxygen-vacancy density. These effects offer a potential means for increasing the ionic conductivity [24, 25], particularly in nanostructured materials with a very high fractional volume represented by the grain boundaries. Nanostructured thin-film electrolytes in anode-supported cells (ASC) may therefore be able to reduce the portion of ohmic losses significantly.

With respect to cathode application, higher ionic conductivity inevitably leads to an enlargement of the electrochemically active volume and a potential increase of the cathode performance. Furthermore, Adler, Lane and Steele [26] suggested that the cathode oxygen-reduction performance depends amongst others on the active inner surface of the cathode. By the deliberate introduction of nanoporosity in LSC thin-film cathodes, the inner surface area would substantially increase entailing an increase of the electrochemically active cathode volume and low cathode polarization losses.

Using nanostructured ionic and mixed ionic-electronic conducting materials within fuel cells could potentially facilitate lower temperature operation. However, thorough studies of the thin-film processing, the structural and chemical stability of the thin films and the transport characteristics and electrochemical properties are necessary to gain an understanding, which is prerequisite for the utilization of nanoionics effects. At the best, nanoscaled thin films applied in solid oxide fuel cells provide faster start-up times, improved stability, reduced cost and less complicated thermal management.

1.2 Goal of this Work and Outline

For the development of SOFC systems in the intermediate-temperature regime of $500\ °C \leq T \leq 750\ °C$, nanoscaled thin films are of substantial interest. Goal of the present work is the study of the role of interfaces, grain size and porosity in nanoscaled electrolyte and cathode thin films. Thereto, thorough investigations of the microstructural, electrical and electrochemical properties of the thin films are performed to derive an understanding of their charge-carrier transport. Established transport models are evaluated and applied at the nanoscale.

One of the main objectives of this work is the processing, design and electrochemical characterization of nanoscaled electrolyte and electrode structures, where the electrolytes are realized as nominal 8 mol% yttria-doped ZrO_2 (YSZ) and the cathodes are realized as $(La_{0.5}Sr_{0.5})CoO_{3-\delta}$ (LSC) thin films. With respect to SOFC application, special emphasis is put on the stability of the thin films and the cathode – electrolyte interface at the nanoscale. The restrictions concerning lifetime and upper temperature limit of the individual thin films are examined by detailed microstructural analyses as well as thermodynamic calculations and electrical investigations.

In the following chapter 2 (p. 7), the fundamentals of the material systems YSZ and LSC are developed. Special emphasis is put on the transport phenomena of the material systems and the chosen stoichiometry. The sol-gel processing as well as the comprehensive experimental efforts for the characterization of the nanostructured layers including complementary techniques like electrochemical impedance spectroscopy (EIS) in a symmetrical setup and the use of microprobes, scanning electron microscopy (SEM), (high-resolution) transmission electron microscopy (TEM, HRTEM) and thermodynamic calculations are described in chapter 3 (p. 43). The results of the performed experiments are presented in detail in chapter

4 (p. 55). A comprehensive understanding of the grain-size effects and transport properties of oxygen ions in YSZ thin films is derived by the discussion of the results with respect to the fundamentals (chapter 5.1, p. 93). Subsequently, the oxygen-reduction mechanism in nanoscaled LSC thin films with special emphasis on stability considerations is discussed (chapter 5.2, p. 103). A brief summary of the essential findings of this work is given in chapter 6 (p. 117).

2 Fundamentals

This chapter comprises the fundamental properties of yttria-doped zirconia electrolytes (2.1) and lanthanum strontium cobaltite cathodes (2.2) with regard to SOFC application. Special emphasis is put on the chemical stability of the material systems and the transport processes of the charge carriers. Furthermore, the stoichiometry of $(Zr_{0.84}Y_{0.16})O_{2-\delta}$ and $(La_{0.5}Sr_{0.5})CoO_{3-\delta}$ is motivated. A literature review of thin-film deposition methods is given in 2.3 exemplarily for YSZ and LSCF thin films.

2.1 Yttria-Stabilized Zirconia (YSZ) Thin-Film Electrolytes

Although many oxide formulations have been examined during the past decades, zirconia-based compositions are still the best electrolytes at present owing to their beneficial properties regarding SOFC application (2.1.1) and the well-understood material properties of polycrystalline YSZ electrolytes (2.1.2). However, a substantial decrease of the mean grain size into the nanometer regime may change these material properties by grain-boundary effects (2.1.3). These *nanoionics* effects potentially lead to better ionic transport properties meeting the need for high ionic conduction at IT-SOFC application. For the calculation of the specific grain-boundary properties and a deeper understanding of the transport phenomena, the so-called *brick-layer model* is applied (2.1.4).

2.1.1 YSZ Electrolytes in SOFC Application

Several requirements are addressed to SOFC electrolytes [13, 27]: Firstly, electrolytes must be gas-tight to separate two gas-filled compartments with different oxygen partial pressures. Secondly, any substantial electronic conduction would short-circuit the electrolyte internally. The electrolyte must therefore be purely ionic conducting, thus enabling only the transport of oxygen ions from the cathode to the anode. Thirdly, the electrolyte needs to be chemically stable under oxidizing and reducing atmospheres to prevent chemical decomposition. Chemical interface reaction between the electrolyte material and the electrodes reduces the electrochemical performance of the cell as discussed exemplarily for the cathode-site in chapter 2.2.4. Fourthly, mechanical stability of the electrolyte is an important issue in the case of electrolyte-supported cells (ESC). Fifthly, the SOFC undergoes temperature cycles during production and operation, which requires adjusted thermal expansion behavior between the electrolyte and the electrodes to prevent cracking of the electrolyte or delamination at the cathode / electrolyte interface in the course of thermocycling. Lastly, low cost materials and processing techniques are favorable.

2.1.2 Material Properties of $(Zr_{0.84}Y_{0.16})O_{2-\delta}$

Oxygen-ion conductivity was first observed in 15 atm% Y_2O_3 doped ZrO_2 (YSZ) by Nernst already in the 1890s [28]. Ionic transport in zirconia is facilitated via oxygen vacancies, which arise by a negligible extent by thermodynamic reactions (intrinsic defects) and mainly by cation doping of zirconia (extrinsic defects). The conductivity not only depends on the concentration of the oxygen vacancies, but also on the mobility of the oxygen ions. The mobility, however, is determined by the affinity of the dopant to form clusters, by the ion radius of the cation with respect to the host lattice and by the microstructure of the compound including grains and grain boundaries. Based on different dopants, it is shown in this chapter that the cation yttrium (Y) not only governs the transport properties of zirconia but also its crystal structure.

<u>Ionic Conductivity</u>

In the pure, undoped zirconia (ZrO_2) compound (Fig. 2 left), very few intrinsic defects are formed thermodynamically according to

$$O_O^x \leftrightarrow V_O^{\bullet\bullet} + 2e' + \frac{1}{2}O_2$$

$$\left[V_O^{\bullet\bullet}\right]n^2 = K_0 \cdot e^{-\frac{\Delta G}{kT}} \left[O_O^x\right]pO_2^{-\frac{1}{2}}$$

Eq. 6
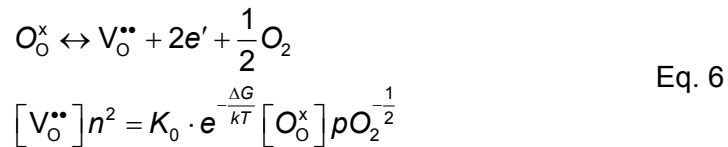
where O_O^x denotes an oxygen ion on the regular lattice site, $V_O^{\bullet\bullet}$ a double negatively charged oxygen vacancy, n the concentration of electrons and K_0, ΔG and k are constants; the Kröger-Vink notation is used [29]. Eq. 6 shows that the intrinsic defects (oxygen vacancies) increase with temperature and decrease with ambient pO_2. At the same time, electronic charge carriers accumulate with T and deplete with pO_2, respectively.
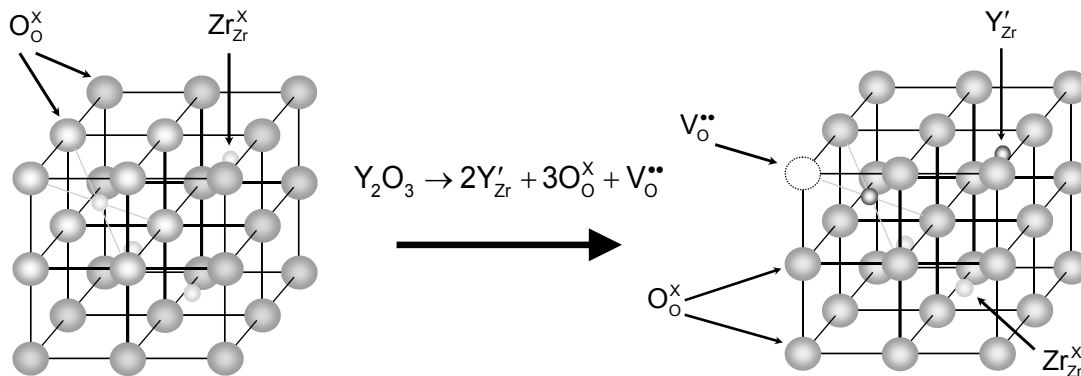
Fig. 2 Effect of Y doping on the ZrO_2 fluorite structure [27]
Oxygen vacancies emerge upon doping of tetravalent Zr by trivalent Y.

The doping of zirconia with earth alkali or noble earths (CeO, CaO, MgO, Yb_2O_3, Gd_2O_3, Nd_2O_3, Y_2O_3, Sc_2O_3, etc.) drastically increases the oxygen-vacancy concentration, entailing extrinsic defects, according to

$$MeO \rightarrow M_{Zr}^{''} + O_O^x + V_O^{\bullet\bullet}$$

$$Me_2O_3 \rightarrow 2M_{Zr}^{'} + 3O_O^x + V_O^{\bullet\bullet}$$

Eq. 7
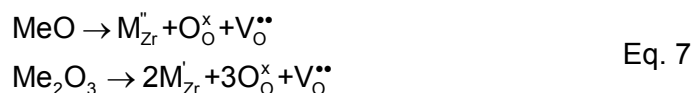
as depicted in Fig. 2 in the case of Y_2O_3. For every two Y ions incorporated into the zirconia host lattice (Y_{Zr}'), one oxygen vacancy $V_O^{\bullet\bullet}$ is generated. Exemplarily, the majority charge carriers of 10 mol% Y_2O_3 doped ZrO_2 (10YSZ) are plotted in Fig. 3a with respect to pO_2 and T.
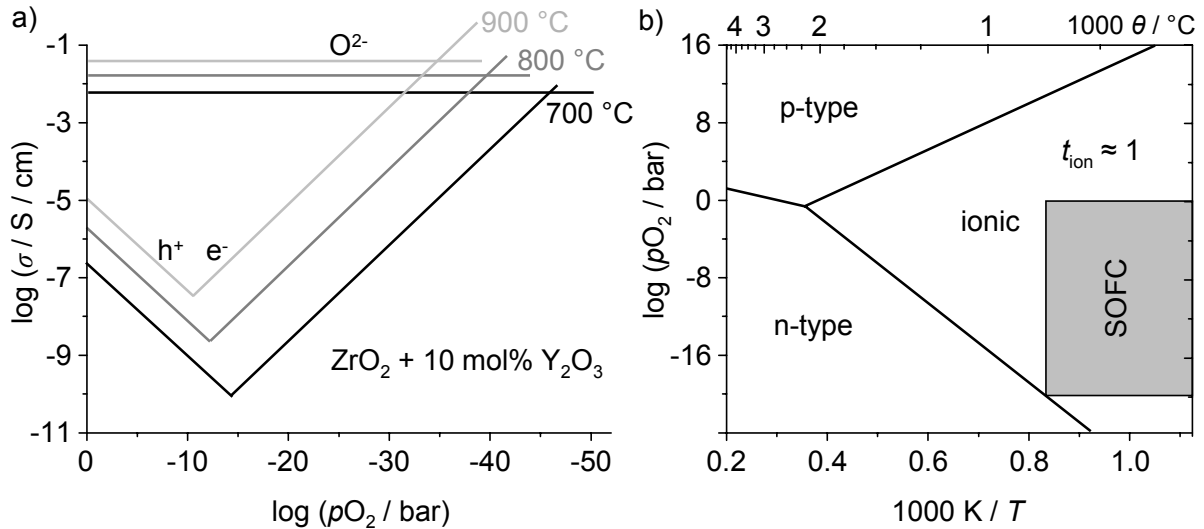
Fig. 3 Electronic (electrons, holes) and ionic (oxygen ions) conductivity of 10YSZ a) Electrical conductivity σ plotted vs. pO_2; diagram redrawn after [30] b) dominant charge transport with respect to pO_2 and T; grey area indicates operation regime of the solid oxide fuel cell (SOFC).

Whereas the ionic conduction (O^{2-}) is due to extrinsic defects virtually independent from the oxygen partial pressure and at constant high levels, holes (h^+) and electrons (e^-) arise from intrinsic defects and dominate the electronic conductivity at very low and very high pO_2, respectively. However, except for $pO_2 < 10^{-30}$ bar and $pO_2 > 10^8$ bar (900 °C), the overall conductivity is dominated by ionic charge transport. This is far beyond the normal SOFC operating range of $0.21 - 10^{-20}$ bar and $T \leq 950$ °C, where ionic conduction prevails (grey area in Fig. 3b). This regime is characterized by an oxygen-ion transference number of $t_{ion} \approx 1$.

Generally, an increase of the cation doping increases the concentration of charge carriers and thereby the ionic conductivity, which is shown in Fig. 4a for different cations at 1000 °C. However, the curves run through a maximum of the conductivity und decline, depending on the dopant, at 7.5 < mol% M_2O_3 < 11. The decrease in conductvity is related to diminished oxygen-ion mobility in the lattice. At high cation concentrations, clusters of the form $\left[Y_{Zr}'' - V_O^{\bullet\bullet} \right]^x$, $\left[Y_{Zr}' - V_O^{\bullet\bullet} \right]^{\bullet}$ or $\left[Y_{Zr}' - V_O^{\bullet\bullet} - Y_{Zr}' \right]^x$ are generated [31-36]. These associates accumulate due to Coulomb's interactions between the vacancies and the cations, which decrease both the mobility of the oxygen ions and the concentration of active vacancy sites and entail a decrease of the electrical conductivity at high dopant concentrations (Fig. 4a).

The tendency to form clusters increases with increasing mismatch between the ion radius of the cation and the ion radius of zirconium. The activation energy for association or clustering

H_A (∇) decreases with increasing mismatch of the radii from Sc to Gd (Fig. 4b). Therefore, less Zr^{4+} ions can be replaced by M^{3+} without clustering, which explains the shift of the maximum conductivity from Sc to Gd (Fig. 4a).
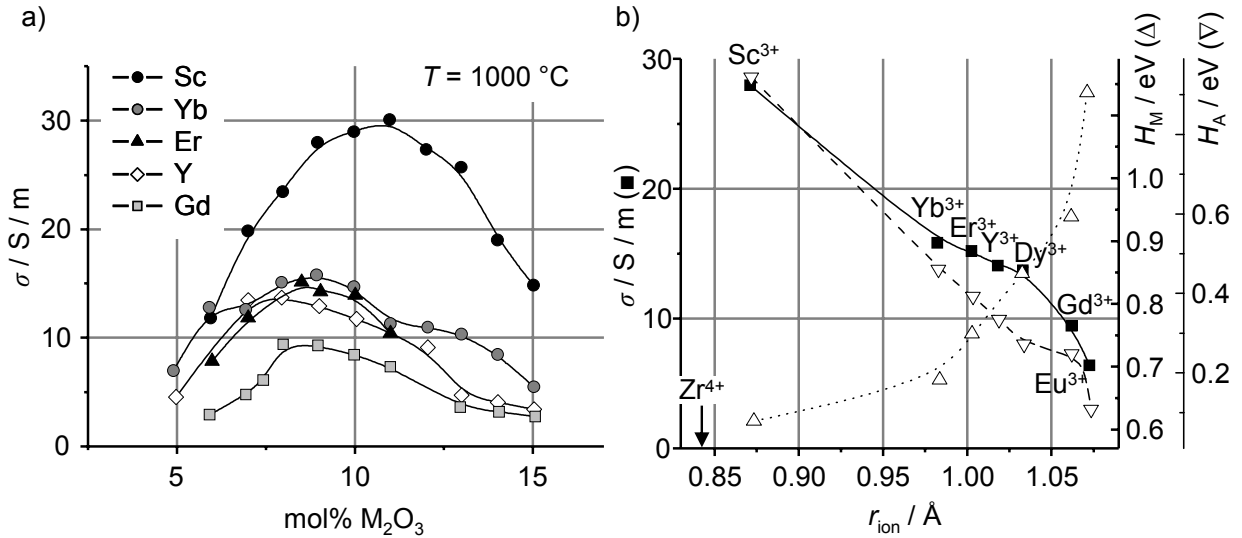
Fig. 4 Influence of the dopant on the electrical conduction of ZrO$_2$

a) The oxygen-ion conductivity of doped zirconia increases upon increasing dopant concentration until a maximum is reached and clusters are formed; diagram redrawn after [37]

b) electrical conductivity σ (■), ion-migration enthalpy H_M (Δ) and association enthalpy H_A (∇) versus dopant ionic radius r_{ion}; diagram redrawn after [38].

The mobility of the oxygen ions does not only depend on clusters but also on lattice distortions, which arise if the ion radius of the cation is greater than the ion radius of the host lattice. The more the cation radius is adapted to the ion radius of Zr^{4+} (r_{ion} = 0.84 Å), the less the transport path of the anions is disrupted and the higher is the mobility of the oxygen ions. Therefore, Sc-doped (r_{ion} = 0.87 Å) zirconia shows a higher conductivity than Y-doped (r_{ion} = 1.02 Å) zirconia and Gd-doped (r_{ion} = 1.06 Å) zirconia. Fig. 4b depicts the maximum conductivity of doped zirconia with respect to cation radius. For a small deviation in ion radii between dopant and Zr^{4+}, the migration enthalpy H_M (Δ) is low and therefore the mobility high. For a large deviation of the radii, the activation energy for migration is increased and consequently the mobility and the conductivity decreased.

The oxygen-ion transport in doped zirconia takes place by means of a hopping mechanism via the vacant lattice sites, resulting in a thermal activation behavior of the diffusion coefficient according to [34]

$$D = D_0 \cdot e^{-\frac{E_A}{k \cdot T}} \qquad \text{Eq. 8}$$

where D_0 is a constant, E_A the activation energy of the hopping mechanism, k Boltzmann constant and T the absolute temperature. The activation energy E_A comprises of H_M and H_A [13]. In case of a doped zirconia compound lacking of clusters, E_A equals H_M. By application of the Nernst-Einstein equation [34], the mobility of the oxygen ions can be derived by

$$\mu = \frac{qD}{kT} \qquad \text{Eq. 9}$$

with the electrical charge q. The oxygen-ion conduction σ is therefore exponentially temperature dependent:

$$\sigma = nq\mu$$

$$\sigma = \frac{\sigma_0}{T} \cdot e^{-\frac{E_A}{k \cdot T}} \qquad \text{Eq. 10}$$

where σ_0 is a constant.
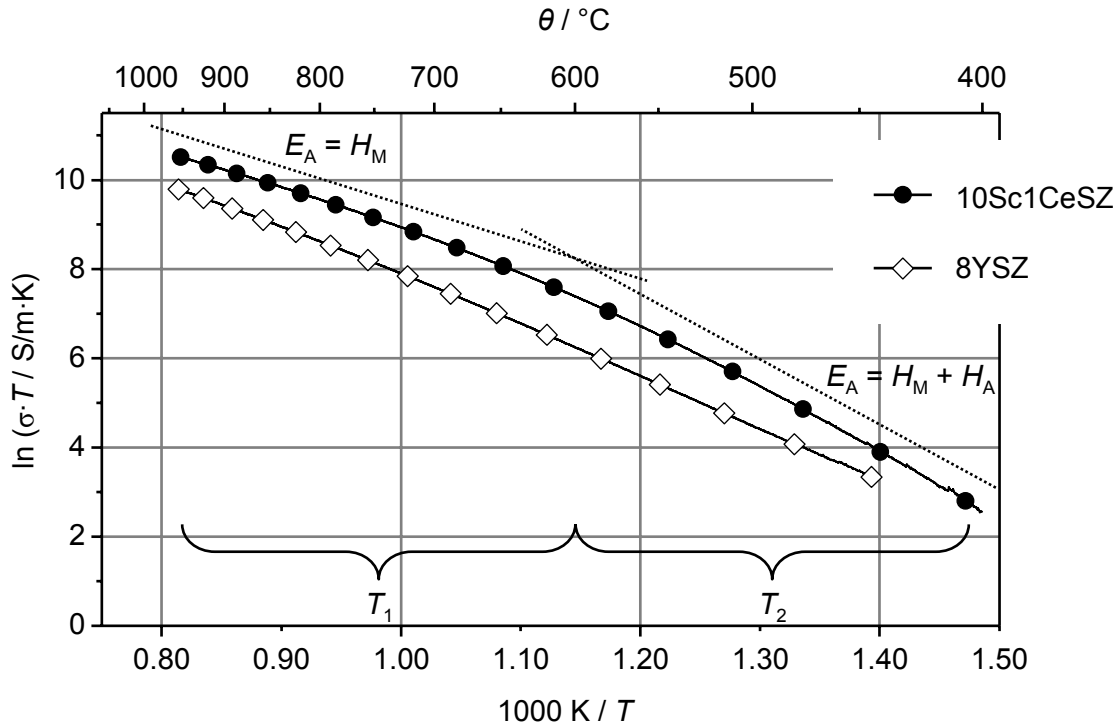
Fig. 5 Arrhenius plot of the electrical conductivity of 10Sc1CeSZ and 8YSZ [38]
Both data sets show Arrhenius-type temperature dependencies with a change in the activation energies at $T \approx 600$ °C.

Fig. 5 depicts the electrical conductivity of 10 mol% scandia and 1 mol% ceria-doped zirconia (10Sc1CeSZ) and 8 mol% yttria-doped zirconia (8YSZ) [38]. The data show Arrhenius-type temperature dependencies at 600 °C $\leq T_1 \leq$ 950 °C and 400 °C (450 °C) $\leq T_2 \leq$ 600 °C. Both temperature regimes show different activation energies. To initiate ionic charge transport in the regime T_2, the sum of migration and association energy corresponds to the total activation energy ($E_A = H_M + H_A$). With increasing temperature, the clusters dissociate completely to free $V_O^{\bullet\bullet}$, thereby increasing oxygen-ion mobility and free charge-carrier concentration. In this regime, the association enthalpy is reduced [31, 39]. Consequently, the high-temperature regime T_1 is solely dominated by the migration energy.

Within polycrystalline electrolytes, the transport properties do not only depend on the dopant but also on the microstructure of the sample. The symmetry of the crystal lattice is disrupted at the grain boundaries, which impedes the migration of oxygen ions through the specimen.

Therefore, several groups found the activation energy of the grain-boundary conductivity higher than the activation energy of the bulk transport. This applies especially for reduced temperatures. Therefore, the evaluation of the grain-size effects was studied in a reduced temperature regime at 200 °C ≤ T ≤ 400 °C (cf. chapter 3.3.1). The general trend is that the activation energy of ionic conduction in the grains σ_g ranges between 0.93 eV and 1.09 eV, whereas the activation energy of the grain-boundary conduction σ_{gb} is higher (1.13 eV ≤ E_A ≤ 1.18 eV, Table 1). The higher activation energy of the grain-boundary process might indicate a *blocking* of the trespass of charged oxygen ions via the grain boundaries at the microscale. However, the transport properties and the role of the grain boundaries at the nanoscale might differ significantly (cf. 2.1.3).

Table 1 Activation energies for YSZ as a function of temperature

Temperature regime / °C	Activation energy E_A / eV			Stoichiometry	Source
	total	grain boundary	grain		
200 – 400	-	-	1.08	8YSZ	[40]
200 – 500	-	1.16	1.05	8YSZ	[41]
200 – 600	1.06	-	-	7YSZ	[42]
300 – 650	-	1.13	0.93	8YSZ	[43]
325 – 425	-	-	1.02	8YSZ	[44]
327 – 727	-	1.13	1.08	8YSZ	[45]
375 – 475	1.03	1.18	0.98	8YSZ	[46]
395 – 500	1.11	-	-	8YSZ	[44]
600 – 800	0.92	-	-	8YSZ	[47]
650 – 1000	-	1.13	1.09	8YSZ	[43]
850 – 1000	0.88	-	-	8YSZ	[44]
950 – 1050	0.82	-	-	8YSZ	[48]

Further oxygen-ion conductors like doped ceria (CeO_2) [49] and lanthanum gallate (LSGM: $(La_{1-x}Sr_x)(Ga_{1-y}Mg_y)O_{3-\delta}$, x,y = 0.1 ... 0.2) [50] have been suggested as a replacement of doped zirconia due to their substantially increased ionic conductivity – especially at reduced operating temperatures – and their chemical compatibility with state-of-the-art cathode materials. However, these alternative electrolyte materials bear disadvantages concerning electronic conduction (ceria, [51, 52]) or chemical instability (lanthanum gallate, [53]) in a reduced environment, chemical incompatibility with Ni anodes (lanthanum gallate) or poor mechanical stability (ceria, lanthanum gallate). Although Sc-doped zirconia features excellent chemical and mechanical stability and high ionic conductivity, the price and availability of scandia is a drawback in terms of industrial application. Until today, 8 mol% Y_2O_3 stabilized ZrO_2 is still the state-of-the-art material for SOFC electrolytes with favorable properties regarding oxygen-ion transport, mechanical stability, chemical stability and production costs that meet the requirements for SOFC application best.

Crystal Structure
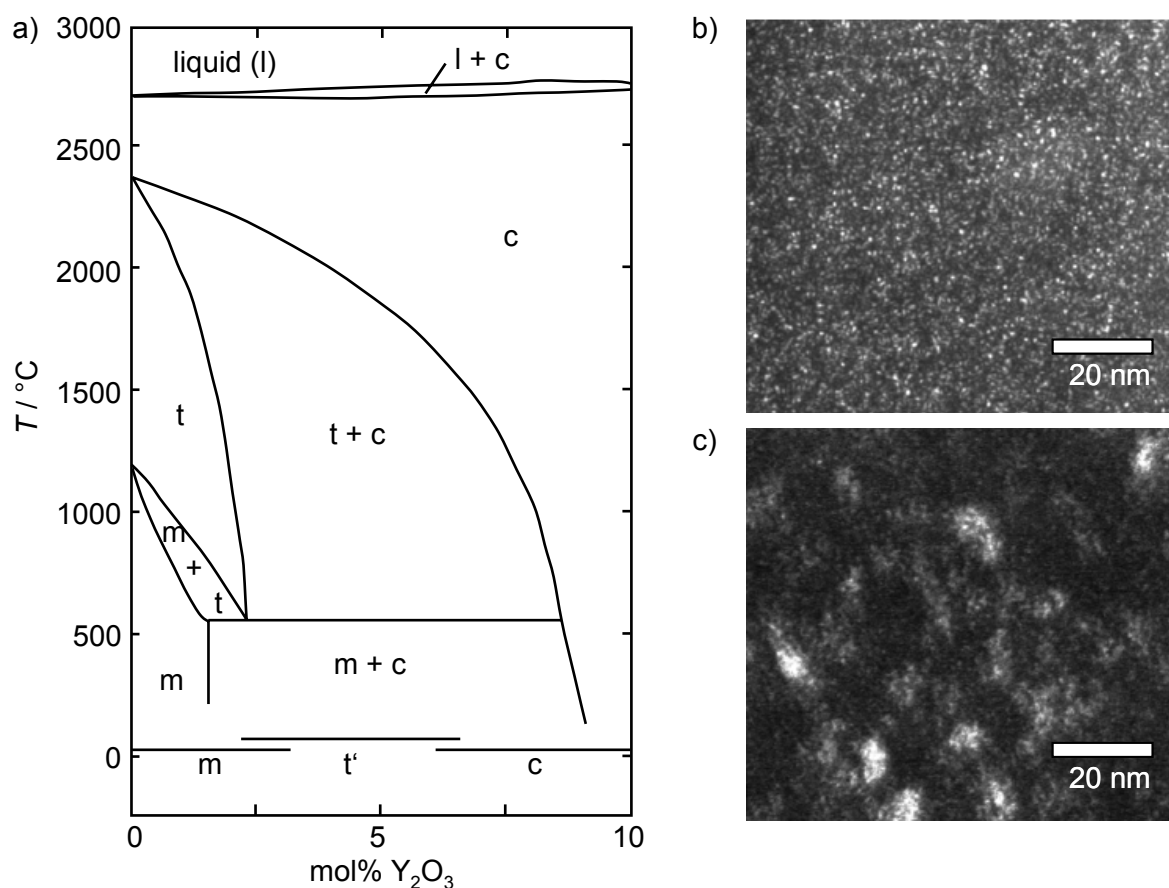
Fig. 6 Chemical phase stability of the system ZrO$_2$ – Y$_2$O$_3$

Phase diagram of Y$_2$O$_3$-stabilized ZrO$_2$ according to [54]; b) and c) depict dark-field images taken with a (112) reflection of the tetragonal phase of b) as-prepared 8YSZ (sintering: T = 1550 °C) and c) 8YSZ after heat treatment at 950 °C (2500 h) and current load (j = 0.17 A / cm²) [55]; the tetragonal precipitates appear as bright contrast.

The dopant concentration does not only govern the transport properties of yttria-doped zirconia but also determines the crystal structure of the lattice. At high temperatures, zirconia crystallizes in the fluorite structure, which is a face-centered cubic arrangement (Fig. 7a). The oxygen anions occupy the tetrahedral sites forming a cubic anionic sublattice in the fluorite structure.

Zirconia exhibits three polymorphs [13]: The crystal structure is monoclinic (m) at room temperature (Fig. 7c), undergoes a phase transition to tetragonal (t) at 1170 °C (Fig. 7b) and exhibits a cubic (c) structure from 2370 °C until 2680 °C (Fig. 7a), which is the melting point of zirconia. The resulting volume changes during phase transition drastically reduce the mechanical stability. By doping with Y$_2$O$_3$ or other earth alkali or noble earths, the tetragonal or cubic structure can be stabilized, eventually even down to room temperature. Fig. 6a depicts the phase diagram of ZrO$_2$ - Y$_2$O$_3$ with respect to temperature according to [13].

Besides the cubic, tetragonal and monoclinic phase, a metastable t' phase arises upon quenching from the cubic or tetragonal phase (for YSZ ca. 3.5 to 7 mol% [40]).

a) cubic   b) tetragonal   c) monoclinic

a = 0.512 nm   a = 0.509 nm   a = 0.516 nm
                  c = 0.518 nm   b = 0.519 nm
                                         c = 0.530 nm
                                         β = 81 °
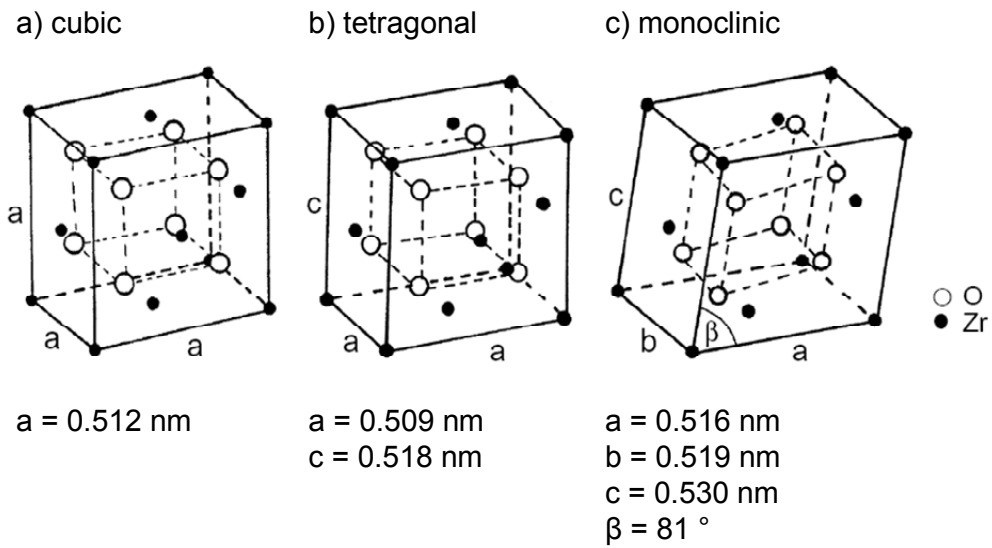
Fig. 7 The three polymorphs of zirconia
Comparison of the a) cubic, b) tetragonal and c) monoclinic structure and the respective lattice constants of ZrO$_2$ [40].

Relevant for industrial application are so-called TZP ceramics (TZP: tetragonal zirconia polycrystal), where the zirconia is doped with e.g. 3 mol% yttria (3YSZ).
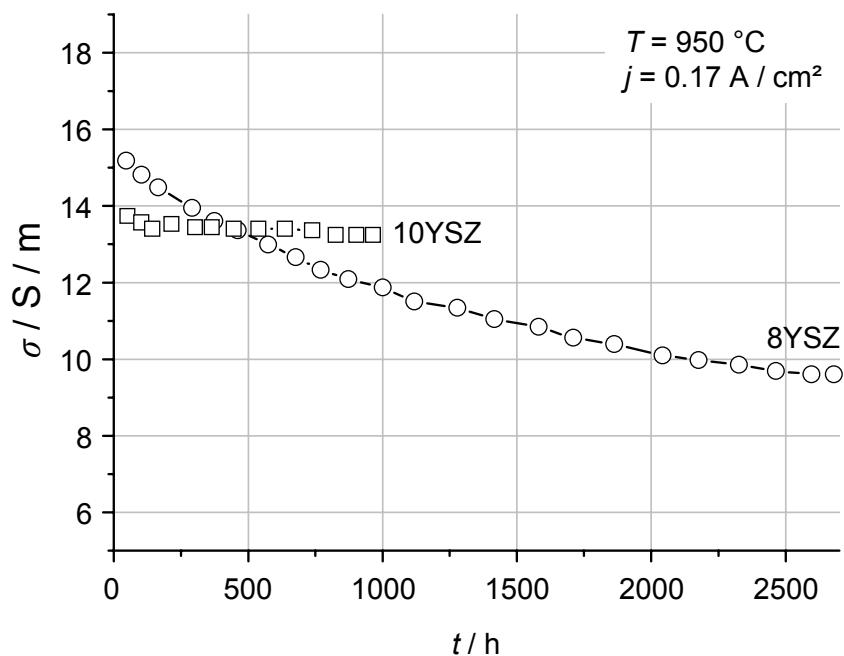
Fig. 8 DC conductivity of 8YSZ and 10YSZ as a function of time at 950 °C [55]
The degradation of the electrical conductivity is linked to the tetragonal precipitates in 8YSZ. The 10YSZ specimen, however, is considered as FSZ.

These ceramics feature a fine microstructure with grain sizes below 500 nm. Thereby, the grains interfinger and prevent the phase transition from t → m according to Fig. 6a, thus stabilize the tetragonal phase of the material. Furthermore, the TZP ceramic features good mechanical properties. For cubic stabilization (FSZ: fully stabilized zirconia), the minimum of doping is 8 mol% Y_2O_3, which coincides with the maximum electrical conductivity (Fig. 4a). New findings derived from electron microscopic studies by Butz et al. [55], however, show that the doping must exceed 8 mol% Y_2O_3 to achieve full cubic stabilization. The extensive TEM studies revealed the existence of tetragonal precipitates in 8YSZ. These tetragonal precipitates appear as bright contrast in Fig. 6b in as-prepared 8YSZ ceramics. After heat treatment at 950 °C and electrical load (j = 0.17 A / cm²) over a duration of 2500 h the precipitates have grown (Fig. 6c) causing a degradation of the electrical conductivity of the electrolyte (Fig. 8, ○) [55]. Upon increase of the Y concentration to 10 mol% (□), however, a stabilization of the electrical degradation was yielded. The authors concluded that a refinement of the phase diagram of the ZrO_2 – Y_2O_3 system is necessary [55]. These observations coincide with the findings of [43, 54], who suggested an Y_2O_3 content of at least 9.5 mol% for full cubic stabilization from room to melting temperature.

<u>Dielectric Properties</u>

The knowledge of the polarization properties of yttria-doped zirconia allows the modeling of its frequency-dependent impedance. By this, characteristic thin-film properties like the specific conductivities, i.e. the electrical conductivity of a single grain boundary, and the specific grain-boundary thickness can be calculated as discussed in chapter 2.1.4.

In general, the relative permittivity ε_r is given by the Clausius-Mosotti equation:

$$\frac{\varepsilon_r - 1}{\varepsilon_r + 2} = \frac{\alpha}{3V\varepsilon_0} \qquad \text{Eq. 11}$$

where α is the polarizability, V the volume of the unit cell and ε_0 the permittivity of free space. Whereas α is given by electron and ion polarization and is almost independent from Y_2O_3 doping, the volume of the lattice changes upon phase change [56]. During the transition from m → t, the unit-cell volume decreases yielding an increase of ε_r. From t → c, the volume change entails a decrease of the dielectric constant. As an example, Thompson et al. [56] found the relative permittivity ε_r to alter from about 23 over 42 to 40 upon change of the crystal structure from monoclinic (pure ZrO_2) over tetragonal (3YSZ) to cubic (8YSZ). However, literature values for 8 mol% yttria-doped zirconia scatter significantly ranging from 28.7 [57] over 29 [58], 38 [59], 40 [56] and 55 [41] to 60 [60, 61].

2.1.3 Reduction of Particle Size: *Nanoionics*

In general, Tuller [22, 23] and Maier [24, 25] suggested that a substantial decrease of the average grain size into the nanometer regime could lead to enhanced ionic conductivity through grain-boundary effects and therefore to a remarkably improved performance of solid-state electrochemical devices. Thereby, Maier distinguishes *trivial size effects* from *true size*

effects [62]. Where the former describe effects that equally occur at single interfaces, but are augmented by the high interfacial density, the latter involves intrinsic modifications of the local physical properties. Due to the segregation of impurities and dopants to the grain boundaries, charge concentration and mobility might be increased along the grain boundaries (black arrows, Fig. 9a). At the nanoscale, the increased grain-boundary density would entail beneficial transport properties compared to the polycrystalline material (which would be an example for a *trivial size effect*). Across the grain boundaries, the impact of the potential barrier might be reduced at the nanoscale if the Debye length λ is greater than the grain size d, where λ is the distance, over which the electrical potential drops to e^{-1} of its initial value. This would even lead to enhanced conduction perpendicular to the grain boundaries (white arrows, Fig. 9a) compared to the polycrystalline material (this would be an example for the *true size effect*).

Therefore, nanostructured systems with their significantly larger density of interfaces and grain boundaries might comprise improved transport properties (Fig. 9b). For the electrolyte-site, higher ionic conductivity allows the application of SOFCs in a reduced temperature regime without bearing the disadvantage of higher ohmic losses. For the electrode-site, increased oxygen-diffusion properties are desired as well since they lower ohmic losses in mixed ionic-electronic conducting cathodes (cf. 2.2.1) and increase the utilization range, where the electrochemical reaction takes place (cf. 2.2.3). Both effects are eligible to increase SOFC performance in a reduced temperature regime.
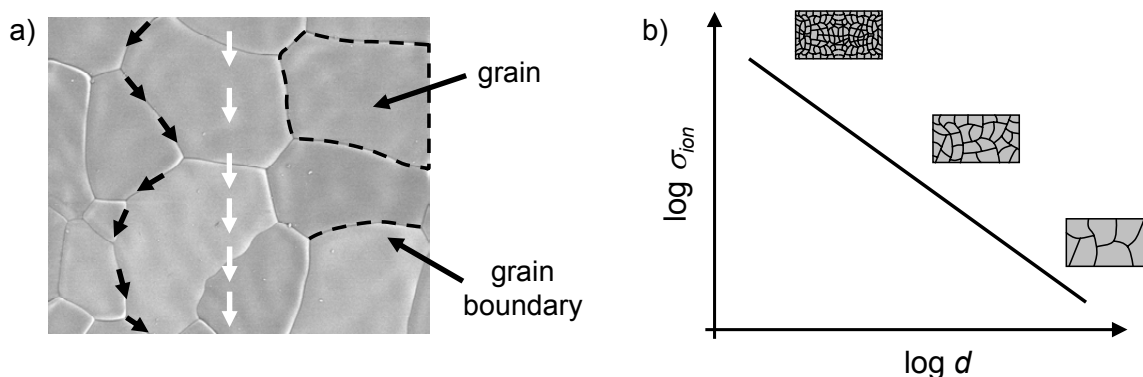
Fig. 9 Principle grain-boundary effects on the transport properties
a) Transport paths in polycrystalline materials with respect to microstructure; b) potential increase of the ionic transport properties at the nanoscale.

Space-charge regions play an essential role for enhanced conduction at boundaries. According to the core-space charge layer model [63], a grain boundary consists of a grain-boundary core and two adjacent space-charge layers. Charged species, impurities, dopants or defects, which segregate to the grain boundaries to lower the strain and the electrostatic energy of the system, are compensated by the formation of space charges in the adjoining grains. If the bulk defect with high mobility is accumulated in the space-charge region, the overall conductivity of the solid should increase. For nanostructured YSZ thin films, a positive

space charge with a high amount of $V_O^{\bullet\bullet}$ would be required to increase the oxygen-vacancy density (Fig. 10). Consecutively, a negatively charged grain-boundary core, i.e. the depletion of $V_O^{\bullet\bullet}$ is needed to preserve electroneutrality. Reducing the mean grain size d into the nanometer regime and ultimately lowering the grain size to $d \leq 4\lambda$, where λ is the Debye length, leads to an overlap of the space-charge regions. Thus, the defect density no longer approaches the bulk value at the center of the particle. The entire particle is expected to show enhanced ionic conduction [22]. Whereas the oxygen vacancies are considered mobile even for $T \ll 500$ °C, the built-in cation concentration (Y) is constant with the space coordinate x in the investigated temperature regime.
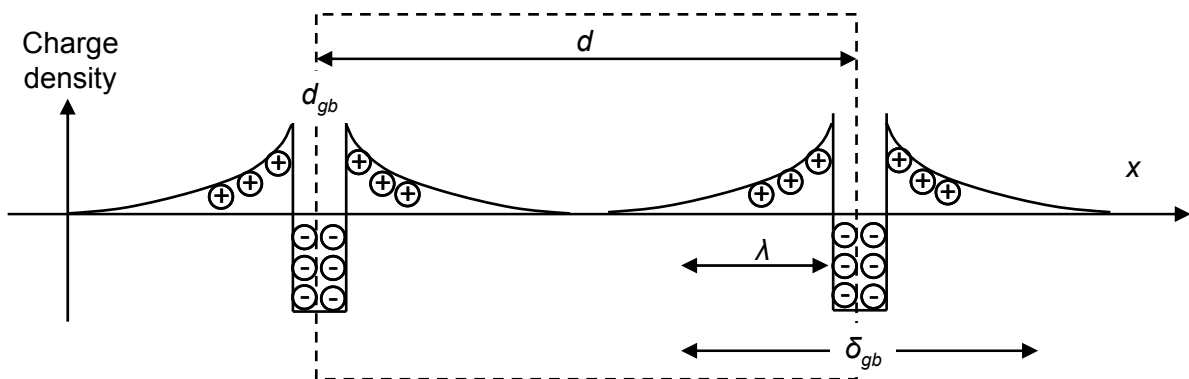
Fig. 10 Schematic representation of two grain boundaries
The area enclosed by the dotted line is electrically neutral [64]. Decreasing the grain size d into the range of the Debye length λ ($d \leq 4\lambda$) leads to an overlap of the space-charge regions [65]. d_{gb} and δ_{gb} denote the *microstructural* and *electrical* grain-boundary thickness, respectively, where the latter includes potential space-charge regions on both sides of the grain-boundary core.

For yttria-stabilized zirconia, an enhanced performance with decreasing grain size and therefore increased fractional volume of material near the disrupted boundary region was reported by several groups. Kosacki et al. [66] reported for nanocrystalline YSZ an increase of two order of magnitude in conductivity compared to polycrystalline and single crystalline YSZ. In a later work, Kosacki et al. [67] observed significantly enhanced electrical conductivity of highly textured 10YSZ thin films (thickness $t < 60$ nm) deposited onto MgO substrates. Interfacial conductivity was found to be over three orders of magnitude larger than lattice limited conductivity. Cheikh et al. [68] also reported on a pronounced contribution of grain boundaries to the ionic conductivity with respect to the volume contribution within 4YSZ material with an average grain size of 300 nm. Additionally, enhanced oxygen diffusivity at the interfaces compared to oxygen bulk diffusion within 7YSZ was shown in the work of Brossmann et al. [69]. Similar effects of enhanced oxygen diffusion in nanocrystalline 6.9YSZ samples were observed by Knöner et al. [70] who reported an increase of three orders of magnitude of oxygen diffusion along the grain boundaries compared to the bulk.

In contrast, Mondal et al. [71] measured that the electrical conductivity in the grain boundaries of 1.7 and 2.9 mol% yttria-stabilized zirconia is 2-3 orders of magnitude smaller

than in the crystallite volume. Correspondingly, the activation energy of the electrical conduction at interfaces with 1.0-1.2 eV is significantly higher than 0.84-0.93 eV observed for the bulk conductivity. Chun et al. [72] deposited 3YSZ onto Al_2O_3 (102), MgO (100) and SiO_2 glass. The activation energies for the oxygen-vacancy conduction were determined in the single crystal (0.86 eV), the grain (0.83 eV) and the grain boundaries (1.03 eV) of polycrystalline ceramic samples (grain size: 500-1000 nm) and thin films (1.22 eV, grain size: 100-200 nm). These results suggest that the activation energy for the thin film is determined by the grain boundaries because the volume fraction of the grain boundaries increases with decreasing grain size. Ning et al. [73] prepared 4.5YSZ thin films via atmospheric plasma spraying (APS) onto aluminum substrates, which were dissolved after thin-film deposition. The electrical conductivity of the YSZ coatings in the direction perpendicular to the coating surface was found to be much lower than that of bulk materials. SIMS studies on cubic 10YSZ bicrystals exhibited an abrupt decrease of the oxygen profile around the boundary plane indicating the oxygen-diffusion blocking of the grain boundary [74]. As early as 1981, Verkerk et al. [45] stated that for polycrystalline samples the grain-boundary conductivity is about 100 times lower than the bulk conductivity. Guo and Zhang [75] and Guo and Ding [76] also found the grain-boundary conductivity to be lower than the bulk conductivity within 3YSZ and 8YSZ, respectively. However, they observed an increase of the grain-boundary conductivity with decreasing grain size. Boulc'h et al. [77] investigated the electrical properties of tetragonal nanostructured 2.5YSZ. According to this group, the grain-boundary blocking effect is linked to different levels of yttrium segregation, which depend on the thermal history of the 2.5Y-TZP (tetragonal zirconia polycrystal). The matrix conductivities were found to be equal for both nanocrystalline (60 nm) and microcrystalline (600 nm) tetragonal zirconia. Park et al. [78] attributed the lower conductivity of 8YSZ thin films compared to bulk 8YSZ to poor crystallinity, whereas Wanzenberg et al. [79] suggested that the decrease in the conductivity is evoked by an artifact of the contacting electrodes during the measurement and not by the deposited films themselves. A variety of groups suggested that an intergranular siliceous phase accounts for the very low grain-boundary conductivity [80-82]. However, Guo et al. stated that the siliceous phase does not alter the grain-boundary conduction mechanism; rather a depletion of oxygen vacancies in the space-charge layers accounts for the blocking effect of the grain boundaries [41].

In summary, the role of interfaces in YSZ is still controversially discussed in literature.

2.1.4 Modeling of the Transport Properties

The so-called *brick-layer model* [83] describes the macroscopic impedance of a polycrystal with microscopic grain and grain-boundary characteristics. For the evaluation of the transport properties of polycrystals consisting of grain boundaries and grains, the complex microstructure of the polycrystalline 8YSZ thin film is transferred into the simplified brick model as depicted in Fig. 11. The model comprises cubic grains with an edge length of the

mean grain size d of the YSZ grains and grain boundaries with a constant thickness δ_{gb} surrounding the cubes.
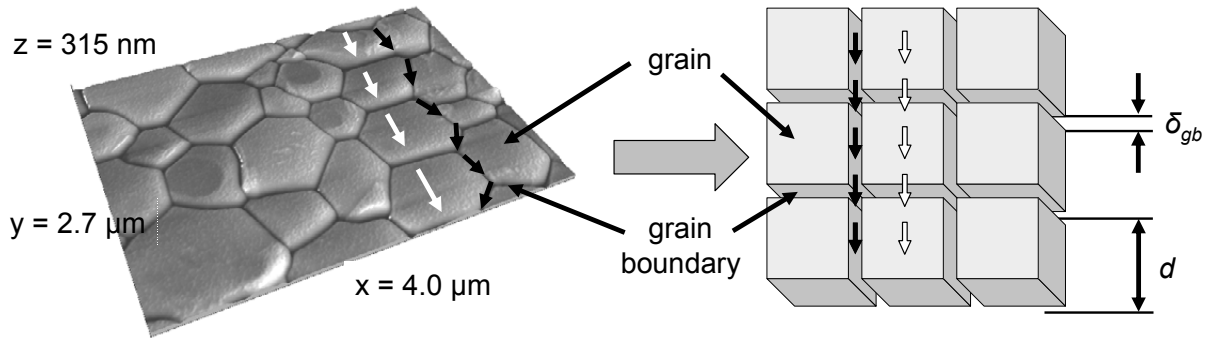
Fig. 11 Transfer of the thin-film microstructure into the brick-layer model [83]

The mean grain size d evaluated by means of electron microscopy or X-ray diffration analysis, is represented by the cubes with an edge length of d. The grain-boundary thickness is represented by spacings of δ_{gb} between the cubes.

Analytical results can be evaluated from the model and even space-charge effects can be included in the overall analysis (e.g. [75]). However, in real systems the grains are neither cubic and of constant size nor is the microstructure of a simple geometry. In order to evaluate the influence of the microstructure on the calculated grain-boundary properties, Fleig et al. performed finite-element (FE) calculations [84]: deviations from the brick-layer model are e.g. caused by the *detour effect*, which means that current detours around blocking grain boundaries if this lowers the impedance. Consequently, both the effective grain-boundary capacitance and the grain-boundary conductance differ from the brick-layer values [85]; the relaxation angular frequency $\omega_0 = 1 / (RC)$, however, is barely influenced by detour effects and always close to the true relaxation frequency of the grain boundaries [86]. For a variety of computer-generated microstructures analyzed in [84, 85] (e.g. orthogonal, zigzagged, hexagonally shaped grain boundaries), the maximum deviation between the "true" grain-boundary properties and the properties derived from the brick-layer model was found to be a factor of two. However, the authors concluded that this deviation is significantly reduced in polycrystalline ceramics, since the analyzed geometry effects cancel out.

For the application of the brick-layer model to the YSZ thin films, the following assumptions are made: The grain boundaries are assumed to be of constant thickness δ_{gb}, where δ_{gb} does not denote the microstructural grain-boundary thickness d_{gb} but the effective electrical one comprising the grain-boundary core and two times λ if space charges are present (Fig. 10). The bulk and grain-boundary conductivity are assumed frequency independent, and the permittivity of the bulk and the grain boundary is identical: $\varepsilon_g = \varepsilon_{gb}$. This seems to be plausible since even large deviations of the grain-boundary stoichiometry from the bulk chemistry would not entail further polarization mechanisms increasing ε_{gb}. The permittivity data of different YSZ stoichiometries are within the scattering range of the literature data (cf. 2.1.2 and table C.2 in [40]).

According to [41, 75, 76, 80, 87] the following equations can be derived from the brick-layer model and the previously noted assumptions:

The total conductivity of the thin film σ_{tf} is given by

$$\sigma_{tf} = \frac{1}{R_{tf}} \cdot \frac{l_{cl}}{l_{el} \cdot t} = \frac{const}{T} \cdot e^{-\frac{E_{A,tf}}{k \cdot T}} \qquad \text{Eq. 12}$$

where R_{tf} is the total resistance of the thin-film sample including the resistance of the grains and the grain boundaries, l_{cl} denotes the electrode clearance (l_{cl} equals 68 µm for all analyzed samples) and the effective area is given by the electrode length l_{el} times the film thickness t. The activation energy is denoted by $E_{A,tf}$ (cf. Eq. 10). The respective values for σ_g and σ_{gb} are calculated accordingly. The values for the resistances are extracted from the fit of the impedance spectra (chapter 3.3.3).

Although the *total* grain-boundary conductivity σ_{gb}^T is a parameter of practical importance widely reported in the literature, for the purpose of this work, it is necessary to characterize the *specific* grain-boundary conductivity σ_{gb}^S corresponding to the conductivity of a grain-boundary region of thickness δ_{gb}. The specific grain-boundary conductivity is determined from the total grain-boundary conductivity as

$$\sigma_{gb}^S = \sigma_{gb}^T \cdot \frac{n}{l_{cl}} \cdot \delta_{gb} = \sigma_{gb}^T \cdot \frac{\delta_{gb}}{d + \delta_{gb}} \qquad \text{Eq. 13}$$

where d is the mean grain size and n the number of grain boundaries to be trespassed in the measurement direction. The effective electrode clearance (l_{cl}) and the effective cross-section of the thin film (l_{el} x t) is adjusted according to the brick-layer model in this work.

A negligible contribution of conduction *parallel* to the grain boundaries to the total conductivity is assumed (and later verified). Thus, σ_{gb}^S in this work refers implicitly to the conductivity *normal* to the boundary.

The grain-boundary thickness δ_{gb} can be calculated from the capacitances according to

$$\delta_{gb} = d \cdot \frac{C_{bulk}}{C_{gb}} = \frac{d}{C_{gb}} \cdot \varepsilon_{gb}\varepsilon_0 \cdot \frac{A}{l_{cl}} \qquad \text{Eq. 14}$$

The capacitances of the bulk and the grain-boundary processes can be derived from fitting the electrical impedance data to equivalent circuits consisting of three parallel RQ elements (cf. Fig. 25), which each represents the electrode process, the bulk process and the grain-boundary contribution. The constant phase element Q can be calculated into the capacitance C according to [41] by

$$C = (R^{1-n} \cdot Q)^{\frac{1}{n}} \qquad \text{Eq. 15}$$

where n is a fitting parameter less or equal to unity correlating amongst others with the grain-size distribution.

Thus, by application of the brick-layer model, the grain-boundary thickness as well as the specific grain-boundary conductivity can be obtained.

2.2 Lanthanum Strontium Cobaltite (LSC) Thin-Film Cathodes

The efficiency of solid oxide fuel cells (SOFC) depends on the polarizations of the electrolyte and the electrodes (2.2.1). For the development of high-performance cathodes in the temperature regime 500 °C ≤ T ≤ 750 °C, transition metal oxides emerged to be auspicious (2.2.1). Due to their mixed ionic-electronic (MIEC) transport mechanism (2.2.2) and their advantageous oxygen-reduction properties (2.2.3), the material $(La,Sr)CoO_{3-\delta}$ features high catalytic performance. However, drawbacks of these materials from the perovskite system are usually a mismatch of thermal expansion coefficients (*TEC*) between cathode and substrate (2.2.2) and their chemical incompatibility (2.2.4). Thin-film technology (2.3) potentially overcomes the mismatch of the *TEC*s and the chemical incompatibility due to its low processing temperatures and the unique microstructure of the thin films.

2.2.1 Cathode Polarization Losses

The cell voltage and thereby the electrical efficiency of a solid oxide fuel cell (SOFC) crucially depend on the polarizations occurring in correlation with the electrochemical reactions (Eq. 1 - Eq. 3). Polarization is a voltage loss or overpotential, which is a function of current density [88]. The polarization is usually given by the overpotential or by the area specific polarization resistance (*ASR*$_{pol}$ [89]). One distinguishes ohmic polarization or ohmic loss, concentration polarization and activation polarization. Fig. 12 shows a schematic polarization curve of voltage versus current density of a typical SOFC.

Without current flowing through the cell, the Nernst voltage U_N (Eq. 4) equals the open circuit voltage (OCV) U_0. However, when an external load is connected to the cell and the flow rates of fuel and oxidant are not sufficiently high compared to the gas consumption, U_N becomes a function of current density [88]. At any given current density, the voltage over the cell U_C (Eq. 5) equals

$$U_C(j) = U_N(j) - \eta_\Omega(j) - \eta_{act}^c(j) - \eta_{act}^a(j) - \eta_{conc}^c(j) - \eta_{conc}^a(j) \qquad \text{Eq. 16}$$

where $\eta_\Omega, \eta_{act}^c, \eta_{act}^a, \eta_{conc}^c, \eta_{conc}^a$ are the voltage losses regarding activation ("act") and concentration ("conc") polarization of the cathode ("c") and the anode ("a"). The difference between $U_N(j)$ and $U_N(j=0)$ is a measure of the change in gas phase compositions just outside of the electrodes [88].

Ohmic losses emerge from the motion of electrical charge. They typically arise in the electrolyte (oxygen-ion resistance) and in the contact of the electrodes, i.e. the current collector (electronic resistance). However, in most SOFCs, the main contribution to η_Ω can be attributed to the electrolyte, since its ionic resistivity (2.1.2) is much greater than the electronic resistivities of the cathode (2.2.2) and the anode. The relative contribution of the ohmic losses to the overall polarization losses may vary extensively due to different cell designs: electrolyte-supported cells (thickness $t \approx 150$ µm) bear greater ohmic losses than electrode-supported cells with a thickness of approximately $t \approx 10$ µm. Ohmic resistances are

considered as independent from current load and time-invariant. However, as the fuel cell heats up, the resistance of the electrolyte strongly depends on the operation temperature (2.1.2).
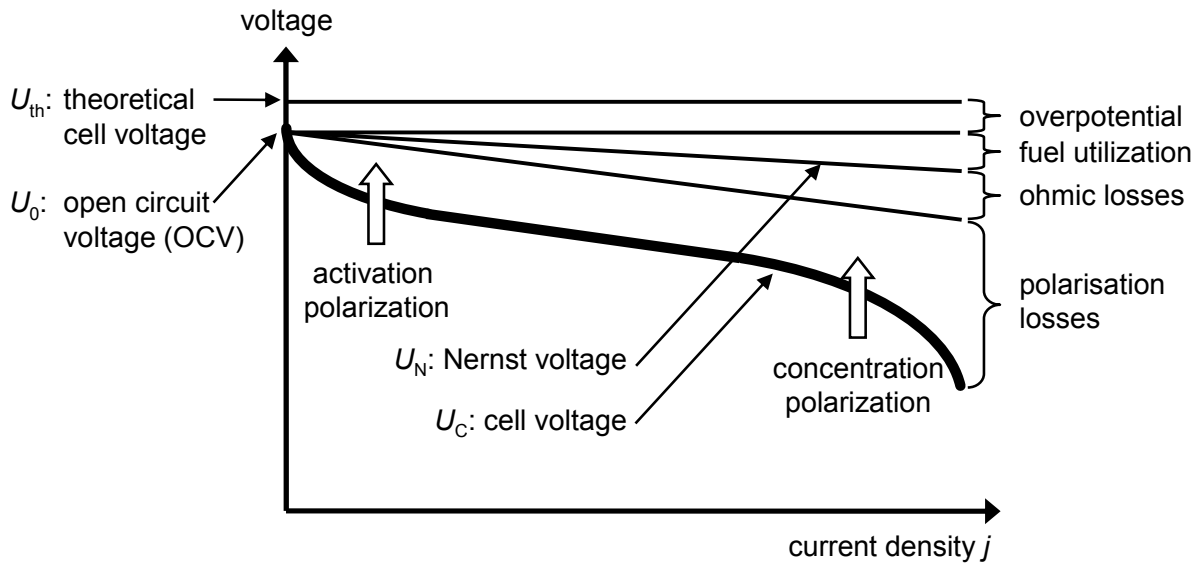
Fig. 12 Schematic plot of voltage versus current density of an SOFC [88, 90]
showing different types of polarizations: activation polarization is dominant at low current densities; concentration polarization is dominant at high current densities when the transport of reactive species to the electrolyte / electrode interface becomes a limiting factor for the cell reaction [88]. The losses occurring during SOFC operation decrease the maximum theoretical cell voltage U_{th} (in dependence from temperature and gas composition ca. 0.9 to 1.2 V) to the smaller cell voltage U_C (in dependence from electrical load and further operating conditions ca. 0.5 to 0.8 V) [90].

Transport of gaseous species occurs by binary diffusion and Knudsen diffusion in microstructures with a small pore size [91]. This transport of fuel and oxidant to the respective electrodes is reflected by an electrical voltage loss called concentration polarization $\eta_{conc}^c, \eta_{conc}^a$. The concentration polarization at the cathode η_{conc}^c is related to the transport of oxygen and nitrogen through the porous cathode. The flux of O_2 from the gas stream through the cathode to the cathode / electrolyte interface, is linearly proportional to the current density [88]. Therefore, η_{conc}^c is a function of the binary diffusion coefficient of O_2 / N_2, the microstructure of the cathode, the partial pressure of the oxidant gas and the current density of the cell.

The activation polarization at the cathode η_{act}^c is linked to the electrochemical reaction, i.e. the oxygen-reduction reaction (ORR, Eq. 1) and the charge transfer from the cathode in the electrolyte.

On the atomistic scale, the physical processes occurring during the oxygen reduction are still matter of research. However, the basic procedure of the ORR is known. It is mainly

determined by the transport properties of the cathode; one differentiates purely electronic conducting cathodes and mixed ionic-electronic conducting (MIEC) cathodes.

In case of a purely electronic-conducting material, the electrochemical reaction is confined to the triple-phase boundary (tpb) between the electronic conducting cathode, the ionic conducting electrolyte and the gas phase (Fig. 13a). The tpb is characterized by a line, extending along the electrolyte surface. According to Ivers-Tiffée and Virkar [88], the electrochemical reaction in a purely electronic conducting cathode material is characterized by the following reaction steps:

- Surface adsorption of oxygen molecules

- Dissociation of the adsorbed oxygen molecules into adsorbed atoms

- Surface diffusion of the adsorbed oxygen atoms to the tpb

- Formation of oxygen ions by electron transfer with incorporation of these ions into the electrolyte

Fig. 13a depicts possible transport paths of the molecular, gaseous oxygen O_2 (g), adsorbed oxygen $O_{x,ads}$ and ionized oxygen O^{2-} in an electronic conducting cathode. Many of the above steps are thermally activated. The voltage drop, which is associated with the cathode reaction or the passage of current at the cathode, is the activation polarization η_{act}^c. The relationship between η_{act}^c and the current density is usually nonlinear, except at very low current densities. In general, η_{act}^c is a function of the cathode material properties, the microstructure, the temperature, the atmosphere and the current density [88]. A phenomenological theory, which gives a quantitative relation between the current density and η_{act}^c, is the Butler-Volmer equation [88, 90]:

$$j\left(\eta_{act}^c\right) = j_0^c \cdot \left(e^{\frac{\beta \cdot const}{RT} \cdot \eta_{act}^c} - e^{-\frac{(1-\beta) \cdot const}{RT} \cdot \eta_{act}^c} \right) \qquad \text{Eq. 17}$$

where β is the transference number and j_0^c is the exchange current density, which is a measure for the effectiveness of the electrode.

In principle, MIEC cathode materials exhibiting both ionic and electronic conductivity feature lower polarization losses since the electrochemical reaction is not restricted to the tpb [92, 93]. Instead, the entire cathode surface may be utilized for the ORR. In reality, the electrochemically active volume is restricted to some μm from the cathode / electrolyte interface in state-of-the-art cathodes depending on the material properties [26]. The correlation between utilization range l_δ and surface exchange and oxygen-diffusion coefficients is thoroughly discussed in 2.2.3. In case of MIEC cathodes, at least three reaction steps have to be considered as rate determining [88]: the surface exchange at the gas phase / MIEC surface, the bulk diffusion in the MIEC and the incorporation of oxygen ions into the electrolyte at the MIEC / electrolyte interface (cf. Fig. 13b).

a) Electronic conductor (e.g. LSM)   b) Mixed ionic-electronic conductor (e.g. LSC)

$$\frac{1}{2}O_2 + 2e^- \rightarrow O^{2-}$$
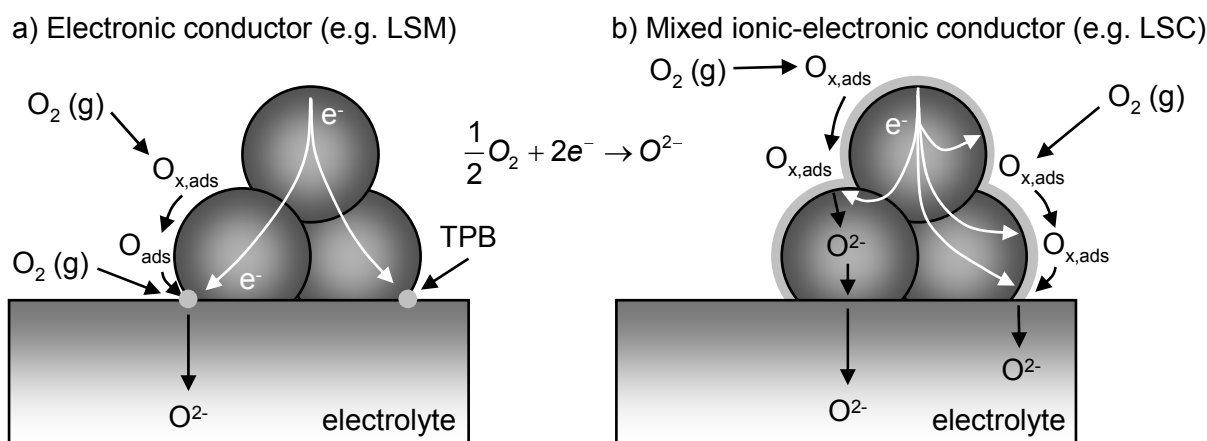
Fig. 13 Principle of cathodic oxygen reduction
of a) a purely electronic conducting material (e.g. LSM) via the surface path and b) a mixed
conducting material (e.g. LSC, LSCF) via the bulk path.

In the 1980s and 1990s, the electronic-conducting transition metal manganese was mainly employed as $(La,Sr)MnO_{3-\delta}$ (LSM) (a comprehensive literature review is given in [94]). Due to its long process of development and its chemical stability [95], LSM was successfully applied as an SOFC cathode [96] (and ref. therein) in SOFC stacks (e.g. HEXIS concept [12]). In the recent past, the transition metals cobalt and iron got into focus as $(La,Sr)(Co,Fe)O_{3-\delta}$ (LSCF). As MIEC materials, they are utilized in state-of-the-art cells and are object matter of research (e.g. [12, 94, 97]).

From the previous considerations, the following requirements for powerful, effective SOFC cathodes can be derived: Since the concentration of active sites determines the activation polarization, the cathode microstructure should be very fine, thus facilitating a high number of triple-phase boundaries in case of an electronic conducting material. Even better, a MIEC material should be employed, which extends the ORR from a line to an area. Besides chemical stability of the cathode material with respect to temperature, oxidant, current load and the electrolyte material (cf. 2.2.4), the role of porosity is an essential issue. Open porosity is of decisive advantage since the molecular diffusion of oxygen in the pores causes much lower losses than the solid-state diffusion of oxygen ions in the bulk. Since the surface exchange in MIEC cathodes may be rate determining, a high surface area is auspicious. A high porosity of the cathode increases the surface area, thus lowers the activation polarization. This matter of fact can be utilized to a maximum extend in nanoscaled MIEC cathodes featuring nanopores. As derived in 2.2.3, the electrochemical reaction in a MIEC cathode is restricted to the utilization range l_δ, which characterizes the active thickness of the cathode from the electrolyte surface. Therefore, an optimized microstructure of the cathode for a minimized activation polarization would feature a coarse microstructure with large pores above l_δ to facilitate binary diffusion and nanoscaled grains and nanopores near the electrolyte / electrode interface to increase the surface of the cathode.

This approach has been pursued by Ivers-Tiffée et al. and Herbstritt et al. [88, 98-101] who observed a significant increase in power density by the introduction of a nanoporous and nanocrystalline LSM film at the cathode-electrolyte interface. The increase of power density was explained by the high concentration of active sites on the electrolyte surface.

2.2.2 Material Properties of $(La_{0.5}Sr_{0.5})CoO_{3-\delta}$ (LSC)

Cobalt-based perovskites like $(La_{1-x}Sr_x)CoO_{3-\delta}$, $0 \leq x \leq 1$ show a high electronic conductivity, besides tolerating large oxygen-vacancy concentrations. This particular feature results in a significant ionic conductivity and catalytic activity. Therefore, gas separation membranes [102-104], oxidation catalysts [104, 105], oxygen sensors [106] and electrodes in solid oxide fuel cells [94] (and ref. therein) are possible applications for these materials. Within the state-of-the-art $(La,Sr)(Co,Fe)O_{3-\delta}$ system, the chemical diffusion and oxygen-exchange properties of $(La_{0.5}Sr_{0.5})CoO_{3-\delta}$ (LSC) excel the material properties of the cathode material $(La_{0.6}Sr_{0.4})(Co_{0.2}Fe_{0.8})O_{3-\delta}$ (LSCF). Therefore, LSC was selected as object of research in this work.

This chapter comprises the material properties of $(La_{0.5}Sr_{0.5})CoO_{3-\delta}$ (LSC). It is shown that the Sr concentration governs the chemical phase of the ternary compound as well as its lattice constant and its thermal expansion coefficient *TEC*. Moreover, the substitution of La by Sr determines the concentration of oxygen vacancies in the material and thereby its defect chemistry yielding directly the superior electronic and ionic conductivity of LSC. Additionally, all material properties depend on ambient conditions like oxygen partial pressure pO_2 and temperature *T*.

Crystal Structure
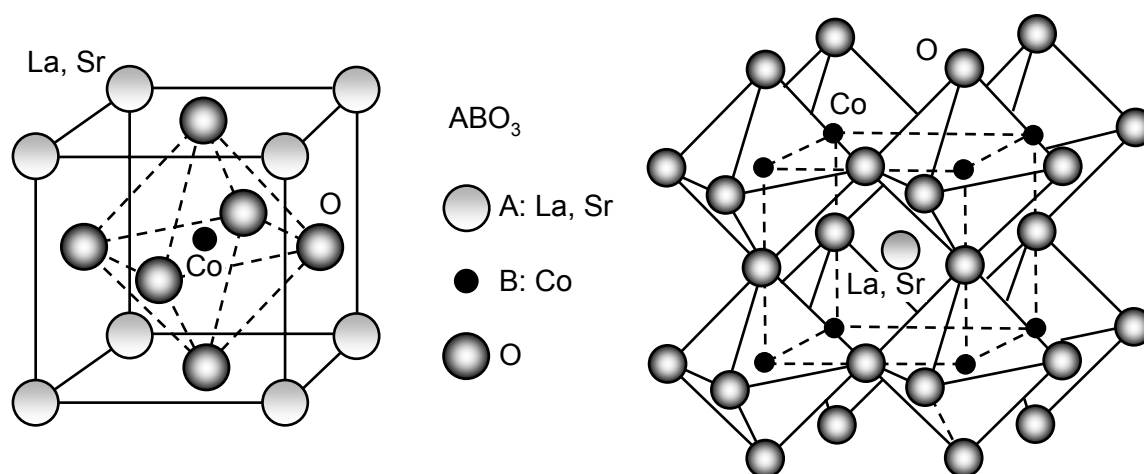
Fig. 14 Cubic perovskite crystal structure ABO$_3$
La and Sr occupy the cornered site "A" and Co the centered "B" site. Oxygen atoms are face centered.

Materials of the $(La_{1-x}Sr_x)CoO_{3-\delta}$ family crystallize in the perovskite structure ABO$_3$ (Fig. 14). The B-site ion is centered in the structure, the A-site ions are found at its corners. Oxygen

ions are located on the cube faces. Due to their similar ionic radii, La^{3+} (r_{ion} = 1.36 Å [107]) and Sr^{2+} (r_{ion} = 1.44 Å [107]) ions occupy the A-sites and Co^{3+} ions (r_{ion} = 0.61 Å [107]) the B-site in the perovskite structure.

At room temperature, $(La_{1-x}Sr_x)CoO_{3-\delta}$ (x = 0) has a rhombohedral structure, which transforms into the cubic structure between 750 K and 1673 K (there is a large discrepancy in the data obtained by Petrov et al. [108] (■) and Mizusaki et al. [109] (▲), Fig. 15). With increasing Sr concentration, the published data on transition temperatures converge. At x = 0.4, the data approximately coincide with the findings of Søgaard et al. [110] (●) and the data of Wang et al., who determined the phase transition from rhombohedral to cubic at 673 K for $(La_{0.6}Sr_{0.4})CoO_{3-\delta}$ [111] (♦, Fig. 15). Further increase of the Sr concentration to x = 0.5-0.6 leads to a reduction of the transition temperature to room temperature.
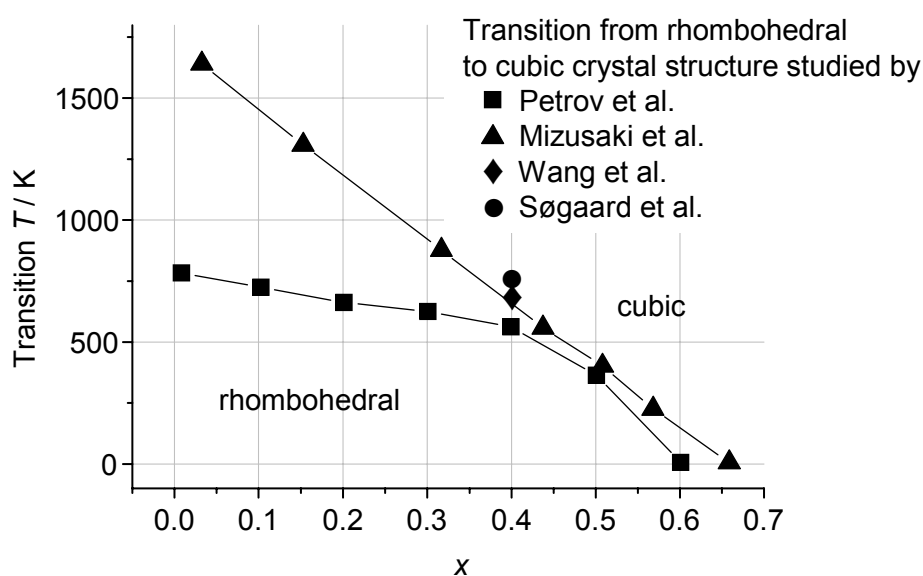
Fig. 15 Phase transition with respect to temperature and stoichiometry
Temperature vs. composition, x, diagram showing the phase transition of the $(La_{1-x}Sr_x)CoO_{3-\delta}$ system from the rhombohedral to the cubic structure studied by Petrov et al. [108] (■), Mizusaki et al. [109] (▲), Wang et al. [111] (♦) and Søgaard et al. [110] (●).

Thermal Expansion

Haggerty et al. [112] calculated the lattice parameters of $(La_{1-x}Sr_x)CoO_{3-\delta}$ (x = 0.5) by Rietveld refinement with respect to oxygen non-stoichiometry and compared them to the pseudocubic cell parameters calculated from the volume of the cell: the lattice constant ranges between 3.833 Å (δ = 0.01) to 3.846 Å (δ = 0.21) at room temperature where δ is the oxygen deficiency. Thus, the expansion of the perovskite lattice upon heating is not only associated with usual thermal lattice expansion ("thermal expansivity" [113]), but also with a "chemical expansivity" [113] associated to a major part with the formation of oxygen vacancies [114]. For $(La_{0.5}Sr_{0.5})CoO_{3-\delta}$, Minh [115] and Petric et al. [116] published a coefficient of thermal expansion TEC_{LSC} of $23.7 \cdot 10^{-6}$ 1/K and $22.3 \cdot 10^{-6}$ 1/K (30 ≤ T ≤ 1000 °C), respectively. These values are in conflict with the thermal expansion coefficients of yttria-doped zirconia (YSZ)

(TEC_{YSZ} = 10.5·10^{-6} 1/K [115]) and gadolinia doped ceria (GCO) substrates (TEC_{GCO} = 12.5·10^{-6} 1/K [117]). This distinct mismatch results in mechanical stress upon heating and cooling of the cell and ultimately leads to cracking and breakdown of the SOFC system. Fortunately, the application of the LSC cathodes by thin-film technology provides the excitatory opportunity to outflank this mismatch in thermal expansion coefficients between cathode and substrate as discussed in chapter 2.3.

Phase Stability

Chemical secondary phases may form easily in $(La_{0.5}Sr_{0.5})CoO_{3-\delta}$ [118] due to its extremely narrow stability field of 0.997 < La / Sr < 1.003 [119]. Furthermore, Petrov et al. [108] stated that due to the high defect concentration in $(La_{0.5}Sr_{0.5})CoO_{3-\delta}$ the ideal dilute solution model may not remain applicable. Instead, new defect structures may develop in the material involving the association of defects with the formation of defect complexes and clusters and the formation of microdomains with ordered defects. These would lead to an inhomogeneous distribution of oxygen vacancies within the material. This is supported by Sitte et al. [120], who observed superstructures in $(La_{1-x}Sr_x)CoO_{2.71}$ (x = 0.6), which were attributed to the ordering of oxygen vacancies (also cf. [121]) or aperiodically alternating La-rich and Sr-rich (001) lattice planes. Several other groups reported the formation of superstructures in LSC by the ordering of oxygen vacancies [122, 123], which is well known in anion deficient perovskites [124]. Wang et al. explained the superstructure firstly as cation ordering [125, 126]. Later they described it as combined cation/anion-vacancy ordering [127] for a Sr/La ratio of approximately unity.

Defect Model

The transport properties of LSC (and thereby its electronic and ionic conductivity and oxygen-reduction characteristics) depend crucially on the defects in the $(La_{1-x}Sr_x)CoO_{3-\delta}$ crystal [108, 109, 128-135]. Assuming statistically distributed, non-ordered oxygen vacancies, the following defect model is developed on the basis of the cited literature.

Mizusaki et al. [128] stated that cobalt ions predominately assume valence states between Co^{3+} and Co^{4+}, while the valence state of La^{3+}, Sr^{2+}, and O^{2-} are fixed (Eq. 18).

$$\left(Sr_{La}^{2+}La_{La}^{3+}\right)\left(Co_{Co}^{3+}Co_{Co}^{4+}\right)O_{3-\delta}^{2-} \qquad \text{Eq. 18}$$
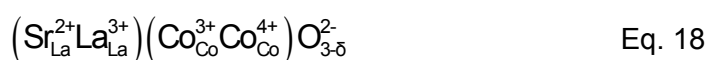
The substitution of La^{3+} ions on the A-sites of the $La^{3+}Co^{3+}O_3^{2-}$ lattice by the dopant Sr^{2+} requires charge compensation. Electroneutrality in $(La_{1-x}Sr_x)CoO_{3-\delta}$ is maintained in two ways: Either by a valence change of the B-site Co cation (creation of holes, electronic compensation) or by the formation of oxygen vacancies (ionic compensation). In general, both processes occur and compete with each other, depending on composition, oxygen partial pressure and temperature. The lanthanum substitution by strontium ions and its effects on electroneutrality can be described by the Kröger-Vink notation [29]:

$$2\left[V_O^{\cdot\cdot}\right]+\left[Co_{Co}^{\cdot}\right]=\left[Sr_{La}^{'}\right] \qquad \text{Eq. 19}$$

For sake of simplicity, the oxygen vacancies $V_O^{\bullet\bullet}$ are assumed to be doubly positively charged, but the charge of the vacancies is in reality expected to be a function of temperature [108]. The cobalt ions are tetravalent Co^{4+} and positively charged with respect to the host lattice, while the bivalent strontium ions Sr^{2+} are negatively charged with respect to the host lattice La^{3+}. The relation between $Co_{Co}^{\bullet}$ and $V_O^{\bullet\bullet}$ may be expressed by the following defect reaction and mass equation at equilibrium [108]:

$$2Co_{Co}^{\bullet} + O_O^x = 2Co_{Co}^x + V_O^{\bullet\bullet} + \frac{1}{2}O_2(g) \qquad \text{Eq. 20}$$
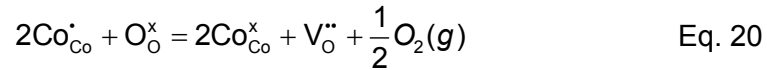
$$\left[V_O^{\bullet\bullet}\right]\left[Co_{Co}^x\right]^2 = K_0 \cdot e^{-\frac{\Delta G}{kT}} \cdot \left[Co_{Co}^{\bullet}\right]^2 \left[O_O^x\right] pO_2^{-\frac{1}{2}} \qquad \text{Eq. 21}$$

where K_0 is the equilibrium constant, ΔG the free reaction enthalpy, k Boltzmann constant and T the absolute temperature. Hence, the general trends are that the oxygen-vacancy concentration (ionic compensation) grows with T and decreases with pO_2, whereas the concentration of tetravalent cobalt (electronic compensation) decreases with T and increases with pO_2.
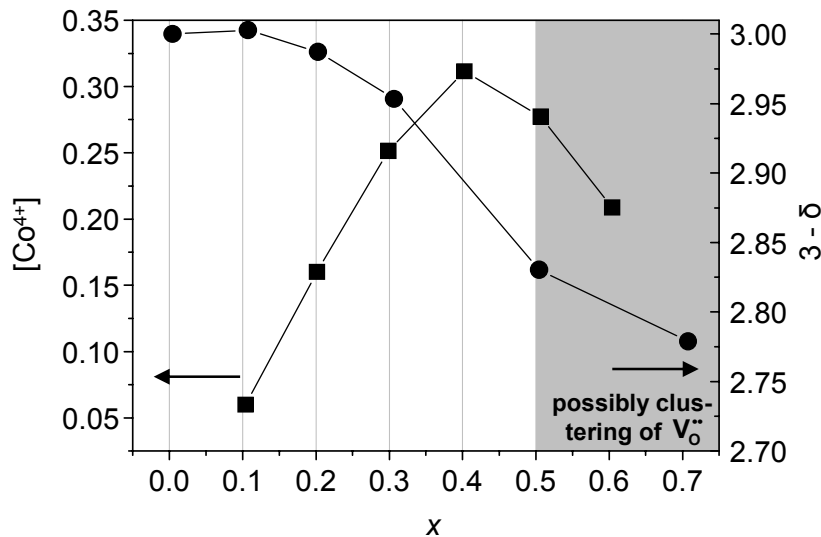
Fig. 16 Influence of stoichiometry on cobalt valence and oxygen-vacancy concentration
Concentration of tetravalent cobalt ions ([Co^{4+}], ■) and oxygen non-stoichiometry (3-δ, ●) vs. composition x of the (La$_{1-x}$Sr$_x$)CoO$_{3-δ}$ system. The [Co^{4+}] was taken from [108] (measurements performed at 1000 °C in air atmosphere) and the (3-δ) from [109] (measurements performed at 800 °C, 0.1 atm O$_2$); for x ≥ 0.5 the oxygen vacancies potentially form clusters [108, 120].

To preserve electroneutrality, the mean cobalt valence n for (La$_{1-x}$Sr$_x$)CoO$_{3-δ}$ is given by [109]:

$$n = 3 + x - 2\delta \qquad \text{Eq. 22}$$

where x accounts for the stoichiometry and δ for the oxygen deficiency in the material system. For x ≤ 0.3, the increase in x mainly contributes to an increase of tetravalent cobalt [Co^{4+}] as depicted in Fig. 16. With increasing x, the [Co^{4+}] reaches a maximum and is approximately constant for 0.3 ≤ x ≤ 0.5, whereas the oxygen-vacancy concentration

increases with x. For x > 0.5, the increase in x results in the increase of the mean cobalt valence. Hence, one can conclude that the strontium additions are primarily compensated by the formation of the tetravalent cobalt ions for x ≤ 0.3. For 0.3 ≤ x ≤ 0.5, the relative importance of oxygen vacancies on the compensation mechanism increases. For a Sr concentration of x = 0.5, about 2/3 of the ions are compensated by tetravalent cobalt and about 1/3 by oxygen vacancies.

Charge Transport Properties

Both electronic and ionic conductivities in the $(La_{1-x}Sr_x)CoO_{3-\delta}$ material class are extraordinarily large, i.e. LSC is a mixed ionic-electronic conductor (MIEC). Petrov et al. [108] reported values of σ_{el} = 1500 S / cm at 680 °C (Fig. 17) in air for $(La_{0.5}Sr_{0.5})CoO_{3-\delta}$. Between 700 and 1000°C in air atmosphere, the values of σ_{ion} exceed those of zirconia-based solid electrolytes by about one to two orders of magnitude (Fig. 17). For $(La_{0.5}Sr_{0.5})CoO_{3-\delta}$, an absolute value of 3.90·10^{-4} S / cm at 680°C in air has been reported in [136], seven orders of magnitude below σ_{el}.
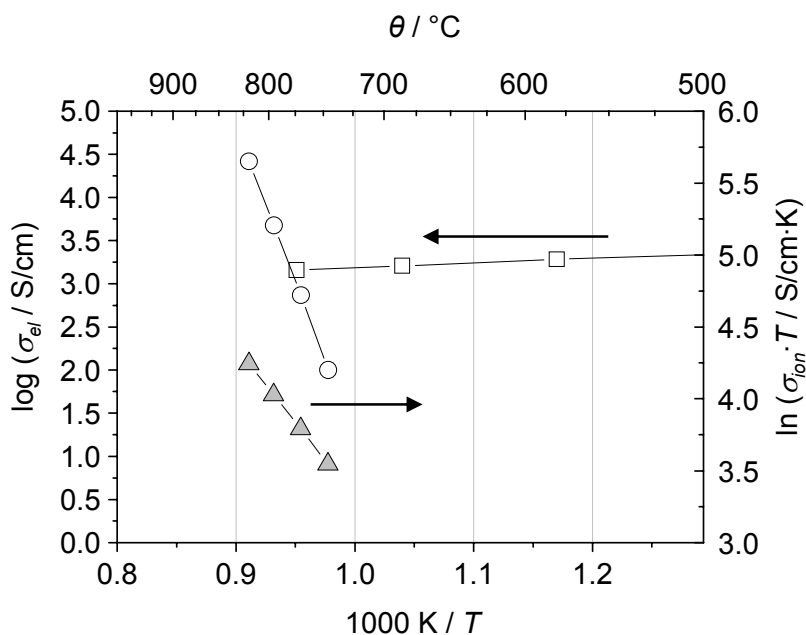
Fig. 17 Temperature dependency of the electrical conductivity of LSC

Electronic (σ_{el}, □, left axis) and ionic (σ_{ion}, ○, right axis) conductivity of $(La_{0.5}Sr_{0.5})CoO_{3-\delta}$ and $(La_{0.4}Sr_{0.6})CoO_{3-\delta}$ respectively over 1000 K / T. The data was taken from [108] (□, measurements performed at 0.21 atm pO_2) and Sitte et al. [120] (○, measurements performed at oxygen nonstoichiometry 3-δ = 2.76). For comparison, the ionic conductivity of polycrystalline 8YSZ substrates (▲) is added.

The electronic (σ_{el}) and ionic (σ_{ion}) conductivities of $(La_{1-x}Sr_x)CoO_{3-\delta}$ are determined by the respective charge-carrier concentration of the electron holes p and the oxygen vacancies v and their mobility $\mu_{el,ion}$ (Eq. 23, Eq. 24).

$$\sigma_{el} = e_0 \cdot p \cdot \mu_p \qquad\qquad \text{Eq. 23}$$

$$\sigma_{ion} = 2e_0 \cdot v \cdot \mu_V \qquad\qquad \text{Eq. 24}$$

As the charge-carrier concentrations of $(La_{1-x}Sr_x)CoO_{3-\delta}$ are closely related to the concentration of its defects, the electronic carrier concentration is given by the positively charged tetravalent cobalt ions (Eq. 25); the electronic conductivity σ_{el} is therefore p-type. The concentration of the oxygen vacancies is given by (Eq. 26).

$$\left[Co_{Co}^{\bullet} \right] = p \qquad\qquad \text{Eq. 25}$$

$$\left[V_O^{\bullet\bullet} \right] = \delta = v \qquad\qquad \text{Eq. 26}$$

Therefore, the curves of σ_{el} and σ_{ion} show a similar dependency on Sr dopant concentration x as $\left[Co_{Co}^{\bullet} \right]$ and $\left[V_O^{\bullet\bullet} \right]$ (Fig. 16): as the electronic conductivity increases with x and reaches a maximum at x = 0.4 ($\square$, Fig. 18), its value drops parallel to the concentration of $\left[Co_{Co}^{\bullet} \right]$ ($\blacksquare$, Fig. 16). The ionic conductivity is low for small values of $\left[V_O^{\bullet\bullet} \right]$ at x ≤ 0.3. For larger values of x, higher ionic conductivity values are determined experimentally ($\circ$, Fig. 18), which correlates with the increase of $\left[V_O^{\bullet\bullet} \right]$ with x ($\bullet$, Fig. 16).

The mobility of the charge carriers depends on the prevailing transport mechanism that is discussed controversially in literature:

The <u>electronic transport mechanism</u> of $(La_{1-x}Sr_x)CoO_{3-\delta}$ has been considered to take place by the Co-3d electrons through the chain of Co-O-Co bonds [130], whether by a rigid band composed of Co-3d and O-2p levels [137, 138] (i.e. non-localized electron holes are considered to occupy a partially filled electron band [132]) or by the hopping of electron holes localized at the cobalt ions [109]. The first transport mechanism implies a negative temperature dependence of the electron-hole mobility, the latter a positive one.

Which conduction mechanism prevails, depends on the degree of overlapping of the Co-3d and O-2p levels. The overlap is governed by the Sr concentration: higher [Sr] raises the amount of Co^{4+} / Co-3d and V_O^{2+} / O-2p that leads to a higher degree of overlapping of the energy levels. The electron holes change from the *localized* to the *delocalized* state switching the conduction mechanism from polaron hopping conduction to metallic conduction behavior.

As the Sr concentration also determines the volume of the LSC unit cell, coherence between the type of conduction and the lattice parameters can be expected [133]. Mizusaki et al. [109, 128] found a close relationship between the temperature dependence of the conduction mechanism and the rhombohedral angle α. For $(La_{1-x}Sr_x)CoO_{3-\delta}$ with $\alpha < 60.4°$ (x > 0.5), the conductivity decreases with temperature, suggesting metallic conduction. For $(La_{1-x}Sr_x)CoO_{3-\delta}$ with $\alpha > 60.4°$ (x < 0.5), the conductivity increases with temperature suggesting a hopping mechanism. In contrast to that, Petrov et al. [108] did not find a direct correlation between the structure and the electrical conductivity.

Sitte et al. [134] evaluated the isostoichiometric conductivity of $(La_{0.6}Sr_{0.4})CoO_{3-\delta}$ over T^{-1} yielding activation energies of $0.02 \leq E_A \leq 0.05$ eV ($0.12 \leq \delta \leq 0.16$). This indicates a

thermally activated polaron hopping mechanism. For $(La_{0.4}Sr_{0.6})CoO_{3-\delta}$, negative activation energies were obtained at $0.12 \leq \delta \leq 0.20$. Therefore, it was stated that an itinerant electron model [137], i.e. delocalized electrons, which form a rigid band, would probably be more appropriate for describing the electronic conduction mechanism of $(La_{0.4}Sr_{0.6})CoO_{3-\delta}$. However, Søgaard et al. [110] could explain the oxygen nonstoichiometry in $(La_{0.6}Sr_{0.4})_{0.99}CoO_{3-\delta}$ satisfactorily using the itinerant electron model as well. They concluded that the electron-hole mobility decreases with increasing Sr content and that the mobility is inversely proportional to the absolute temperature entailing metallic type conduction in LSC40.
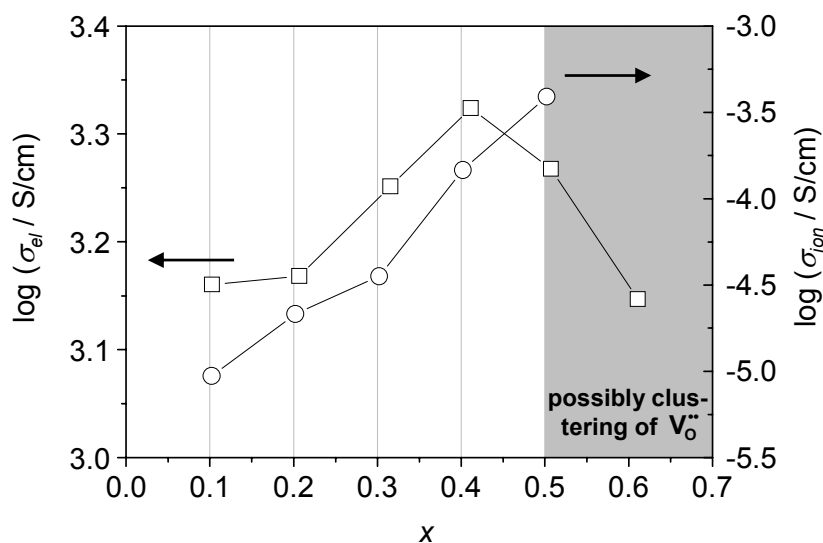
Fig. 18 Electronic and ionic conductivity versus stoichiometry of $(La_{1-x}Sr_x)CoO_{3-\delta}$

Electronic (σ_{el}, □, left axis) and ionic (σ_{ion}, ○, right axis) conductivity of the $(La_{1-x}Sr_x)CoO_{3-\delta}$ system with respect to Sr dopant concentration x. The data was taken from [108] (measurements performed at 600 °C, 0.21 atm pO_2) and Zipprich et al. [136] (measurements performed at 680 °C, 0.21 atm pO_2); for $x \geq 0.5$ the oxygen vacancies potentially form clusters [108], [120].

In summary, the general trends of the electronic conductivity are an increasing σ_{el} for higher Sr content reaching a maximum at $x = 0.4$, and a decreasing σ_{el} towards lower oxygen partial pressures (Fig. 19) and higher temperatures (Fig. 17) [111, 114, 139-141]. With increasing temperature or decreasing pO_2 the concentration of oxygen vacancies grows, these are compensated by the Co^{4+} and the decrease of free electron holes [108]. The dependencies of σ_{el} on T and pO_2, however, are rather moderate. For $(La_{0.5}Sr_{0.5})CoO_{3-\delta}$, a decrease of the electronic conductivity from 3600 to 1600 S/cm between 25 and 688 °C has been measured [108] (cf. Fig. 17), and a reduction from 1400 to 900 S/cm at 600°C was observed upon lowering the oxygen partial pressure from 0.15 to $1.4 \cdot 10^{-4}$ bar [109] (cf. Fig. 19). Whether the physical nature of the electronic transport process is polaron-type or obeys the itinerant electron model, is still controversially discussed in literature.
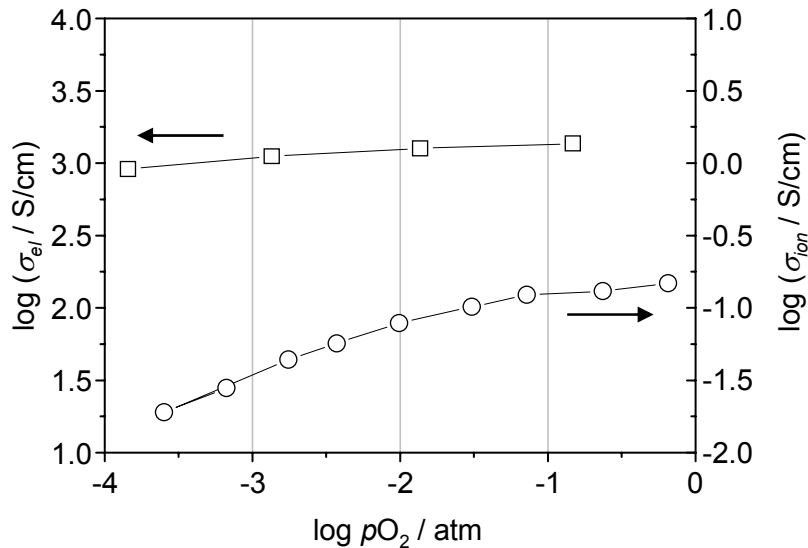
Fig. 19 Electrical conductivity versus pO_2

Electronic (σ_{el}, □, left axis) and ionic (σ_{ion}, ○, right axis) conductivity of $(La_{1-x}Sr_x)CoO_{3-\delta}$ (x = 0.4, 0.5) with respect to pO_2. The data were taken from [109] (□, $(La_{0.5}Sr_{0.5})CoO_{3-\delta}$, measurements performed at 600 °C) and [120] (○, $(La_{0.6}Sr_{0.4})CoO_{3-\delta}$, measurements performed at 750 °C).

The <u>ionic conductivity</u> σ_{ion} is mainly determined by the concentration of oxygen vacancies. Assuming statistically distributed, non-interacting oxygen vacancies and a hopping mechanism, the dependencies of σ_{ion} from Sr-dopant concentration [Sr], temperature T and oxygen partial pressure pO_2 can be derived accordingly to the previously presented defect model:

- As $\left[V_O^{\cdot\cdot} \right]$ increases continuously with the Sr-dopant concentration, this leads to a strong increase of σ_{ion} with Sr (○, Fig. 18). In [136] a decrease of the activation energy from 2.2 to 1.1 eV has been measured in the system $(La_{1-x}Sr_x)CoO_{3-\delta}$ upon increasing the Sr content from 0.1 to 0.5. For $(La_{1-x}Sr_x)CoO_{3-\delta}$ with x = 0.4, an activation energy of 1.0 eV [142] was obtained.

- With temperature, both $\left[V_O^{\cdot\cdot} \right]$ and μ_{ion} increase leading to an increase of σ_{ion} with T (Fig. 17).

- Lower oxygen partial pressures lead to an increase of $\left[V_O^{\cdot\cdot} \right]$ and thereby should facilitate higher ionic conductivities. For a Sr concentration of x = 0.2, this behavior has been confirmed by [136, 143]. However, as depicted in Fig. 19, falling oxygen partial pressure results in a decrease of σ_{ion} for x ≥ 0.4. Bucher et al. [144, 145] found that the increase of σ_{ion} upon increasing $\left[V_O^{\cdot\cdot} \right]$ is only true until a maximum value of 3 - δ ≈ 2.77 (T = 825 °C) for $(La_{0.4}Sr_{0.6})CoO_{3-\delta}$. With further increase of δ, the conductivity decreases continuously. This was explained with the formation of "blocking" microdomains of the size 5 – 50 nm [121]. Several superstructures were identified in $(La_{1-x}Sr_x)CoO_{3-\delta}$ perovskites: They were ascribed either to ordering of the A-cations (La and Sr) [125] or to ordering of oxygen vacancies [123, 146]. According to Petrov et al. [108] the formation of ordered microdomains in LSC at high Sr and low oxygen levels can be described by neutral

complex defects $(Sr_{La}V_OSr_{La})^x$. These microdomains, which have been analyzed by means of high-resolution transmission electron microscopy (HRTEM), can be expected at (i) high vacancy concentrations and (ii) high temperatures [120]. Furthermore, Sitte et al. [120] observed an increase of the activation energy for ionic conduction with increasing nonstoichiometry, which is in accordance with the assumption of progressive vacancy ordering. Hence, although the oxygen-vacancy concentration increases upon pO_2 reduction, the overall ionic conductivity is determined by a decrease of the oxygen-ion mobility at high oxygen deficiencies. The indication that the ionic conductivity goes through a maximum is a well-known behavior and has been discussed for yttria-doped zirconia in chapter 2.1.2. Søgaard et al. identified this maximum at δ = 0.15 for $(La_{0.4}Sr_{0.6})CoO_{3-\delta}$ [110].

2.2.3 Surface Exchange and Oxygen Diffusion

The catalytic properties of the SOFC cathode are governed by the oxygen exchange and oxygen-diffusion properties of the electrode material. Therefore, all developments for high-capacity fuel cell cathodes strive to enhance oxygen exchange and oxygen-diffusion properties mostly by employing mixed ionic-electronic conductors (MIEC) like $(La_{1-x}Sr_x)(Co_{1-y}Fe_y)O_{3-\delta}$. A direct consequence of this MIEC behavior is that oxygen reduction can take place along the surface of the grains and is not restricted to the triple-phase boundary (tpb) in case of a purely electronic conducting cathode material like $(La_{1-x}Sr_x)MnO_{3-\delta}$ (Fig. 13).

Whereas the bulk diffusion in the ABO_3 perovskite structure simply occurs by the hopping of oxygen vacancies, the overall surface reaction may involve many steps such as adsorption, dissociation, transfer of charge to oxygen molecules, and incorporation of oxygen ions in the oxide bulk [147] (cf. chapter 2.2.1). The diffusion mechanism is described by the diffusion coefficient D, the surface reactions are summarized by the oxygen-exchange coefficient k.

Different sets of variables and nomenclatures are used in literature to describe the oxygen exchange and oxygen-diffusion properties in $(La_xSr_{1-x})CoO_{3-\delta}$. This is due to the different measuring techniques, which are applied:

- *Impedance spectroscopy* is used by Adler to extract the oxygen-diffusion coefficient and the oxygen-exchange coefficient from a model [94, 148].

$$k^q$$
$$D^q$$

Eq. 27

- The *conductivity relaxation* technique involves time-sensitive measurement of the electrical conductivity of a sample after a stepwise change in the ambient oxygen partial pressure. The relaxation data are fitted to theoretical equations using the chemical diffusion coefficient and the surface-transfer coefficient as fitting parameters. This method is employed besides others by [110, 119, 147]. The oxygen-exchange coefficient k and

the oxygen-diffusion coefficient D obtained from these "chemical" experiments are denoted as

$$k_{chem}, k^{\delta}, \tilde{k}$$
$$D_{chem}, D^{\delta}, \tilde{D}$$

Eq. 28

- Oxygen isotopes (O^{18}) are utilized for *tracer experiments* to obtain D and k. After thermal treatment, the time-dependent diffusion profile is investigated by secondary ion mass spectroscopy (SIMS) [26, 94, 132, 148-151]. The coefficients k and D obtained from tracer experiments are denoted as

$$k_{tr}, k^0, k^*, k_{ex}$$
$$D_{tr}, D^0, D^*, D_{O^{2-}}$$

Eq. 29

In the following, k_{chem} / D_{chem} and k_{tr} / D_{tr} are used to refer to the electrical (impedance spectroscopy and conductivity relaxation) and tracer measurements, respectively.

The value of D_{chem} reflects both the oxygen-vacancy concentration and the thermodynamic factor Γ, while D_{tr} is more directly related to the structure and composition of the oxide [119]. Eq. 30 relates the chemical diffusion coefficient D_{chem} to the diffusion coefficient of the oxygen ions D_{tr} [119]:

$$D_{chem} = \Gamma_0 \cdot D_{tr}$$

Eq. 30

$$k_{chem} = \Gamma_0 \cdot k_{tr}$$

Eq. 31

$$\Gamma_O = \frac{1}{2} \cdot \frac{\partial \ln pO_2}{\partial \ln c_{O2-}}$$

Eq. 32

where Γ_0 is the thermodynamic factor [152] and c_{O2-} the concentration of oxygen ions. For $(La_{0.5}Sr_{0.5})CoO_{3-\delta}$, Γ_0 was determined to 124, 120 and 114 for 619°C, 649°C and 696°C within the experimental range of Wang et al. [119] (0.01 atm < pO_2 < 1 atm, 600 °C < T < 700 °C). This is consistent with the calculations of Søgaard et al., who determined Γ_0 to 115 (700 °C) based on the itinerant electron model [110]. Applying Eq. 32 to Eq. 30 and Eq. 31, respectively, oxygen diffusion and oxygen-exchange properties derived from different experimental methods can be compared. All data show Arrhenius-type temperature dependency (Fig. 20) and rather large deviations from the mean values.

Kilner et al. [149] noted an empirical relationship between the surface-exchange coefficient and the oxygen-diffusion coefficient:

$$k_{tr} = \sqrt{D_{tr}}$$

Eq. 33

irrespective of A and B cation types, temperature, pressure and dopant level. This strong correlation between the oxygen exchange and oxygen-diffusion properties suggests that oxygen vacancies play a major role both in the diffusion mechanism and in the surface

oxygen transfer [147]. This is supported by Fig. 21, which depicts a similar pO_2 dependence of k and D.
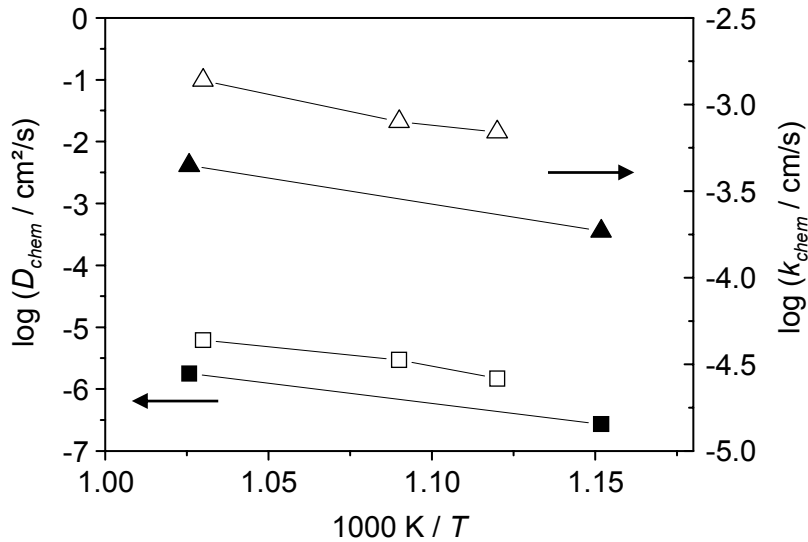
Fig. 20 Oxygen exchange and oxygen diffusion of LSC vs. temperature
Oxygen-diffusion coefficient D_{chem} and k_{chem} of $(La_{0.5}Sr_{0.5})CoO_{3-\delta}$ at pO_2 = 1 atm with respect to 1000 / T. The data was taken from [119] ($\triangle$, $\square$) and [132] ($\blacktriangle$, $\blacksquare$).

The activation energies of D_{chem} and k_{chem} were determined to 133 and 67 kJ / mol for pO_2 = 1 atm [119]. This is close to the activation energies for D_{tr} (E_A = 136 kJ / mol) and k_{tr} (E_A = 78 kJ / mol) obtained from tracer experiments by DeSouza et al. [132] at $pO_2 \approx$ 1 atm. Van der Haar et al. [147] observed that the activation energies increase with decreasing pO_2 ranging from E_A = 106 kJ / mol (pO_2 = 0.11 bar) to E_A = 131 kJ / mol (pO_2 = 4·10^{-4} bar) for D_{chem}, which correlates with the decrease of oxygen diffusion with decreasing pO_2 (Fig. 21).
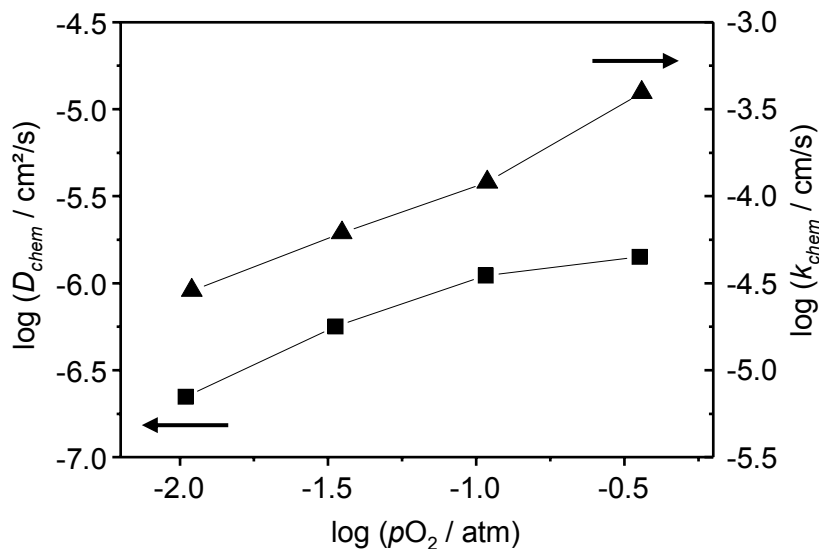
Fig. 21 Oxygen exchange and oxygen diffusion of LSC vs. oxygen partial pressure
Oxygen-diffusion coefficient D_{chem} and k_{chem} of $(La_{0.5}Sr_{0.5})CoO_{3-\delta}$ at T = 650 °C with respect to pO_2. The data was taken from [147].

Although there is still debate around the oxygen-reduction reaction (ORR) in LSC on the atomistic scale [94], the rate-determining steps (rds) of the ORR are generally discussed in terms of oxygen exchange and oxygen diffusion. Bouwmeester et al. [153] suggested that the critical length L_c of a dense LSCF cathode, at which the rds switches from exchange-controlled to diffusion-controlled follows:

$$L_c = \frac{D_{tr}}{k_{tr}}$$

Eq. 34

At L_c, the electrochemical reaction is neither diffusion nor exchange controlled. Larger oxygen-diffusion properties of the cathode material lead to an extended electrochemically active regime. For different compositions $(La_{1-x}Sr_x)CoO_{3-\delta}$, different pO_2 and different T, L_c was found to vary between 50 and 150 µm [147]. Adler et al. added a geometry term to Eq. 34 [26]:

$$l_\delta = \sqrt{\frac{1-\varepsilon}{\tau \cdot a} \cdot L_c} \approx \sqrt{l_g \cdot \frac{D_{tr}}{k_{tr}}}$$

Eq. 35

where l_δ is the utilization range, ε denotes the porosity of the cathode, τ its tortuosity, a the inner surface area and l_g the particle dimension. For l_g = 50 nm (20 nm), the utilization range of an LSC50 cathode becomes 1323 nm (826 nm) at 650 °C. In case of a nanoscaled LSC thin film with a thickness of approximately 300 nm, the rds is therefore considered to be exchange-controlled. This is supported by experiments conducted by Baumann et al. [154], who applied nanoscaled dense LSCF thin-film cathodes as geometrically well-defined model electrodes (t = 100 nm) onto single-crystal YSZ. Via electrical impedance spectroscopy the surface-exchange resistance was identified as the dominant oxygen-reduction mechanism [155].

For oxygen-exchange controlled cathodes, however, the role of porosity becomes essential (cf. 2.2.1). An optimized cathode structure needs to feature a maximum surface area within the utilization range, which entails a decrease of the oxygen-exchange losses and an increase of SOFC efficiency. The combination of a fine microstructure and a distinct nanoporosity leads to the maximization of the active cathode surface. This can be attained by the application of a sol-gel technique (metal-organic deposition), which is described in detail in 2.3. The influence of microstructure (grain size, thickness, porosity) on the cathode polarization losses is studied by Rüger et al. by 3-dim simulations [91] in a continuing work.

2.2.4 Chemical Stability of the LSC / Substrate Interface

The chemical stability between the cathode material LSC and the YSZ substrate is a critical issue. The formation of zirconate layers ($SrZrO_3$ and / or $La_2Zr_2O_7$) was described in detail for $T \geq 900$ °C by many groups [156-161].

However, for lower temperatures (T = 700 °C) Sase et al. [162] analyzed the interface reaction between a dense $(La_{0.6}Sr_{0.4})CoO_{3-\delta}$ thin film and (100) YSZ in a 3800 h testing

procedure. Post-test SIMS examination indicated the crystallization of $SrZrO_3$ with slow kinetics (the parabolic rate constant k_p was estimated to 10^{-18} cm²/s $< k_p < 10^{-17}$ cm²/s).

The formation of a chemical reaction layer between LSC and YSZ entails three negative effects: Firstly, the precipitation of La or Sr rich zirconates leads to changes of the cathode stoichiometry (predominately depletion of Sr) and thereby to different material properties (predominately decrease of oxygen exchange and oxygen diffusion) as shown in chapter 2.2.2 and 2.2.3. Secondly, according to the ternary phase diagram of the system La_2O_3-SrO-CoO [163] the thermodynamic stability for the $(La_xSr_{1-x})CoO_{3-\delta}$ system is given for a narrow band with 0.997 < La / Sr < 1.003 [119]. Even slight deviations from this stoichiometry lead to the formation of CoO (also cf. [118]). Thirdly, insulating [164, 165] zirconates, which precipitate at the LSC / YSZ interface, impede the ionic transport processes across the cathode-electrolyte interface and lead to increased polarization losses (charge-transfer polarization ASR_{ct} (iv), Fig. 73).

Gadolinia-doped ceria was suggested as a barrier layer by Chen et al. [20] in 1993 to block interdiffusion. Steele [21] and other groups [166-168] investigated CeO_2 and its cation diffusion inhibiting properties. They could not detect any reaction between $(La_xSr_{1-x})CoO_{3-\delta}$ and Gd-doped CeO_2 (GCO). Further investigations of the chemical compatibility between GCO and LSC can be found in [14, 20, 169-171]. The chemical compatibility between GCO and the state-of-the-art cathode material LSCF was shown by [19, 20, 159, 172].

In this work, the $(La_{0.5}Sr_{0.5})CoO_{3-\delta}$ thin films are processed by a sol-gel method, which contents itself with processing temperatures of $T \leq 900$ °C and short dwell times ($t_{RTA} \leq 15$ min), which is fairly below the known crystallization conditions of the interface reaction between LSC and YSZ. However, the LSC thin-film cathodes are analyzed on both surfaces YSZ ("design 1") and GCO ("design 2") with special emphasis on the interfacial stability.

2.3 Thin-Film Processing

For the evaluation of grain-size effects in nanoscaled electrolyte and cathode thin films, a variety of demands is addressed to the samples and thereby to the thin-film deposition technique. Two different material systems are deposited as thin films in this work: yttria-stabilized zirconia and lanthanum strontium cobaltite. Whereas the YSZ thin films need to be free of nanopores, the LSC thin films are to exhibit distinct nanoporosity. Three different substrates were selected: single-crystalline sapphire for the YSZ thin films and polycrystalline YSZ electrolytes and screen-printed GCO surfaces for the LSC thin films. Due to the interface reaction between LSC and YSZ (cf. chapter 2.2.4), the deposition method needs to content itself with processing temperatures fairly below the crystallization temperature of zirconates. Additionally, low temperatures during thin-film preparation facilitate a variation in grain size (and pore size) down to the nm-scale. This fine microstructure reduces the

stresses caused by different coefficients of thermal expansions (TEC) between deposited material and substrate (cf. 2.2.2). Finally, all thin films need to have high purity.

Tremendous efforts are undertaken to process high-quality YSZ and LSC / LSCF thin films for different purposes. The potential of thin-film synthesis was demonstrated in the 1990s [173, 174] with $(La,Sr)(Co,Fe)O_{3-\delta}$ cathodes. Some groups take advantage of the nanoporosity of the films and its high inner surface area [97] (also cf. 2.2.1 and 2.2.3), others structure the thin films predominately by a lithography and etching procedure to process model electrodes with a well-defined geometry [175, 176] to elucidate the rate-determining oxygen-reduction steps of the cathode [150, 155, 162, 177-179]. Furthermore, for IT-SOFC application, thin-film electrolytes are inevitable. The sticking point here is to ensure gas-tightness of the YSZ thin film, although the thin films usually have to be deposited onto undulated anode or cathode substrates.

Table 2 Chemical deposition methods for the processing of YSZ and LSCF thin films

Deposition Method	Thin Film	Substrate	Source
Chemical Vapor Deposition (CVD)	YSZ	Al_2O_3 (102)	[72]
	YSZ	MgO (100), SiO_2	[72]
	YSZ	ceria	[180]
	YSZ	Al_2O_3	[181]
Sol-gel	YSZ	NiO / YSZ	[182]
	YSZ	Sc_2O_3, Al_2O_3	[183]
	YSZ	Al_2O_3	[66, 184]
	YSZ	LSM	[185]
	LSCF	various	[173]
	LSC	fused silica	[174]
	LSC	silica	[186, 187]
	LSC	YSZ	[98, 100, 188]
	LSC	LSGM	[189]
Spray Pyrolysis (SP)	YSZ	NiO / YSZ	[190]
	YSZ	inconel foil	[191]
	YSZ	inconel foil	[192]
	YSZ	Si (100)	[193]
	LSCF	silica, glass	[194]
	LSCF	sapphire	[194]
	LSCF	GCO	[97]

Conventionally, SOFC electrolytes and cathodes with a thickness in the range of 200 µm and 50 µm, respectively, are prepared by tape casting or screen-printing. During the screen-printing process, a highly viscous paste consisting of a mixture of ceramic powder, organic

binder and plasticizer is forced through the open meshes of a screen [195]. Subsequently, the screen-printed films are dried and sintered at high temperatures. By the tape-casting technique, green tapes are produced, which may be cut into different shapes and subsequently sintered to a ceramic. Although these techniques are considered very cost-effective, they are not eligible for the processing of thin films due to the large shrinkage associated with the removal of the polymeric binders.

The challenge in processing electrolyte and cathode thin films is to find suitable processing techniques, which allow a cost-effective deposition of high-quality YSZ and LSC films. Further demands are low investment costs, high yield, high deposition rates, flexibility in the deposition material, high purity of the films, large area deposition, and tunable porosity of the films. A comprehensive review of the suitability of processing techniques for high-quality thin films has been given by Will et al. [195].

Several different approaches are pursued to obtain dense YSZ and nanoporous LSC or LSCF thin films. All methods can be differentiated into chemical and physical thin-film deposition. A literature review for the electrolyte and cathode thin films processed by chemical deposition techniques is given in Table 2. Physical deposition approaches are summarized in Table 3.

Chemical deposition methods include chemical vapor deposition (CVD) and thin-film deposition by a liquid precursor route. CVD is a chemical process, in which the reactant vapors are transported to the surface of the substrate where a chemical reaction and subsequent solid crystal growth takes place. For SOFC application, metal-organics have become important as precursor materials (MOCVD). For the liquid precursor route, molecular precursors are utilized, which entails a high purity and uniformity of the thin films. During sol-gel deposition, wet precursors are deposited by a variety of techniques (spin-coating, tampon-printing, dip-coating) onto the substrate. Consecutive heat treatment leads to the crystallization of the targeted material. This deposition method is capable of processing large-area, high-quality thin films at favorable low cost on a variety of substrates. The sol-gel approach, which was used to process the thin films studied in this work, is described in detail in chapter 3.1. For spray pyrolysis, a metal salt solution is sprayed onto a heated substrate to obtain the corresponding metal oxide films. The sprayed constituents react to form a chemical compound and crystallize upon heat-treatment.

Physical deposition methods utilize thermal spray technology, laser-deposition techniques or physical-vapor deposition techniques. Thermal spray technology comprises techniques, which heat up the coating material before it is projected at high velocity onto a substrate, e.g. air plasma spraying or atmospheric plasma spraying (APS). The laser-deposition techniques feature the ability to deposit a broad range of materials. The pulsed-laser deposition (PLD) method involves evaporation of a target by means of short and high-energy laser pulses and subsequent deposition of the vaporized material on the substrate in form of a thin film. Physical vapor deposition (PVD) is a generic term for a variety of sputtering techniques including direct current (DC) and radio frequency (RF) sputtering, which holds relatively low

deposition rates and reactive magnetron sputtering, which exhibits much higher yield. The sputtering technique relies on a plasma, which breaks a few atoms from the target material, followed by the deposition of the ablated material on a substrate.

Table 3 Physical deposition methods for the processing of YSZ and LSCF thin films

Deposition Method	Thin Film	Substrate	Source
Air Plasma Spraying (APS)	YSZ	stainless steel	[196]
	YSZ	aluminum	[73]
	YSZ	substrate removed	[197]
Pulsed Laser Deposition (PLD)	YSZ	Pt, sapphire	[198]
	YSZ	MgO (100)	[67]
	YSZ	steel	[199]
	YSZ	MgO (100), Si (100)	[199]
	LSC	YSZ (100)	[162, 200, 201]
	LSC	Ca doped ceria	[150, 171, 177, 202]
	LSCF	YSZ	[155, 203]
DC and RF Sputtering	YSZ	Ni/YSZ	[190]
	YSZ	NiO / YSZ	[79]
	LSC	YSZ	[156]
	LSC	GCO	[175]
Reactive Magnetron Sputtering	YSZ	Si (100)	[204]
	YSZ	aluminum (porous)	[78]
	LSC	$LaAlO_3$ (001)	[205]
	LSC	$SrTiO_3$ (001)	[205]

Whereas dense and crack-free thin films can be expected by application of the PVD methods (DC, RF and magnetron sputtering) or laser ablation (PLD), these techniques hold relatively small deposition rates. By contrast, spray pyrolysis and thermal spray technologies (APS) offer high deposition rates and the possibility for up-scaling. However, in case of thermal spraying, the high growth rates lead to thick and porous coatings. In terms of flexibility, chemical vapor deposition (CVD) and liquid deposition techniques offer a broad range of possible precursors. Especially the latter bears the disadvantage of many process parameters. However, if all parameters are kept under control, sol-gel deposition not only features low processing temperatures and high flexibility in the coating material, but also offers thin films with exceptionally high purity. Therefore, the sol-gel technique was chosen in this work to process dense YSZ and nanoporous LSC thin films.

All thin films presented in this work were processed within cooperation between the IWE and Fraunhofer Institute for Silicate Research (ISC), Würzburg. The cathode thin films were prepared by Dr. U. Guntow and co-workers and the electrolyte thin films by Dr. M.

Bockmeyer, Dr. R. Krüger and co-workers. The foundation for the processing has been laid down in the previous project "Compound Thin-Film Electrolyte / Cathode Substrate (Verbundstruktur Dünnschichtelektrolyt / Kathode)" supported by the Deutsche Forschungsgemeinschaft (DFG IV 14/1, DFG IV 14/2). In this work, Ivers-Tiffée et al. and Herbstritt et al. [88, 98-101] showed that the power density of solid oxide fuel cells can be significantly increased by the introduction of a porous electronic-conducting LSM film at 950 °C.

3 Experimental

A variety of techniques was applied to elucidate experimentally the role of interface density, grain size and porosity on the transport properties of nanoscaled thin films. This chapter comprises the sol-gel processing of the YSZ and the LSC thin films (3.1), the techniques applied for the evaluation of the microstructure and the structural properties (3.2) as well as the methods for the electrical and the electrochemical characterization of the thin films (3.3).

3.1 Thin-Film Preparation

3.1.1 Sol-Gel Deposition of Thin Films

Sol-gel processing has become a versatile method for preparing thin films on an industrial scale [206]. Sol-gel describes a technique, which processes non-metallic inorganic materials from wet, molecular dispersive precursors. A variety of advantages excels this method over other deposition methods as there are [207, 208]: high quality of the films, processing at favorable low cost, large-area processing, and depending on sol composition and processing parameters a variety of film properties that can be realized for diverse applications like catalytic applications (porous) or separating membranes (dense) (cf. chapter 2.3). However, a variety of demands is addressed to a coating sol, such as high yield, low crystallization temperature and good properties in wetting, filming and evaporation, which makes the development of the sols challenging. In the case of the nanoscaled thin-film cathodes, nanoporous thin films are aspired. For the electrolyte thin films, pore- and crack-free thin films are aimed.

Even though the preparation of materials from the liquid phase has a vast potential for applications, the sol-gel processing of inorganic films has the disadvantage of limited maximum film thickness. Due to the tensile stresses evolving during uniaxial densification, the ceramic sol-gel coatings have an upper ("critical") limit [209]. Therefore, the thin films in this work consist of 1 – 10 individual coatings on top of each other to achieve film thicknesses up to 500 nm.

The thin films were developed within close cooperation with the Fraunhofer Institute for Silicate Research (ISC), Würzburg. The cathode thin films were prepared by Dr. U. Guntow and co-workers, the electrolyte thin films by Dr. M. Bockmeyer, Dr. R. Krüger and co-workers.

Three different thin-film deposition techniques are applied in this work: dip-coating, spin-coating and tampon-printing of liquid sol. Whereas the *dip-coating* technique is used to process the 8YSZ thin films on sapphire substrates and the LSC thin films on gadolinia

doped ceria surfaces, the LSC thin films on yttria-doped zirconia are fabricated by spin-coating or tampon-printing.

During *dip-coating* the liquid film is obtained by transfer of the coating solution to a moving substrate. The film thickness is governed by numerous factors such as withdrawal rate v_0, sol viscosity η, and density ρ [206]. The final film thickness is described by the law of Landau-Levich:

$$d = 0{,}8 \cdot \sqrt{\frac{\eta \cdot v_0}{\rho \cdot g}}$$
Eq. 36

where v_0 was in the range of 3 cm / min.

During the *spin-coating* process [210], a solution is placed on a substrate, which is then rotated at high speed; the centrifugal force spreads the fluid over the substrate. The spin-coating parameters were set to 2000 rpm, 60 s.

During the *tampon-printing* process, an elastic polymer plunger carries the liquid sol from a printing plate to the substrate. By structuring the printing plate, this method is eligible to deposit thin films with a well-defined geometry.

3.1.2 Sol-Gel Deposition of YSZ Electrolytes

For the 8 mol% yttria-doped zirconia thin films, precursor powder was prepared based on a method previously reported [211, 212] (Fig. 22a). By slow addition of 1.0 mol (100.2 g) acetylacetone to 1.0 mol (424.9 g) zirconium-n-propoxide a yellow sol was obtained, which was stirred at 40 °C for one hour. After cooling down to room temperature 3.0 mol (54.0 g) distilled water and 0.173 mol (58.8 g) yttrium-acetate hydrate were added. The sol was stirred for 30 minutes at room temperature followed by 30 minutes at 80 °C. Subsequently, all volatile components were removed from the reaction mixture by rotational evaporation at reduced pressure with a maximum bath temperature of 80 °C. The resulting fine yellowish powder was X-ray amorphous and had a solid yield of 53 wt% with respect to 8YSZ. Coating sols (Fig. 22a) were prepared by dissolution of the precursor powder in a mixture of 90% ethanol and 10% 1.5-pentandiol, stirred over night and filtered through a 0.2 µm membrane. By adding 1.5-pentandiol to the sol thin film cracking can be significantly reduced or completely avoided because a higher degree of network flexibility is preserved [207].

To prepare the 8YSZ thin films, sapphire substrates (52.5 x 52.5 x 0.53 mm³, one side polished, average roughness R_a = 0.06 nm, Crystec, Germany) were dip-coated ten times into the molecular disperse sol. After each coating step, the samples were tempered by RTA for 10 min at 500 °C. Subsequently, the specimens were exposed to a final tempering step at temperatures between 500 °C and 1400 °C for 24 h (heating ramp 5 K/min) respectively.

As mentioned in chapter 3.1.1, all YSZ thin-film electrolytes were prepared by colleagues at the ISC.

a) 8YSZ sol

```
┌─────────────────────┐
│  1 mol Zr(OPr)₄     │
└─────────────────────┘
        │   ┌─────────────────────────────┐
        │◄──│    1 mol acetylacetone      │
        │   └─────────────────────────────┘
        │   ┌─────────────────────────────┐
        │◄──│        3 mol H₂O            │
        │   └─────────────────────────────┘
        │   ┌─────────────────────────────┐
        │◄──│  0.17 mol Y(acac)₃ * x H₂O  │
        ▼   └─────────────────────────────┘
┌─────────────────────┐
│ 8YSZ precursor powder│
└─────────────────────┘
        │   ┌─────────────────────┐
        │◄──│   90% ethanol       │
        │   │   10% pentandiol    │
        ▼   └─────────────────────┘
┌─────────────────────┐
│  8YSZ coating sol   │
└─────────────────────┘
```

b) LSC sol

```
┌───────────────────────────────────────────┐
│ Educts: La₂(CO₃)₃, Sr metal, Co(OH)₂       │
└───────────────────────────────────────────┘
                    │
                    ▼
┌───────────────────────────────────────────┐
│ Precursor powder: La, Sr, Co acetates      │
└───────────────────────────────────────────┘
                    │
                    ▼
┌───────────────────────────────────────────┐
│ Solvent: propionic acid (CH₂H₅COOH)        │
│          nonanoic acid (CH₃(CH₂)₇COOH)     │
│          acetic acid (CH₃COOH)             │
└───────────────────────────────────────────┘
                    │
                    ▼
┌───────────────────────────────────────────┐
│ (La₀.₅Sr₀.₅)CoO₃₋δ coating sol (11-13 wt%) │
└───────────────────────────────────────────┘
```
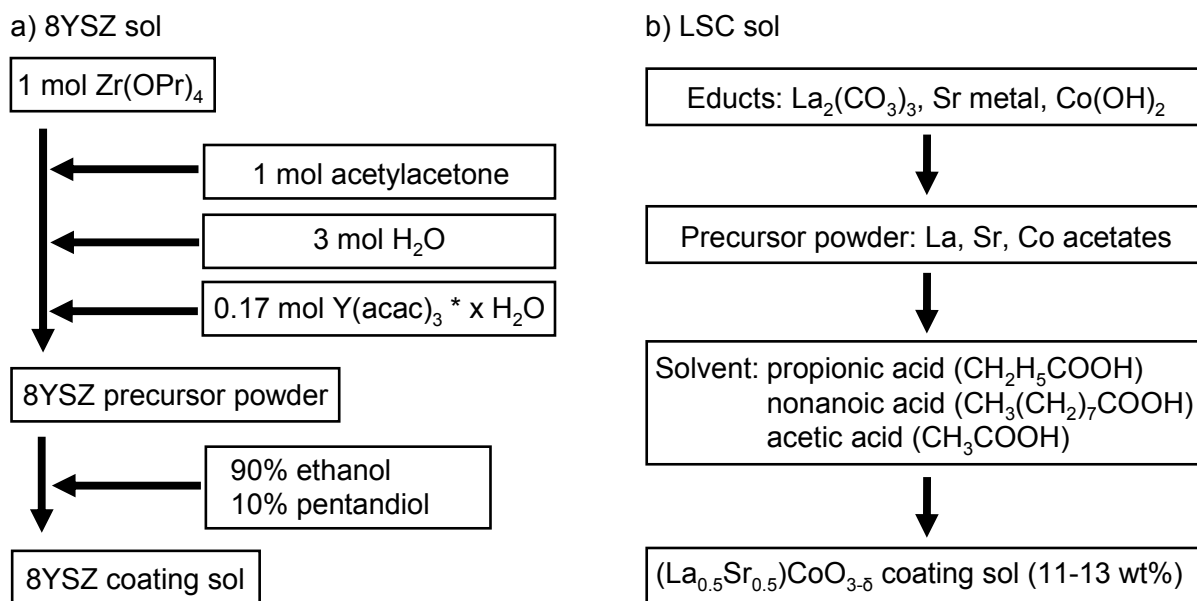
Fig. 22 Chemical processing routes of the coating sols for the preparation of a) $(Zr_{0.84}Y_{0.16})O_{2-\delta}$ and b) $(La_{0.5}Sr_{0.5})CoO_{3-\delta}$ thin film.

3.1.3 Sol-Gel Deposition of LSC Cathodes

$(La_{0.5}Sr_{0.5})CoO_{3-\delta}$ (LSC) thin films were deposited onto 8 mol% yttria-doped zirconia (8YSZ, Itochu Europe, Brussels, Belgium) electrolytes and screen-printed gadolinia-doped ceria (GCO) buffer layers by the sol-gel method [174]. The metallorganic precursors necessary for the preparation of the coating solutions were synthesized by using commercially available $La_2(CO_3)$, $Co(OH)_2$ and metallic Sr as starting materials (Fig. 22b). The synthesis was performed by reaction of these components with propionic acid (in excess) in the presence of propanoic anhydride or solely in the presence of acetic acid. After precipitation and filtration, precursor powders were obtained, which were mixed stoichiometrically. Coating sols were prepared by the dissolution of the precursor powder in a mixture of propanoic, nonanoic and acetic acid. The final composition of the coating solutions was controlled by inductively coupled plasma atomic emission spectroscopy (ICP-AES). The concentration of the coating solutions was typically adjusted between 11 mass% and 13 mass% content. Substrates were either multiple spin-coated (2000 rpm, 60 s) [213] or tampon-printed or dip-coated into the liquid sol. Subsequently, the coated samples were exposed to three rapid thermal annealing (RTA) steps at 170, 700 and 900 °C for 5 minutes each, which led to the oxidation of all organic moieties.

All LSC thin-film cathodes were prepared by colleagues at the ISC (cf. chapter 3.1.1).

3.1.4 Evaluation of the Precursor Calcination by Means of Thermal Analysis

The calcination temperatures (i.e. rapid thermal annealing, RTA) of the thin films were obtained by thermal analyses. The oxidative removal of organic components with respect to temperature was studied by thermal gravimetry (TG; TG439, Netzsch-Gerätebau GmbH,

Selb, Germany) and differential scanning calorimetry (DSC; DSC404, Netzsch-Gerätebau GmbH, Selb, Germany).

Both setups were calibrated using α-Al_2O_3 as a reference powder. The measurements were conducted using platinum crucibles in dry air atmosphere. No chemical reaction was observed between the platinum crucible and LSC precursor powder after calcination in the furnace at 850 °C (6 h). Heating ramps were chosen to 10 K / min and 1K / min, respectively.

To analyze the properties of the YSZ gel, glass plates were multiple dip-coated (30 times). After drying at 60 °C for 15 min, the coating was scraped off. Differential thermal analysis (DTA) and thermogravimetric analysis (TGA; Setaram TAG24, Caluire, France) of the obtained powder were carried out with a heating rate of 10 K / min in dry air atmosphere. These experiments were conducted by Dr. M. Bockmeyer, ISC [212].

The evaluation of the TG and DSC data was conducted with the software Proteus Analysis (Netzsch-Gerätebau GmbH, Selb, Germany). By applying the MARSH algorithm the characteristic (extrapolated) temperatures T_{onset}, T_{mean}, T_{peak}, T_{end} were obtained (a detailed description is given in the respective user manuals 03.88 (DSC) and 12.88 (TG)).

3.2 Analytics for Thin Films

A variety of analytical tools was applied to the sol-gel derived LSC and YSZ thin films. Whereas the microstructure of the thin films was studied by scanning electron microscopy (SEM), the crystallization and the phase composition were evaluated by transmission electron microscopy (TEM) and X-ray diffraction (XRD).

3.2.1 Microstructure Characterization by SEM

The dependence of thin-film processing and temperature treatment on the microstructure of the thin films was evaluated by scanning electron microscopy (SEM; LEO 1530, Zeiss, Oberkochen, Germany). For plan-view examination, the samples were mounted with a conductive carbon pad onto an aluminum SEM sample holder. For the study of the cross sections, the fraction surfaces were mounted perpendicular to the C-pad and the sample holder. All samples were contacted with silver paste to facilitate sufficient conductivity of the primary electrons of the SEM gun. Working distance and acceleration voltage were chosen to 5 – 8 mm and 1 – 5 kV, respectively.

3.2.2 Structural Characterization by (HT)XRD and (HR)TEM

The crystallization and chemical homogeneity of the precursor powders and the YSZ and LSC thin films were investigated by X-ray diffraction (XRD; Siemens D5000, Bruker-AXS, Karlsruhe, Germany). The setup was equipped with a copper radiation source ($CuK_{\alpha 1}$, λ = 0.15406 nm) followed by a monochromator (Bruker-AXS). Partly, a scintillator together with a soller slit (both Bruker AXS) was used.

The chemical reaction and the formation of secondary phases between the LSC and YSZ was studied by high-temperature (HT) XRD analyses of a powder mixture of 1 mol LSC derived from the sol-gel precursor powder and 1 mol YSZ powder. For these experiments, a heating module (HTK 16, Anton Paar GmbH, Graz, Austria) was used.

Individual samples were selected for thorough investigations by means of transmission electron microscopy (TEM). The studies on the YSZ thin films were performed by B. Butz and Dr. H. Störmer, Laboratory for Electron Microscopy (LEM), Universität Karlsruhe (TH) in the joint DFG-NSF project "Nanoionics". The experiments on the LSC thin films were mainly conducted by Levin Dieterle (LEM) within the common project D5 "Functional Electrode Structures" of the Center for Functional Nanostructures (CFN), Universität Karlsruhe (TH). Most of the results on the microstructure of the LSC thin films were published in [214]. The essential findings of the structural properties of the YSZ thin films were published in [215]. Selected-area electron diffraction (SAED), conventional and high-resolution TEM (TEM / HRTEM) imaging was performed with a 200 keV Philips CM200 FEG/ST equipped with a field-emission gun. The local chemical composition of the samples was analyzed by energy dispersive X-ray spectrometry (EDXS) by means of a Noran Vantage system with a Ge detector. Electron-spectroscopic imaging (ESI) was performed with a 200 kV LEO 922 Omega transmission electron microscope with an in-column Omega energy filter. Based on electron spectroscopic images, the element distribution was revealed by means of the three-window technique [216].

Two different techniques were applied for TEM sample preparation. Plan-view samples were prepared conventionally by grinding, polishing and Ar-ion milling. Cross-section samples with a homogeneous thickness of about 100 nm were prepared by focused ion beam (FIB) milling using the H-bar technique [217] with the following preparation steps. Two sample pieces with an area of 1 mm – 2 mm were glued together with the thin-film LSC layers oriented against each other. Top and bottom sides of this sandwich were polished to an overall thickness of about 40 µm. The front face, which is used for the ion milling was polished, too. Subsequently, the sandwich was mounted into a halved TEM aperture grid. In a combined SEM / FIB system (ZEISS EsB 1540 Crossbeam), a focused Ga-ion beam was used to cut out two 40 µm long cuboids perpendicular to the glue gap until a thin membrane remains, which was stabilized by the surrounding thicker material. A thin line of Pt was deposited previously by ion-beam induced deposition on the glue gap to protect the front face of the milled membrane against the tail of the Ga ion beam [214].

3.2.3 Grain-Growth Analysis

The grain-growth behavior of the LSC thin films was studied by SEM analyses. For grain-growth investigation of the 8YSZ thin films both SEM and XRD analyses were applied.

The mean grain sizes of the thin films were statistically evaluated from the SEM micrographs using the image processing software SPIP^{TM} (Image Metrology A/S; Lyngby, Denmark). Each grain diameter was calculated as a circle equivalent diameter from the grain area.

While SEM was used to evaluate grain sizes in the micrometer and sub micrometer range, XRD offers means to characterize grain-growth behavior of several tens of nanometers and below. The line widths of the Bragg peaks provide information on both the average grain size *d* and the internal strain *e* of the thin films. Broadening by grain size and strain can be separated by means of Halder and Wagner plots ("Method of Integral Breadth") where *Δ²/tan²Θ* is plotted versus *Δ/(tanΘsinΘ)* [218] (Eq. 37).

$$\frac{\Delta^2 (2\Theta)}{\tan^2 \Theta_0} = \frac{K\lambda}{d}\left(\frac{\Delta(2\Theta)}{\tan\Theta_0 \sin\Theta_0}\right) + 16e^2 \qquad \text{Eq. 37}$$

Δ denotes the full width at half maximum (FWHM) in 2Θ of (111) and (222) reflections; *λ* is the wavelength of the setup (cf. chapter 3.2.2); *K* takes a value of 0.89 for spherical grains [219]. Θ_0 and FWHM values were obtained from XRD spectra by Fourier analysis (Software EVA 9.0). The FWHM results from peak broadening due to instrumental broadening $FWHM_i$ and due to the microstructure $FWHM_c$ [219]. The instrumental peak broadening ($FWHM_i$ = 0.05°) of the diffractometer was determined by measuring an 8YSZ electrolyte (Itochu, Tokyo, Japan) with micrometer sized grains and was eliminated from the FWHM by the equation of Warren and Biscoe [219] (Eq. 38).

$$FWHM_c^2 = FWHM^2 - FWHM_i^2 \qquad \text{Eq. 38}$$

To facilitate grain growth, the 8YSZ and LSC specimens were exposed to annealing temperatures of 500 °C and 1400 °C for 24 h and to annealing temperatures of 500 °C to 900 °C for 2 h, 10 h and 100 h, respectively.

3.3 Electrochemical Experiments

One experimental key tool to evaluate the transport processes in nanoscaled thin films was their electrochemical characterization by electrical impedance spectroscopy (EIS) [220]. Two different setups, which were designed during this work, emerged to be eligible: Microelectrodes were used for the analysis of the in-plane conductivity of the YSZ thin films and a symmetrical setup was applied for the evaluation of the polarization losses of the LSC thin-film cathodes.

3.3.1 Microprobing

The electrical conductivity of the nanoscaled YSZ thin films was studied using a Micro-Prober Module (Kammrath & Weiß GmbH, Dortmund, Germany) and a Heater Module (Kammrath & Weiß GmbH) (Fig. 23, left)[1]. The samples were contacted by gold needles with a peak radius of approximately 100 nm (Fig. 23, right), which were positioned onto sputtered platinum electrodes (100 µm x 4 mm). A Novocontrol Alpha frequency response analyzer (Novocontrol Technologies GmbH, Hundsangen, Germany) was used for impedance spectroscopy

---

[1] This setup was designed within the diploma thesis of Barbara Szöke: „Elektrische Charakterisierung von Nanoschichten" (*Electrical Characterization of Nanoscaled Thin Films*), IWE, March 2006

measurements, which were performed between 200 °C and 400 °C in air atmosphere. The temperature of the samples was measured by two thermocouples fitted onto the surface of the sample and underneath the sample in the Heater Module.
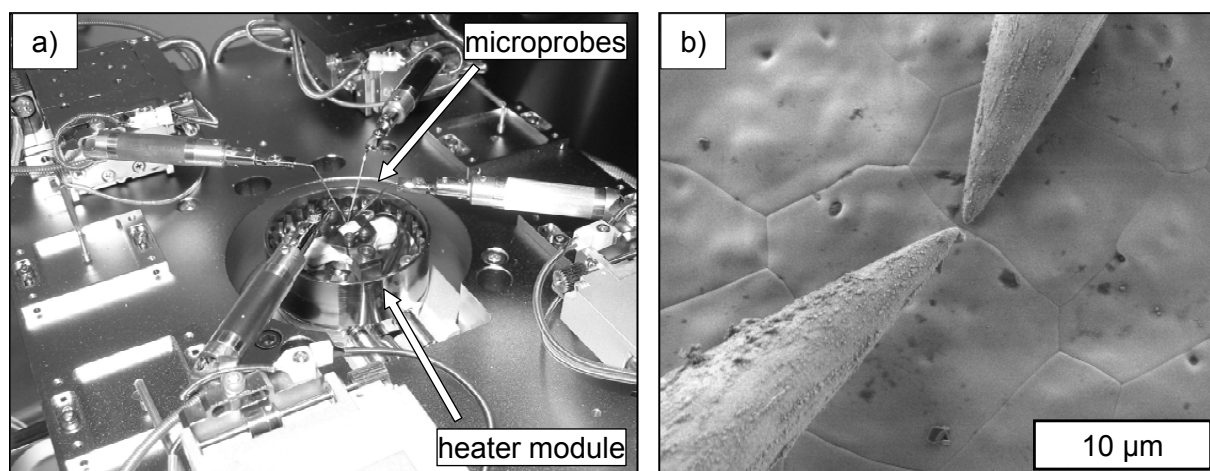
Fig. 23 Images of the microprobing setup

a) Microprobes and heater module used for the electrical characterization of the 8YSZ thin films; b) SEM image of two gold needles on top of a coarse crystalline 8YSZ electrolyte (Itochu, Japan).

The accuracy of the testing setup was evaluated by a comparison measurement of a coarse crystalline SOFC electrolyte (8YSZ, Itochu, Japan, mean grain size: 9.6 µm) in the microprobing AC setup (Fig. 24b, ▼) and in a four contact AC setup (Fig. 24b, ■). Fitting the impedance data (Fig. 24a) with a nonlinear least-squares fitting algorithm (software ZView, Scribner Associates, Inc., North Carolina, USA) and equivalent circuits consisting of three serial RQ elements representing the grains, the grain boundaries and the electrodes, a reasonable fit was obtained (Fig. 24a, grey curve). Details on the evaluation of the setup were published in [221].

The error bars in the Arrhenius plot (Fig. 24b) account for uncertainties during the electrical characterization in both setups, namely temperature measurement as well as geometrical considerations associated with the screen-printed (four contact AC setup) or sputtered (microprobing AC setup) platinum electrodes and the measuring accuracy of the electrical equipment (manufacturers' data). In chapter 4.1.3, the transport properties of YSZ thin films are studied with respect to grain size. The data presented in this chapter comprise additional errors due to the evaluation of the mean grain size and the mean film thickness. The comparison of the obtained results shows a consistency of the data within a deviation of the activation energy of ΔE_A < 2% and confirms accuracy within the temperature range 200 °C ≤ T ≤ 400 °C.

By open circuit measurements, the stray capacitances of the setup, which arise because of non-ideal shielding of the wiring and the electrodes, were determined to C_{setup} = 7.4·10^{-14} F (Fig. 25).
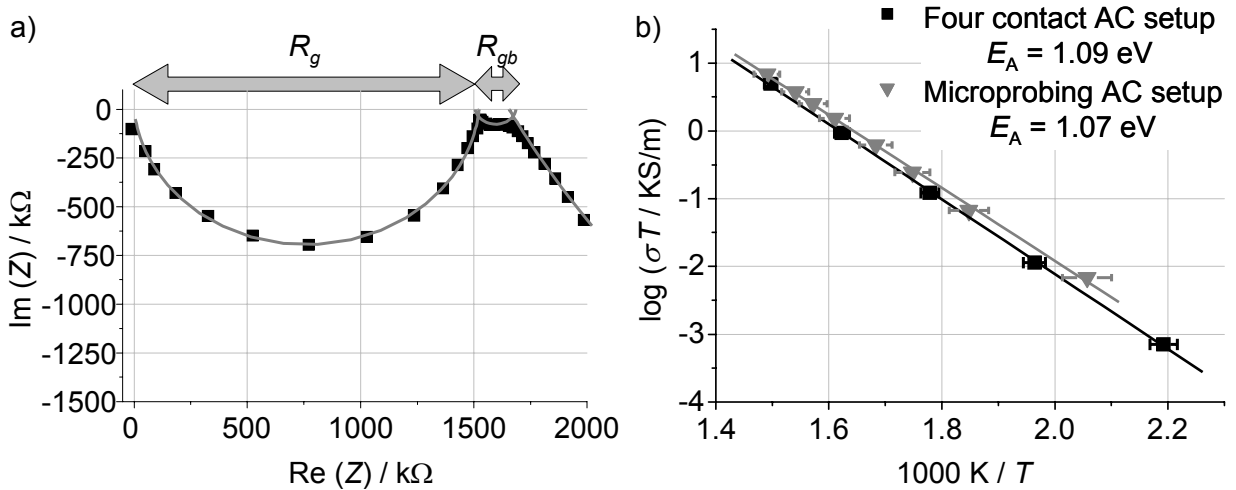
Fig. 24 Evaluation of the microprobing setup

a) Nyquist plot of an 8YSZ electrolyte analyzed in the microprobing setup at 300 °C, the fit of the impedance data is depicted in grey; b) Arrhenius plot shows a comparison between the ionic conductivity of the 8YSZ electrolytes obtained by measurements in the four contact AC setup (■) and the microprobing AC setup (▼).
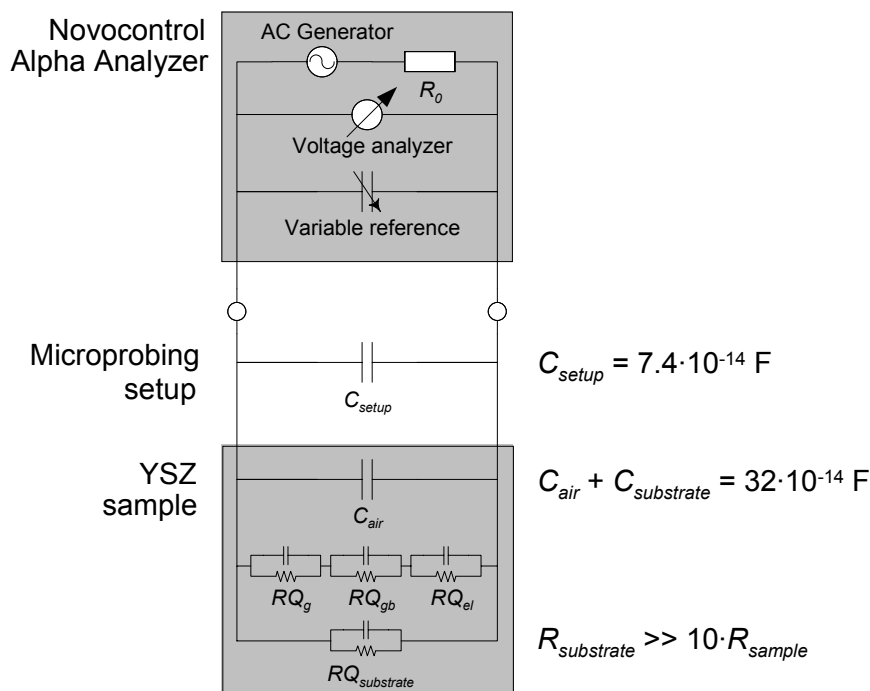
Fig. 25 Electrical equivalent circuits of the microprobing setup and the YSZ sample

For the fit of the EIS data, parallel capacitances originating from the substrate (sapphire), the environment (air atmosphere) and the setup (microprobes and wiring) were considered. The YSZ specimen itself is characterized by three serial RQ elements representing the grains (RQ$_g$), the grain boundaries (RQ$_{gb}$) and the electrodes (RQ$_{el}$). The figure also depicts the equivalent circuits of the frequency response analyzer (Novocontrol, Alpha).

The capacitances of the environment (C_{air}) and the substrate ($C_{substrate}$) were determined by a reference measurement (C_{air} + $C_{substrate}$ = $32 \cdot 10^{-14}$ F). These capacitances were taken into

account as parallel paths for the EIS data evaluation. The resistance of the substrate appeared to be much higher than the 8YSZ thin-film resistance over all temperatures. The sapphire substrate can therefore be assumed to be insulating. This is consistent with FEM simulations (conductivity data taken from [222]), which showed that the substrate resistance of the sapphire substrate is about two decades higher than the 8YSZ thin-film resistance.

3.3.2 Symmetrical Cell Measurements

Electrochemical properties of the thin-film cathodes were examined by electrical impedance spectroscopy (EIS). The experiments were carried out with symmetrical cells (screen-printed current collector | nanoscaled LSC cathode | electrolyte substrate (either YSZ or screen-printed GCO on YSZ) | nanoscaled LSC cathode | screen-printed current collector) in a single chamber reactor (Fig. 26)[2].

A: Al_2O_3 sample holder
with gas channels

B: Pt / Rh thermocouple
(Type S)

1: Au mesh
1024 meshes / cm², 0.06 mm wires

2: Screen-printed current collector
$(La,Sr)(Co,Fe)O_{3-\delta}$, thickness approx. 30 µm

3: Thin film cathodes
$(La_{0.5}Sr_{0.5})CoO_{3-\delta}$, thickness approx. 300 nm

4: 8YSZ / GCO substrate
thickness approx. 200 µm
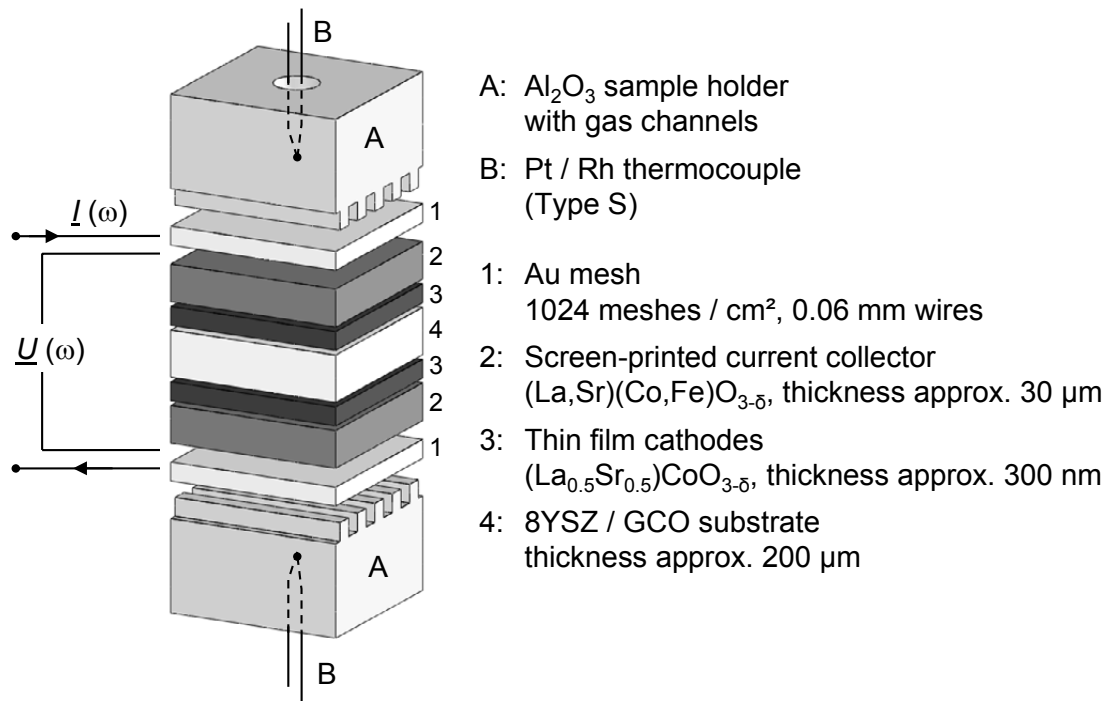
Fig. 26 Sketch of the symmetrical measuring setup for EIS characterization
The symmetrical cells consist of LSCF current collector / LSC thin film / electrolyte substrate / LSC thin film / LSCF current collector.

As a current collector $(La,Sr)(Co,Fe)O_{3-\delta}$ paste was applied, which was consecutively dried at 70 °C for 12 h in air. Together with a spot-welded Au-mesh (> 99.99% Au, 1024 meshes / cm², 0.06 mm wires) the current collector allowed a homogeneous current distribution over the electrode and assured a negligible contact resistance of less than

---

[2] This setup was evaluated within the study project of Holger Götz: „Einfluss der Mikrostruktur auf den Polarisationswiderstand einer LSC-Nanokathode" (*Influence of the Microstructure on the Polarization Losses of a nanoscaled LSC Thin-Film Cathode*), IWE, June 2007.

10 mΩ·cm² [223]. The symmetrical cells were placed into an Al_2O_3 sample holder. A weight of 120 g applied to a 1 cm² electrode area ensured a reliable contacting. EIS measurements were carried out using a Solartron 1260 frequency response analyzer (FRA) at frequencies between 10^{-1} Hz and 10^6 Hz. The electrical impedance measurements were conducted with amplitudes below 20 mV to ensure a linear system response (this was verified in current – voltage measurements with Zahner IM6 (Zahner-Elektrik, Kronach, Germany), also cf. [224] and the discussion on cathode polarization in chapter 2.2.1). All measurements were carried out in ambient air. Two thermocouples (type S: Pt - Pt/Rh), which were fitted into the contact blocks (Fig. 26), ensured that the cell temperature (T_{cell}) remained constant during each EIS measurement.
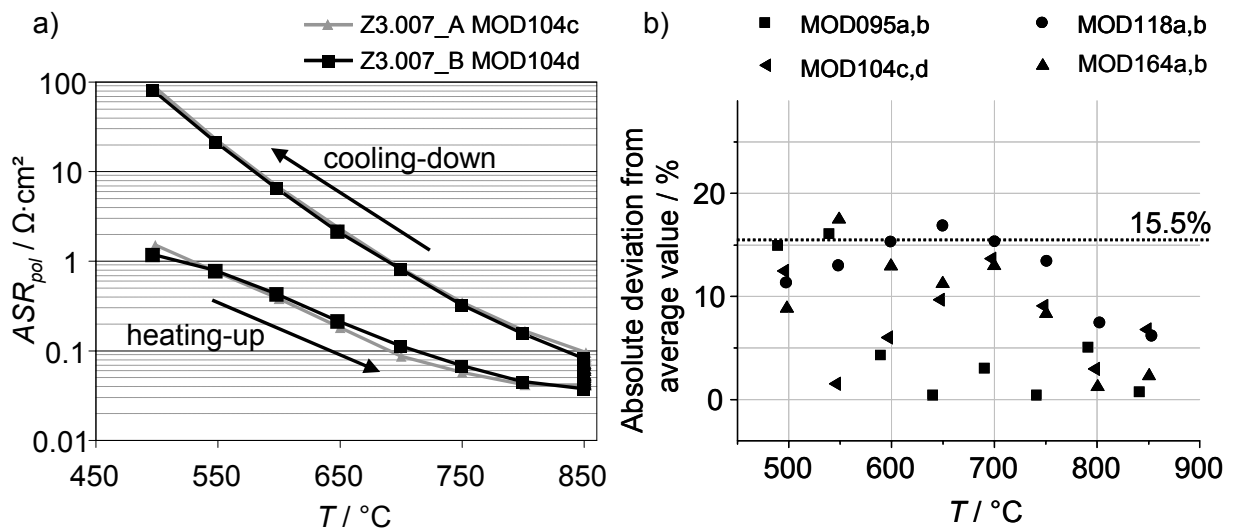
Fig. 27 Reproducibility of symmetrical cell measurements
a) Example for reproducibility measurement over temperature; b) summary of the reproducibility measurements over temperature.

Reproducibility measurements of identical LSC thin-film samples (the as-prepared samples were cut into two parts prior to electrochemical characterization) are depicted in Fig. 27. The graph Fig. 27a shows good agreement of two samples during the standard measuring procedure (room temperature $RT \rightarrow 850\ °C \rightarrow RT$). The absolute values of four reproducibility measurements are summarized in Fig. 27b, where the deviation from the mean value of each sample pair is given in percent over measuring temperature. This deviation of Δ_{max} = 17.5% comprises errors evoked during the processing of the thin films (±2%), the sample preparation (paste flow: +2%, layer misalignment: -9.8%), measuring accuracy of the frequency response analyzer and the thermocouples (Solartron 1260: ±0.2%, "type S" thermocouples: ±1.5%, inhomogeneous temperature distribution in the furnace: ±3%) and subsequent analyses of the EIS data (±1%). An additional error arises from potential lateral conduction within the LSC thin film, which increases the electrochemically active area to maximum 11 x 11 mm², which corresponds to an error of +21.6% as estimated

by FEM modeling. These maximum errors are inserted as error bars in the respective charts within this work.

3.3.3 Evaluation of the Electrical Impedance Data

Two approaches are employed to analyze the complex impedance data: (i) a *physical approach*, which needs an a-priori knowledge about the electrochemical processes, from which electrical equivalent circuits are derived and (ii) a *general approach*, which goes without previous knowledge about the electrochemistry.

If the underlying physical processes are known, the obtained impedance spectra can be analyzed by a **c**omplex **n**onlinear **l**east **s**quares (CNLS) approximation to a model function represented by an equivalent circuit. In this case, the equivalent circuit model needs to be defined *a-priori*. However, in reality the real number of polarization processes contributing to the overall polarization loss of the cell is often unknown leading to a severe ambiguity of the adopted model. Alternatively, a pre-identification of the impedance response can be obtained by calculating and analyzing the corresponding distribution function of relaxation times (DRT) as reported in details in [225, 226]. This approach uses „generalized equivalent circuits", consisting of a serial connection of RC elements (80 elements in this work). These electrical elements do not evitably correspond to physical processes, but solely describe the dynamics of the system. The analysis leads to a distribution function of relaxation processes $g(\tau)$, which describes the frequency dependent losses of the system (Eq. 39). The distribution function exhibits a significantly higher resolution than the impedance data, because dynamic processes are usually separated on the frequential scale.

$$\underline{Z}(j\omega) = \int_0^\infty \frac{g(\tau)}{1 + j\omega\tau} d\tau \qquad \text{Eq. 39}$$

For the solution of this Fredholm integral equation of the first kind, the Tikhonov regularization is applied within the program "FTIKREG" [227] (and ref. therein). This algorithm has been implemented into a user-friendly Microsoft Excel sheet "Tikcel 0.99.xls" by Volker Sonn, IWE.

The high frequential resolution of the DRT approach is used to visualize the impact of the grain boundaries on the overall conductivity of the YSZ thin films (cf. Fig. 39). By applying the CNLS fit on the impedance data, the grain-boundary conductivity and the bulk conductivity were calculated (cf. Fig. 40).

The impedance data of the LSC thin-film cathodes were fitted to equivalent circuits using both the CNLS fitting algorithm (software ZView, Scribner Associates, Inc., North Carolina, USA), from which the area specific polarization resistance (ASR_{pol} [89]) was derived and the DRT analysis to evaluate individual polarization parts.

4 Results

To elucidate the transport properties of charge carriers in nanoscaled YSZ and LSC thin films, the results of the electrical and electrochemical experiments are presented. In case of the YSZ thin films (4.1), the analysis focuses on their ionic conductivity with respect to grain size. In case of the LSC thin films (4.2), transport in terms of the oxygen-reduction mechanism and its dependency from grain size and nanoporosity is studied. Regarding the discussion of these results in chapter 5, special emphasis is put on the evaluation of the processing of the thin films and their chemical and microstructural stability. An overview of the conducted experiments is given in the Appendix 7.1.

4.1 Grain-Size Effects in YSZ Electrolytes

This chapter comprises the results of the processing of YSZ thin films (4.1.1), the temperature related change of the thin-film microstructure, i.e. grain growth (4.1.2) and the study of the ionic transport properties of the thin films with respect to mean grain size (4.1.3).

4.1.1 Processing of the YSZ Thin Films

For the processing of crack-free, homogeneous YSZ thin films, temperature treatment of the samples is an essential issue. Therefore, thermal analysis was applied to determine the rapid thermal annealing (RTA) procedure, which the samples were exposed to.
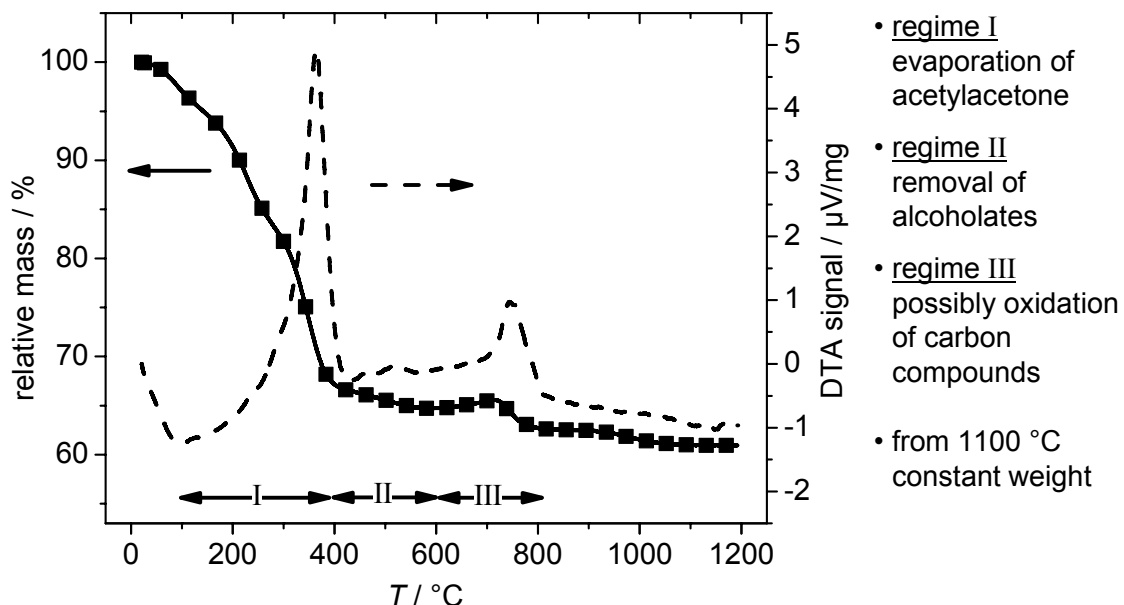

Fig. 28 Thermal analysis of scratched-off YSZ precursor powder

Heating rate: Δ*T* = 10 K / min in synthetic air. TG measurements (left axis) show a relative mass loss of 39 wt% and mass constancy for *T* > 1100 °C.

Chemical decomposition and oxidation of the sol-gel precursor powder were analyzed by differential thermal analysis (DTA, Fig. 28) and thermogravimetric analysis (TG, Fig. 28) in cooperation with Dr. M. Bockmeyer (Fraunhofer Institute for Silicate Research ISC, Würzburg).

The DTA analysis shows three exothermic chemical reactions in a temperature range between room temperature and 1200 °C. All three processes are accompanied by mass losses as indicated by TG measurements. Between room temperature and 400 °C (region I) the major part of the total mass loss (83%) occurs. The first part below 100 °C is attributed to the evaporation of water. The DTA and TG data between 100 °C and 400 °C are explained by the oxidative removal of organic groups (acetylacetone, extrapolated onset $T_{onset,I}$ = 300 °C, $T_{peak,I}$ = 360 °C) [228]. In the same temperature range, pycnometry shows a significant increase of powder density of 37% [229]. Two further exothermic processes can be identified between 400 °C and 600 °C (region II) and 600 and 800 °C (region III). Since both chemical reactions are accompanied by mass losses (15%), they cannot be attributed to phase changes. Instead, DTA analysis with a varying ratio of ethanol and other alcoholates suggests that the second regime is attributed to their removal from the powder. Skeletal density increases linearly in region II and III to 90% of the theoretical value of 8YSZ (5.8 g/cm^3 [230]) [229]. The third exothermic process, which is accompanied by a change of the powder color from black to white, might be attributed to the removal of remaining carbon compounds. This would explain further densification in this temperature regime and would lead to a significant relaxation of the microstrain in the thin films. From 1100 °C, TG analysis indicates a final weight of 61% relative mass, which correlates with 98% of the theoretical density of 8YSZ at this temperature [229].

Optical and scanning electron microscopic analyses exhibit crack-free surfaces over an area of 40 x 50 mm². Fig. 29 shows 2.5 x 1.25 µm² sections of the surface with respect to calcination temperature (1st and 4th row). With increasing temperature, grain growth is apparent. The cross-section analysis (Fig. 29, 3rd and 5th row) displays constant film thicknesses between 300 and 450 nm and an excellent adhesion to the sapphire substrate. Prior to SEM evaluation, the samples were coated with silver paste, dried and subsequently cut to ensure a good electronic contact. Some remainings of the silver paste can be seen on the cross-section images.

The porosity of the thin films was verified by HAADF STEM imaging visualizing porous regions as local changes in density, as those appear darker in contrast. Fig. 29a-c (2nd row) show HAADF STEM micrographs of the thin films calcined at T_{cal} = 650 °C, 850 °C and 1000 °C, respectively, where the pore sizes are of similar dimension as the average grain size in the thin films. Specimens, heat-treated at temperatures exceeding 1100 °C, were found to be dense.
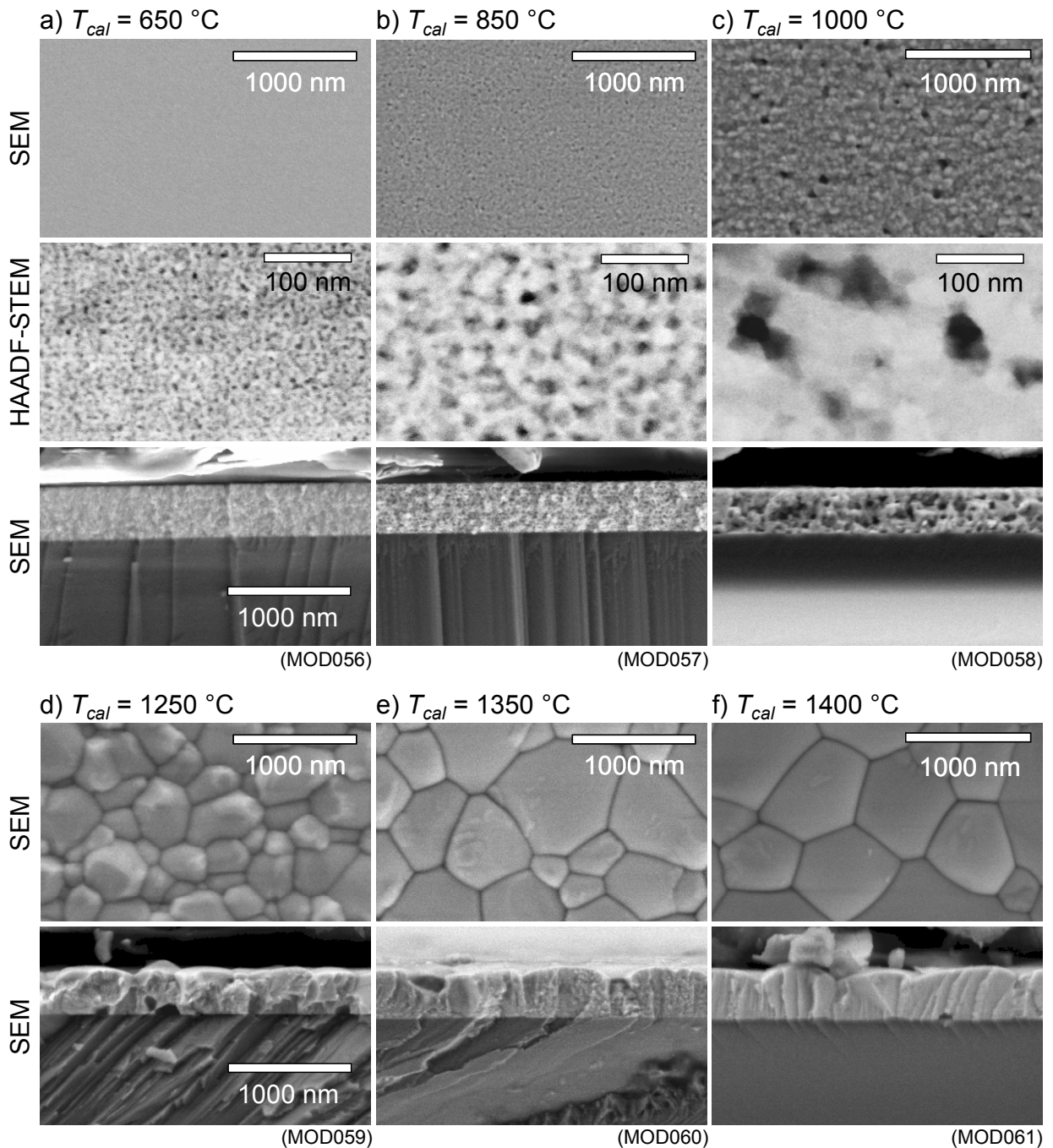
Fig. 29 SEM and HAADF STEM analyses of 8YSZ thin films

SEM top-view (1st and 4th row) and cross-section (3rd and 5th row) images of YSZ thin films calcined at a) 650 °C (MOD056), b) 850 °C (MOD057), c) 1000 °C (MOD058), d) 1250 °C (MOD059), e) 1350 °C (MOD060) and f) 1400 °C (MOD061); the films are crack-free over 40 x 50 mm²; the film thickness *t* ranges between 300 and 450 nm. 2nd row: HAADF STEM micrographs of a) MOD056, b) MOD057 and c) MOD058 visualize pores, which appear darker in contrast. All samples were calcined for 24 h.

X-ray measurements of the 8YSZ thin films in the glancing incidence mode show the characteristic reflection data of 8 mol% yttria-doped zirconia ($92ZrO_2 \cdot 8Y_2O_3$, JCPDS[3] PDF#00-030-1468) and exhibit cubic crystallization as demonstrated with a representative sample calcined at 1350 °C (Fig. 30). With decreasing calcination temperature of the thin films, a broadening of the diffraction peaks is observed, which is employed for grain-growth analyses (4.1.2).
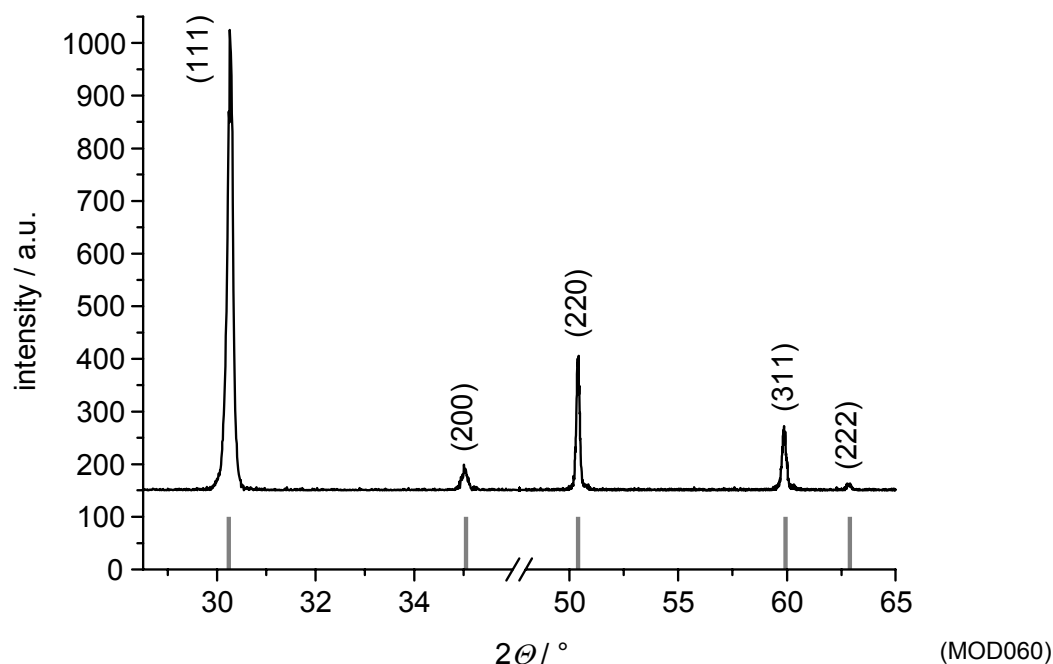
Fig. 30 XRD analysis of 8YSZ thin film (1350 °C / 24 h)
Comparison between the diffraction data and PDF#00-030-1468 exclusively shows cubic single-phase crystallization of the $(Zr_{0.84}Y_{0.16})O_{2-\delta}$ thin film.

Quantitative analysis of the yttria-dopant concentration revealed a Zr : Y ratio of 83.4 : 16.6 corresponding to 8.3 ± 0.3 mol% Y_2O_3 in the YSZ [215], which is in good agreement with the desired 8 mol% Y_2O_3.

TEM bright-field micrographs of the cross-section of specimens MOD056 (650 °C) and MOD057 (850 °C) are given in Fig. 31a and Fig. 31b, respectively. Specimens MOD056 as well as MOD057 show a layered structure created by the 10-fold dip-coating process. No evidence for a layered structure was found in specimens that were calcined at temperatures above 850 °C.

Whereas the specimens annealed up to 1000 °C are characterized by a uniform film thickness, the samples calcined at $T_{cal} \geq 1250$ °C exhibit grain diameters larger than the film thickness entailing a variation of the film thickness between grain boundary and bulk (e.g. MOD060 ($T_{cal} = 1350$ °C), Fig. 29e). The relationship between thickness of the thin films with

---

[3] JCPDS-ICDD: Joint Committee on Powder Diffraction Standards – International Centre for Diffraction Data, Newton Square, USA

remained porosity to thickness of the pore-free thin films gives an estimate of the volume fraction of the pores (cf. [215]). For all calcination temperatures, the same density of the crystalline phase can be assumed since the yttria contents and thus the lattice parameters of the YSZ are similar in all thin films. The porosity is highest for MOD056 (T_{cal} = 650 °C) with 15.4 vol% and remains zero for MOD059, MOD060 and MOD061 (Table 4).

a)

(MOD056)

b)

200 nm
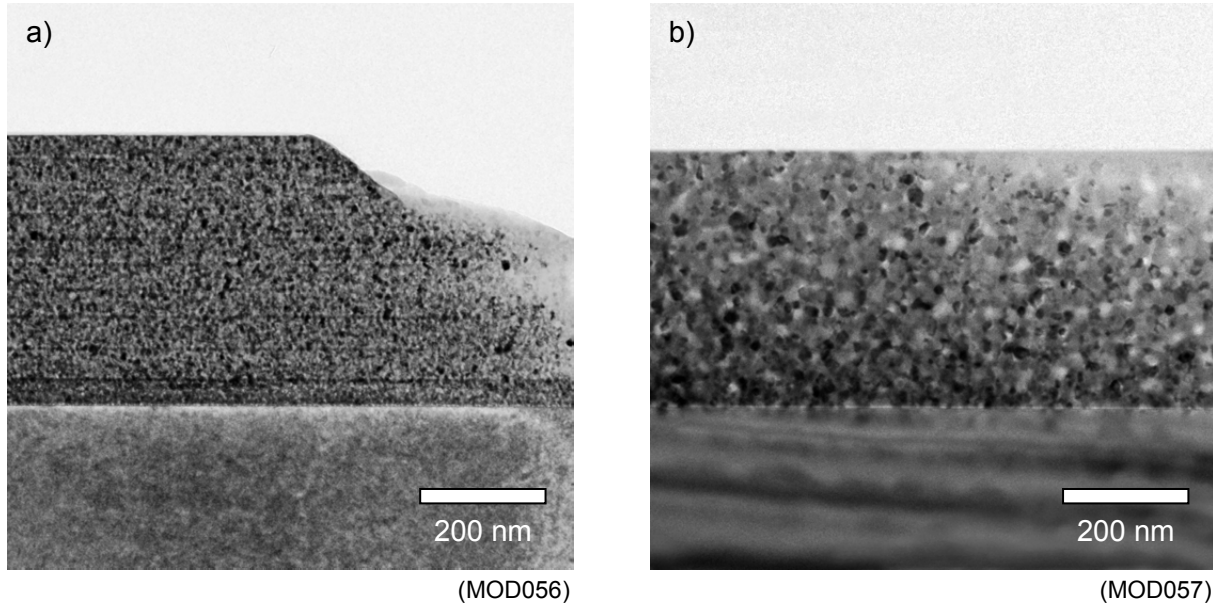
(MOD057)

Fig. 31 TEM cross-section bright-field micrographs
of a) MOD056 (T_{cal} = 650 °C, 24 h) and b) MOD057 (T_{cal} = 850 °C, 24 h) show a layered structure created by the 10-fold dip-coating process; MOD057 exhibits grain growth in comparison to MOD056.

TEM analysis was applied to analyze the chemical phase of the YSZ thin films [215]: Fig. 32a shows a homogeneous distribution of small precipitates with a size of a few Å and tetragonal structure, which are visible as a bright contrast within the dark cubic matrix in the sample calcined at 650 °C. The bright regions with sizes of about 5 to 20 nm, marked by arrows in Fig. 32a, are cubic ZrO_2 regions with strongly excited (200) or (220) reflections. Fig. 32b shows a grain boundary in the specimen calcined at 1250 °C marked by arrows. This micrograph demonstrates that the density of tetragonal precipitates inside the grains and close to the grain boundaries is homogeneous, which applies also to all other specimens. In contrast to the nanocrystalline specimens, the precipitates in the specimen calcined at 1350 °C tend to coarsen as visualized by the inhomogeneous distribution of the bright regions in Fig. 32c.

Special emphasis was put on the thorough analyses of the grain boundaries in the YSZ thin films [215]. Representative HRTEM images of the grain boundaries are shown in Fig. 33. The arrow-marked grain boundaries do not yield any evidence for amorphous grain-boundary phases. This result even applies to the samples calcined at 650 °C (MOD056), which were annealed at the lowest temperature, indicating the absence of carbon residues at the grain

boundaries. EDXS analyses, additionally performed at several grain boundary and triple-point regions, with probe diameters of approximately 1 nm did not yield any indication for segregation of impurities or yttrium ions within the detection limit of 0.1–1 at.% in the illuminated volume in any of the specimens.

(MOD056)   (MOD059)   (MOD060)
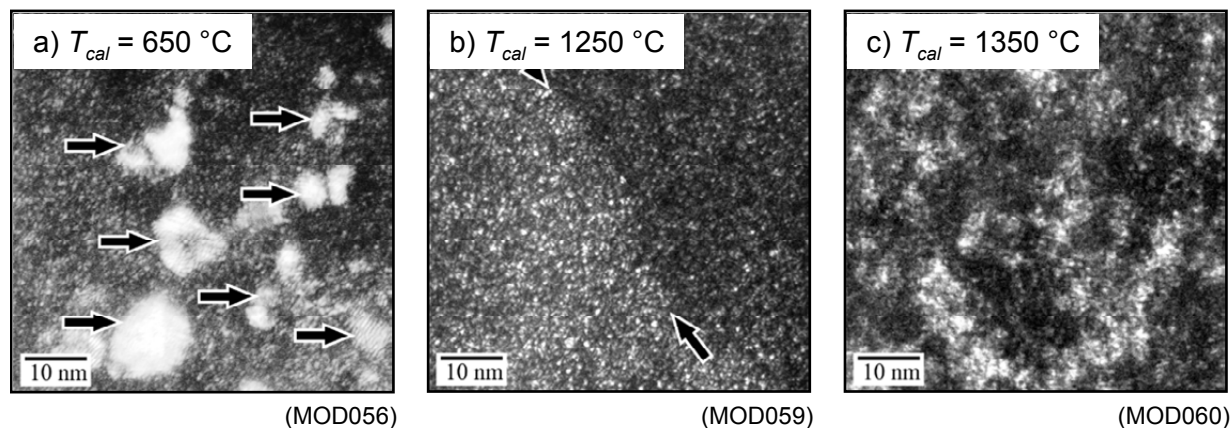
Fig. 32 Dark-field micrographs taken with the (112) reflection [215]
of a) the sample calcined at 650 °C (24 h, MOD056), the arrows mark bright contrast of cubic matrix of excited grains caused by the aperture size; b) the sample calcined at 1250 °C (24 h, MOD059), the arrows mark a grain boundary; c) the sample calcined at 1350 °C (24 h, MOD060). Tetragonal precipitates are visible as a bright contrast.

(MOD057)   (MOD058)
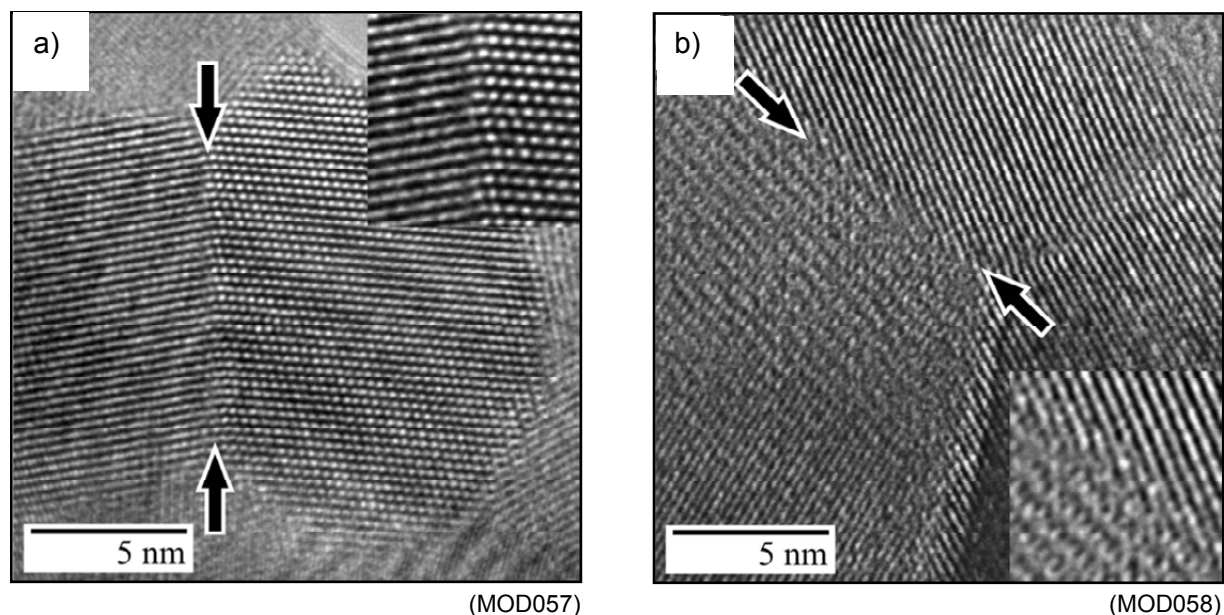
Fig. 33 HRTEM micrographs of samples calcined 24 h at a) 850 °C and b) 1000 °C [215]
The arrow-marked grain boundaries are additionally enlarged shown in the insets.

4.1.2 Temperature-Dependent Grain Growth

Coarsening of the YSZ thin films was studied by image processing of the SEM micrographs (Fig. 29) and the evaluation of the XRD data (Fig. 30). Additionally, single grains were evaluated by TEM analysis. While large grains were analyzed by SEM, the grain growth in the tens of nanometer regime was evaluated by TEM and XRD. Thereby, the full width at half maximum (FWHM) of the XRD spectrum was employed to the method of integral breadth as described in 3.2.3. Fig. 34a depicts the (111) peak at $2\Theta = 30.2°$ noting the FWHM value at 50 % of the maximum peak intensity. With decreasing calcination temperature, a broadening of the XRD peaks becomes apparent as depicted in Fig. 34b entailing information on both the mean grain size and the microstrain of the films.

Between 600 °C and 850 °C, a reduction of the internal strain of 50% was observed, which correlates with the third exothermic process of the DTA analysis and was attributed to the removal of carbon compounds [229].
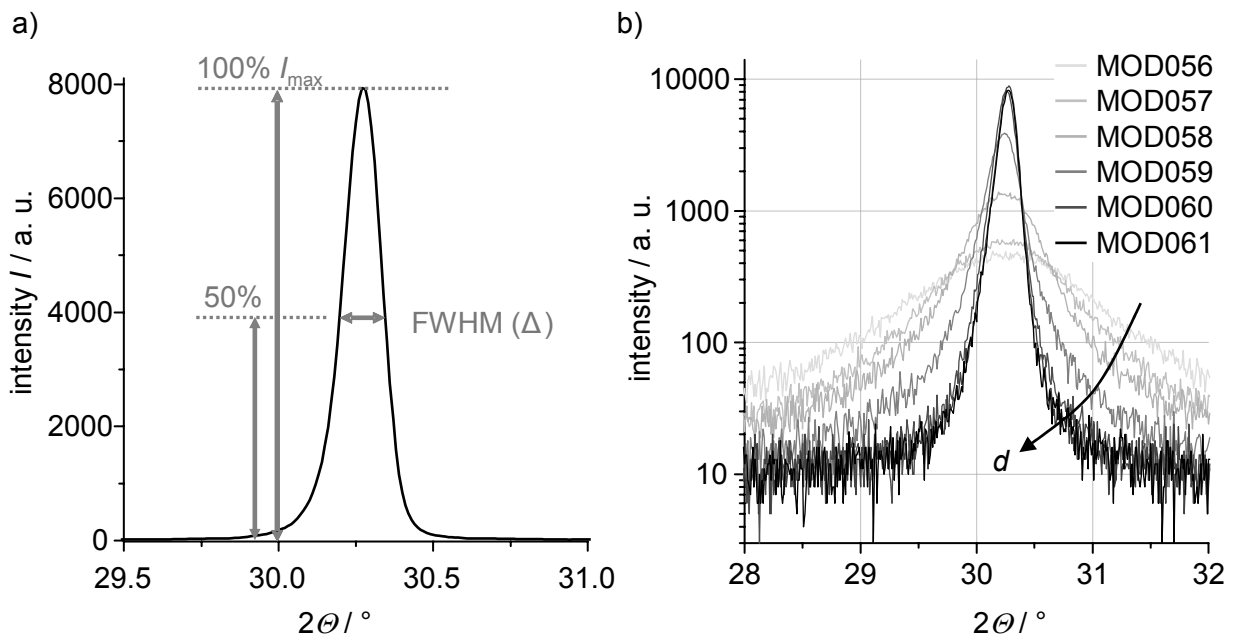
Fig. 34 Grain-size evaluation by application of the method of integral breadths
a) Evaluation of the (111) XRD peak; b) (111) peak of the YSZ thin films with respect to calcination temperature (650 °C ≤ T_{cal} ≤ 1400 °C) and mean grain size d.

While the grain sizes do not exceed a few tens of nanometers between 650 and 1250 °C (characterized by XRD and TEM), the mean grain sizes at $1350 ≤ T_{cal} ≤ 1400$ °C (characterized by SEM and TEM) were found to be in the submicron range (Fig. 35). The mean grain size rises by more than two decades from 5 nm at 650 °C to 782 nm at 1400 °C calcination temperature. This grain-size variance is considerably larger than in other studies on zirconia thin films [231-237]. The data obtained by XRD, SEM and TEM analyses coincide well suggesting two grain-growth regimes with different activation energies. Grain growth can be described by the equation [238] (cf. Eq. 45 and Eq. 46)

$$d^n = k_0 \cdot t \cdot e^{-\frac{Q}{RT}} \qquad\qquad \text{Eq. 40}$$

where d represents the grain size, Q the activation energy for the predominant transport mechanism, and t the calcination duration. The exponent n may vary significantly between 2 and 4 [238]. It cannot be determined on the basis of the experiments conducted in this work, where only the temperature was changed using always the same calcination time. Plotting ln (d / nm) as a function of 1000 / T in Fig. 35 (left axis) yields a straight line for the three porous specimens (MOD056, MOD057, MOD058). This indicates that the same processes dominate during grain growth in the porous regime. An acceleration of the grain growth upon densification is observed for MOD059, MOD060 and MOD061, which implies a possible change of both n and Q. The transition temperature at approximately T_{cal} = 1100 °C correlates with the presence of nanoporosity in the studied 8.3 mol% yttria-doped zirconia thin films (Fig. 35, right axis).
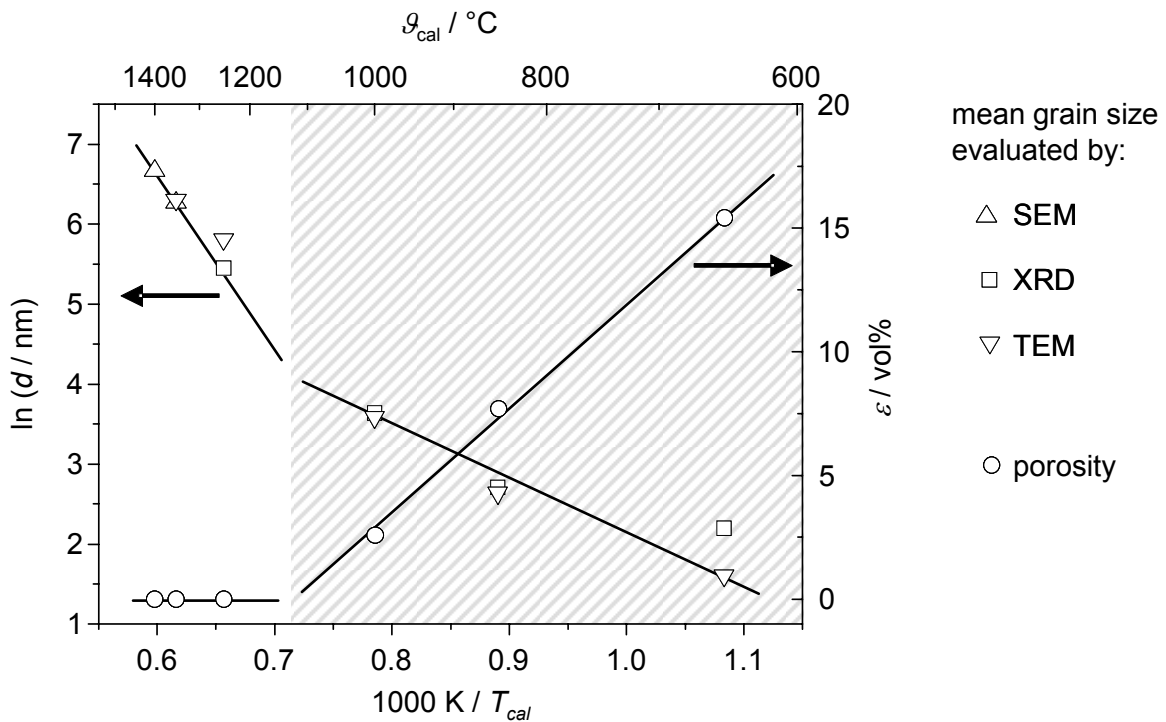
Fig. 35 Mean grain size d and volume porosity ε as a function of calcination temperature
left axis: Arrhenius plot of grain growth, i.e. the average grain size as a function of reciprocal temperature, in YSZ thin films evaluated by TEM (∇), XRD ($\square$) and SEM (Δ); right axis: porosity ($\circ$) of the thin films with respect to calcination temperature, studied by TEM analysis; fits are guide to the eye. Whereas the porosity of the films decreases with T_{cal}, the mean grain size increases from 5 nm (T_{cal} = 650 °C, 24 h) to 782 nm (T_{cal} = 1400 °C, 24 h).

Table 4 summarizes the morphological and structural properties of the 8YSZ thin films with respect to calcination temperature. With increasing grain size, the deviation of the film thickness from the mean value increases.

Table 4 Morphological and structural properties of the calcined 8YSZ thin films
where *d* denotes the mean grain size obtained by XRD, SEM and TEM studies, t_{min} and t_{max} the minimal and maximal film thickness, *ε* the nanoporosity and *e* the microstrain in the YSZ films.

T_{cal} / °C	650	850	1000	1250	1350	1400
MOD-ID	056	057	058	059	060	061
$d_{XRD,SEM}$ / nm	9	15	38	232	628	782
d_{TEM} / nm	5	14	36	335	548	-
t_{min} / nm	450	420	400	342	270	236
t_{max} / nm	450	420	400	390	390	390
ε / vol%	15.4	7.7	2.6	0	0	0
e / %	0.53	0.15	0.16	0.20	-	-

4.1.3 Electrical Transport in YSZ Thin Films

The transport properties of the 8.3 mol% yttria-doped zirconia thin films were electrochemically analyzed by means of impedance spectroscopy using microprobes (3.3.1). A simulation of the current-density distribution showed that the electric field in the YSZ thin films was homogeneous in good approximation (the aspect ratio between electrode clearance l_{cl} and film thickness *t* was greater than 120).

As denoted in 4.1.1 and 4.1.2, the YSZ thin films calcined at T_{cal} ≤ 1000 °C exhibited homogeneously distributed nanopores ($ε_{YSZ-650}$ = 15.4 vol%, $ε_{YSZ-850}$ = 7.7 vol%, $ε_{YSZ-1000}$ = 2.6 vol%). This nanoporosity entails an extension of the transport path and causes current constrictions in the specimens, thus, increases the resistance compared to a completely dense sample. To account for this increase and to obtain the intrinsic transport properties, the effective sample geometry was modeled applying a 3-dim model set up by Rüger [91].

The microstructure of the model, which consisted of 10 x 10 x 20 cubes representing either insulating nanopores or conductive YSZ grains, was randomly generated by a geometry generator [91]. Ten randomly generated pore distributions were calculated and subsequently analyzed. Thereby, the increase of the thin-film resistance by insulating nanopores compared to a sample without porosity was determined to 30.9% (MOD056, T_{cal} = 650 °C), 13.5% (MOD057, T_{cal} = 850 °C) and 4.3% (MOD058, T_{cal} = 1000 °C).

From the EIS data, the total thin-film resistance was obtained consisting of the bulk resistance R_g and the grain-boundary resistance R_{gb}. The total resistance R_{tf} was transformed into the ionic conductivity of the electrolyte by applying:

$$\sigma = \frac{1}{R_{tf}} \cdot \frac{l_{cl}}{A} \qquad \text{Eq. 41}$$

where l_{cl} denotes the electrode clearance (l_{cl} = 68 μm) and *A* the cross-section of the active thin-film volume (electrode length l_{el} = 4 mm times film thickness *t*, cf. Table 4).
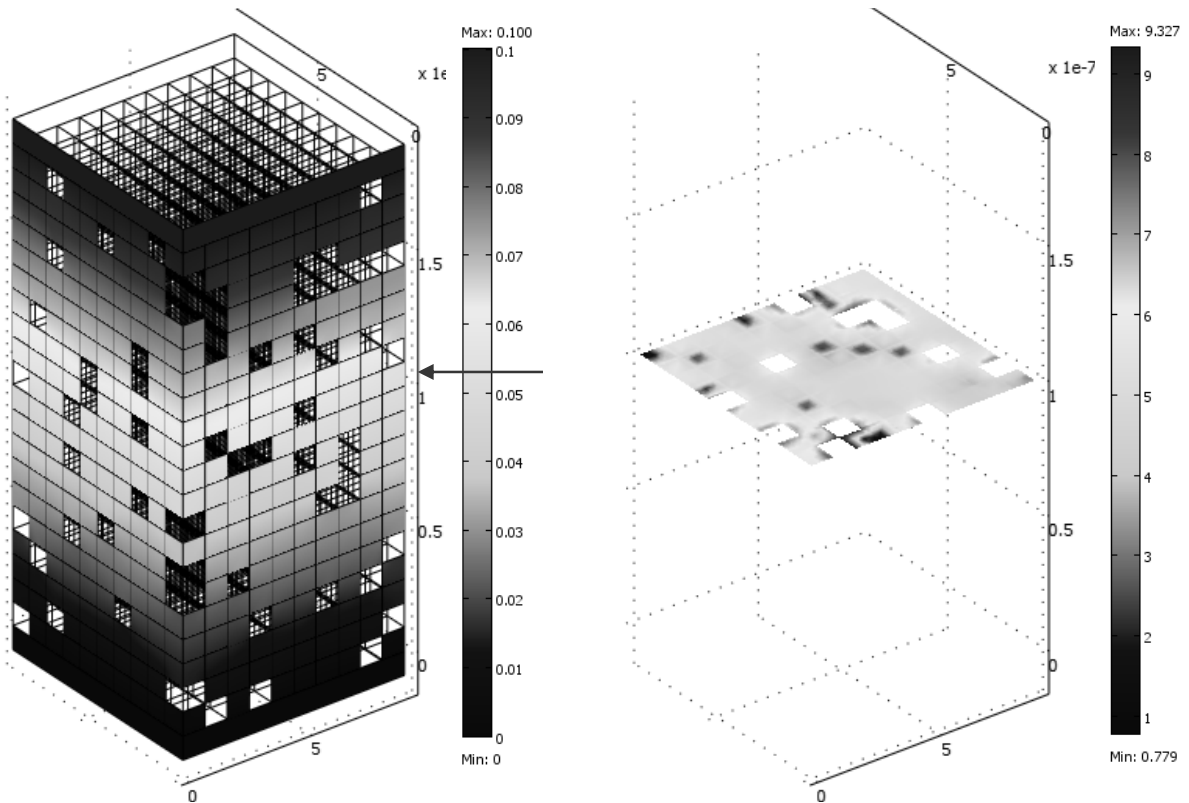
Fig. 36 Three-dimensional model [91] to account for the nanoporosity in the YSZ thin films
The model comprises 10 x 10 x 20 cubes representing either YSZ material (filled) or pores (empty).
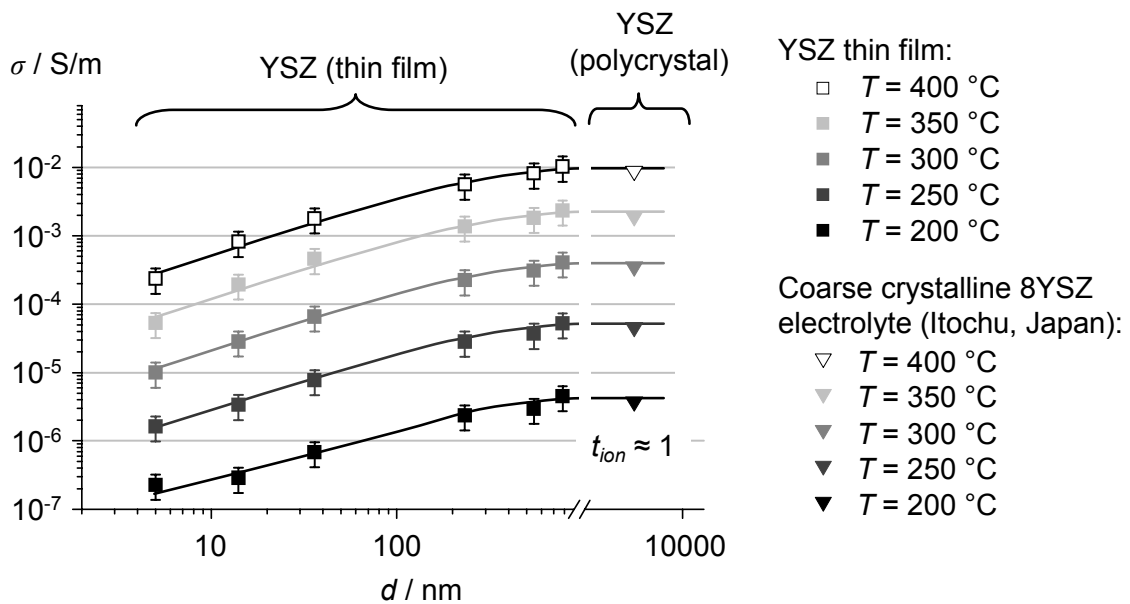
Fig. 37 Total electrical conductivity with respect to mean grain size
The conductivity data of MOD056, MOD057, MOD058 (T_{cal} ≤ 1000 °C, d ≤ 36 nm) were emended by the influence of nanopores. For comparison, the electrical conductivity of a polycrystalline YSZ electrolyte (∇) is depicted; fits are guide to the eye.

Considering the correction of the detour effect and the current constrictions, which arose through the nanopores, the electrical conductivity of the YSZ thin films can be plotted versus mean grain size (5 nm ≤ d ≤ 782 nm). The data are depicted in Fig. 37 with respect to measuring temperature (200 °C ≤ T ≤ 400 °C). With increasing mean grain size, the electrical conductivity increases continuously by 1 - 2 decades reaching a plateau at d ≈ 500 nm. The electrical conductivity of the thin films with these large YSZ grains (e.g. d = 782 nm: σ_{tf} = $1.0 \cdot 10^{-2}$ S/m, T = 400 °C) coincides with a deviation of 10% with the electrical conductivity of coarse crystalline Itochu-8YSZ ($\sigma_{polycrystal}$ = $0.9 \cdot 10^{-2}$ S/m, T = 400 °C). The oxygen-vacancy transference number of the 8YSZ electrolyte is close to unity, which suggests that oxygen vacancies are mainly involved in the charge transport in the 8YSZ thin films due to the congruence of the electrical conduction values. However, the decrease of the mean grain size into the nanometer regime goes along with a diminution in electrical conduction by 98 % (d = 5 nm: σ_{tf} = $2.4 \cdot 10^{-4}$ S/m, T = 400 °C).
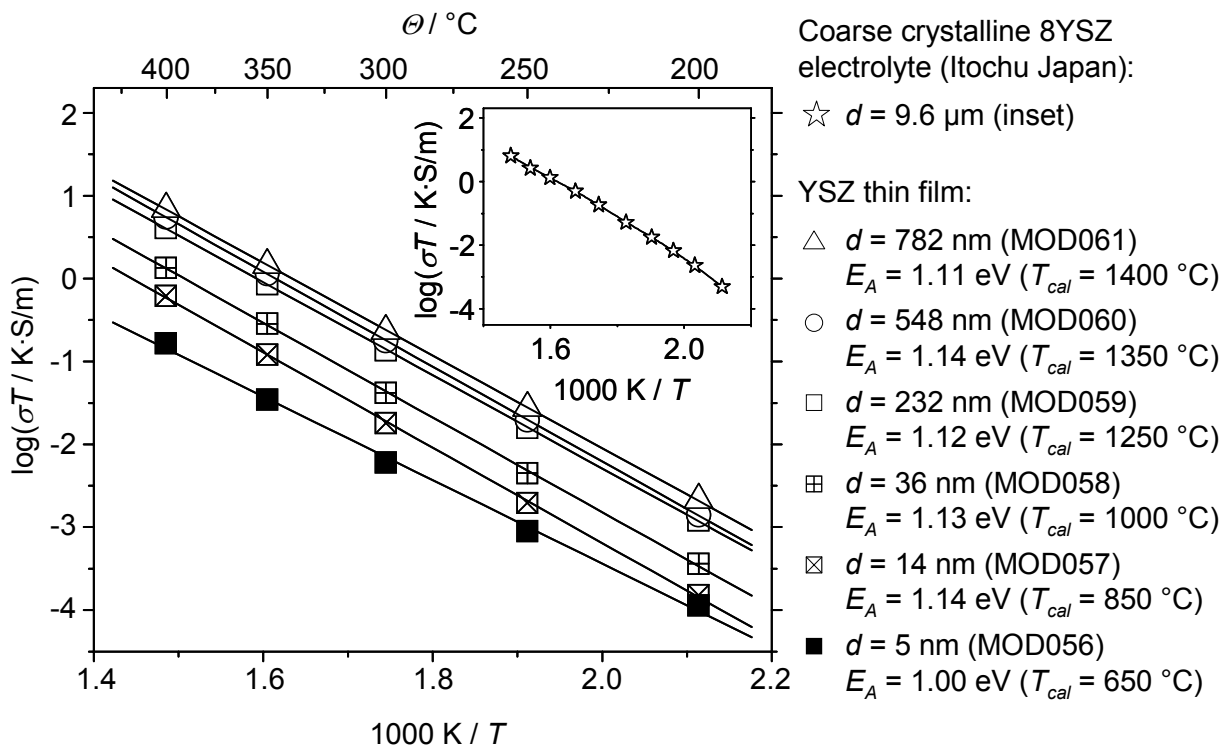
Fig. 38 Arrhenius plot of the total electrical conductivity with respect to mean grain size
The data of MOD056, MOD057 and MOD058 (T_{cal} ≤ 1000 °C, d ≤ 36 nm) were emended by the influence of nanopores. The conductivity diminishes with decreasing mean grain size. Inset: extrapolated electrical conductivity of a coarse crystalline 8YSZ electrolyte (Itochu, Japan) obtained by Simonin [38].

As discussed in 2.1.2, ionic transport in YSZ obeys the Arrhenius law (Eq. 10). The activation energies of the thin films were fitted to 1.13 ± 0.02 eV (Fig. 38). The sample with the smallest mean grain size (5 nm) shows an activation energy of E_A = 1.00 eV. For comparison, the electrical conductivity of coarse crystalline Itochu-8YSZ is depicted in the plot (inset). The data coincides well with the conductivity data of MOD061 featuring the largest grains.
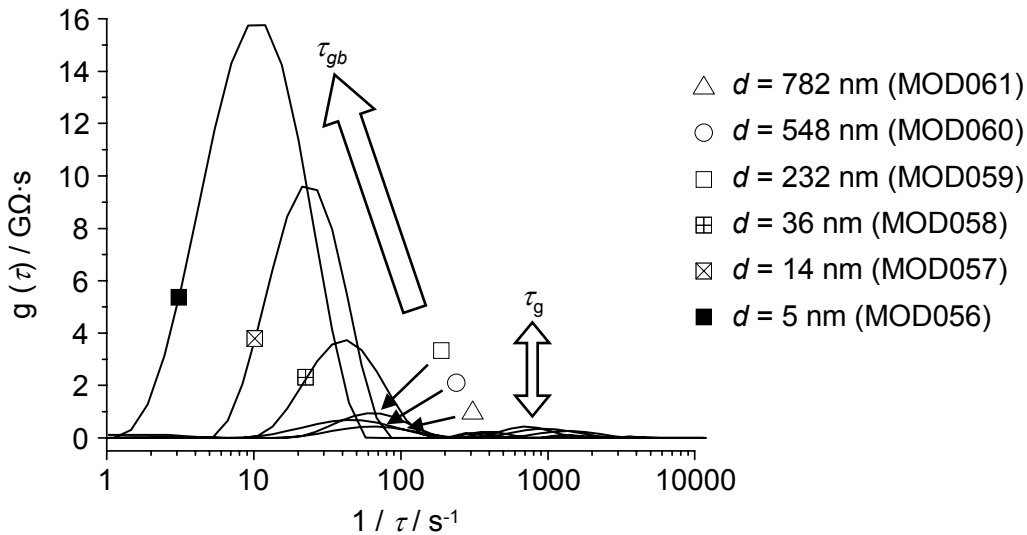
Fig. 39 Distribution of relaxation times of the 8YSZ thin films at *T* = 250 °C
Whereas the low-frequency process is attributed to the grain-boundary process with the relaxation time τ_{gb}, the high-frequency process indicates the transport through the YSZ grains (relaxation time τ_g).

To elucidate the cause of this decrease in ionic transport upon decreasing mean grain size, the impedance spectra of the 8YSZ thin films were analyzed by calculating the distribution function of relaxation times (DRT) (cf. chapter 3.3.3), which enables the distinct separation of the processes related to grain transport and grain-boundary transport. Fig. 39 depicts the DRT at *T* = 250 °C. Two distinct processes with different relaxation times are apparent. Whereas the low-frequency process is allotted to the grain boundaries, the high-frequency part is attributed to the bulk processes. Since the area enveloped by the curve is a measure for the resistance of the particular process, the DRT spectra portend a constant, grain-size independent contribution of the bulk resistance to the total resistance. The grain-boundary resistance, however, decreases with increasing grain size and causes an overall decrease of the total resistance. The shift of the grain-boundary relaxation ($1/\tau_{gb}$) towards lower frequencies can be explained by this increase of the resistance according to

$$\omega_{gb} = 2\pi \cdot f_{gb} = \frac{1}{\tau_{gb}} = \frac{1}{R_{gb} \cdot C_{gb}} \qquad \text{Eq. 42}$$

With increasing R_{gb}, the relaxation frequency takes lower values. The complex impedance data were fitted to equivalent circuits comprising transport processes of the grains and the grain boundaries (Fig. 40a). Parallel capacitances are taken into account due to measuring-setup considerations (chapter 3.3.1). Applying the electrical equivalent circuits and a CNLS approximation (chapter 3.3.3), the resistances and capacitances for the YSZ grains and the grain boundaries can be derived, respectively. Fig. 40b depicts a typical Nyquist plot of the impedance data at 400 °C. In grey, the respective CNLS fits are plotted. It is noteworthy, that the grain-boundary resistance exceeds the grain resistance by more than a factor of 100 for

$d \leq 36$ nm. In this grain-size regime, the grain process and the grain-boundary process cannot be resolved from the impedance data by the CNLS fit.
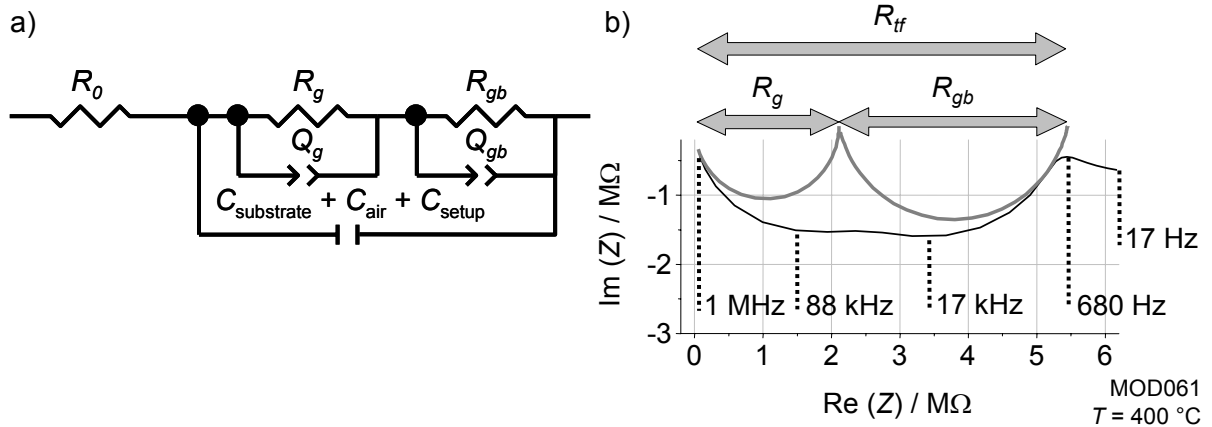
Fig. 40 a) Electrical equivalent circuits; b) Nyquist plot of MOD061 at $T = 400$ °C
The complex impedance data was fitted to the equivalent circuits by a CNLS fit yielding a separation of the total thin-film resistance R_{tf} into the bulk resistance R_g and the grain-boundary resistance R_{gb}.
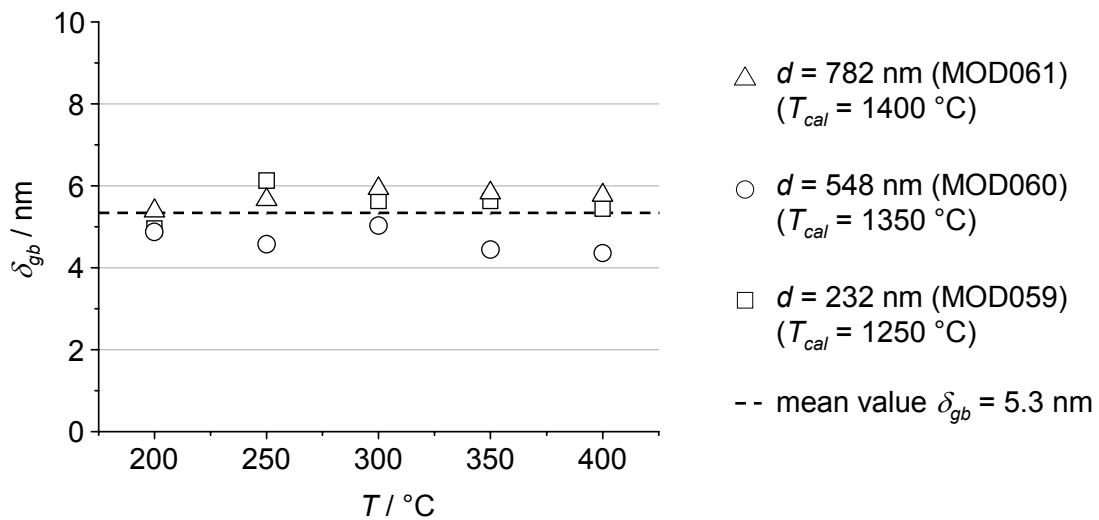
Fig. 41 Electrical grain-boundary thickness δ_{gb} with respect to the mean grain size
The values were derived at 200 °C ≤ T ≤ 400 °C by the application of the brick-layer model to the complex impedance data (cf. chapter 2.1.4). Deviations from the mean value of δ_{gb} = 5.3 nm are mainly caused by errors in the evaluation of the mean grain size.

The bulk and grain-boundary capacitances can be calculated from the constant phase elements according to Eq. 15. The application of Eq. 14 yields the "electrical" grain-boundary thickness δ_{gb}, which was derived to 4.36 nm ≤ δ_{gb} ≤ 6.13 nm. The calculated grain-boundary thickness is independent of the mean grain size (232 nm ≤ d ≤ 782 nm) and the measuring temperature (200 °C ≤ T ≤ 400 °C). All values of δ_{gb} are constant within the uncertainty of the grain-size evaluation. Thus, a mean value of δ_{gb} = 5.3 nm, which is inserted as a dashed line in Fig. 41, can be utilized for further analyses of the impedance data.

Applying Eq. 13, the specific bulk and grain-boundary conductivities can be derived, i.e. the conductivities related to the effective grain and the grain-boundary thickness. As depicted in Fig. 42, the specific bulk conductivities excel the specific grain-boundary conductivities by approximately two decades in the Arrhenius plot. The grain transport (1.08 eV $\leq E_A \leq 1.09$ eV) shows lower activation energies than the grain-boundary conduction (1.14 eV $\leq E_A \leq 1.15$ eV). This difference of the activation energies corresponds in principle to the published data on µm-scaled YSZ electrolytes (Table 1). No grain-size dependence of the data can be observed for 232 nm $\leq d \leq 782$ nm.

For smaller grains ($d \leq 36$ nm), the resolution of the impedance data is limited by the large ratio of R_{gb} / R_g. In this grain-size regime, the bulk process cannot be separated from the grain-boundary process and thus, the grain-boundary thickness δ_{gb} cannot be calculated from the data. In order to evaluate the existence of potential grain-size effects, the total resistance of the 8YSZ thin films featuring grain sizes of 5 nm $\leq d \leq 36$ nm is calculated by the application of the brick-layer model in chapter 5.1.

specific bulk conductivity σ_g^s :

△ $d = 782$ nm (MOD061)
$E_A = 1.09$ eV ($T_{cal} = 1400$ °C)

○ $d = 548$ nm (MOD060)
$E_A = 1.08$ eV ($T_{cal} = 1350$ °C)

□ $d = 232$ nm (MOD059)
$E_A = 1.08$ eV ($T_{cal} = 1250$ °C)

specific gb conductivity σ_{gb}^s :

△ $d = 782$ nm (MOD061)
$E_A = 1.15$ eV ($T_{cal} = 1400$ °C)

○ $d = 548$ nm (MOD060)
$E_A = 1.14$ eV ($T_{cal} = 1350$ °C)

□ $d = 232$ nm (MOD059)
$E_A = 1.15$ eV ($T_{cal} = 1250$ °C)
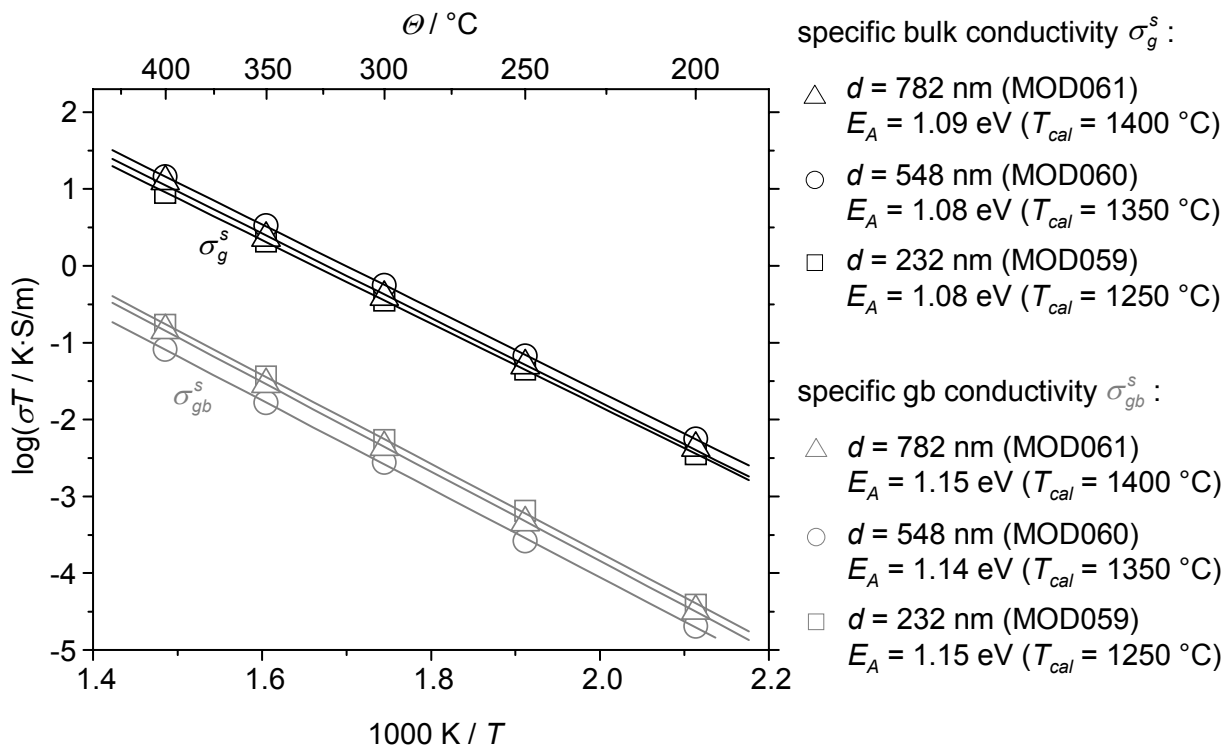
Fig. 42 Arrhenius plot of the specific conductivities with respect to mean grain size
The specific bulk conductivity σ_g^s is depicted in black, the specific grain-boundary conductivity σ_{gb}^s in grey color.

4.2 Nanoscaled LSC Cathodes for SOFC Application

This chapter comprises the results of the crystallization of the chemical LSC phase (4.2.1), the temperature related change of the thin-film microstructure, i.e. grain growth (4.2.2), the stability of the LSC / substrate interface (4.2.3) and the electrochemical characterization of the LSC thin-film cathodes (4.2.4).

4.2.1 Crystallization of the Chemical LSC Phase

Insights about the decomposition and oxidation of the sol-gel precursor powder are inevitable for the processing of homogeneous LSC thin films. The rapid thermal annealing (RTA) steps, which the coated substrates were exposed to during the processing, were investigated by differential thermal analysis (DTA, Fig. 43 right axis) and thermogravimetric analysis (TG, Fig. 43 left axis).

ΔT = 1 K/min
(MOD144)

- regime I: evaporation of water (endothermic) and possibly polymerization (exothermic)
- regime II: thermal decomposition of precursors; formation of oxides and carbonates
- regime III: crystallization of $(La_{0.5}Sr_{0.5})CoO_{3-\delta}$ (LSC)
- from 700 °C constant weight
- 41.0 wt% LSC
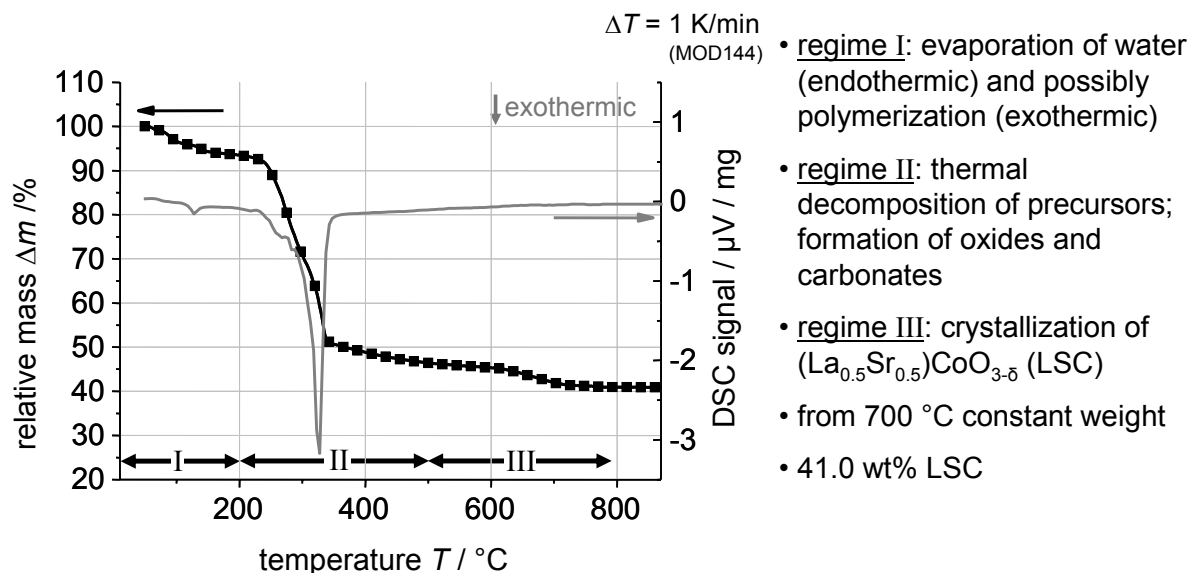
Fig. 43 Thermal analysis of $(La_{0.5}Sr_{0.5})CoO_{3-\delta}$ sol-gel precursor powder
Heating rate: ΔT = 1 K / min in synthetic air. The TG measurement (left axis) shows a relative mass loss of 59 wt% and mass constancy for T > 700 °C. According to the DTA signal (right axis), the thermal decomposition of the organic moieties occurs for T < 355 °C.

The DTA analysis shows two exothermic chemical reactions within the analyzed temperature range from room temperature to 850 °C. Both processes are accompanied by mass losses as indicated by the TG measurement. After the evaporation of water below 100 °C, the exothermic chemical reaction in regime I may be attributed to a polymerization of the precursor powder (extrapolated onset $T_{onset,I}$ = 115 °C, $T_{peak,I}$ = 128 °C). The exothermic chemical reactions in regime II (extrapolated onset $T_{onset,II}$ = 238 °C, $T_{peak,II}$ = 326 °C) coincide with a mass loss of 42 %. The chemical reactions in regime II are caused by the thermal decomposition of the precursors and the oxidative removal of organic groups. In regime III (mass loss 5%), distinct chemical reactions are not apparent in the DTA signal. From 700 °C TG analysis shows constant weight (41.0 wt% of the starting value) indicating the complete removal of the organic compounds and the complete crystallization of the perovskite phase.

To increase the resolution of the TG measurement in region III and to obtain a distinct temperature, at which constant weight can be observed, the precursor powder was calcined at 500 °C (12 h) prior to characterization.
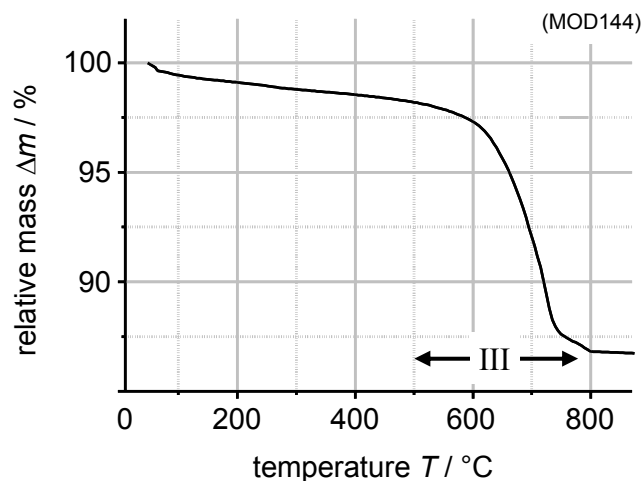
Fig. 44 Thermal analysis of calcined (500 °C, 12 h) LSC sol-gel precursor powder
Heating rate: ΔT = 1 K/min in synthetic air.

Until 500 °C minor mass losses are observed as the TG curve drops by Δm = 10.9% in regime III (extrapolated onset T_{onset} = 621 °C, T_{end} = 711 °C, Fig. 44). Besides the rapid thermal annealing steps (RTA) at 170 °C and 700 °C the additional step at 900 °C determines the surface quality and mean grain size of the LSC thin films.
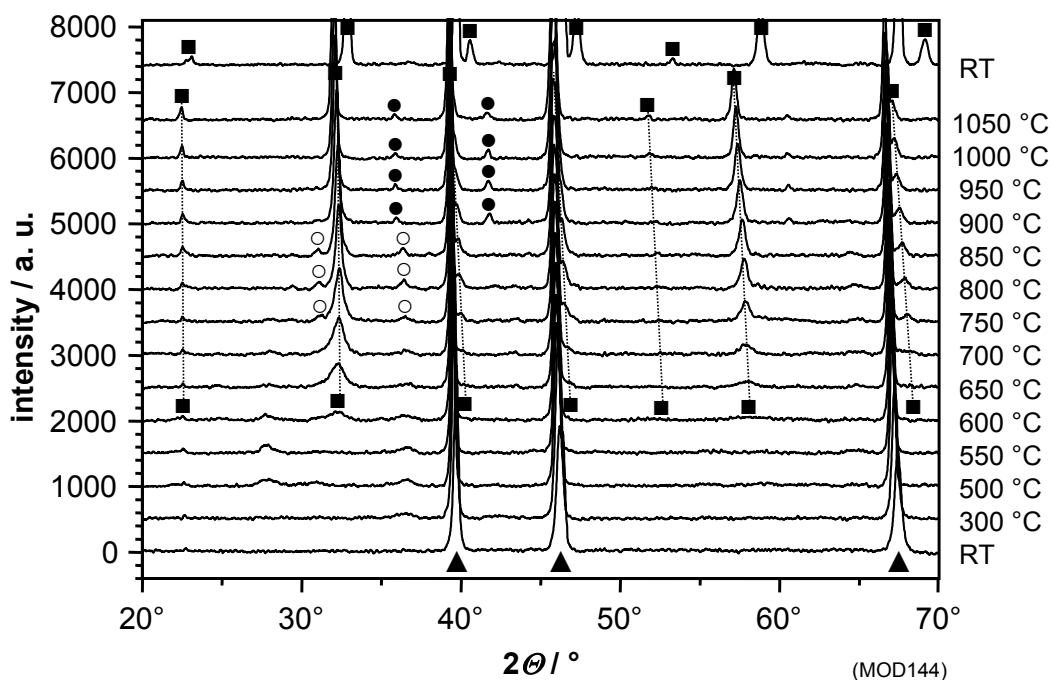
Fig. 45 High-temperature XRD analysis of LSC precursor powder at RT ≤ T ≤ 1050 °C
"▲" denotes the Pt phase (heater material Pt, PDF#00-004-0802), "■" denotes the LSC phase
(($La_{0.5}Sr_{0.5}$)$CoO_{3-\delta}$, PDF#00-048-0122), "○, ●" the cobalt oxide phase (Co_3O_4, PDF#00-043-1003
and CoO, PDF#01-071-1178, respectively). The crystallization of the LSC phase occurs between
550 °C and 600 °C; heating rate: ΔT = 1 K / s, annealing time: t = 45 min.

The crystallization process of the LSC precursor powder with respect to temperature has been studied by in-situ high-temperature XRD (HT-XRD). Fig. 45 presents the temperature-dependent XRD patterns ascending between room temperature (RT) and 1050 °C. It is noteworthy, that the XRD peaks shift towards lower reflection angles upon heating. In general, the distance between atomic layers in the crystal d_{crys} and the X-ray reflection angle Θ are linked by Bragg's law:

$$n \cdot \lambda = 2 \cdot d_{crys} \cdot \sin \Theta$$
Eq. 43

where $n \cdot \lambda$ is a whole-number multiple of the X-ray wavelength ($\lambda = 0.15406$ nm). Upon heating, the atomic lattice expands (increasing values of d_{crys}) resulting in smaller reflection angles Θ. Additionally, the expansion of the platinum heating band leads to a slight displacement of the samples from the X-ray plane. Both effects contribute to the peak shift with increasing measuring temperature.

a) photograph of coated electrolyte

b) top view: LSC-MOD surface

$(La_{0.5}Sr_{0.5})CoO_{3-\delta}$

20 mm

(MOD077)

6 µm

(MOD079)
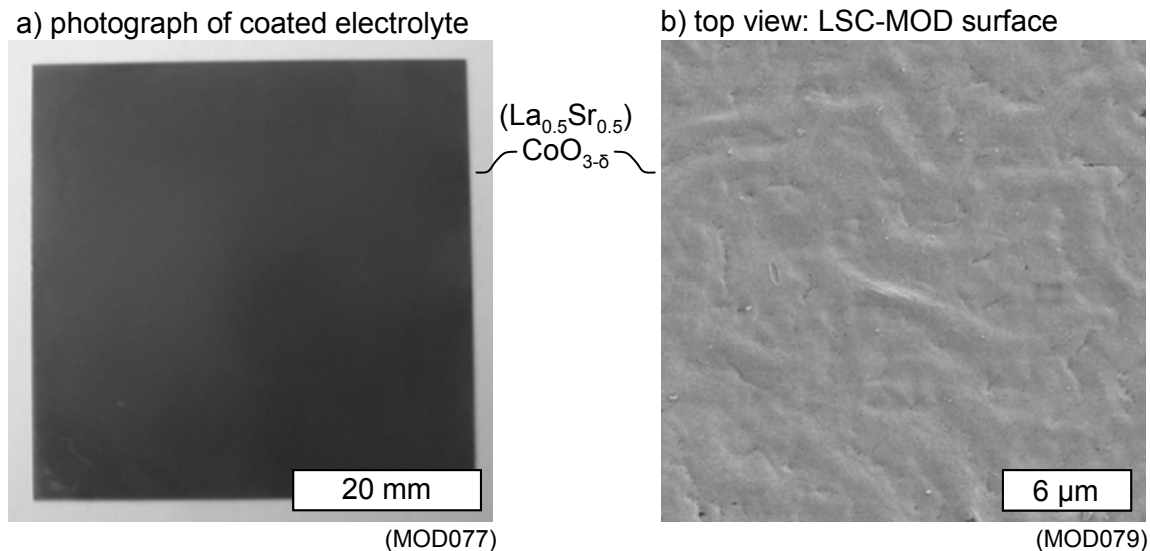
Fig. 46 Top-view analysis of a YSZ substrate (52.5 x 52.5 mm²) coated with LSC
The thin film was exposed to thermal treatment (170 °C, 700 °C, 900 °C for 5 min each);
a) photograph of the LSC thin-film surface; b) SEM image of the LSC thin-film surface.

The platinum peaks (▲, JCPDS[4] reference data: PDF#00-004-0802) in the spectra account for the heater material. The phase transition from the predominantly amorphous state to the rhombohedral phase (■, PDF#00-048-0122) can be recognized between 550 °C and 600 °C for LSC. This crystallization regime is consistent with the transition temperature in the study of $(La_{0.5}Sr_{0.5})CoO_{3-\delta}$ thin films deposited by pulsed laser deposition on (100) silicon [177]. Additionally, a minor impurity phase is identified from 750 °C. This phase can be attributed to the crystallization of cobalt oxide (○, PDF#00-043-1003), which changes its valence to

---

[4] JCPDS-ICDD: Joint Committee on Powder Diffraction Standards – International Centre for Diffraction Data, Newtown Square, USA; PDF: powder diffraction file

bivalent cobalt at 900 °C (●, PDF#01-071-1178). Consecutive thermocycling showed that the switching of the Co valence is a reversible process. After final cooling-down to room temperature (separated by a blank line in Fig. 45), the XRD spectrum shows a well-crystallized, virtually chemically pure $(La_{0.5}Sr_{0.5})CoO_{3-\delta}$ phase.

a) Deposition method: spin-coating
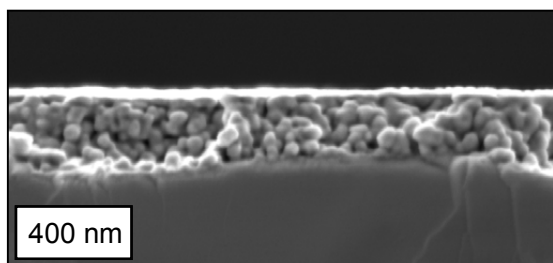
(MOD094b)

ID: MOD094b, ISC217
Sol: $(La_{0,5}Sr_{0,5})CoO_{3-\delta}$ (Rez. 082006)
            13 wt% LSC
            solvent: propionic acid
Coatings: 1
Substrate: 8YSZ (Itochu)
RTA: 170 °C, 700 °C, 900 °C (5 min)
Thickness: approx. 300 nm

b) Deposition method: tampon-printing
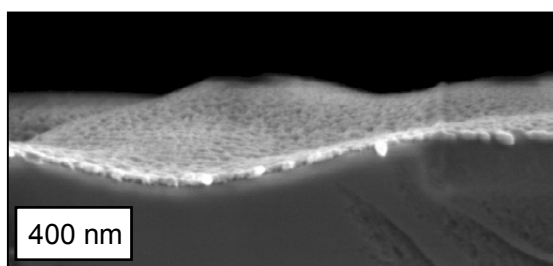
(MOD164)

ID: MOD164, ISC1-310
Sol: $(La_{0,5}Sr_{0,5})CoO_{3-\delta}$ (Rez. LSC_210507)
            12 wt% LSC
            Solvent: propionic acid
Coatings: 1
Substrate: 8YSZ (Itochu)
RTA: 170 °C, 700 °C (5 min)
Thickness: approx. 60 nm

c) Deposition method: dip-coating
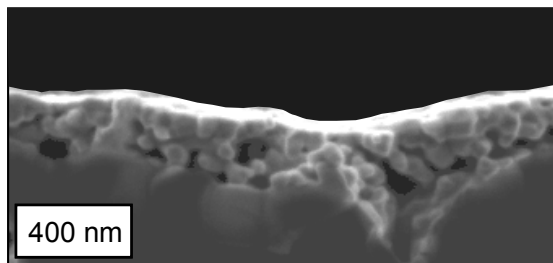
(MOD086)

ID: MOD086, ISC147
Sol: $(La_{0,5}Sr_{0,5})CoO_{3-\delta}$ (Rez. new)
            20 wt% LSC
            Solvent: propionic acid
Coatings: 3
Substrate: GCO screen-printed layer
RTA: 170 °C, 700 °C, 900 °C (5 min)
Thickness: approx. 200 nm

Fig. 47 The effect of deposition techniques on thin-film microstructure
a) spin-coating; b) tampon-printing and c) dip-coating.

The deposition of viscous LSC sol on 8YSZ substrates via sol-gel and consecutive thermal treatment (rapid thermal annealing at 170 °C, 700 °C and 900 °C for 5 min, respectively) leads to black thin films with a metallic glint. Optical (Fig. 46a) and SEM (Fig. 46b) top-view examinations show a predominantly smooth LSC surface lacking of macroscopic cracks.The SEM side-view images of the LSC – YSZ (Fig. 47a, Fig. 47b) and LSC – GCO (Fig. 47c) interfaces display homogeneous LSC thin films with no instances of delamination. Whereas a spin-coating (Fig. 47a) and tampon-printing (Fig. 47b) technique was used for the relatively smooth YSZ electrolyte surfaces, a dip-coating method (Fig. 47c) turned out to be adequate for the screen-printed GCO layers. Depending on processing technique the solids content of

the coating sol was adjusted accordingly. The film thicknesses ranged between 60 nm for the tampon-printed thin films and 300 nm in case of spin-coated thin films.
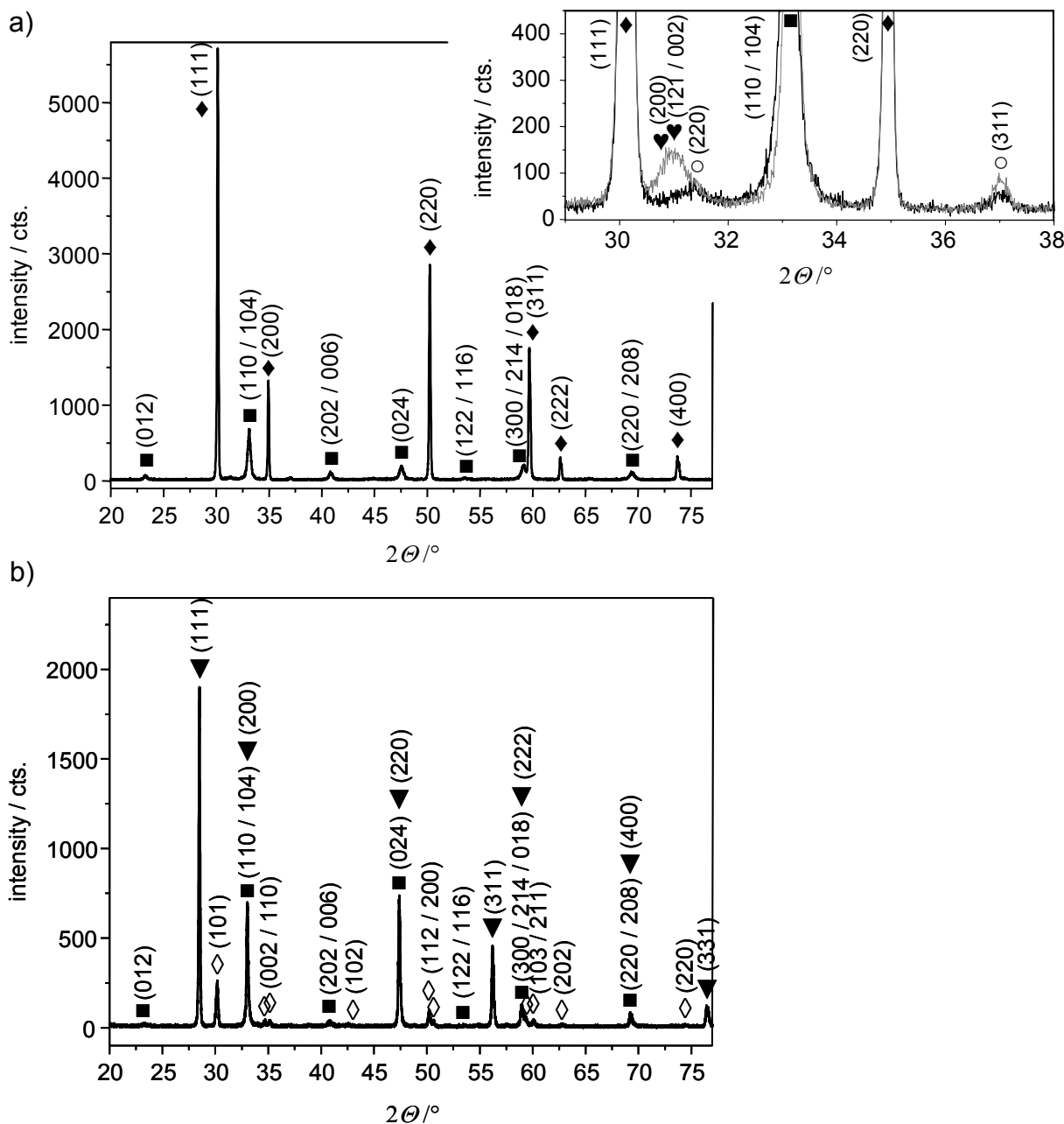
Fig. 48 XRD diffractograms of well-crystallized single-phase LSC thin films

which were deposited on a) 8YSZ substrate ("design 1") and b) GCO thick film on a 3.5YSZ substrate ("design 2") as received by a rapid thermal annealing procedure (RTA); "■" denotes the rhombohedrally distorted LSC phase (($La_{0.5}Sr_{0.5}$)$CoO_{3-\delta}$, PDF#00-048-0122), "♦" the cubic 8YSZ phase (($Zr_{0.85}Y_{0.15}$)$O_{1.93}$, PDF#00-030-1468), "◊" the tetragonal 3.5YSZ phase (($Zr_{0.92}Y_{0.08}$)$O_{1.96}$, PDF#00-048-0224) and "▼" the cubic GCO phase (($Ce_{0.8}Gd_{0.2}$)$O_{1.90}$, PDF#01-075-0162); a) Inset: XRD pattern of LSC / YSZ ("design 1") ranging from 29° < 2Θ < 38° compares as received by RTA (black line) and after consecutive annealing at 800 °C for 10 hours (grey line); secondary phases are identified as "○" for the cobalt oxide phase (Co_3O_4, PDF#00-043-1003), and "♥" for the strontium zirconate phase ($SrZrO_3$, PDF#00-044-0161).

73

Fig. 48a exhibits the XRD spectrum of an LSC thin film on YSZ ("design 1"), where "■" denotes the LSC phase (PDF#00-048-0122) and "♦" the 8YSZ phase (PDF#00-030-1468). The rather broad peaks of the LSC phase indicate a small crystallite size. The Miller indices are included in brackets. The magnification of the XRD spectrum presumably indicates a secondary phase in the range of the detection limit of the XRD at $2\Theta = 31.4°$ (220) and $2\Theta = 37.0°$ (311), denoted with "○" (black graph in Fig. 48, inset) and attributed to Co_3O_4 (PDF#00-043-1003). Annealing of the sample at 800 °C for 10 h in air results in a slight increase of the (311) Co_3O_4 peak intensity (grey graph in Fig. 48, inset) in combination with weak, but characteristic reflections at $2\Theta = 30.8°$ (200) and $2\Theta = 30.9°$ (121), (002) indicating the formation of $SrZrO_3$ ("♥", PDF#00-044-0161). In case of the LSC thin film on GCO ("design 2"), XRD analysis shows as expected single-phase crystallization (Fig. 48b). The diffraction data was attributed to the characteristic reflections of the rhombohedrally distorted $(La_{0.5}Sr_{0.5})CoO_{3-\delta}$ phase ("■", PDF#00-048-0122), the cubic $(Ce_{0.8}Gd_{0.2})O_{1.90}$ phase ("▼", PDF#01-075-0162) and the tetragonal $(Zr_{0.92}Y_{0.08})O_{1.96}$ phase ("◊", PDF#00-048-0224).

4.2.2 Temperature-Dependent Grain Growth

The surface microstructure of the LSC thin films on 8YSZ with respect to annealing temperature is studied via top-view SEM examination (Fig. 49). For that purpose, the specimens were annealed in air between 500 °C and 900 °C for 10 h, respectively. With increasing annealing temperature, pore and grain growth occurred.

The grain sizes were statistically evaluated using the image processing software SPIP^{TM} (Image Metrology A/S; Lyngby, Denmark). Each grain diameter was calculated as a circle equivalent diameter from the grain area [229]. The error bars in Fig. 51 account for the standard deviation evaluated by statistical image processing of the SEM images.

Fig. 50 depicts the isothermal grain growth exemplarily for $T = 700$ °C and $T = 900$ °C after annealing for 2 h, 10 h and 100 h. Whereas the mean grain size is approximately constant over time at 700 °C (Fig. 50a-c), grain growth and an increase of the thin-film porosity is apparent at 900 °C (Fig. 50d-f). The isothermal grain-growth data of the LSC thin films on YSZ with respect to annealing temperature is depicted in Fig. 51a. The grain growth occurs mostly in the first 10 h of dwell. For larger annealing times, the grain growth perishes for $T \leq 800$ °C resulting in a maximal grain size of 83.5 nm. This self-limiting grain growth was fitted to a relaxation function [219]:

$$d - d_0 = \left(d_L - d_0\right)\left(1 - e^{-\frac{t}{\tau}}\right)$$

Eq. 44

where d is the mean grain size at the time t, d_0 is the initial grain size at the time t_0 and τ the relaxation time. For the annealing temperature of 800 °C, the relaxation time was found to be $\tau = 4.33 \pm 2.01$ h.

a) RTA (900 °C, 5 min)
mean d = 55 ± 20 nm

b) RTA + 500 °C (10 h)
mean d = 52 ± 20 nm

c) RTA + 600 °C (10 h)
mean d = 59 ± 21 nm

(MOD102d)

(MOD106c)

(MOD106d)

d) RTA + 700 °C (10 h)
mean d = 62 ± 21 nm

e) RTA + 800 °C (10 h)
mean d = 83 ± 30 nm

f) RTA + 900 °C (10 h)
mean d = 165 ± 60 nm

1 µm

(MOD107a)

(MOD107b)

(MOD107c)
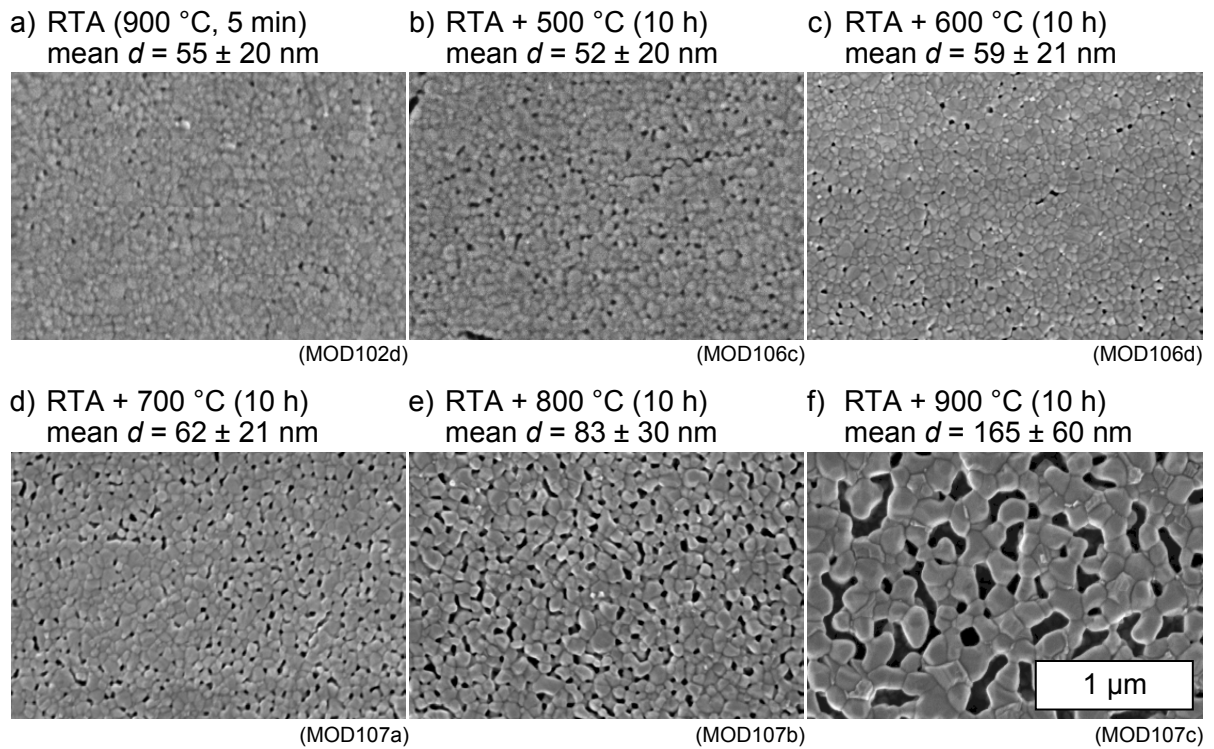
Fig. 49 Grain growth of LSC thin films with respect to annealing temperature

SEM top-view analyses after a) rapid thermal annealing and subsequent annealing for 10 h in air at b) 500 °C; c) 600 °C; d) 700 °C; e) 800 °C; f) 900 °C [5]. The increasing annealing temperature fosters both grain growth and increase of porosity. Solvent: propionic acid, deposition technique: spin coating, substrate: 8YSZ.

For higher annealing temperatures (T = 900 °C), grain growth occurs during the whole experiment according to the generalized grain-growth law ([219] and ref. therein; cf. Eq. 40):

$$d^n - d_0^n = k_n \left(t - t_0 \right)$$
Eq. 45

where d denotes the mean grain size at the time t, d_0 the initial grain size at the time t_0 and k_n is given by ([215] and ref. therein):

$$k_n = k_0 \cdot e^{-\frac{Q}{kT}} \propto D$$
Eq. 46

where k_0 is a material constant, Q the activation energy, k the Boltzmann constant and T the temperature in Kelvin. This term is proportional to the diffusion coefficient D.

For the isothermal hold at 900 °C (Fig. 51a), a grain-growth exponent of n = 7.5 ± 1.1 was determined from Eq. 45. Rupp et al. stated that the grain-growth exponent ranges between n = 2 for the parabolic grain growth up to n = 10 [219]. This deviation from the theoretically

---

[5] The grain growth in LSC thin films was studied within the study projects of Irene Netsch „Mikrostrukturanalyse nanoskaliger Dünnschichtkathoden" (Microstructral Analysis of nanoscaled Thin-Film Cathodes), 2007, IWE.

expected parabolic grain growth was explained by pores, which affect the grain-growth kinetics. These pores are well apparent in Fig. 49.

a) RTA + 700 °C (2 h)
mean d = 60 nm

b) RTA + 700 °C (10 h)
mean d = 62 nm

c) RTA + 700 °C (100 h)
mean d = 60 nm

(MOD105c)

(MOD107a)

(MOD108c)

d) RTA + 900 °C (2 h)
mean d = 118 nm

e) RTA + 900 °C (10 h)
mean d = 165 nm

f) RTA + 900 °C (100 h)
mean d = 209 nm

1 µm

(MOD106a)

(MOD107c)

(MOD109a)
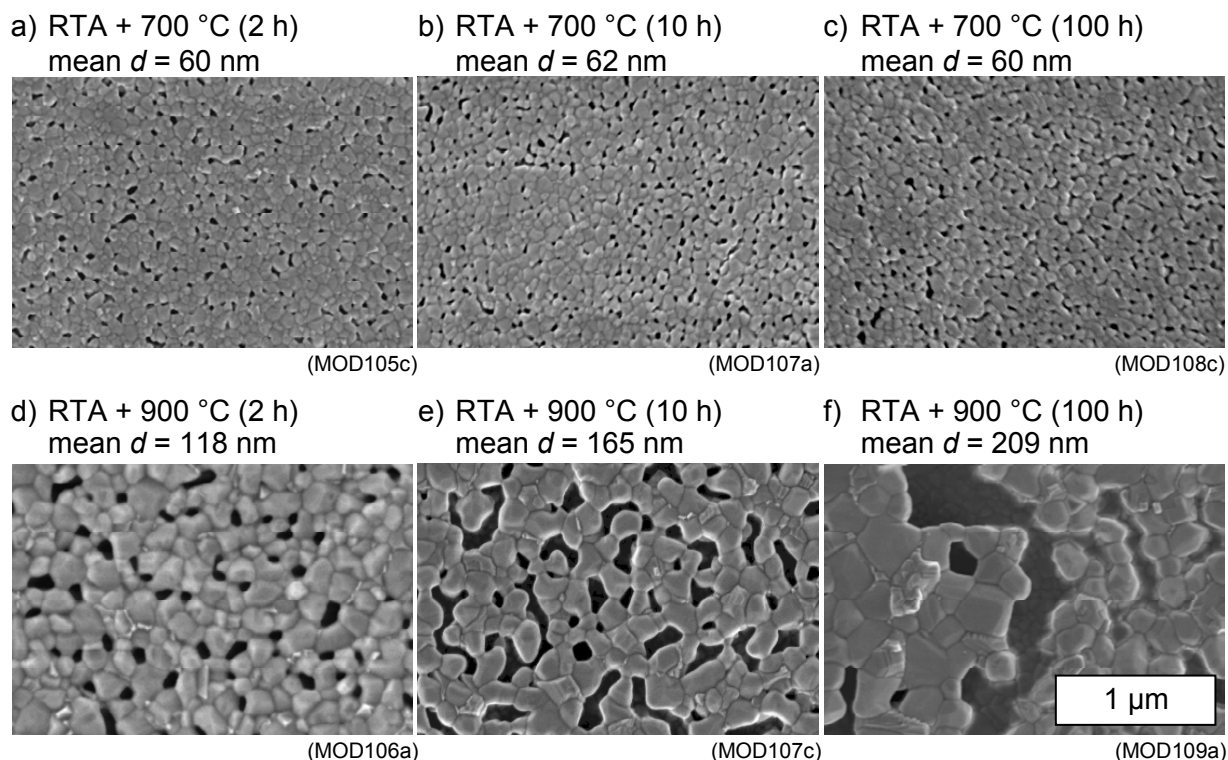
Fig. 50 Grain growth of LSC thin films with respect to annealing time
SEM top-view analyses after rapid thermal annealing and subsequent annealing in air at 700 °C for a) 2 h, b) 10 h, c) 100 h and at 900 °C for d) 2 h, e) 10 h, f) 100 h. Whereas grain growth is apparent at 900 °C, the images at 700 °C show similar grain sizes irrespective of thermal annealing. Solvent: propionic acid, deposition technique: spin coating, substrate: 8YSZ.

The temperature-dependent grain growth at a constant dwell of 10 h is depicted in Fig. 51b. Between 700 °C (10 h) and 900 °C (10 h) the mean grain sizes range from 62 ± 21 nm (700 °C) over 83 ± 30 nm (800 °C) to 165 ± 60 nm (900 °C) in diameter. Applying the non-parabolic grain growth law (Eq. 39) to Fig. 51b a reasonable fit can be obtained.

Besides LSC grains, the SEM top-view images depict nanopores. Whereas the pore size is constant during the annealing at 700 °C (Fig. 50a-c), at 900 °C substantial pore growth can be observed (Fig. 50d-f). This suggests that the changes in the pore size follow the analyzed grain-growth behavior. Furthermore, the SEM images of the specimens annealed at 900 °C show inhomogeneities besides the LSC grains. This indicates the presence of chemical secondary phases, which are caused by an interface reaction between the LSC thin film and the YSZ substrate (cf. the thorough study of this interface reaction in chapter 4.2.3 and the discussion of the results in chapter 5.2.1).
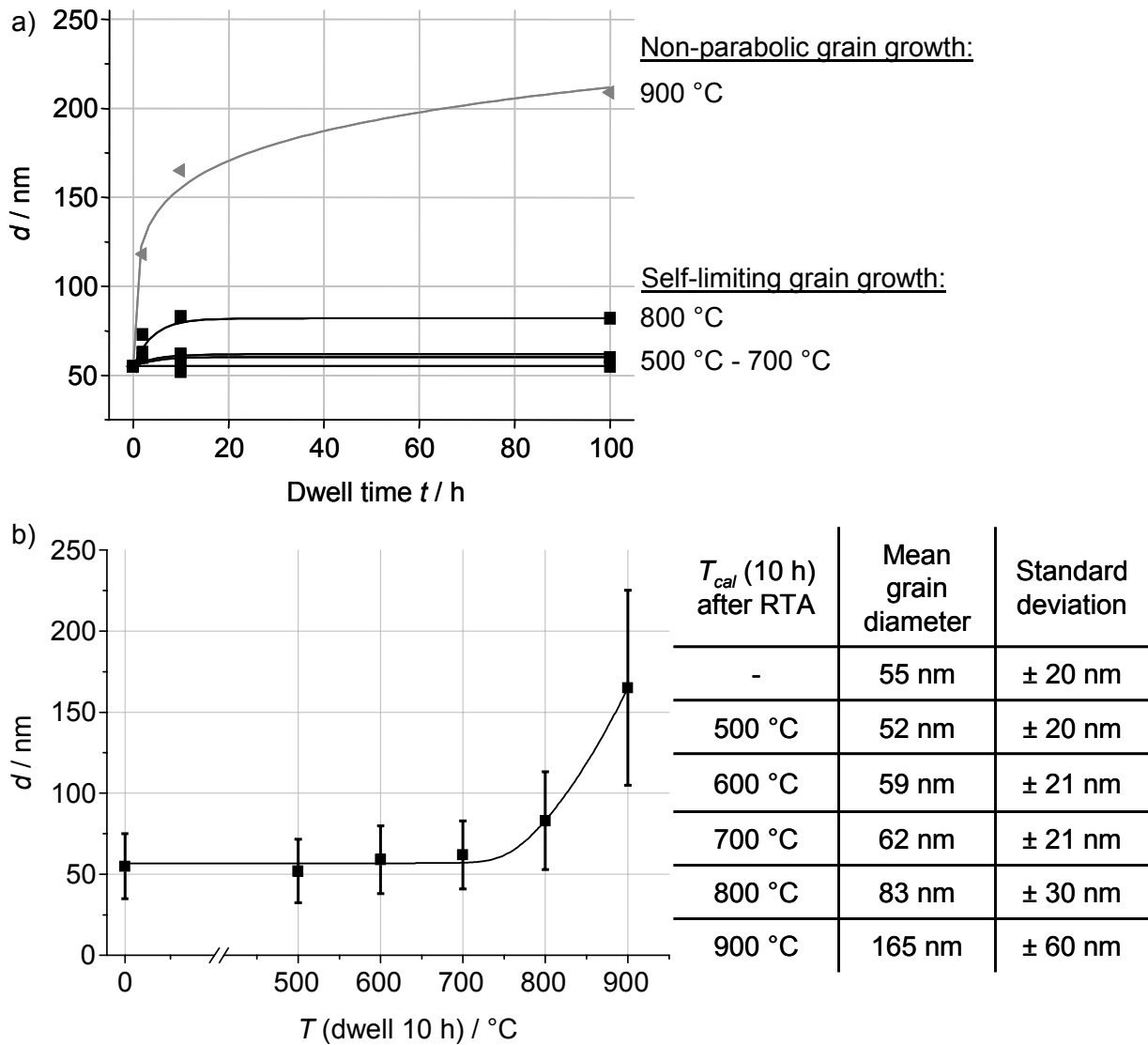
Fig. 51 Mean grain size _d_ as a function of calcination time and calcination temperature
a) Average grain size of the LSC thin films as a function of dwell time (0 h, 2 h, 10 h, 100 h) and
annealing temperature (500 °C ≤ _T_ ≤ 900 °C). Black symbols (■) represent grain growth data
following self-limiting grain growth. Gray symbols (◄) follow the generalized non-parabolic
grain growth law; b) Statistically evaluated mean grain sizes of LSC thin films with respect to
annealing temperature after rapid thermal annealing (RTA) (500 °C ≤ _T_ ≤ 900 °C, 10 h). The table
states the mean grain diameter with its standard deviation with respect to annealing
temperature.

4.2.3 Stability of the LSC Thin-Film Cathodes

The stability of LSC and the interface reactivity to the adjoining substrate is evidential for the
evaluation of grain-size effects in nanoscaled cathodes and potential SOFC application.
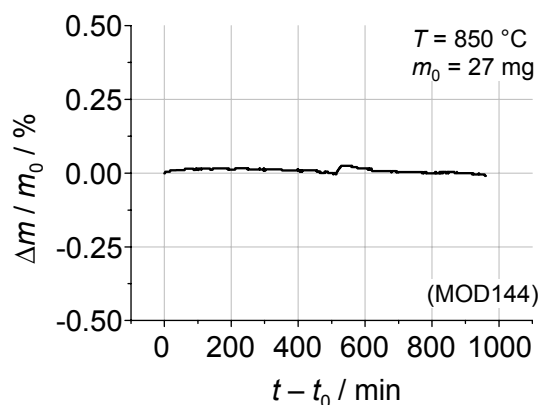
Fig. 52 Mass loss of LSC powder (obtained from precursor powder) at 850 °C

The drift was determined by a reference measurement and was subtracted from the curve. TG439 resolution: Δm = 0.1 µg.

Via a TG measurement the question should be answered whether individual chemical elements, predominately Sr, evaporate into the gas phase during the processing of the thin films and thereby change the targeted stoichiometry of La:Sr:Co = 1:1:2 of the perovskite. Fig. 52 depicts the mass loss of LSC powder at 850 °C, which has crystallized from the precursor powder during the heating up. Within the dwell of 16 h, no mass loss is recognized. Furthermore, the LSCF current collector applied for the electrochemical characterization increases the chemical vapor pressure above the LSC thin film, which allows the conclusion that evaporation of single chemical elements is improbable during the electrical characterization at T = 850 °C. However, this leaves the possibility that chemical elements may have evaporated during the heating-up (cf. the discussion on the chemical stability of LSC in chapter 5.2.1)

The sol-gel deposition method contents itself with processing temperatures fairly below the known crystallization temperature of the interface reaction between LSC thick film cathodes and YSZ (the formation of insulating zirconate layers ($La_2Zr_2O_7$ and / or $SrZrO_3$) was described in detail for $T \geq 900$ °C by many groups [156-159]). However, the chemical stability between the cathode material and the substrate is essential in terms of long-term stability for SOFC application and cathode polarization properties (cf. chapter 2.2). Two approaches were chosen to elucidate the stability of the LSC / YSZ interface with respect to temperature: on the one hand, the chemical reactivity between LSC and YSZ was calculated thermodynamically; on the other hand, a variety of experiments was conducted to account for the kinetics of the chemical interface reaction.

The chemical stability of the LSC cathode / YSZ electrolyte interface and the decomposition of the perovskite phase was calculated thermodynamically within cooperation with Dr. Harumi Yokokawa[6] using the software MALT (MAterials oriented Little Thermodynamic

---

[6] National Institute of Advanced Industrial Science and Technology (AIST), Energy Technology Research Institute, AIST Central 5, Higashi 1-1-1, Tsukuba 305-8565, Japan

database) [239]. Equilibrium calculations based on the thermodynamic properties of the applied materials were carried out with the program gem (Gibbs Energy Minimizer), which is included in the software package MALT. This thermodynamic approach provides decisive information about the stability of the interface and the formation of parasitic secondary phases [240-242].

a) Overview
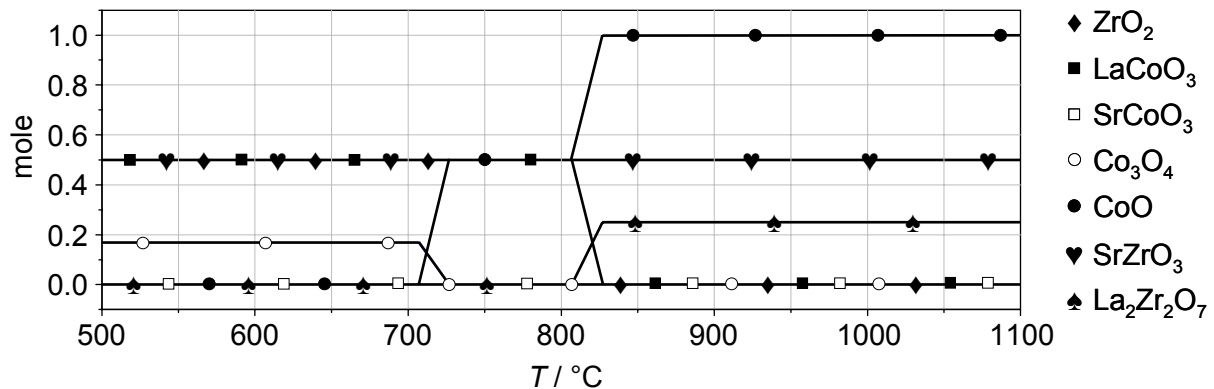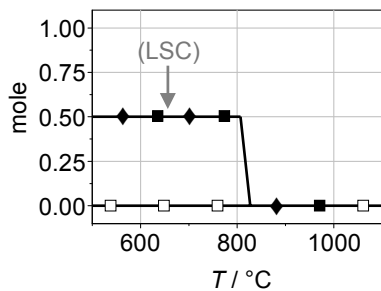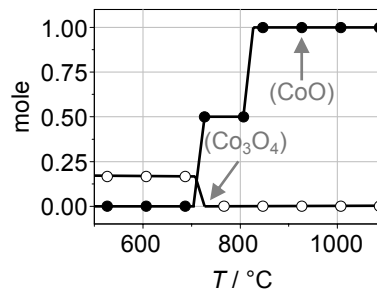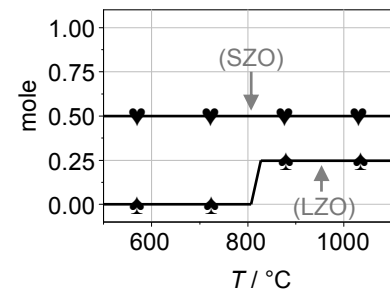
Fig. 53 Chemical stability calculations of a virtual LSC / YSZ powder mixture
The thermodynamic calculations of LSC (0.5 mol $LaCoO_3$, 0.5 mol $SrCoO_3$) and ZrO_2 (1 mol)
were performed in MALT; ZrO_2 (♦), $LaCoO_3$ (■), Co_3O_4 (○), CoO (●), $SrZrO_3$ (♥) and $La_2Zr_2O_7$ (♠).
As starting conditions pO_2 = 0.21 bar and T = 25 °C were chosen. An overview of the resulting
chemical phases with respect to temperature (500 °C < T < 1100 °C) is given in a); b) – d) show
the chemical phases of ZrO_2 and $(La_{0.5}Sr_{0.5})CoO_3$, cobalt oxide and zirconates, respectively. The
brackets include the detection temperatures of the respective phases obtained by XRD
analysis of a powder mixture from LSC precursor powder and YSZ (cf. Fig. 54).

The thermodynamic data for the present calculations were taken mainly from MALT, which is based on the NBS chemical thermodynamic data [243] combined with available heat capacities; except for $(La,Sr)CoO_3$, numerical values are given in [244], references quoted therein and [245-248]. The data for the $SrCoO_{3-\delta}$ component in LSC was determined so as to reproduce the oxygen nonstoichiometry in $SrCoO_{3-\delta}$ [249] and the phase relation in the La-Sr-Co-O system [250].

The starting conditions of these thermodynamic calculations were 0.5 mol $LaCoO_3$, 0.5 mol $SrCoO_3$ and 1 mol ZrO_2. The calculations were performed at an oxygen partial pressure of

pO_2 = 0.21 atm. The presence of thermodynamically stable phases between 500 °C and 1100 °C is shown in Fig. 53. At 500 °C the strontium in LSC reacts with 0.5 mol ZrO_2 (♦) to form 0.5 mol $SrZrO_3$ (♥) and 0.167 mol of Co_3O_4 (○). The remaining $LaCoO_3$ (0.5 mol) reacts with ZrO_2 at 825 °C due to the crystallization of 0.25 mole of $La_2Zr_2O_7$ and the decomposition of $LaCoO_3$. The formation of lanthanum zirconate results in an increase of cobalt oxide, which changes its valence from Co_3O_4 (○) to bivalent cobalt (●) at 700 °C [242, 248].

According to these results, the strontium in the LSC perovskite layer should react completely with the zirconia substrate to SZO even at 500 °C whereas a pure $LaCoO_3$ should be stable up to 800°C.

However, these thermodynamic calculations do not account for kinetic considerations, which may lead to time constants of the chemical interface reaction, which are irrelevant to the application of LSC thin-film cathodes. Therefore, the following experiments were conducted to shed light on this issue.
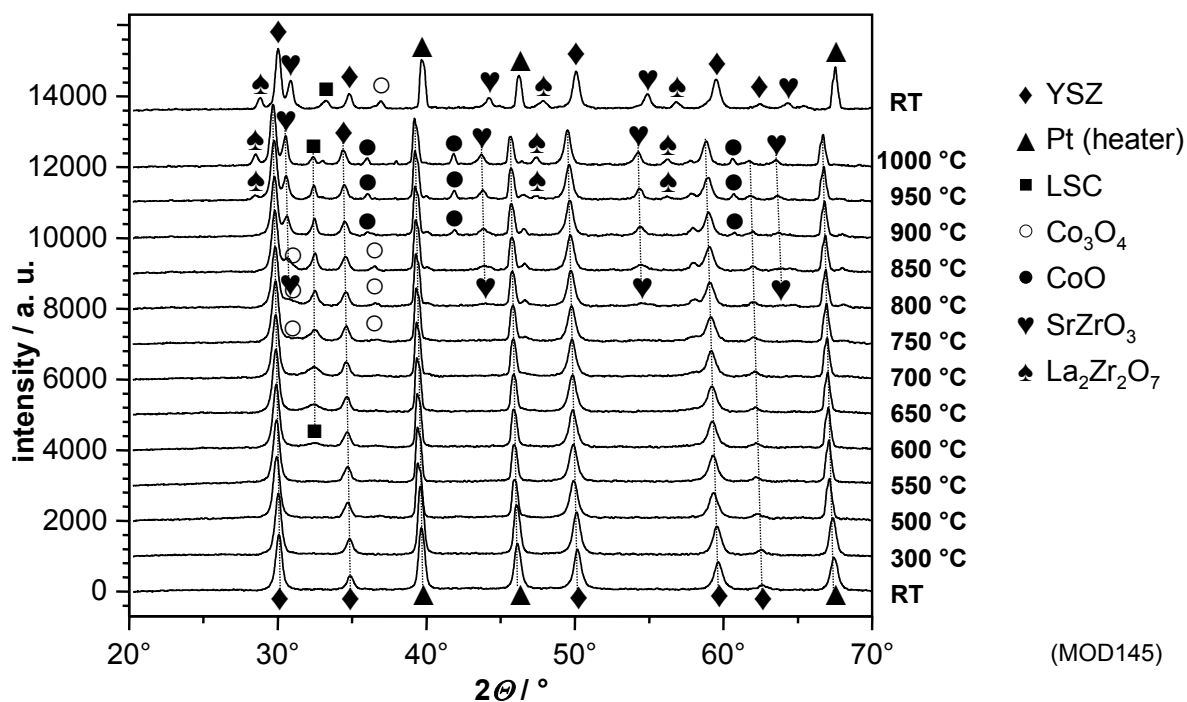
Fig. 54 HT-XRD analysis of an LSC / YSZ powder mixture for RT < *T* < 1000 °C
The mixtures composes of LSC precursor powder and YSZ powder; Pt (▲, PDF#00-004-0802), $(Zr_{0.85}Y_{0.15})O_{1.93}$ (♦, PDF#00-030-1468), $(La_{0.5}Sr_{0.5})CoO_{3-\delta}$ (■, PDF#00-048-0122), Co_3O_4 (○, PDF#00-043-1003), CoO (●, PDF#01-071-1178), $SrZrO_3$ (♥, PDF#00-044-0161) and $La_2Zr_2O_7$ (♠, PDF#00-050-0837). The crystallization of parasitic secondary phases (SZO) is apparent between 750 °C and 800 °C.

Due to the deficient signal to noise ratio of the XRD signal of an LSC thin film on YSZ, a powder mixture of LSC precursor powder and 8YSZ powder was prepared for HT-XRD analysis (Fig. 54). At room temperature the Bragg reflections can be attributed to the platinum heater (Pt, ▲, PDF#00-004-0802) and YSZ from the powder mixture

$((Zr_{0.85}Y_{0.15})O_{1.93}$, ♦, PDF#00-030-1468). The precipitation of the LSC phase and the crystallization of cobalt oxide correlate with the findings in Fig. 45 (study of pure LSC precursor powder). The chemical interface reaction between 8YSZ and LSC can be observed for $T > 750$ °C with the crystallization of parasitic secondary phases. Strontium zirconate precipitates between 750 °C and 800 °C ($SrZrO_3$, ♥, PDF#00-044-0161) and lanthanum zirconate ($La_2Zr_2O_7$, ♠, PDF#00-050-0837) between 900 °C and 950 °C. Compared to the XRD data at 1000 °C the spectrum after cooling-down to room temperature shows the same chemical phases. However, the spectrum is staggered to higher reflection angles, which is explained by the reduction of the spacing between the planes in the atomic lattice.

Further examinations of the LSC / YSZ interface have been performed by SEM and TEM on thin films. SEM cross-section analysis of the coated 8YSZ electrolytes after RTA is depicted in Fig. 55a. After annealing at 800 °C for 100 h a chemical interface reaction between YSZ and LSC can be observed (Fig. 55b). This secondary phase has a thickness of approximately 80 nm and emerges as a homogeneous band between the nanoscaled LSC thin film and the substrate.

For further information, LSC thin films on 3.5YSZ were exposed to 700 °C ("LSC700") and 1000 °C ("LSC1000") for 8 h each. Cross-section samples were studied to analyze the distribution of the different phases as a function of the distance from the interface. Fig. 56a and Fig. 56b display zero-loss-filtered TEM images of both samples [214], which show layers with a thickness of about 240 nm on top of the YSZ substrate. An interfacial layer marked by white dashed lines in Fig. 56a and Fig. 56b is observed in both samples with an average thickness of 42 ± 5 nm in LSC700 (Fig. 56a) and a larger thickness of 130 ± 20 nm in LSC1000 (Fig. 56b).

a) Calcination: RTA (T_{max} = 900 °C)   b) Calcination: RTA + 800 °C (100 h)

(MOD102d)   (MOD108d)
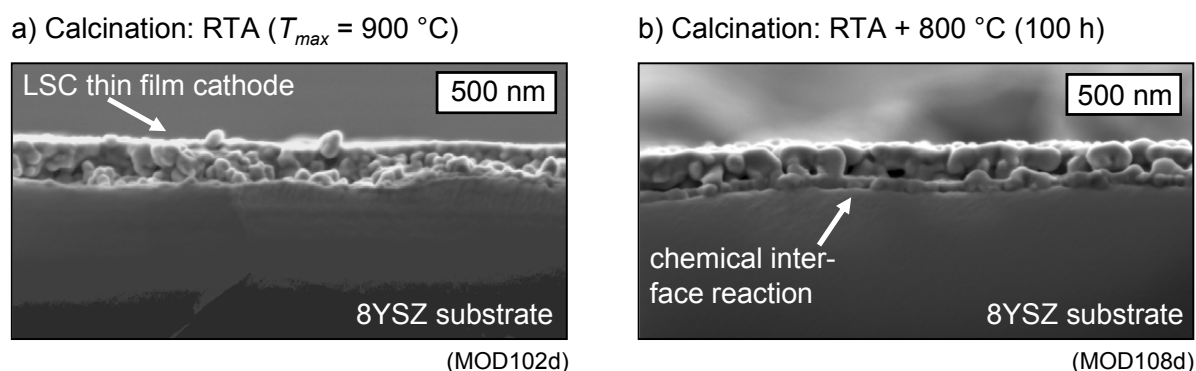
Fig. 55 SEM cross-view analysis of the LSC - YSZ interface
a) after RTA (170 °C, 700 °C, 900 °C, 5 min each) and b) after annealing (800 °C, 100 h). A band-like secondary phase is displayed at the LSC / YSZ interface.

Electron spectroscopic images were recorded to obtain a comprehensive overview of the element distribution in the LSC / YSZ interface region [214]. The La-$N_{4,5}$ edge (edge onset at an energy loss ΔE = 90 eV) was used for imaging the La distribution (bright regions in

Fig. 56c and Fig. 56d). LSC700 (Fig. 56c) exhibits an inhomogeneous La distribution. Even grains without La were detected. These grains are partly located within the La-rich region and at the substrate / layer interface. In LSC1000 (Fig. 56d), La is confined completely to the surface region. Only a small amount of La is located in subjacent grains. In contrast, Sr mapped with the Sr-$L_{2,3}$ edge at ΔE = 1940 eV is depleted at the surface and enriched at the interface. This effect is more pronounced in LSC1000 (Fig. 56f) than in LSC700 (Fig. 56e). The Sr-enriched layer corresponds to the interfacial layer in Fig. 56a and Fig. 56b. The symmetry of the SAED patterns (not shown) and the evaluated lattice-plane distances correspond well to the perovskite structure of the $SrZrO_3$ (SZO) phase. The Co distribution imaged with the Co-$L_{2,3}$ edge (ΔE = 779 eV) shows that the grains depleted in Sr and La are cobalt oxides (as also verified by EDXS and SAED). These regions correspond to the grains with bright and speckled contrast in Fig. 56a and Fig. 56b. In case of LSC700 (Fig. 56g) the Co_3O_4 grains are embedded in the LSC layer. In LSC1000 (Fig. 56h), the CoO grains lie between the LSC and the Sr-rich reaction layer. As expected for the SZO reaction layers, the Zr distribution (imaged with the Zr-$L_{2,3}$ edge at ΔE = 2222 eV) shows a higher Zr content exactly in those regions where an enrichment of Sr is found. This effect is more pronounced in LSC1000 (Fig. 56j) than in LSC700 (Fig. 56i). The Zr signal, which is visible in the LSC layer, can be ascribed to Zr redeposition during FIB milling. Owing to a large sample drift particularly caused by high electron-irradiation doses, the lateral resolution of the maps for elements with high energy-loss edges like Zr and Sr is deteriorated. The element distribution obtained by ESI could be confirmed by corresponding EDXS maps.

Cross-section images of an as-prepared LSC thin film after RTA (not shown here) demonstrate that the SZO phase is already formed during the RTA process at the LSC / YSZ interface with an average thickness of 16 ± 3 nm. In addition to reflections of the rhombohedrally distorted LSC structure, Debye diffraction patterns contain reflections of the Co_3O_4 phase, which is formed likewise during the RTA process.

EDXS analyses of plan-view samples yield a Sr deficiency of LSC grains in both samples LSC700 and LSC1000 with a more pronounced deficiency and chemical inhomogeneity in LSC1000. Although strontium evaporation during the calcination process cannot be excluded (cf. chapter 4.2.1), analyses by EFTEM, SEM, XRD and MALT evidenced that one reason for this inhomogeneity of the LSC grains is the reaction of strontium with the YSZ electrolyte.

The chemical stability of the "design 2" (LSC / GCO) was studied by a HT-XRD measurement of a powder mixture between LSC precursor powder and GCO powder. The mixture was heated up to 1200 °C and the spectrum was recorded at 500 °C ≤ T ≤ 1200 °C in 100 °C steps. Consistently to Fig. 45 and Fig. 54, the chemical LSC phase and the cobalt oxide phase precipitate at 600 °C and 800 °C, respectively. The switching of the cobalt valency at 900 °C is also observed at the LSC / YSZ powder mixture. However, until 1200 °C no chemical interface reactions between LSC and GCO can be detected, which proves the efficiency of a GCO buffer layer in "design 2".
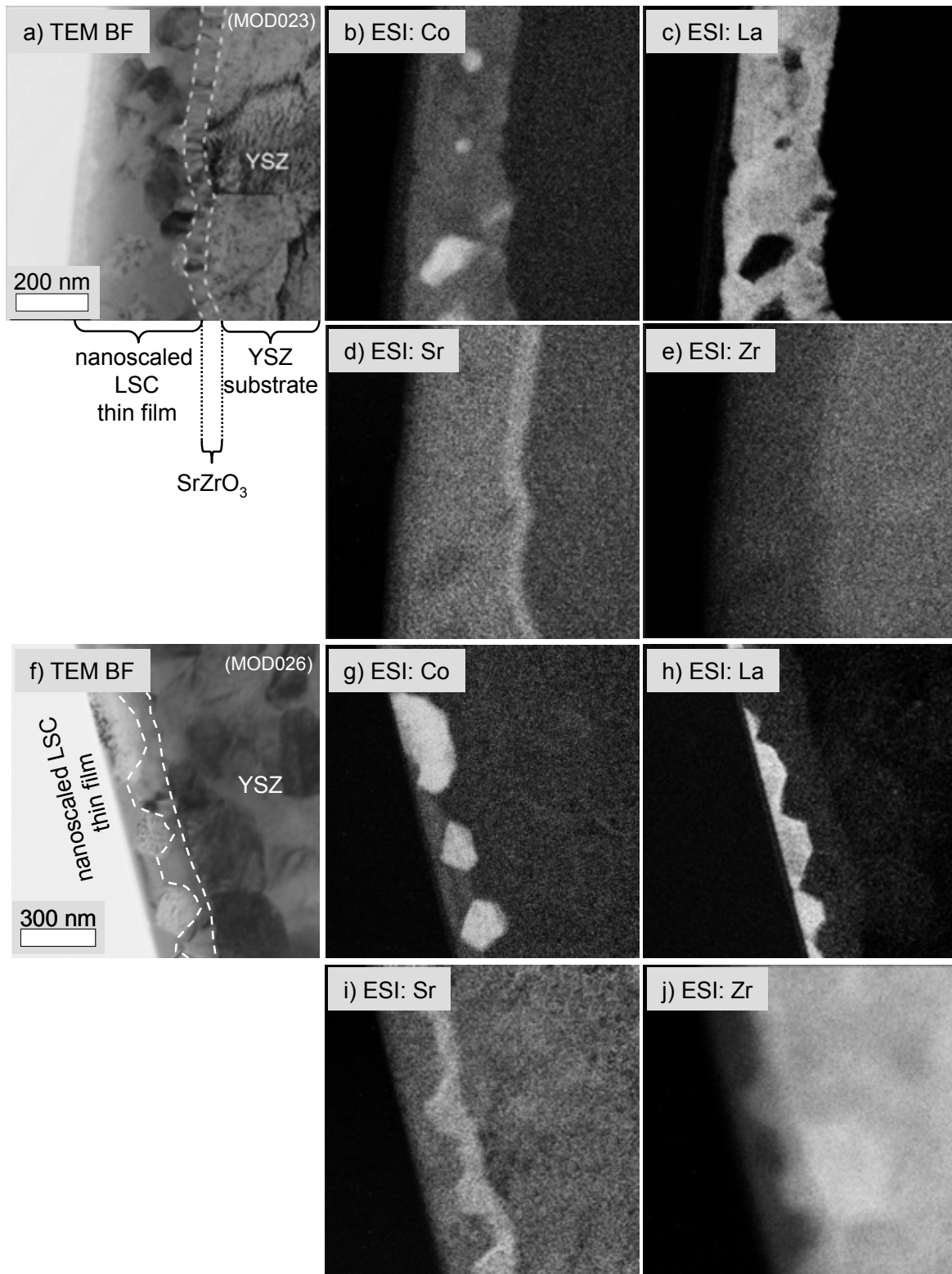
Fig. 56 High-resolution EFTEM cross-section analyses of LSC thin films on 3.5YSZ [214] calcined at 700 °C for 8 h (images a - e) and at 1000 °C for 8 h (images f – j); a) and f) depict bright-field (BF) images; the following elemental distributions were analyzed by ESI: Co (b, g), La (c, h), Sr (d, i) and Zr (e, j).
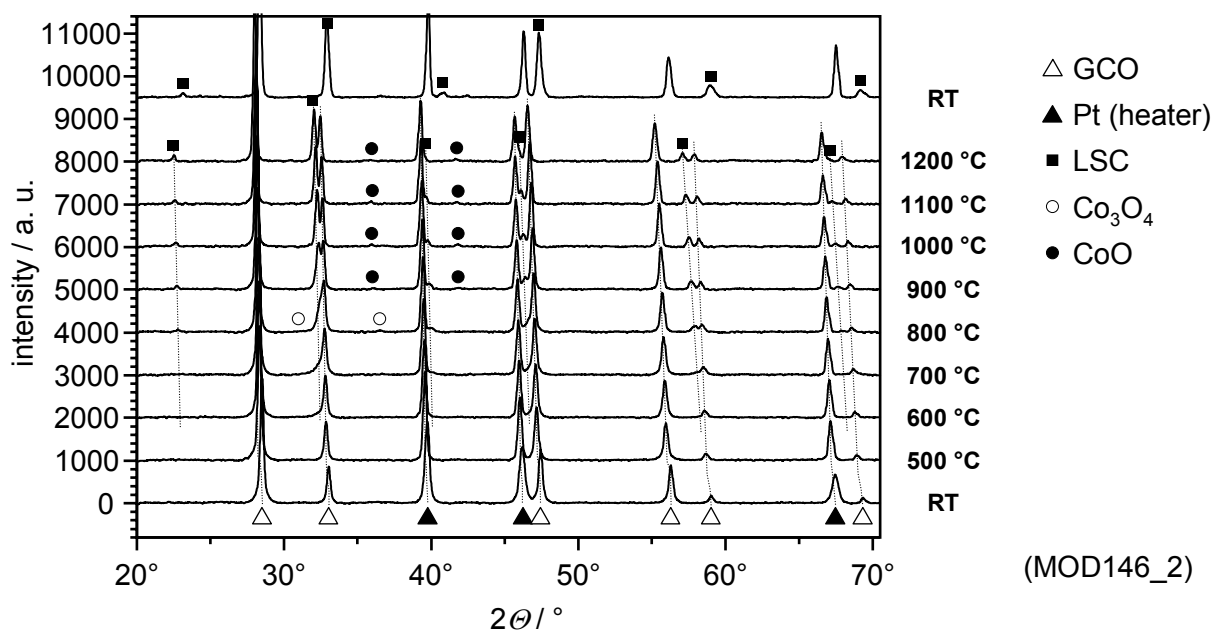
Fig. 57 High-temperature XRD analysis of an LSC / GCO powder mixture
LSC precursor powder and GCO powder $((Gd_{0.1}Ce_{0.9})O_{1.95}$, Treibacher Industrie AG, Althofen, Austria) for $RT < T <$ 1200 °C; Pt (▲, PDF#00-004-0802), $(Gd_{0.1}Ce_{0.9})O_{1.95}$ (Δ, PDF#01-075-0161), $(La_{0.5}Sr_{0.5})CoO_{3-\delta}$ (■, PDF#00-048-0122), Co_3O_4 (○, PDF#00-043-1003) and CoO (●, PDF#01-071-1178).

4.2.4 Electrochemical Properties of the Nanoscaled LSC Cathodes

Nanoscaled $(La_{0.5}Sr_{0.5})CoO_{3-\delta}$ thin films were successfully deposited on 8YSZ electrolytes ("design 1", Fig. 58a) and GCO buffer layers ("design 2", Fig. 58d) by MOD. The deposition of viscous LSC sol via MOD and consecutive thermal treatment (rapid thermal annealing at 170 °C, 700 °C and 900 °C for 5 min each) led to homogeneous, crack-free LSC surfaces (Fig. 58b, Fig. 58e). In the case of LSC on YSZ, a slightly higher porosity was observed in comparison with LSC on the screen-printed GCO buffer layer. The SEM side-view images of the LSC / YSZ (Fig. 58c) and the LSC / GCO interfaces (Fig. 58f) display LSC thin films with a thickness of 200 - 300 nm and good adhesion to the adjoining electrolyte material.

Fig. 59a depicts the temperature profile for the electrochemical impedance analyses of LSC on YSZ ("design 1") and LSC on GCO ("design 2") where each EIS measurement is denoted by an arrow. The complex impedance plot (Cole-Cole view) of a symmetrical cell (□, "design 1") at 850 °C is shown in Fig. 59b. Three regimes can be identified from the plot, denoted as (I), (II) and (III). Regime (I) is attributed to the ohmic losses of the electrolyte and the (negligible) contact resistance [223] of the setup. The regimes (II) and (III) are associated with electrochemical and gas diffusion processes. The total area specific polarization resistance ASR_{pol} of the cathode is given by the intercept of the spectra with the real axis divided by a factor of two to account for the electrodes on both sides. The temperature-dependent cathode-polarization losses of the nanoscaled LSC thin-film cathode on YSZ (□, "design 1") and GCO (■, "design 2") are given in Fig. 59c. From 500 °C to 650 °C the ASR_{pol}

values decrease continuously with increasing temperature from 489 mΩ·cm² (T_{cell} = 498 °C) to 85 mΩ·cm² (T_{cell} = 649 °C) (LSC on YSZ) and from 910 mΩ·cm² (T_{cell} = 489 °C) to 81 mΩ·cm² (T_{cell} = 643 °C) (LSC on GCO). As from 650 °C upwards, the performance of LSC / YSZ and LSC / GCO differs significantly. In the case of LSC / YSZ (□, "design 1") the gradient flattens out until 750 °C, changes sign for further increasing temperature and reaches 48 mΩ·cm² at 850 °C. Within 20 h at 850 °C the ASR_{pol} increases to 78 mΩ·cm² (Fig. 59d), resulting in an ASR_{pol} of 94 Ω·cm² at 498 °C after cooling-down.

a) „design 1":
LSCF | LSC thin film | YSZ

(La,Sr)(Co,Fe)O$_{3-\delta}$
(porous, 30µm)

8YSZ substrate
(100 µm)

$(La_{0.5}Sr_{0.5})CoO_{3-\delta}$
(300 nm)

d) „design 2":
LSCF | LSC thin film | GCO | YSZ

(La,Sr)(Co,Fe)O$_{3-\delta}$
(porous, 30 µm)

GCO (thick-film, 5 µm)

3.5YSZ substrate
(100 µm)

b) Top view: nanoscaled LSC thin film

600 nm

(MOD094b)

c) Side view: LSC / YSZ interface

LSC thin film

600 nm

RTA (T_{max} = 900 °C)   (MOD094b)

e) Top view: nanoscaled LSC thin film

600 nm

(MOD086)

f) Side view: LSC / GCO interface

LSC thin film

600 nm

RTA (T_{max} = 900 °C)   (MOD086)

Fig. 58 Symmetrical cells prepared for electrochemical testing
comprise a 30 µm thick screen-printed LSCF current collector and a nanoscaled LSC thin-film
cathode deposited on a) an 8YSZ electrolyte ("design 1") and d) a GCO buffer layer ("design
2"); SEM top-view images of nanoscaled LSC thin films on YSZ (b) and GCO (e) after rapid
thermal annealing (RTA), SEM cross-section images of LSC / YSZ (c) and LSC / GCO (f)
interfaces.

The applied temperature profile and the dwell of 20 h at 850 °C leads to a tremendous change in cathode performance, yielding an increase by two orders of magnitude for ASR_{pol} of LSC / YSZ at 498 °C (489 mΩ·cm² to 94 Ω·cm²). In contrast, in the case of LSC / GCO (■, "design 2"), an excellent durability even at temperatures as high as 845 °C could be observed: The ASR_{pol} decreases continuously for increasing temperature between 492 °C

and 845 °C and results in a fairly low value of 23 mΩ·cm² at 845 °C. During 20 h dwell at 845 °C the ASR_{pol} shows constant performance and levels off at 21 mΩ·cm² (Fig. 59d). During cooling-down the ASR_{pol} matches approximately the initial values during heating-up, resulting in an increase of the polarization resistance of 25 % between start and finish of the measuring cycle (910 to 1140 mΩ·cm² at 492 °C) (Fig. 59c).
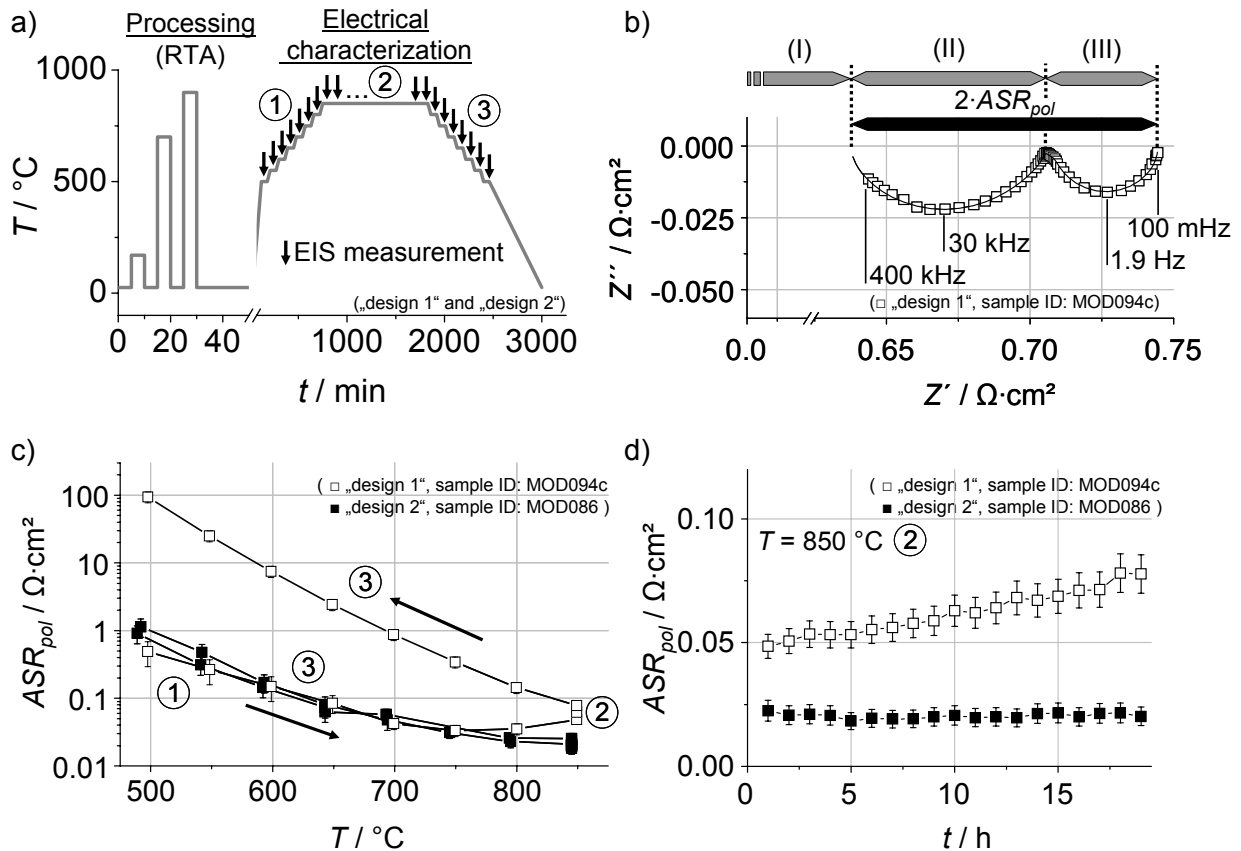
Fig. 59 Symmetrical EIS characterization of LSC thin-film cathodes
a) Temperature history of samples: processing (rapid thermal annealing (RTA)) followed by electrical characterization during heat-up (1), 850 °C (2) and cool-down (3); arrows (↓) indicate impedance measurements (EIS); b) Nyquist plot of a nanoscaled LSC thin-film cathode on 8YSZ (□, "design 1") in a symmetrical setup at 850 °C: (I) ohmic resistance, (II+III) polarization resistance ASR_{pol}; c) ASR_{pol} temperature course for a nanoscaled LSC thin-film cathode on i) YSZ (□, "design 1") and on ii) GCO (■, "design 2") with heat-up (1), 850 °C (2) and cool-down (3); d) monitoring of ASR_{pol} for 20 hours at T = 850 °C for nanoscaled LSC thin-film cathode on i) YSZ (□, "design 1") and on ii) GCO (■, "design 2"). The microstructure of the specimens is depicted in Fig. 58; note that the microstructure of the samples MOD094b and MOD094c corresponds.

The error bars in Fig. 59c - Fig. 59d account for uncertainties during the characterization, namely the reproducibility of the thin-film processing as well as geometrical considerations associated with the screen-printing process of the current collector (layer misalignment,

paste flow) and the measuring accuracy of the electrical equipment (manufacturers' data) (cf. 3.3.2).

The results of Fig. 59c - Fig. 59d must be attributed to chemical or structural changes within the LSC / YSZ system as a function of thermal treatment and time, whereas the LSC / GCO system exhibits a stable performance. According to [156-159, 161, 251], the formation of zirconates at the LSC / YSZ interface has been reported for $T \geq 900$ °C. The results shown in Fig. 59d (T_{max} = 850 °C), however, suggest application of an extended testing procedure (100 h) at even lower temperatures, thus allowing an assessment of the maximum temperature, up to which the material combination LSC / YSZ remains stable. The slight increase in ASR_{pol} of the LSC / GCO, on the other hand, might be attributed to morphological changes of the nanoscaled LSC thin film, which was previously studied in chapter 4.2.2.
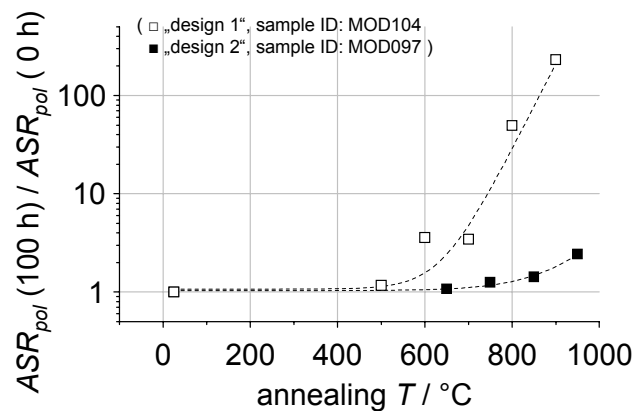
Fig. 60 Normalized ASR_{pol} of LSC thin-film cathodes vs. annealing temperature at i) 600 °C (nanoscaled LSC on YSZ (□, "design 1")) and at ii) 650 °C (nanoscaled LSC on GCO (■, "design 2")) after aging between 500 °C and 950 °C for 100 h, respectively; dashed lines are guide to the eye [7].

Fig. 60 shows the results of this extended testing procedure, applied to LSC / YSZ and LSC / GCO samples, respectively. After annealing at different temperatures between 500 °C and 900 °C for 100 h, the ASR_{pol} was subsequently determined at a fixed temperature in each case and normalized with respect to its initial value (ASR_{pol} (0 h)). In the case of the LSC / YSZ samples, annealing led to a very pronounced increase of the normalized ASR_{pol}, commencing at a threshold value of about 500 °C and ranging from a factor of 1.16 (annealing at 500 °C for 100 h) to 231.7 (900 °C, 100 h).

For a better understanding of this rise of the polarization resistance of the LSC / YSZ cells (□, "design 1"), the impedance spectra at the dwell (20 h) at T = 850 °C were analyzed by calculating the distribution function of relaxation times (DRT, cf. chapter 3.3.3). The DRTs of

---

[7] The effect of annealing on the polarization of nanoscaled LSC thin-film cathodes has been investigated by Holger Götz within the study project „Einfluss der Mikrostruktur auf den Polarisationswiderstand einer LSC-Nanokathode" (Influence of the Microstructure on the Polarization Losses of a nanoscaled LSC Thin-Film Cathode), 2007, IWE.

LSC / YSZ and LSC / GCO enable the distinct separation of the polarization processes (Fig. 61a, Fig. 62a). Whereas the gas phase process is approximately constant during the twenty hours dwell (○, Fig. 61b), the remaining polarization processes increase with operating time and cause the overall increase of the polarization resistance ASR_{pol} in case of LSC / YSZ. As depicted in Fig. 59d the total area specific polarization resistance of the LSC / GCO cells (■, "design 2") is constant over 20 h at 850 °C. The DRT graph (Fig. 62a) and its evaluation (Fig. 62b) depict both constant gas-phase polarization ASR_{gas} and invariant remaining polarization processes.
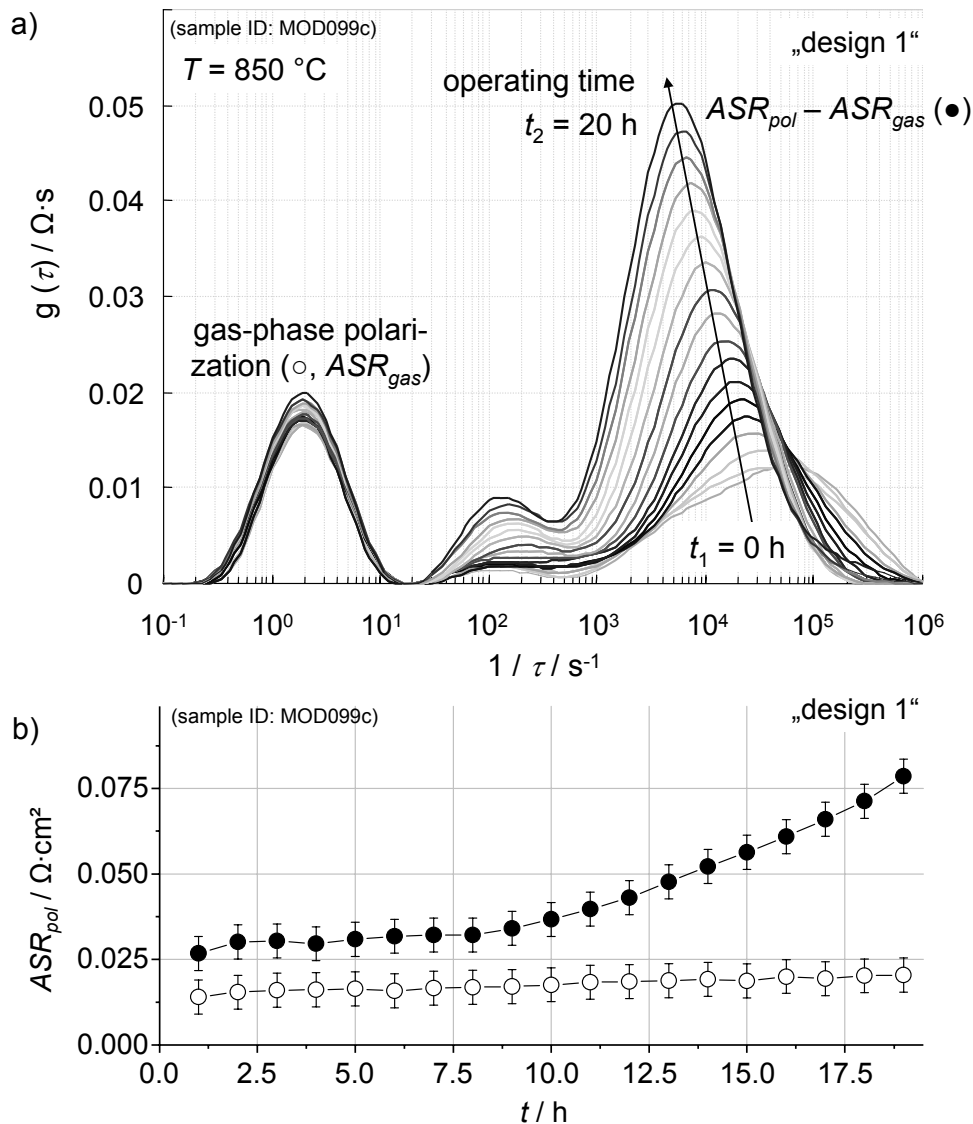
Fig. 61 Analyses of the polarization losses of "design 1" at T = 850 °C over time
a) Distribution of relaxation times $g(\tau)$ (DRT [226]) versus $1/\tau$ of the nanoscaled LSC thin-film cathode on YSZ ("design 1") derived from the evaluation of EIS spectra ranging from t = 0 h to t = 20 h at T = 850 °C; gas-phase polarization (process III in Fig. 59b and Fig. 63) remains constant, charge-transfer polarization (process II in Fig. 59b and Fig. 63) generates a distinctive change in magnitude and frequency; b) ASR_{pol} split up into gas-phase polarization (○) and charge-transfer polarization (●) with respect to measuring time at 850 °C.

The polarization resistance of the LSC / GCO samples shown in Fig. 60 (■, "design 2"), however, exhibited steady values after annealing at 650 °C for 100 h (normalized ASR_{pol} = 1.08) and increased values for $T \geq 750$ °C (normalized ASR_{pol} = 1.26 (750 °C, 100 h), ASR_{pol} = 1.42 (850 °C, 100 h), ASR_{pol} = 2.43 (950 °C, 100 h)). As the chemical compatibility of LSC / GCO was previously proven (Fig. 57), this increase cannot be attributed to an interface reaction. Instead, the temperature dependency the ASR_{pol} in Fig. 60 (■) corresponds to the coarsening of the microstructure for $T > 700$ °C (Fig. 51b) suggesting a linkage between the two thin film properties.
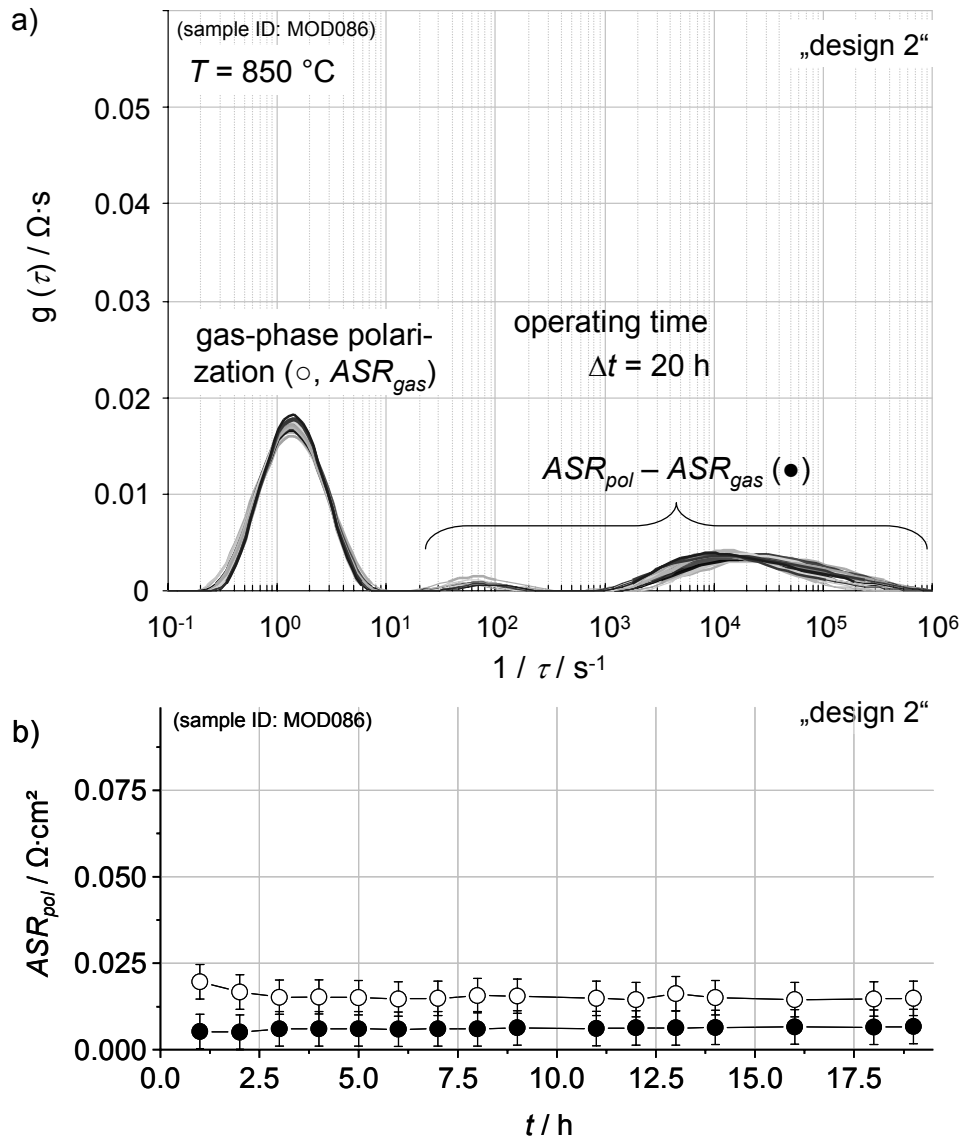
Fig. 62 Analyses of the polarization losses of "design 2" at T = 850 °C over time
a) Distribution of relaxation times $g(\tau)$ (DRT [226]) versus $1/\tau$ of the nanoscaled LSC thin-film cathode on GCO ("design 2") derived from the evaluation of EIS spectra ranging from t = 0 h to t = 20 h at T = 850 °C; gas-phase polarization (process III in Fig. 59b and Fig. 63) and charge-transfer polarization (process II in Fig. 59b and Fig. 63) remain constant.

The temperature dependency of the electrode conductivity (1 / ASR_{pol}) is analyzed in Fig. 63 (LSC / GCO cells, "design 2"). The complex impedance spectra at 650 °C (A) and 850 °C (B) (Fig. 63, right plots) show two major processes (II, III), which govern the total polarization resistance at the respective temperatures.
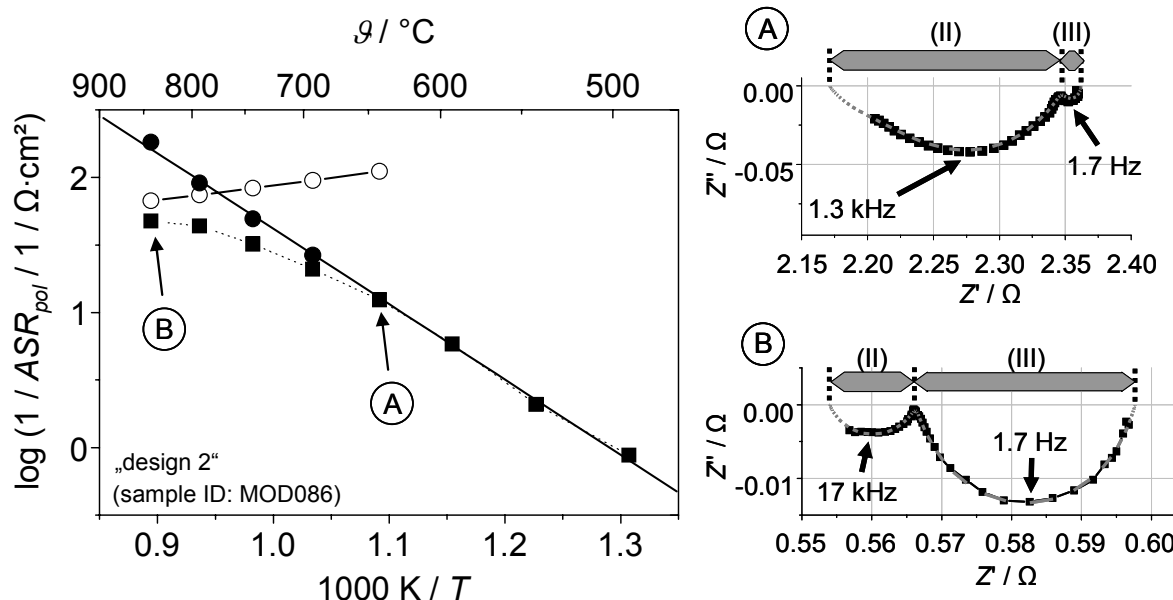
Fig. 63 Separation of ASR_{gas} from ASR_{pol}

left: Temperature dependence of the electrode conductivity 1/ASR_{pol} and right: Nyquist plots at 650 °C (A) and 850 °C (B) of a nanoscaled LSC thin-film cathode on GCO ("design 2"). Semicircles II and III sum up to the total polarization resistance ASR_{pol} (■), semicircle III is attributed to gas-phase polarization (○, ASR_{gas}), semicircle II to oxygen-reduction polarization (●, mainly ASR_{ex}); fits are depicted in grey color.

Throughout this work, a variety of processing parameters for the thin-film preparation were varied to obtain homogeneous LSC thin films with a distinct nanoporosity. In the course of the variation of deposition technique, solvent composition, number of coatings and temperature treatment by rapid thermal annealing, specimens with a variety of different microstructures were obtained. The polarization losses with respect to morphological properties of these LSC thin films are depicted in Fig. 64 and Fig. 65. The polarization losses range from ASR_{pol} = 0.08 Ω·cm² to ASR_{pol} = 2.66 Ω·cm² at 600 °C depending on film thickness (60 nm ≤ t ≤ 300 nm), particle size (10 nm ≤ d ≤ 70 nm) and film porosity (17.5% ≤ ε ≤ 50%). The deposition technique and the number of coatings govern the film thickness as shown exemplarily in Fig. 47; the mean particle size is determined by the calcination procedure, i.e. RTA. All morphological parameters were obtained from the SEM examinations and optical valuations and are therefore afflicted with errors as discussed in chapter 5.2.2. The correlation between the electrochemical and geometrical properties is derived by application of a transport model in chapter 5.2.2.

- *ASR$_{pol}$* (IS2.077)
  = 0.08 ± 0.02 Ω
- *d* = 33 ± 8 nm
- *t* = 300 ± 30 nm
- *ε* = 42.5 ± 10 %

(MOD079)   (MOD079)

- *ASR$_{pol}$* (IS2.079)
  = 0.21 ± 0.05 Ω
- *d* = 10 ± 3 nm
- *t* = 100 ± 10 nm
- *ε* = 25 ± 10 %
- microcracks

(MOD084)   (MOD084)

- *ASR$_{pol}$* (IS2.073)
  = 0.15 ± 0.04 Ω
- *d* = 50 ± 13 nm
- *t* = 300 ± 30 nm
- *ε* = 35 ± 10 %

(MOD094b)   (MOD094b)

- *ASR$_{pol}$* (Z3.028)
  = 0.40 ± 0.12 Ω
- *d* = 20 ± 5 nm
- *t* = 60 ± 6 nm
- *ε* = 50 ± 10 %

(MOD164)   (MOD164)

Fig. 64 SEM analyses of differently prepared LSC thin films

in top-view (left) and cross-section (right); polarization resistance (*ASR$_{pol}$*) at 600 °C, particle size (*d*), film thickness (*t*) and estimated porosity (*ε*) are given in between. For the evaluation of the electrochemical and geometrical properties, the following errors were assumed: *ASR$_{pol}$* ± 29.3%, *d* ± 25%, *t* ± 10%, *ε* ± 10% (absolute error).

- ASR_{pol} (IS2.082)
  = 0.29 ± 0.08 Ω
- d = 70 ± 18 nm
- t = 200 ± 20 nm
- ε = 35 ± 10 %
- undulated

(MOD114c)

(MOD114c)

- ASR_{pol} (Z3.007)
  = 0.38 ± 0.11 Ω
- d = 50 ± 13 nm
- t = 200 ± 20 nm
- ε = 17.5 ± 10 %

(MOD102d)

(MOD102d)

- ASR_{pol} (IS2.086)
  = 1.06 ± 0.31 Ω
- d = 30 ± 8 nm
- t = 100 ± 10 nm
- ε = 17.5 ± 10 %
- microcracks
  (cf. inset)

(MOD120)

(MOD120)

- ASR_{pol} (IS2.075)
  = 2.66 ± 0.78 Ω
- d = 65 ± 16 nm
- t = 130 ± 13 nm
- ε = 17.5 ± 10 %

(MOD095d)

(MOD095d)
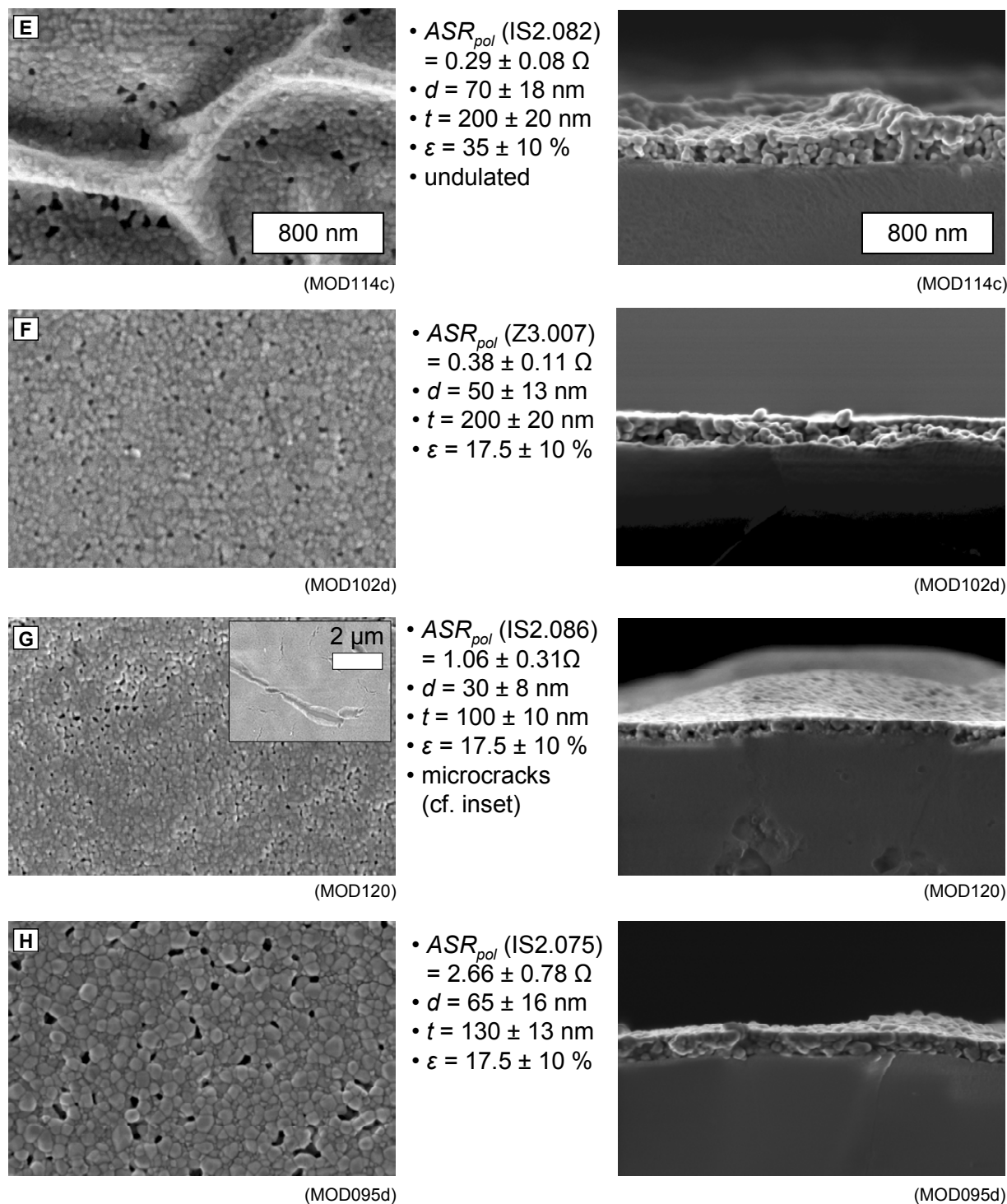
Fig. 65 SEM analyses of differently prepared LSC thin films

in top-view (left) and cross-section (right); polarization resistance (ASR_{pol}) at 600 °C, particle size (d), film thickness (t) and estimated porosity (ε) are given in between. For the evaluation of the electrochemical and geometrical properties, the following errors were assumed: ASR_{pol} ± 29.3%, d ± 25%, t ± 10%, ε ± 10% (absolute error).

5 Discussion

In this chapter, the results of the conducted experiments concerning the transport properties of nanoscaled yttria-doped zirconia (5.1) and lanthanum strontium cobaltite (5.2) thin films are discussed. Special emphasis is put on potential IT-SOFC application of the thin films at 500 °C ≤ T ≤ 750 °C.

5.1 Grain-Size Effects in Nanoscaled YSZ Thin Films

Grain-size effects at the nanoscale potentially facilitate improved charge transport in yttria-doped zirconia. Significantly enhanced transport properties, in turn, are of profound interest for YSZ thin-film electrolytes in IT-SOFC application. However, the effects of grain-size on the transport properties in nanoscaled YSZ thin films are controversially discussed in literature. Enhanced oxygen diffusion at the interfaces was observed by [66-70] (cf. chapter 2.1.3). On the other hand, several groups reported a "blocking effect" of the grain boundaries, which entails a decreasing electrical conduction upon decreasing of the mean grain size [41, 45, 71-78].

To elucidate the role of interfaces at the nanoscale, this work studies the electrical transport properties of 8YSZ thin films within a broad grain-size regime. This chapter discusses the processing, design and electrical characterization of nanoscaled YSZ thin films. Special emphasis is put on the evaluation of grain-size effects.

For the evaluation of the transport properties with regard to microstructure, thin-film electrolytes were processed with a broad variation of the mean grain size. A sol-gel method was applied for the preparation of dense YSZ thin films on insulating sapphire substrates. As shown by Bockmeyer and Löbmann for sol-gel derived TiO_2 [207], temperature treatment turned out to be crucial for the surface quality of the thin films. A rapid thermal annealing step at 500 °C (10 min) and subsequent calcination at 650 °C ≤ T (24 h) ≤ 1400 °C led to crack-free thin films with a broad grain-size distribution (Fig. 29). Since the sol-gel method contents itself with low processing temperatures compared to other chemical or physical thin film deposition techniques (chapter 2.3), possible carbon residues from the sol-gel process in the films are an essential issue. Thermal analyses of YSZ powder after RTA at 500 °C showed an exothermic chemical reaction between 600 °C and 800 °C (region III in Fig. 28). Since this reaction was accompanied with mass loss (15 wt%), this indicates the removal of remaining carbon compounds from the films. Additionally, a relaxation of the thin film was observed at 650 °C ≤ T_{cal} ≤ 850 °C correlating with the TG results. The samples, calcined at T_{cal} ≥ 850 °C, however, are completely free of carbon residues. This was confirmed by high-resolution transmission electron microscopy (HRTEM) studies, which did not evidence any

amorphous phases in the thin films or residues of carbon remainings from the sol-gel precursors (Fig. 33).

The stoichiometry of the yttria-doped zirconia films was evaluated to 8.3 mol% yttria. Single-phase crystallization was shown by XRD analysis (Fig. 30). However, TEM studies revealed the presence of tetragonal precipitates in the cubic matrix (Fig. 32). These precipitates were homogeneously distributed and with a size of a few Å. In general, Butz et al. stated that tetragonal precipitates are always present in 8 mol% yttria-doped zirconia materials – even in state-of-the-art polycrystalline 8YSZ electrolytes, which are often considered as completely stabilized in the cubic phase [55, 215] (cf. YSZ phase diagram in Fig. 6). Due to the small size of the tetragonal precipitates and their homogeneous distribution in the YSZ grains and due to the fact that these precipitates do not accumulate at the grain boundaries, they do not alter the transport properties of the thin films by an extent distinguishable by state-of-the-art experimental methods. For potential long-term stability in IT-SOFC application, however, the tetragonal precipitates may be a cause for degradation as discussed in 2.1.2 (Fig. 8).

Grain boundaries in nanocrystalline YSZ electrolytes deserve particular attention because they might strongly affect the overall ionic conductivity. The segregation of alumina and silica to the grain boundaries, for example, was found to significantly increase the grain-boundary resistance as investigated by Aoki et al. [80] and others [81, 82]. However, extensive EDXS analyses confirmed, within the detection limits, the absence of contaminants in the sol-gel layers. Applying HRTEM, the existence of amorphous phases at the grain boundaries can be excluded as well – at least for calcination temperatures $T_{cal} \geq 850$ °C (Fig. 33). A local segregation of yttrium ions in the grain-boundary regions is expected to lead to a local depletion of the tetragonal phase in the vicinity of grain boundaries [252, 253]. This was disproved by experimental observations as well (Fig. 32). Additionally, TEM analysis determined a minor volume percentage of nanopores at $T < 1100$ °C. The presence of porosity can be understood by considering the preparation method based on a sol-gel precursor with a considerable volume fraction of organic material. During the RTA process, the organic components of the precursor are pyrolyzed resulting in pores (Fig. 29). Upon heat treatment, the YSZ layers densify, accompanied by grain growth (Fig. 29, Fig. 31), resulting in completely dense YSZ films for calcination temperatures of $T > 1100$ °C.

Depending on calcination temperature, the mean grain sizes of the investigated YSZ thin films could be varied by two decades, ranging from 5 nm ($T_{cal} = 650$ °C, $t_{dwell} = 24$ h) over 36 nm ($T_{cal} = 1000$ °C, $t_{dwell} = 24$ h) to 782 nm ($T_{cal} = 1400$ °C, $t_{dwell} = 24$ h). This grain size variance is considerably larger than in other studies on zirconia thin films [231-237], but correlates well with the studies of 8YSZ thin films on sapphire substrates performed by Kosacki et al. [66]. Fig. 35 suggests exponential grain growth with two grain-growth regimes with different activation energies at 650 °C $\leq T_{cal} \leq$ 1100 °C and 1100 °C $\leq T_{cal} \leq$ 1400 °C. Grain growth is known to be limited during the densification of microcrystalline ceramic materials [254] and increases upon full densification as observed by Díaz-Parralejo et al. for 3YSZ films [231]. Therefore, the nanoporosity in the studied 8.3 mol% yttria-doped zirconia

thin films (Fig. 35, right axis) is considered to impede grain growth until approximately 1100 °C. At higher calcination temperatures, the samples completely densify and coarsen during the calcination period.

Electrical impedance spectroscopy (EIS) was applied to evaluate both the total resistance of the thin films and the individual losses related to grain and grain-boundary transport. The impact of nanoporosity for $T \leq 850$ °C was evaluated by a 3-dim model of the thin-film microstructure (Fig. 36). With increasing mean grain size, the total electrical conductivity of the YSZ thin films increases continuously by 1 - 2 decades reaching a plateau at $d \approx 500$ nm (Fig. 37). The conductivity of this plateau coincides well with the electrical conductivity of coarse crystalline Itochu-8YSZ. Due to the known transference number of unity of the polycrystalline electrolyte (Fig. 3), this suggests that the measured charge transport in the thin films is of pure ionic character. Except the sample with the smallest grains ($d = 5$ nm, $T_{cal} = 650$ °C, MOD056), all others show Arrhenius-type conductivity yielding activation energies of $E_A = 1.13 \pm 0.02$ eV. These activation energies correlate with the activation energies for the grain-boundary conductivity summarized in Table 1 suggesting that the total electrical conductivity of the thin film is governed by the grain-boundary transport.

The general trend of Fig. 38 is a substantial decrease in ionic conduction upon increase of the grain-boundary density. These findings are in contrast to the observations of Kosacki et al. [66] who found the ionic conduction in nanoscaled 8YSZ thin films to be substantially enhanced. It is noteworthy, that the thin films studied in [66] were processed very similar to the samples investigated in this work: 8 mol% yttria-doped zirconia thin films were processed on sapphire substrates via a polymeric precursor spin-coating method (cf. Table 2).

The conductivity data of the thin films obtained in this work (grey) and by Kosacki et al. [66] (black) are depicted in Fig. 66. Comparing similar mean grain sizes ($d = 14$ / 20 nm vs. $d = 782$ / 2400 nm), the controversial trend becomes apparent. Whereas the activation energies of the microcrystalline thin films approximately coincide ($E_A = 1.11$ / 1.19 eV) and the data match well with the conductivity data of coarse crystalline Itochu-8YSZ (Fig. 66, inset), the activation energies for the nanocrystalline grains differ distinctly ($E_A = 0.93$ / 1.14 eV) suggesting different transport processes in the thin films. With decreasing mean grain size, Kosacki et al. observed an enhancement of about two orders of magnitude at 600 °C in the ionic conductivity for nanocrystalline YSZ. Whereas Kosacki et al. attributed the increase in electrical conduction to enhanced ion mobility in the extended grain-boundary volume, the data of this work suggests a blocking of oxygen ions at the grain-boundary. This is supported by the DRT analysis (Fig. 39), which shows two distinguished electrochemical processes: in accordance to reported models (e.g. [41, 255]), the low-frequency process was attributed to the grain-boundary process and the high-frequency process to the bulk transport of oxygen ions (Fig. 40). Whereas the latter is approximately constant for all investigated samples, the resistance related to the grain-boundary transport increases with decreasing mean grain size.
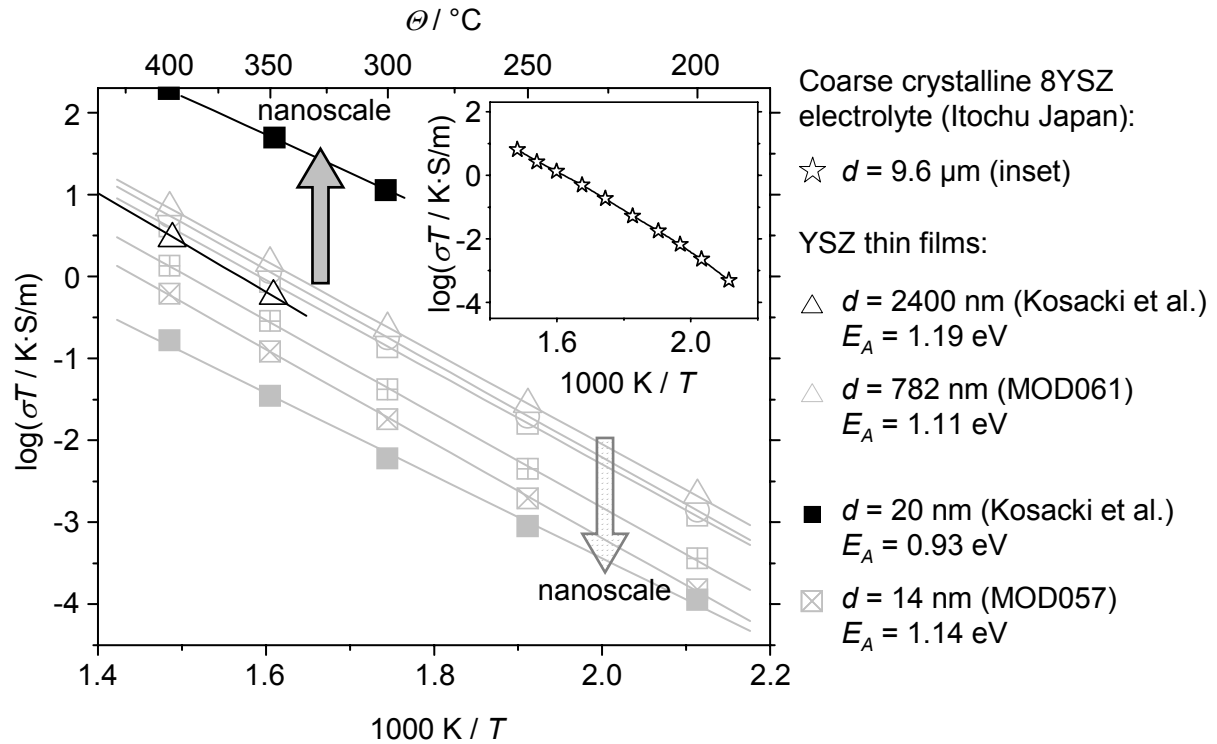
Fig. 66 Arrhenius plot of the total electrical conductivity with respect to mean grain size
Whereas the findings of this work show that conductivity decreases with mean grain size (grey data points), Kosacki et al. [66] observed an increase of electrical conduction at the nanoscale. Inset: extrapolated electrical conductivity of a coarse crystalline 8YSZ electrolyte (Itochu, Japan) obtained by Simonin [38].

From CNLS fits of the complex impedance spectra (Fig. 41), the electrical grain-boundary thickness could be derived to 4.36 nm $\leq \delta_{gb} \leq$ 6.13 nm. This thickness was found to be independent of grain size (232 nm $\leq d \leq$ 782 nm) and measuring temperature (200 °C $\leq T \leq$ 400 °C). The grain-boundary thickness is in good agreement with values for polycrystalline 8YSZ derived by Guo et al. (δ_{gb} = 4.8 nm [41, 87]), Verkerk et al. (δ_{gb} = 5.4 nm [45]) and Boulfrad et al. (δ_{gb} = 5.15 ± 2.45 nm [256]). It is noteworthy, that the grain-boundary thickness decreases significantly for zirconia dopants that deviate from 8 mol% yttria as shown in Table 5.

Table 5 Evaluation of the grain-boundary thickness δ_{gb} in doped zirconia samples

Stoichiometry / doping of ZrO$_2$	film / polycrystal	d / nm	δ_{gb} / nm	source
8.3 mol% Y$_2$O$_3$	thin film	232 / 548 / 782	5.3	this work
8 mol% Y$_2$O$_3$	polycrystal	16,000	4.8	[41, 87]
8 mol% Y$_2$O$_3$	polycrystal	350 – 55,000	5.4	[45]
8 mol% Y$_2$O$_3$	polycrystal	25 / 51	2.8 / 3.5	[256]
8 mol% Y$_2$O$_3$	polycrystal	76 / 95	7.6 / 2.7	[256]
10 mol% Y$_2$O$_3$	thin film	-	1.6	[67]

Stoichiometry / doping of ZrO$_2$	film / polycrystal	d / nm	δ_{gb} / nm	source
2.5 mol% Y$_2$O$_3$	polycrystal	60	1.3	[77]
15 mol% CaO	polycrystal	140 – 11,400	1	[80]

Applying the brick-layer model, the specific bulk and grain-boundary conductivities could be obtained accounting for the charge transport in grains and grain boundaries with respect to their specific geometry. The conductivities were found to be Arrhenius-type with activation energies of E_A = 1.085 ± 0.005 eV for the bulk process and E_A = 1.145 ± 0.005 eV for the grain-boundary process (Fig. 42). This deviation in activation energies corresponds to the findings of [41, 43, 45, 46] as summarized in Table 1. Since the bulk conductivities excel the specific grain-boundary conductivities by approximately two decades (Fig. 42), the previously discussed blocking effect of the grain boundaries is confirmed. For 232 nm ≤ d ≤ 782 nm, the specific bulk and grain-boundary conductivities were independent of the mean grain size, where deviations of the curves among each other were mainly related to the brick-layer model (cf. chapter 2.1.4). Thus, constant values of σ_{gb}^s suggest the presence of *trivial size effects* [62], i.e. the physical effects are augmented by the high interfacial density but do not change principally upon geometry modifications at 232 nm ≤ d ≤ 782 nm. For smaller grains (d ≤ 36 nm), the resolution of the impedance data is limited by the large ratio of R_{gb} / R_g. In this grain-size regime, the bulk process cannot be separated from the grain-boundary transport and thus, the grain-boundary thickness δ_{gb} cannot be calculated from the data. In order to evaluate the existence of potential grain-size effects at the nanoscale, the total resistance of the 8YSZ thin films featuring grain sizes of 5 nm ≤ d ≤ 36 nm is calculated by the application of the brick-layer model and compared to the experimental results.

Possible transport paths in the YSZ thin films with respect to bulk ("g"), grain boundary ("gb") and grain-boundary core ("$core$") are depicted in Fig. 67. Following [76], the charge transport can be described by electrical equivalent circuits consisting of three parallel transport paths. Generally, both ionic "ion" and electronic "el" conduction may occur, firstly through the bulk and perpendicular to the grain boundaries, secondly parallel to the space-charge layers in the grain boundaries and thirdly parallel in the grain-boundary core.

Then the total thin-film resistance R_{tf} is given by

$$\frac{1}{R_{tf}} = \frac{1}{\left(R_g^{ion} + R_{gb}^{\perp,ion}\right)} + \frac{1}{\left(R_g^{el} + R_{gb}^{\perp,el}\right)} + \frac{1}{R_{gb}^{\|,ion}} + \frac{1}{R_{gb}^{\|,el}} + \frac{1}{R_{gb}^{core,ion}} + \frac{1}{R_{gb}^{core,el}} \qquad \text{Eq. 47}$$

The transport properties of the YSZ thin films evaluated in this work can be summarized as following: The overall conductivity of the thin films with the largest grains (d = 782 nm) matches with the conductivity of ionically conducting electrolytes (Fig. 37). Thus, electronic conduction parallel to the grain boundaries $R_{gb}^{\|,el}$ and $R_{gb}^{core,el}$ or perpendicular to the grain boundaries via $R_g^{el} \rightarrow R_{gb}^{\perp,el}$ can be excluded. With decreasing mean grain size, the overall resistances of the films increase. However, assuming the presence of ionic conduction

parallel to the grain boundaries $R_{gb}^{\|,ion}$ and in the grain-boundary core $R_{gb}^{core,ion}$, an increase of the grain-boundary density would facilitate ionically conducting channels in the thin film and inevitably lead to a reduction of R_{tf}. Thus, the ionic transport parallel to the grain boundaries or in the grain-boundary core must be nil or negligible compared to the bulk transport. This suggests that the transport in the YSZ thin films occurs via $R_g^{ion} \rightarrow R_{gb}^{\perp,ion}$, where the intrinsic transport properties of the bulk and the grain boundaries are found to be constant upon grain-size reduction from 782 nm to 232 nm.

a)   b)
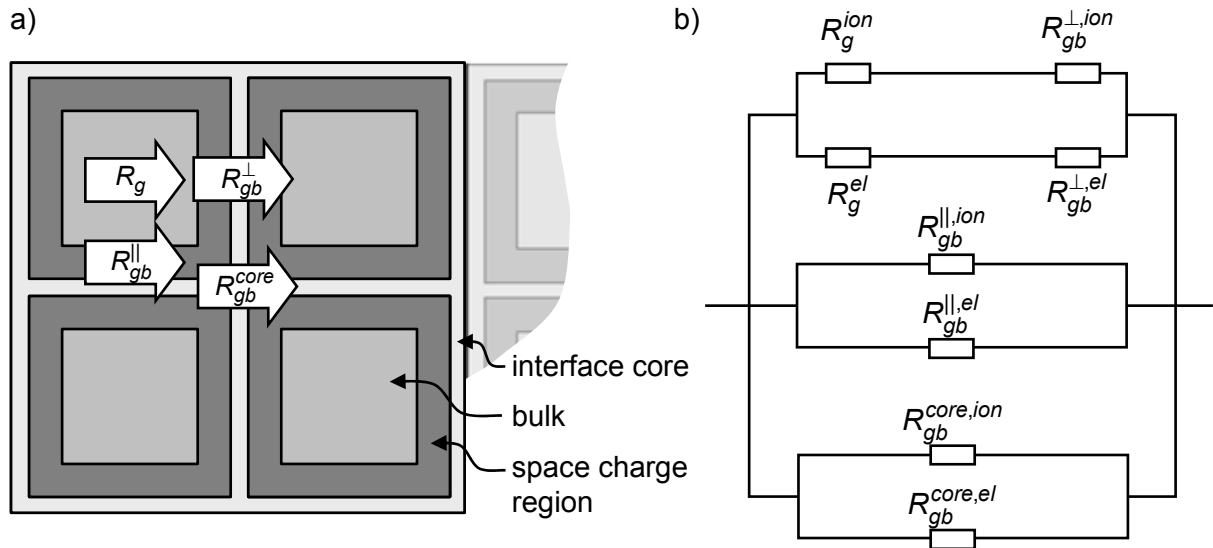
Fig. 67 Brick-layer model and equivalent circuits applied for nanoscaled YSZ thin films
a) Possible transport paths in the crystalline structure; b) equivalent electrical circuits of the ohmic losses where "*ion*" denotes the ionic charge transport and "*el*" the electronic charge transport.

Based on these considerations, the thin-film resistances for smaller grains (5 nm ≤ d < 232 nm) can be calculated. As a thought experiment, it is assumed in the following that the bulk and grain-boundary characteristics (σ_g^s, σ_{gb}^s, δ_{gb}) can be applied at the nanoscale. Evidence for *true* size effects will be provided, if the simulated values excel the measured ones. On the other hand, *trivial* size effects will be proved, if the values coincide.

With reducing mean grain size the effective geometrical lengths of the thin film change according to the brick-layer model (Fig. 68). Thus, for the bulk transport, the effective electrode clearance l_{cl}, the thin-film thickness t and the electrode length l_{el} are reduced by the number of grain boundaries in the respective dimension times their electrical thickness δ_{gb}. For the grain-boundary transport, the effective electrode clearance equals (l_{cl} / d) x δ_{gb}, whereas the entire thin-film cross-section (l_{el} x t) is utilized for conduction. The effective geometrical properties are given in Fig. 68. Additionally, the influence of porosity determined by TEM analysis (Table 4) and FEM modeling (Fig. 36), is considered in the model.

$$l_{cl,bulk} = l_{cl} - \frac{l_{cl}}{d} \cdot \delta_{gb}$$

$$l_{cl,gb} = \frac{l_{cl}}{d} \cdot \delta_{gb}$$

$$l_{el,bulk} = l_{el} - \frac{l_{el}}{d} \cdot \delta_{gb}$$

$$l_{el,gb} = l_{el}$$

$$t_{bulk} = t - \frac{t}{d} \cdot \delta_{gb}$$

$$t_{gb} = t$$

d

δ_{gb} $d - \delta_{gb}$

σ_g^s $\sigma_{gb}^{\perp,s}$

$\sigma_{gb}^{\parallel,s} \approx 0$
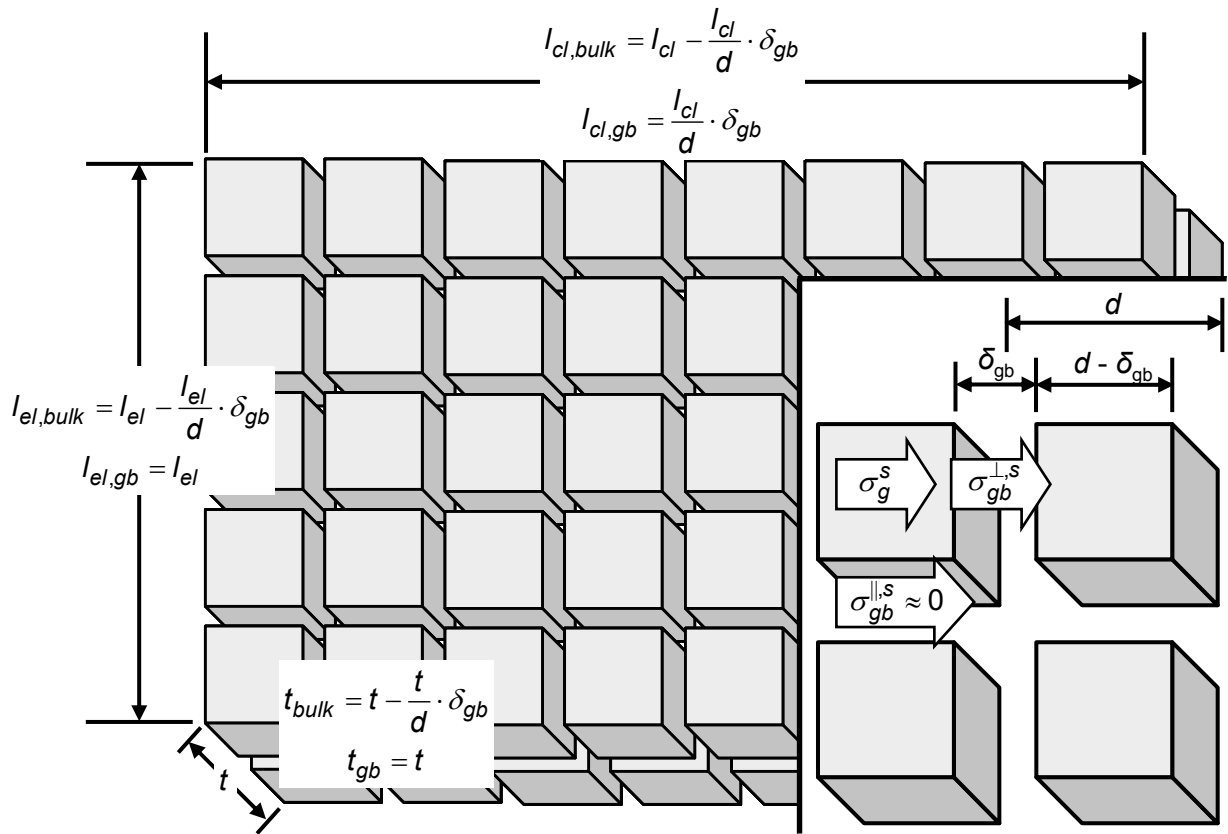
Fig. 68 Brick-layer model appraised for the evaluation of the total R_{tf} for $d \leq 36$ nm
Whereas the transport path perpendicular to the grain boundaries is characterized by σ_g and σ_{gb}, the parallel path does not contribute to the overall conductance.

For the calculation of the overall resistance of the samples with $d \leq 36$ nm, the bulk and grain-boundary characteristics of MOD059 (d = 232 nm) are applied to the brick-layer model. In Fig. 69, the measured data for the total thin-film resistance R_{tf} are given by symbols. An increase of R_{tf} with decreasing mean grain size can be observed consistently to Fig. 37. The modeled resistivity values are depicted as a straight line. Whereas the data coincide well for d = 36 nm (MOD058) and d = 14 nm (MOD057), the sample with the smallest grains (d = 5 nm, MOD056) deviates from the modeled values and exhibits a lower activation energy (■, Fig. 69). This may be related to the substantial release of the microstrain in the thin films observed between T_{cal} = 650 °C (e = 0.53% [229]) and 850 °C (e = 0.15% [229]) (Table 4) and / or to the layered structure and inhomogeneous pore distribution of MOD056 and MOD057 created by the 10-fold dip-coating process and the low calcination temperature (Fig. 31). For calcination temperatures of $T_{cal} \geq 850$ °C, however, the application of the brick-layer model coincides well with the experimental data.

Thus for 14 nm $\leq d \leq$ 36 nm, space-charge effects or other *true size effects* [62] are absent in this grain-size regime because they would entail a decrease of the measured resistance compared to the modeled one where only augmented effects with decreasing mean grain size are considered.
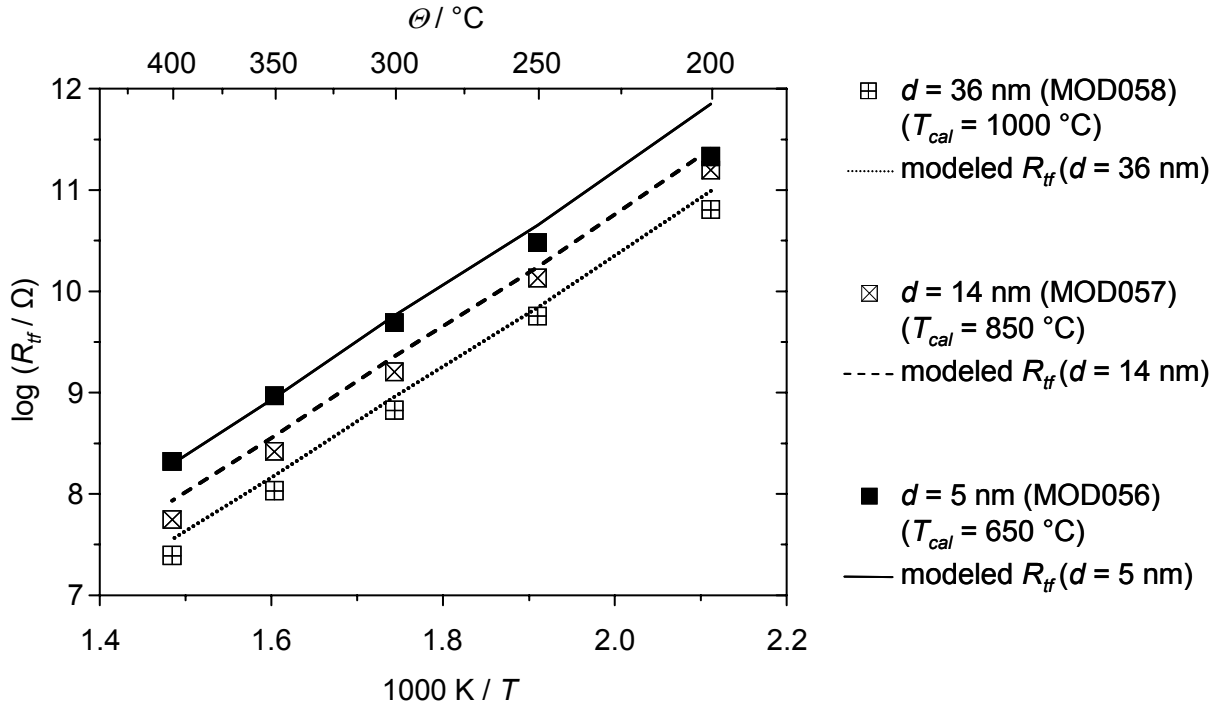
Fig. 69 Total resistances of the YSZ thin films R_{tf} with $d \leq 36$ nm
Measurement data are depicted as symbols, modeled data are shown as straight lines; for the model, the previously obtained bulk and grain-boundary characteristics of the sample calcined at 1250 °C (MOD059) were applied to the brick-layer model according to Fig. 68.

Contrarily to these observations, Kosacki et al. found the overall conductivity $\sigma_{tot}^{Kosacki\ et\ al.}$ significantly enhanced at the nanoscale [66]. The electrical conductivity increased as much as two orders of magnitude as the grain size approaches 20 nm. Kosacki et al. attributed this behavior to size-dependent grain-boundary impurity segregation. The decrease in activation energy from 1.34 eV for polycrystalline YSZ and 1.19 eV for the microcrystalline thin film to 0.93 eV for nanocrystalline materials was related to enhanced ion mobility at the grain boundaries. Unique defect thermodynamics at the nanoscale, which determined the hopping energy for oxygen ions in the extended interfacial area, led, according to the authors, to beneficial transport properties at the nanoscale.

For further analyses of Kosacki's results, two main transport paths are assumed in the following: an ionic path through the grains and perpendicular to the grain boundaries ($R_g^{ion} + R_{gb}^{\perp,ion}$) and a parallel path in the space-charge region of the grain boundaries and in the grain-boundary core ($R_{gb}^{\parallel,core}$, cf. Fig. 67). Where the first transport path has to be ionic due to the ionic conduction of the YSZ bulk, the second transport path may involve both ionic and electronic conduction. These assumptions lead to a simplification of Eq. 47 to

$$\frac{1}{R_{tf}^{Kosacki\ et\ al.}} = \frac{1}{\left(R_g^{ion} + R_{gb}^{\perp,ion}\right)} + \frac{1}{R_{gb}^{\parallel,core}} \qquad \text{Eq. 48}$$

By application of the brick-layer model, Eq. 48 yields to

$$\sigma_{gb}^{\parallel,core} = \frac{d}{\delta_{gb}} \cdot \left(\sigma_{tf}^{Kosacki\ et\ al.} - \left(\frac{1}{\sigma_g^{ion}} \cdot \frac{1}{1-\frac{\delta_{gb}}{d}} + \frac{1}{\sigma_{gb}^{\perp,ion}} \cdot \frac{\delta_{gb}}{d} \right)^{-1} \right) \qquad \text{Eq. 49}$$

where d = 20 nm [66], and δ_{gb}, σ_g^{ion} and $\sigma_{gb}^{\perp,ion}$ are taken from this work. At T = 300 °C, this yields a parallel grain-boundary conductivity $\sigma_{gb}^{\parallel,core}$ of $7.37 \cdot 10^{-2}$ S/m, which is approximately 120 times the bulk conductivity of 8YSZ. For the grain-boundary thickness of 1 nm assumed by Kosacki et al., $\sigma_{gb}^{\parallel,core}$ reaches even higher values (636 times the bulk conductivity of 8YSZ). This conductivity parallel to the grain boundaries may possess ionic and / or electronic character. Assuming a true grain-size effect, i.e. the space-charge region or the grain-boundary core facilitates better ionic conductivity than the bulk (by a factor of 120 / 636), this may be linked to higher mobility or concentration of the oxygen vacancies.

However, Tuller [23] and DeSouza et al. [257] speculated that the substantial rise of the conductivity observed by Kosacki et al. [66] may have originated from the influence of humidity on the exposed side of the specimens during the conducted experiments or strain in the studied films. In another work, Kosacki et al. investigated the influence of the film thickness on the ionic conductivity [67] where the thin films were epitaxially grown on (001) single crystal MgO substrates. According to this study, enhanced conductivity by protonic conduction evoked by water or hydroxyl groups can be excluded. However, previous observations by Kosacki et al. were confirmed: The interface related conductivity was about three to four orders of magnitude larger than that of the lattice with an activation energy of 0.45 eV.

One can only speculate about the reasons of this enhancement. Most probably, an electronic conducting path has been created during the processing of the thin films. It is hard to imagine that either the oxygen-vacancy concentration or the mobility of the vacancies can be increased so far that an increase of the overall conductivity by almost three decades is possible. Hence, most probably, electronic conduction occurs in the samples analyzed by Kosacki et al.. Charge and mobility of electronic conduction may easily be increased, e.g. by the unintentional contamination of the thin films during the processing.

Similar effects of enhanced oxygen diffusion in nanocrystalline YSZ samples were observed by Knöner et al. [70] who reported an increase of the oxygen diffusion along the grain boundaries compared to the bulk by three orders of magnitude. DeSouza et al. [257], however, attributed this observation to open porosity and microcracks in the studied samples. DeSouza et al. themselves studied the oxygen diffusion in nanocrystalline ($d \approx 50$ nm) YSZ at $500 \leq T \leq 700$ °C by ^{18}O / ^{16}O annealing and consecutive SIMS analyses [257]. In contrast to the studies of Kosacki et al. and Knöner et al., DeSouza et al. did not observe enhanced grain-boundary diffusion, since the diffusion data was close to those found for single crystalline material, the authors concluded that the grain boundaries are neither paths of hugely enhanced oxygen diffusivity nor paths of hugely reduced diffusivity.

The grain boundaries of nanoscaled YSZ thin films were found to hinder the charge transport parallel and perpendicular to the grain boundaries. This, consecutively, means that the mobility of the oxygen vacancies is not increased because of "interconnected excess free volume" [23], but decreased in the grain-boundary region because of the low symmetry at the fringe of the crystal lattice [257]. Additionally, the grain boundaries are likely to be depleted of oxygen vacancies, which is in contrast to the proposed *nanoionics* effect. Instead of a positive space charge as discussed in Fig. 10, the depletion of oxygen vacancies in the space-charge regions leads to a negative charge because of the immobile $\left[Y'_{Zr} \right]$ ions (Fig. 70). To account for electroneutrality, the space-charge core needs to be positively charged, e.g. by an accumulation of oxygen vacancies $\left[V_O^{\bullet\bullet} \right]$. However, the core itself does not necessarily provide enhanced oxygen-diffusion properties either because of a potential clustering of the vacancies (cf. discussion of Fig. 4), which consecutively causes a substantial decrease of the oxygen-vacancy mobility. In addition, fast-ion conduction requires a crystal structure of high symmetry and the grain-boundary core has to be considered as a region of greatly reduced symmetry.
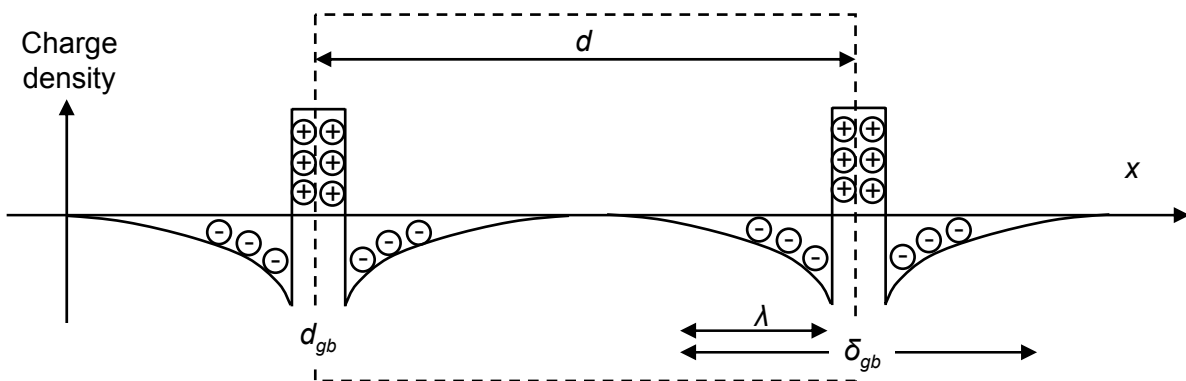
Fig. 70 Schematic representation of two YSZ grain boundaries as studied in this work
Area enclosed by the dotted line is electrically neutral. The grain boundaries were found to be insulating, thus, possibly depleted of oxygen vacancies. Consecutively, the space charge is negative. To preserve electroneutrality, the grain-boundary core needs to be positively charged, e.g. by accumulation of $V_O^{\bullet\bullet}$ at the core. Subsequent clustering of the vacancies entails low charge-carrier mobility and low conductivity.

This model of the space-charge regions (depletion of oxygen vacancies) is supported by the work of Guo et al. [41, 75, 76, 87]. The authors observed an increase of the bulk and grain-boundary conductivity upon exposing the samples in a reduced environment and thereby generating oxygen vacancies [76]. Since grain-boundary conduction increased more than bulk conduction, especially the increase of charge-carrier concentration in the grain-boundary region facilitated improved ionic transport. The authors concluded that the charge-carrier distribution (depletion of oxygen vacancies and accumulation of electrons) in the space-charge layers is responsible for the electrical properties of ZrO_2 grain boundaries.

Hence, the space-charge regions at the grain boundaries of 8YSZ thin films are insulating irrespective of grain size. For a potential application as IT-SOFC electrolytes, the reduction of the mean particle size seems to be counterproductive.

5.2 Nanoscaled $(La_{0.5}Sr_{0.5})CoO_{3-\delta}$ Thin-Film Cathodes

Since stability is a critical issue for the potential application of nanoscaled LSC cathodes and is prerequisite for the interpretation of their transport properties, a separate presentation of the stability regime in terms of microstructure and interface is given in 5.2.1. The transport properties, i.e. the oxygen-reduction mechanism, of the thin-film cathodes are discussed in 5.2.2. The chapter concludes with a comparative review of high-performance SOFC cathodes.

5.2.1 Stability Regime of Nanoscaled LSC Thin-Film Cathodes

For the insight into the cathode polarization mechanism and its potential application as IT-SOFC cathode, the stability of the nanoscaled LSC thin films is of profound interest. Therefore, the morphological and chemical stability of the cathode with special emphasis on the LSC / YSZ interface is discussed.
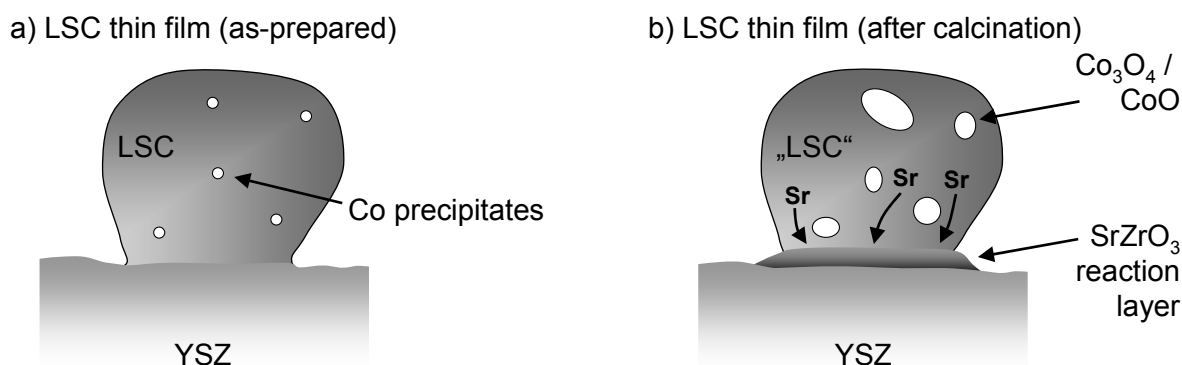
Fig. 71 Model for chemical decomposition of the LSC thin films on YSZ ("design 1")
a) as-prepared LSC thin films exhibit a rhombohedral distortion (cf. XRD analyses, Fig. 48), which suggests an A-site deficiency (Sr) and a B-site surplus entailing potentially small Co precipitates in the range of a few nm (below or near the XRD detection limit, cf. XRD analyses after RTA, Fig. 48a, inset) in the ABO_3 perovskite structure; b) upon annealing (e.g. 700 °C, 8 h) mobile Sr cations diffuse to the interface and chemically react with Zr to $SrZrO_3$ (cf. examinations by XRD (Fig. 48, Fig. 54), SEM (Fig. 55), EFTEM (Fig. 56)). The SZO phase increases A-site deficiency and B-site surplus, respectively, and results in the growth of the Co precipitates as shown by XRD and EFTEM analyses.

The targeted stoichiometry of the $(La_{1-x}Sr_x)CoO_{3-\delta}$ (x = 0.5) thin films was ensured by the thorough analysis of the composition of the coating sols by inductively coupled plasma atomic emission spectroscopy (ICP-AES, chapter 3.1.3). After rapid thermal annealing and accompanying crystallization, the LSC grains in the thin films were found to be single-phase,

though rhombohedrally distorted instead of exhibiting the cubic perovskite structure (LSC / GCO, Fig. 48b). According to Petrov et al. [108] and Mizusaki et al. [109], this rhombohedral distortion is caused by a La / Sr ratio greater than unity (Fig. 15) suggesting a depletion of Sr in the cathode material. Moreover, due to its extremely narrow stability field (0.997 < La / Sr < 1.003) even a slightly depleted Sr concentration on the A-site of the ABO_3 perovskite suggests a surplus of Co ions, thus the precipitation of cobalt oxide, on the B-site (chapter 2.2.2).

From thermogravimetric analysis (TG, Fig. 43, Fig. 44, Fig. 52) and high-temperature X-ray diffraction studies (HT-XRD, Fig. 45) of the LSC precursor powder, the following statements can be derived: During rapid thermal annealing (RTA at 170 °C, 700 °C, 900 °C) constant weight of the crystallized LSC phase is observed from 700 °C. Even during calcination at 850 °C (16 h), the measurements do not indicate any Sr evaporation or the depletion of other chemical elements. According to the ICP-AES results and the targeted stoichiometry prior to crystallization, this suggests that the Sr depletion occurs between 250 °C and 700 °C. This is supported by the HT-XRD data, which shows the precipitation of cobalt oxide (Co_3O_4) at 700 °C < T < 750 °C after calcination for 30 min at each measurement temperature. With regard to the detection limit of the XRD, cobalt oxide precipitates are likely to be present in the powder mixture at even lower temperatures. The lacking of the cobalt phase in the XRD spectrum of the LSC / GCO thin film (Fig. 48b) can be explained by the small size of the cobalt precipitates after calcination of only 5 min (RTA) in comparison to the higher calcination times of the HT-XRD experiments. In summary, although the deposited LSC thin films are apparently single-phase after sol-gel processing, it is highly probable that the thin films are slightly depleted of Sr, which entails the crystallization of cobalt oxide precipitates in the range of a few nanometers (Fig. 71a).

While the XRD spectrum of the LSC / GCO sample ("design 2") is free of secondary phases (with regard to the detection level of the setup, Fig. 48b), the LSC / YSZ sample ("design 1") exhibits distinct signals of secondary phases, especially after calcination at 800 °C (10 h), which are attributed to $SrZrO_3$ (SZO) and Co_3O_4 (Fig. 48a). According to the prior discussion, the detection of cobalt oxide suggests the depletion of Sr on the perovskite A-site. Whereas the HT-XRD analysis of pure LSC precursor powder identifies a small volume percentage of cobalt oxide from 750 °C (Fig. 45), but no increase of the phase until 1050 °C, the HT-XRD study of an LSC precursor / YSZ powder mixture detects an increasing cobalt oxide concentration with raising measuring temperature (Fig. 54). Hence, additionally to the indications for Sr evaporation during processing of the thin films, this increasing Co_3O_4 level suggests the presence of another depletion source: an interface reaction between Sr and Zr (from the YSZ substrate) and the crystallization of $SrZrO_3$. According to the ternary phase diagram of the system La_2O_3-SrO-CoO [163], the formation of SZO results in a shift of the equilibrium towards $CoO/LaCoO_3$ and the formation of Co and La rich secondary phases. At high temperatures ($T \geq 950$ °C), the La surplus also results in a chemical reaction with Zr to $La_2Zr_2O_7$ (Fig. 54). The chemical reaction occurs right at the LSC / YSZ interface as shown

by SEM cross-section analysis (Fig. 55b) after annealing at 800 °C (100 h), where a distinct layer has formed between the LSC thin film and the YSZ substrate. Additional spatial information is obtained by element specific imaging of an LSC / 3.5YSZ interface after annealing at 700 °C (8 h) (Fig. 56a-e): a 42 nm broad reaction layer can be recognized, which is caused by the Sr diffusion to the LSC / YSZ interface and consecutive reaction with Zr. The depletion of Sr occurs in the complete thin film resulting in the precipitation of cobalt oxide grains in the range of tens of nanometers. These observations are consistent with the findings of Sase et al. [162] who detected an increased Sr concentration at the $(La_{0.6}Sr_{0.4})CoO_{3-\delta}$ / (100) YSZ interface by SIMS upon annealing at 700 °C (3800 h). The chemical segregation is even more pronounced for an LSC / 3.5YSZ sample calcined at 1000 °C (8 h) (Fig. 56f-j).

Thermodynamically, the interface reaction between $(La_{0.5}Sr_{0.5})CoO_{3-\delta}$ and ZrO_2 and the crystallization of SZO and Co_3O_4 / CoO is predicted in the whole temperature regime of 500 °C $\leq T \leq$ 750 °C (Fig. 53). However, due to slow kinetics zirconates were formerly considered to precipitate at $T \geq$ 900 °C [156-159, 161, 251] or very long annealing times at T = 700 °C [162]. The microstructural proof of the crystallization of SZO at even lower temperatures and shorter calcination times in case of nanoscaled LSC thin films amends the ongoing discussion of a crucial aspect.

In contrast to thermodynamic calculations, which predict that lanthanum zirconate $(La_2Zr_2O_7)$ secondary phases arise for T > 800 °C (Fig. 53d), neither the results of the XRD analysis (calcination at 800 °C, Fig. 48a) nor the EFTEM studies (calcination at 1000 °C, Fig. 56 f - j) suggest the precipitation of $La_2Zr_2O_7$ in the case of LSC / YSZ diffusion couples. This can be explained by the following: the high activity of Sr in contact with ZrO_2 results in the SZO phase leading to the formation of the SZO structure. Thereby, the band-like SZO structure causes a spatial separation between the La-enriched LSC and the ZrO_2 phase and inhibits the formation of LZO in case of the LSC thin films. In case of a powder mixture, however, the LZO phase can be proved for T > 900 °C (Fig. 54) by HT-XRD measurements consistently to the thermodynamic predictions.

Additionally, a valency change from Co_3O_4 to CoO is determined between 850 °C and 900 °C, which was also observed by Kweon et al. in a sol-gel derived LSC thin film [258]. This switch in the cobalt valency is consistent with the thermodynamic calculations (Fig. 53c) as well.

Besides temperature induced microstructural changes of the LSC, morphological coarsening of the thin films is apparent with increasing annealing temperature (Fig. 49). The evaluation of the average grain size shows that grain growth remains insignificant during annealing at 700 °C (as-prepared thin film: d = 55 nm, after annealing for 2 h: d = 60 nm, 10 h: d = 62 nm, 100 h: d = 60 nm, Fig. 50). Until 800 °C self-limiting grain growth is determined, i.e. the grain coarsening stops at a maximum value (Fig. 51a). For T > 800 °C, the grain growth follows a non-parabolic grain growth law resulting ultimately a destruction of the nanoscale thin-film structure.

The chemical, microstructural and morphological stability of nanoscaled cathode layers with a nominal composition of $(La_{0.5}Sr_{0.5})CoO_{3-\delta}$ on YSZ electrolytes can be summarized as following.

- Cobalt oxide precipitates in the range of a few nanometers are likely to be present in as-prepared thin films due to a Sr deficiency on the A-site of the perovskite (Fig. 71a).

- Sr diffuses to the electrode / electrolyte interface and reacts with Zr to SZO at surprisingly low temperatures (Fig. 71b).

- This leads to an inhomogeneous chemical composition of the cathode layer, where cobalt (II) oxide is formed (Fig. 71b). The CoO formation results from the shift of the composition towards Sr-poor conditions at the boundary between cathode and electrolyte.

- Grain growth is self-limiting for $T \leq 800$ °C (Fig. 72).

a) LSC thin film on YSZ („design 1")   b) LSC thin film on GCO („design 2")
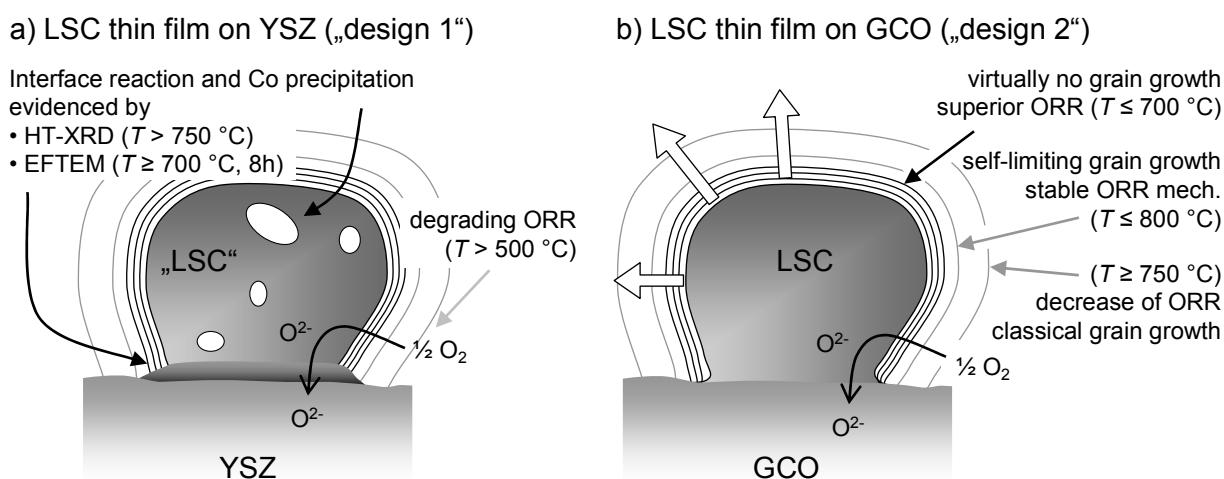
Fig. 72 Stability regime of the LSC thin-film cathodes on a) YSZ and b) GCO
The chemical interface reaction and the precipitation of cobalt oxide in "design 1" can be proved for $T \geq 700$ °C by EFTEM and HT-XRD (Fig. 56, Fig. 54); increasing polarization losses (Fig. 60) suggest a chemical reaction between Sr and Zr for $T \geq 500$ °C; whereas the overall stability of the LSC / YSZ design is governed by the chemical interface reaction, the stability of the LSC / GCO design is controlled by the coarsening of the microstructure, which is self-limiting for $T \leq 800$ °C and classical for $T > 800$ °C entailing an increase of the polarization losses due to a reduction of the active surface as discussed in chapter 5.2.2.

Both the results on the microstructural and morphological stability of the LSC thin films are amended by electrochemical experiments. The area specific polarization resistance ASR_{pol} comprises the oxygen-reduction mechanisms at the cathode and is therefore taken as a benchmark for the catalytic activity of the cathode (chapter 2.2.1). Symmetrical cell measurements were performed not only to obtain the absolute values for the ASR_{pol} but also to determine the relative electrical stability of the cathodes taking advantage of the high sensitivity of the electric testing method in comparison to microstructural investigations.

While a detailed discussion on the polarization losses is given in the next chapter, the stability of the overall ASR_{pol} with respect to operating temperature and time shall be given here. During calcination at 850 °C the ASR_{pol} data of the LSC / YSZ samples („design 1") show a significant increase over time (20 h) (Fig. 59d). Moreover, long-term measurements over 100 h show that this degradation of the polarization resistance is observed above a threshold value of about 500 °C (Fig. 60). The distribution of relaxation times (DRT) of the EIS spectra allocates the increase of the polarization resistance to the charge-transfer process (Fig. 61) at the LSC / YSZ interface (transport step (iv), cf. 5.2.2). Since the previously observed formation of zirconates occurs at the LSC / YSZ interface and since zirconates are known to be poorly oxygen ion conducting [164, 165] and thereby impede the ionic transport across the cathode electrolyte interface, the degradation of the ASR_{pol} can be linked to the precipitation of strontium zirconate at the LSC / YSZ interface. The DRT further portends that the low frequency process (transport step (i), gas phase polarization) is constant during the dwell at 850 °C (○, Fig. 61b) and does not contribute to the increase of the ASR_{pol} for the LSC / YSZ cells ("design 1").

The introduction of a gadolinia-doped ceria (GCO) buffer layer between the nanoscaled LSC thin film and the substrate entails an electrochemical stabilization (cf. Fig. 59c, Fig. 59d, Fig. 60, Fig. 62). Due to its chemical compatibility to LSC (Fig. 57), GCO interferes the interface reaction [14, 21, 169-171] (the chemical compatibility between GCO and the cathode material LSCF was shown by [19, 20, 159, 172]) and successfully averts the precipitation of the $SrZrO_3$. These cells ("design 2") also exhibit a slight increase of the polarization losses after annealing for 100 h at T = 750 °C (plus 26 %, Fig. 60). Given the chemical stability of the LSC / GCO interface, it is shown in the next chapter, that this increase must be attributed to a coarsening of the thin-film microstructure during the EIS measurements (T_{max} = 950 °C) and a diminution of the electrochemically active LSC surface (cf. Fig. 51, where grain growth of the LSC thin films on YSZ was observed for T > 700 °C). The reduction of the surface area upon annealing at 800 °C (4 h) was also held responsible by Beckel et al. [97] for the noted increase of the ASR_{pol} in the case of $(La_{0.6}Sr_{0.4})(Co_{0.2}Fe_{0.8})O_{3-\delta}$ thin films.

The electrical stability of nanoscaled LSC cathode layers on YSZ and GCO substrates can be summarized as following.

- A stable oxygen-reduction reaction at the cathode is observed for $T \leq 500$ °C for LSC / YSZ (Fig. 72a).

- A stable oxygen-reduction reaction at the cathode is observed for $T < 750$ °C for LSC / GCO (Fig. 72b).

These findings limit the scope of applications for the nanoscaled LSC / YSZ system ("design 1") to operation temperatures below 500 °C, which is the targeted temperature regime for micro SOFCs (μ-SOFC) [11]. However, automotive applications like auxiliary power units (APU) demand an operation temperature of 500 °C ≤ T ≤ 750 °C and operation times of more than 1000 h. Due to the shown chemical compatibility between GCO and LSC

and the preserved nanoscaled microstructure (self-limiting grain growth for $T \leq 800 \,°C$), the feasible operation regime thus can be extended to intermediate-temperature SOFC application ($500 \,°C \leq T \leq 750 \,°C$).

5.2.2 Oxygen-Reduction Mechanism in LSC Thin-Film Cathodes

To analyze the polarization phenomena in LSC thin-film cathodes in detail, the following transport steps relevant for the oxygen reduction in MIEC cathodes have to be taken into account (cf. Fig. 13b and discussion in chapter 2.2.1): (i) the diffusion of oxygen molecules in the gas phase (gas diffusion: ASR_{gas}), (ii) the oxygen exchange at the MIEC surface (surface exchange: ASR_{ex}), (iii) the diffusion of oxygen ions through the MIEC to the MIEC / electrolyte interface (bulk diffusion: ASR_d), and (iv) the incorporation of oxygen ions into the electrolyte (charge transfer: ASR_{ct}).
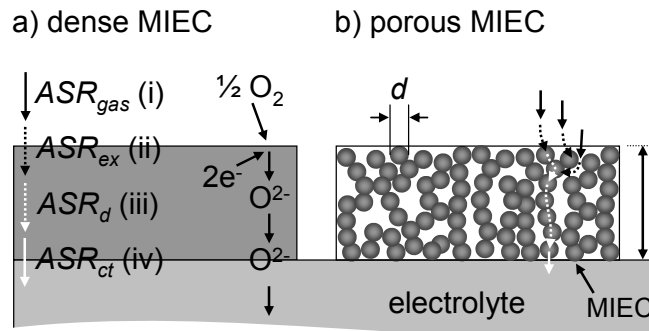
Fig. 73 Model for the appraisement of the ASR_{pol}
showing a) a dense and b) a nanoporous (La$_{0.5}$Sr$_{0.5}$)CoO$_{3-\delta}$ thin-film cathode with the grain size
d and the electrode thickness t.

The effect of gas-phase diffusion limitations (i) is caused by gas diffusion in a stagnant gas layer above the cathode surface and in the pores of the cathode. Due to its time constant it appears as a separate arc in the impedance plot at low frequencies [94] and can easily be separated from the overall polarization losses.

ASR_{ex} and ASR_d values, corresponding to losses at the MIEC surface (ii) and area specific diffusion losses in the bulk (iii) of the nanoscaled LSC thin-film cathode, respectively, can be extracted from the surface-exchange coefficient k_{chem} and the oxygen-diffusion coefficient D_{chem} with the help of literature data (cf. 2.2.3). For a dense (La$_{0.5}$Sr$_{0.5}$)CoO$_{3-\delta}$ cathode (Fig. 73a), these polarization values can be calculated from

$$ASR_{ex,d} = \frac{U_N}{j_{ex,d}}$$

Eq. 50

where U_N is the Nernst voltage, which arises if an oxygen ion flux $j_{Ex,D}$ causes a drop in the chemical potential of the oxygen (for sake of simplicity in the following equations the corresponding oxygen partial pressure will be used). For the oxygen exchange (ii), this drop occurs between the gas phase ($pO_{2,\,gas\,phase}$) and the oxygen potential right below the MIEC

surface ($pO_{2,\text{ MIEC surface}}$). In the case of the bulk diffusion, the pO_2 drop arises between $pO_{2,\text{ MIEC surface}}$ and the oxygen potential above the electrode / electrolyte interface ($pO_{2,\text{ MIEC interface}}$). $U_{N,ex,d}$ (cf. Eq. 4) and $j_{ex,d}$ are given by

$$U_{N,ex} = \frac{RT}{4F} \cdot \ln\left(\frac{pO_{2,\text{ gas phase}}}{pO_{2,\text{ MIEC surface}}}\right)$$

$$U_{N,d} = \frac{RT}{4F} \cdot \ln\left(\frac{pO_{2,\text{ MIEC surface}}}{pO_{2,\text{ MIEC interface}}}\right)$$

Eq. 51

and [91]

$$j_{ex} = k_{chem} \cdot \left(c_{\text{gas phase}} - c_{\text{MIEC surface}}\right)$$

$$j_d = D_{chem} \cdot \frac{c_{\text{MIEC surface}} - c_{\text{MIEC interface}}}{t}$$

Eq. 52

where R is the ideal gas constant (8.314 J/mol/K), T the temperature (923.15 K), F Faraday's constant (96,487 C/mol), k_{chem} and D_{chem} the oxygen-exchange and oxygen-diffusion coefficients in $(La_{0.5}Sr_{0.5})CoO_{3-\delta}$ at 650 °C and pO_2 = 0.3 atm (k_{chem} = 4.0 · 10^{-6} m/s and D_{chem} = 1.4 · 10^{-10} m²/s [147]) and t the cathode thickness (300 nm). The concentrations of oxygen ions (c) in $(La_{0.5}Sr_{0.5})CoO_{3-\delta}$ with respect to pO_2 are obtained from [119] accounting for the stoichiometry of the LSC cathode. For a dense, 300 nm thick LSC thin-film cathode at T = 650 °C, the area specific resistance caused by oxygen exchange is calculated to ASR_{ex} = 784.45 mΩ·cm², whereas the losses caused by oxygen diffusion in the thin film are determined to ASR_d = 6.72 mΩ·cm². Hence, the oxygen-reduction reaction in a dense cathode is dominated by the surface-exchange polarization. This finding is supported by Prestat et al. [178] who investigated the oxygen reduction of dense LSCF thin films. They expected that the influence of oxygen-vacancy diffusion is almost independent of the film thickness at 700 °C, meaning that the bulk diffusion is negligible in this temperature regime.

The incorporation of oxygen ions into the electrolyte (iv) has been studied by isotope-exchange measurements where virtually no resistance for $^{18}O^{2-}$ / $^{16}O^{2-}$ exchange across the LSC / Ca-doped ceria interface was found [150]. Furthermore, Prestat et al. [178] found the charge-transfer resistance between a dense LSCF thin film and a GCO substrate negligible. However, in the case of LSC on YSZ a solid-state reaction results in an increase of the interfacial resistance as discussed above.

This is consistent with the findings of Yang et al. [259] and Baumann et al. [155] who stated that the electrochemical resistance of dense $(La_{0.5}Sr_{0.5})CoO_{3-\delta}$ thin films (thickness 250 nm ≤ t ≤ 500 nm) and $(La_{0.6}Sr_{0.4})(Co_{0.8}Fe_{0.2})O_{3-\delta}$ microelectrodes (thickness t = 100 nm) are dominated by the oxygen-exchange reaction at the gas / electrode interface, respectively.

However, as shown in the SEM micrographs (Fig. 58) the presented LSC thin-film cathodes are not dense as assumed for the calculation above, but they contain a distinct nanoporosity. This yields an increase of the active surface area, entailing smaller values of ASR_{ex} (cf. discussion in chapter 2.2.1). Moreover, the reduced effective diffusion path leads to smaller ASR_d values, which may even be further decreased by grain-boundary effects [23-25].

For a porous MIEC-cathode, the utilization region l_δ, over which the reduction reaction occurs, can be appraised by Eq. 35. In the case of a nanoporous $(La_{0.5}Sr_{0.5})CoO_{3-\delta}$ thin-film cathode with an average grain size of 50 nm, a value of l_δ = 1323 nm can be derived from Adler's equation at 650 °C. Therefore, it can safely be assumed that the entire volume of an LSC cathode with a maximum thickness of t = 300 nm, as depicted in Fig. 58, is electrochemically active.

Hence,

- The polarization impedance of a $(La_{0.5}Sr_{0.5})CoO_{3-\delta}$ thin-film cathode is governed by the oxygen-exchange process (ii). The ASR_{ex} is the rate-determining step for the oxygen-reduction reaction. Other transport steps (ASR_d, ASR_{ct}) are negligible.

- According to Adler's model, the polarization of the cathode is low for a high inner surface area and a large thickness of the cathode.

- The thin-film cathodes ($t \leq$ 300 nm) are completely utilized for the ORR.

For MIEC thin films with $l_\delta \geq t$, Adler [94, 148] [8], derived expression Eq. 53 [9] for the non-charge-transfer processes ASR_{chem}

$$ASR_{chem} = \frac{RT}{4F^2} \cdot \frac{1}{a \cdot t \cdot r_0 \cdot (\alpha_f + \alpha_b)} \qquad \text{Eq. 53}$$

where a is the active surface area and α_f and α_b are kinetic parameters of order unity. The value of $r_0 \cdot (\alpha_f + \alpha_b)$ equals $k_{tr} \cdot c_O$ with c_O as the concentration of lattice sites in LSC [119]. The relevant parameters in Eq. 53 are the thin-film thickness t and the internal surface area a, which is completely utilized for O_2 reduction.

For an entirely dense, 300 nm thick LSC thin-film cathode the active surface area is 3.3 µm^{-1} and equation Eq. 53 results in chemical losses of ASR_{chem} = 719.49 mΩ·cm², which is in good agreement with the calculated value of ASR_{pol} = 791.17 mΩ·cm² (ASR_{ex} = 784.45 mΩ·cm² plus ASR_d = 6.72 mΩ·cm²) according to equation Eq. 50.

The observed cathode polarization losses for nanoscaled LSC thin films on YSZ ("design 1", 85 mΩ·cm² at 649 °C) and on GCO substrates ("design 2", 81 mΩ·cm² at 643 °C) fall significantly short of the estimated polarization losses for a completely dense, 300 nm thick LSC thin-film cathode. The Adler model can account for these experimentally obtained values if the electrochemically active surface is increased by a factor of 8 compared to the completely dense LSC thin-film cathode. According to these results, the nanoscaled LSC

---

[8] Adler's model implies several assumptions, e.g. the mixed conductor is treated as a moderately dilute solid solution, complex particle geometries like sintering necks are not considered; moreover, the sample geometry is taken to be macrohomogeneous. Yang and co-workers [259] observed a deviation of four between surface-exchange coefficients derived from Adler's 1D model and their impedance analyses of a dense, 500 nm thick $(La_{0.5}Sr_{0.5})CoO_{3-\delta}$ electrode.

[9] The prefactor of Eq. 53, given in Ref. [148] and Ref. [94], deviates by a factor of two.

thin-film cathodes exhibit an effective surface area of 27 µm^{-1} due to the nanoporosity of the thin films.

Taking advantage of a broad scope of different thin-film morphologies (Fig. 64, Fig. 65) experimental proof of the validity of Adler's model is given for T = 600 °C. Whereas the polarization losses ASR_{pol} are obtained within a maximal error of 29.3% (chapter 3.3.2), the geometry parameters were evaluated from the SEM images within an estimated error of 25% for the grain size, 10% for the film thickness and 10% for the porosity of the films. By application of a 3-dim finite element model developed by Rüger, IWE, the inner surface area a was modeled from these parameters[10]. Fig. 74 depicts the ASR_{pol} over 1 / ($a \cdot t$) for a variety of different thin-film morphologies. The data (A) to (F) coincide with the general dependency of Adler's 1-dim model within the error bars. For high values of 1 / ($a \cdot t$) the deviations from the model increase, which can partly be attributed to microcracks (cf. Fig. 65G, inset), which lead to an overestimation of the inner surface area and thereby to lower 1 / ($a \cdot t$) values.
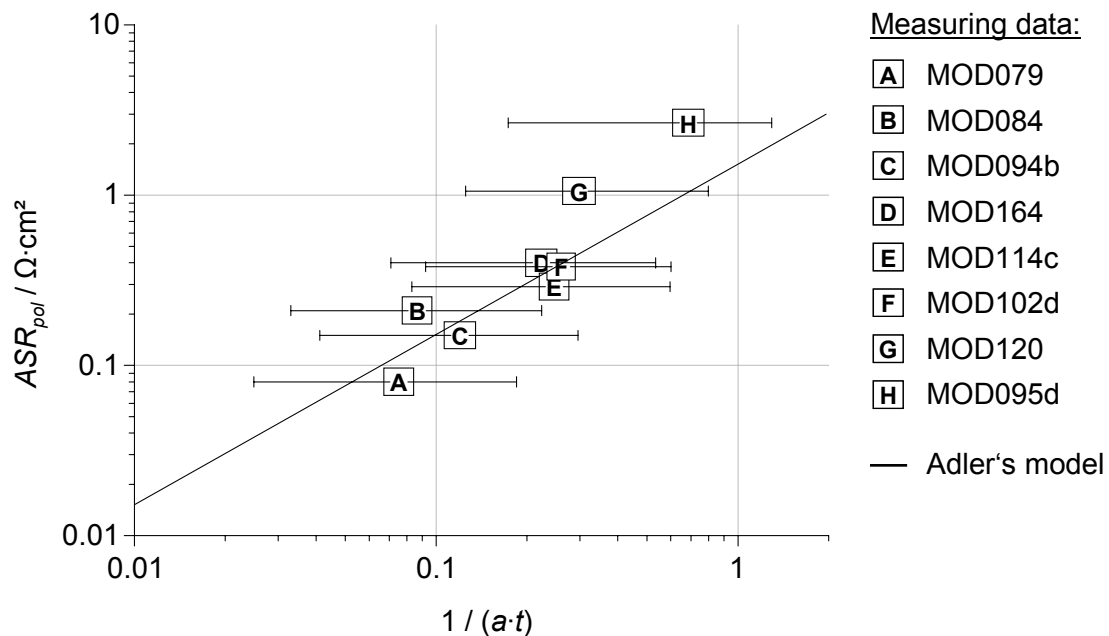
Fig. 74 Application of Adler's model to the properties of the LSC thin-film cathodes
Polarization resistance ASR_{pol} at T = 600 °C over inverse inner surface area a times film thickness t in comparison with Adler's model; the error bars comprise for uncertainties in determination of geometry properties (t, particle size d, porosity ε).

Herefrom, the following conclusion can be drawn:

• Adler's model is confirmed experimentally for nanoscaled LSC thin film cathodes.

• The cathode polarization decreases with increasing thickness of the electrode.

---

[10] The model comprises of 10 x 10 x 20 cubes with the dimension of the particle size. The pores are assumed to be in the same order of magnitude as the grains. The effects of percolations are included.

- ORR efficiency increases with the inner surface area, which mainly depends on the porosity of the films and the grain size.

- These results suggest further studies on the oxygen reduction in MIEC thin-film cathodes on the field of microstructure optimization. The microstructural properties of nanoscaled LSC thin-film cathodes regarding cathode thickness and inner surface area are currently optimized by Rüger and Hayd (both IWE), who respectively model the transport properties by a finite-element method and experimentally validate the results in an ongoing work.

Nanoscaled MIEC cathode (LSC)
- ■ this work: E_A = 1.07 eV

LSCF thin-film cathodes
- "low porosity", processed by PLD
  - ▷ Beckel et al.: E_A = 1.40 eV
  - ● Prestat et al.: E_A = 1.79 eV
- "medium porosity", processed by Spray pyrolysis
  - ▽ Beckel et al.: E_A = 1.47 eV
- "high porosity", processed by Spray pyrolysis and pore former
  - △ Beckel et al.: E_A = 1.27 eV
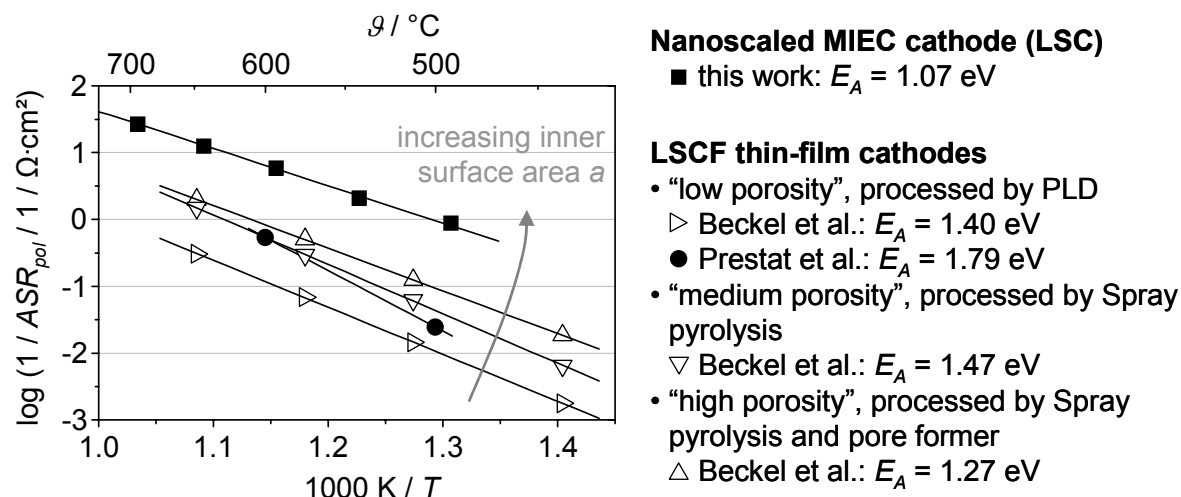
Fig. 75 Polarization losses of selected model electrodes
Literature data of electrode conductivities 1 / ASR_{pol} of LSCF thin-film electrodes with different microstructures among 700 °C ≥ T ≥ 450 °C: LSCF thin-film cathodes evaluated by Beckel et al. [97] and Prestat et al. [178] put opposite to 1 / ASR_{pol} obtained for a nm-scaled thin-film LSC combined with µm-scaled LSCF as current collector (■, "design 2"), as reported in this work.

By comparison of the electrode conductivity (inverse ASR_{pol}) of the nanoporous LSC thin-film cathodes (■) with dense LSCF thin films investigated by Prestat et al. (●) [178], the exceptional importance of the inner surface area becomes apparent (Fig. 75). Since the analyzed thin films exhibit similar film thicknesses (200 nm < t_{LSC} < 300 nm vs. t_{LSCF} = 330 nm), the higher electrode conductivity can be attributed to the nanoporosity of the LSC thin films investigated in this work. For LSCF thin-film electrodes, the determination of the role of the inner surface area results in the same general trend: with increasing nanoporosity, i.e. increasing inner active surface area, cathode oxygen reduction is facilitated. However, due to its beneficial geometrical properties and its good oxygen reduction and oxygen-diffusion properties, the electrode conductivity (1 / ASR_{pol}) of the nanoscaled LSC thin-film cathode (■) excels the performance of the porous LSCF thin film (Δ).

At 600 °C the LSC / GCO cell concept ("design 2", Fig. 58b) exhibits notably high cathode performance (ASR_{pol} = 130 mΩ·cm² at T_{cell} = 592 °C, Fig. 59c). Its dependency on measuring temperature is depicted in Fig. 63 left (■, "design 2"). The logarithmic electrode conductivity

(inverse total ASR_{pol}) of the LSC / GCO cell shows an Arrhenius-type behavior for 500 °C < T < 650 °C. However, for 650 °C < T < 850 °C the curve deviates from the Arrhenius behavior, which can be explained by a detailed analysis of the impedance spectra. Fig. 63 (right plots) shows the spectra at 650 °C (A) and 850 °C (B). The spectra consist of two major processes (II, III). The high-frequency process (f_0 = 1.3 kHz and f_0 = 17 kHz, respectively) shows an Arrhenius-type temperature dependency (II, left plot: ●) with an activation energy of E_A = 1.07 eV and is attributed to the oxygen-reduction processes. Yang and co-workers [259] analyzed a dense $(La_{0.5}Sr_{0.5})CoO_{3-\delta}$ thin film and obtained an activation energy of E_A = 1.1 eV for the oxygen surface exchange, which gives further evidence that the overall ASR_{pol} of the studied nanoscaled LSC thin-film cathodes is dominated by the oxygen surface exchange (ii). The low-frequency process in Fig. 63, right plots (f_0 = 1.7 Hz and f_0 = 1.7 Hz, respectively) shows a minor temperature dependency for 650 °C < T < 850 °C (III, left plot: ○) and can be attributed to the gas-phase polarization (i) [224, 260].
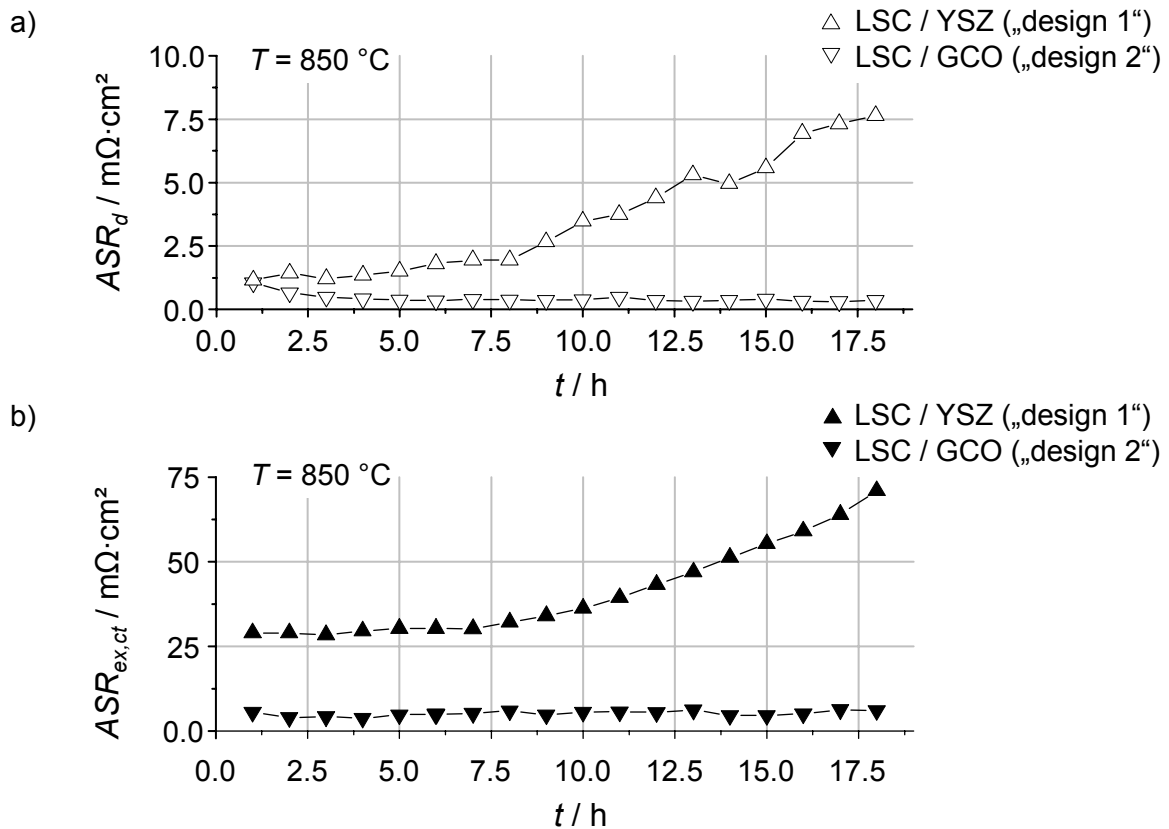
Fig. 76 a) ASR_d and b) ASR_{ex} of LSC / YSZ ("design 1") and LSC / GCO ("design 2")
All data were obtained by fitting of the respective DRT data ("design 2": Fig. 61a, "design 2": Fig. 62a). The general trends are constant values for "design 2" and increasing losses for "design 1".

Based on the previous discussion on the stability of the LSC cathode on YSZ ("design 1") and GCO ("design 2"), further understanding of the electrochemistry of the nanoscaled LSC thin films can be derived from the DRT analyses of the samples ("design 1": Fig. 61a and "design 2": Fig. 62a). Additionally to the already identified gas-phase polarization (ASR_{gas})

two distinct processes at approximately 10^2 Hz and 10^4 Hz, respectively, evolve from the spectra. Assuming an effective diffusion length of 100 nm in the porous thin films, the area specific diffusion losses can be calculated to $ASR_{d,cal}$ = 0.47 mΩ·cm² at 850 °C corresponding to the low-frequency process of the LSC / GCO sample (measured value $ASR_{d,meas}$ = 0.4 mΩ·cm²). Thus, the low-frequency process at 10^2 Hz can be attributed to the oxygen diffusion process (Fig. 76a). It is noteworthy, that the values of ASR_d decrease slightly within the first 3 h (∇, Fig. 76a), which corresponds to the coarsening of the microstructure and a minor reduction of the effective diffusion length. This coarsening is consistent with the observed grain-growth behavior (relaxation time for self-limiting grain growth τ = 4.3 h at 800 °C, Fig. 51a). In case of the LSC / YSZ sample ($\triangle$, Fig. 76a), the initial value at t = 0 h coincides with the LSC / GCO data. With increasing time, however, an increase of ASR_d is observed. As discussed in chapter 5.2.1, the chemical interface reaction between LSC and YSZ entails the precipitation of $SrZrO_3$ and the depletion of Sr from $(La_{1-x}Sr_x)CoO_{3-\delta}$, which involves a decrease in ionic conduction (cf. Fig. 18). The observed increase of ASR_d in Fig. 76a ("design 1", factor 6.6) corresponds to depletion of Sr from x = 0.5 to x ≈ 0.35.

The high-frequency process (10^4 Hz) dominates the overall ASR_{pol} and is therefore – accordingly to the previous findings – attributed to the oxygen surface exchange (ASR_{ex}) in case of LSC / GCO and a combination of ASR_{ex} and charge-transfer polarization (ASR_{ct}) in case of LSC / YSZ. Whereas the values of ASR_{ex} of the LSC / GCO sample ($\blacktriangledown$, Fig. 76b) are constant over the calcination at 850 °C, the polarization losses of the LSC / YSZ cell increase ($\blacktriangle$, Fig. 76b). This can be explained by a depletion of Sr entailing a reduction of the oxygen exchange properties and the crystallization of the insulating $SrZrO_3$ phase inhibiting charge transfer between cathode and electrolyte.

The superior performance of the nanoscaled thin-film cathodes becomes evident by reviewing the literature on high-performance SOFC cathodes: Fig. 77 depicts a comparison of the cathode conductivity ($1/ASR_{pol}$) of the nanoscaled LSC thin-film cathode ("design 2") with literature data of other cathode concepts. Most developments strive to enhance oxygen exchange and bulk-diffusion properties by employing mixed ionic-electronic conductors as a thick film (30 μm $< t <$ 100 μm). Examples given here are a mixed ionic-electronic $(La_{0.6}Sr_{0.4})(Co_{0.2}Fe_{0.8})O_{3-\delta}$ cathode on $(Ce_{0.9}Gd_{0.1})O_{2-\delta}$ ($\square$, E_A = 1.38 eV [261]), a $(La_{0.58}Sr_{0.4})(Co_{0.2}Fe_{0.8})O_{3-\delta}$ cathode on $(Ce_{0.8}Gd_{0.2})O_{2-\delta}$ ($\triangle$, E_A = 1.39 eV [262]), a composite cathode consisting of $(La_{0.6}Sr_{0.4})(Co_{0.2}Fe_{0.8})O_{3-\delta}$ and GCO ($\circ$, E_A = 0.59 eV [263]) and a cathode with differently conducting phases ranging from purely ionic (YSZ) over electronic $((La_{0.85}Sr_{0.15})Mn_{1.1}O_{3-\delta})$ to mixed $((La_{0.84}Sr_{0.16})CoO_{3-\delta})$ conduction (∇, E_A = 1.01 eV [264]). All referred cathodes are applied as thick-film cathodes, which require the thermal expansion coefficient of the cathode material to be adjusted to the *TEC* of the electrolyte. The nanoscaled thin-film cathode of this work, however, outflanks this limitation and enables the application of $(La_{0.5}Sr_{0.5})CoO_{3-\delta}$ with its excellent oxygen exchange and chemical diffusion

properties. The target value of 200 mΩ·cm² of the European project SOFC600 [11] (☆, Fig. 77) is undercut by the electrode conductivity of the nanoscaled LSC thin-film cathode presented in this work. These unique results demonstrate that a nanoscaled $(La_{0.5}Sr_{0.5})CoO_{3-\delta}$ thin-film cathode features notably low polarization losses, which is compulsory for the development of IT-SOFCs for 500 °C $\leq T \leq$ 750 °C. Besides LSC / GCO ("design 2") the material combination LSC / YSZ ("design 1") is also considered promising for µ-SOFC applications (e.g. project "OneBat" [11, 97]) where the maximal temperature is limited to T = 500 °C.
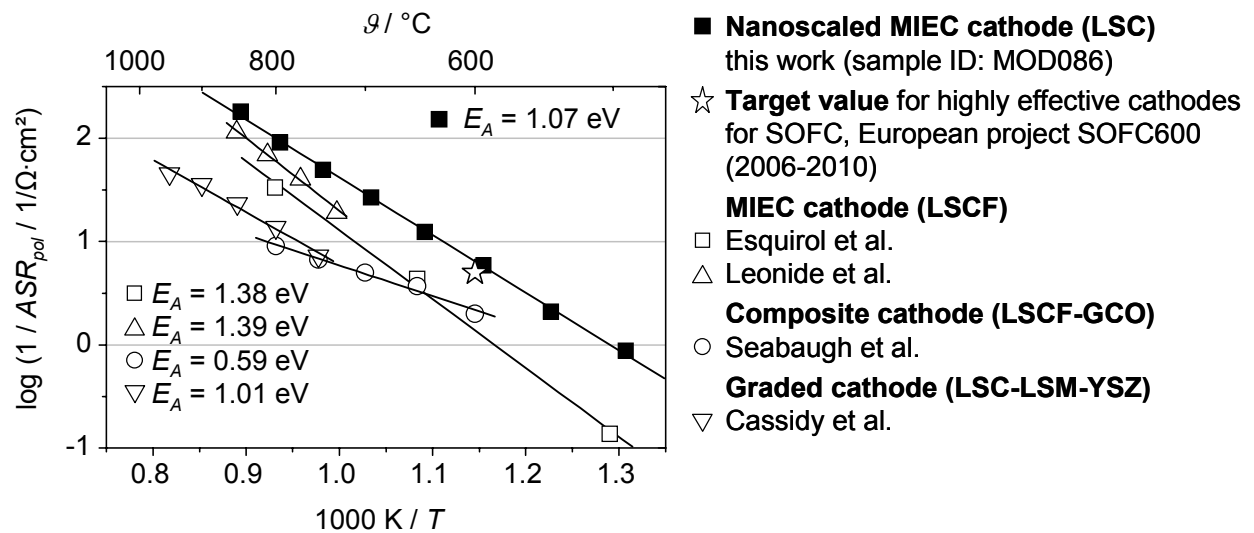
Fig. 77 Comparison of cathode polarization performance

Literature data of electrode conductivities 1/ASR_{pol} and activation energies E_A reported for considerably different concepts based on MIEC cathode structures among 1000 °C $\geq T \geq$ 500 °C: a) µm-scaled single layer LSCF cathodes evaluated by Esquirol et al. [261], Leonide et al. [262]; b) µm-scaled composite layer LSCF + GCO (Gd-doped ceria) studied by Seabaugh et al. [263], µm-scaled functional gradient layers LSC-LSM + YSZ studied by Cassidy et al. [264] put opposite to 1/ASR_{pol} and E_A obtained for a nm-scaled thin-film LSC combined with µm-scaled LSCF as current collector (■, "design 2"), as reported in this work. Except for [262] the reported values were obtained from EIS measurements on symmetrical cells.

---

[11] EUROPEAN COMMISSION, 6th Framework Programme on Research, Technological Development and Demonstration, FP6-2004-Energy-3, project acronym "SOFC600", contract number 020089

6 Summary

Subject matter of the present work is to elucidate the advantages of nanoscaled thin films for solid oxide fuel cells (SOFC). At the nanoscale, the increased grain-boundary density may lead to grain-size effects, which potentially facilitate substantially enhanced electrical conductivity. Enhanced charge-transport properties in turn reduce the ohmic losses in the electrolyte and the polarization of the electrodes. Both effects yield an increased efficiency of SOFCs, especially in the intermediate-temperature regime at 500 °C $\leq T \leq$ 750 °C.

This work systematically comprises fundamental experimental studies concerning grain-size effects in nanoscaled electrolyte and cathode thin films. For the experiments on the electrolyte-site, 8.3 mol% yttria-doped zirconia (YSZ) was studied – a material employed in state-of-the-art SOFC systems. On the cathode-site, $(La_{0.5}Sr_{0.5})CoO_{3-\delta}$ (LSC) was chosen. LSC exhibits excellent oxygen-reduction properties and can therefore be regarded as a model substance for the technologically interesting class of mixed conducting perovskite (ABO_3)-type oxides. For the processing of the thin films, a sol-gel technique was employed, which is eligible to be up-scaled with respect to industrial application.

Nanoscaled electrolyte thin films

Charge transport in YSZ takes place by means of a hopping mechanism of oxygen ions via vacant lattice sites. Goal of the conducted experiments was to clarify if grain boundaries in nanostructured materials possess high densities of oxygen vacancies and / or enhanced mobilities of the oxygen ions facilitating an increase of the ionic conductivity. Thereto, nano- and microcrystalline YSZ thin films were prepared by the sol-gel method on insulating sapphire substrates. The YSZ films are homogeneous, crack-free, about 300 nm thick and exhibit an excellent adhesion to the substrate. Subsequent temperature treatment between 650 °C and 1400 °C (24 h respectively) leads to a variation of the mean grain size d between 5 nm and 782 nm. The purity and crystallinity of the grain boundaries was evidenced by means of electron microscopy. The thin films are single-phase cubic with tetragonal YSZ precipitates in the range of a few nanometers. These precipitates are homogeneously distributed in the grains and the grain boundaries and can therefore be neglected for the analyses of the transport properties.

The electrical conductivity of the YSZ thin films was studied at 200 °C $\leq T \leq$ 400 °C in air. Whereas the electrical conduction data of the thin films with submicron-sized grains coincides well with the data of polycrystalline YSZ electrolytes, the electrical resistivity increases with increasing grain-boundary density at the nanoscale. By means of electrical impedance spectroscopy, this increase can be attributed to the grain boundaries. The specific grain and grain-boundary conductivities can be derived by application of the brick-layer model for 232 nm $\leq d \leq$ 782 nm. The specific conductivity represents the charge

transport of a single grain or a single grain boundary with an electrical grain-boundary thickness of 5.37 nm. Both conductivities show Arrhenius-type temperature dependency. The specific grain-boundary conductivity (E_A = 1.15 eV) ranges approximately two decades below the specific bulk conductivity (E_A = 1.09 eV). The application of the brick-layer model for $d \leq 36$ nm shows that the ionic charge transport at the nanoscale does not principally differ from the transport in polycrystalline YSZ. Instead, the grain boundaries act independently of the grain size as a potential barrier and impede the transport of oxygen ions through the lattice. Due to the high density of grain boundaries at the nanoscale, the nanoscaled YSZ thin films hold an exceptionally high total resistance.

Compared to state-of-the-art polycrystalline YSZ electrolytes, nanoscaled YSZ thin films therefore do not yield a decrease of the ohmic losses and do not contribute to an increase of SOFC efficiency. This work evidences that nanoscaled YSZ thin film do not offer beneficial grain-size effects, which increase oxygen-ion transport.

<u>Nanoscaled Cathode Thin Films</u>

To investigate the effect of microstructure on the oxygen-reduction mechanism of mixed ionic-electronic (MIEC) thin-film cathodes, a sol-gel processing technique was applied to deposit nanocrystalline $(La_{1-x}Sr_x)CoO_{3-\delta}$ (x = 0.5) thin films on YSZ electrolytes and gadolinia-doped ceria (GCO) surfaces. The crystallization of the LSC perovskite phase was studied by thermal analyses and X-ray diffraction, from which the calcination temperatures were derived: 170 °C, 700° C and 900 °C (5 min respectively). The thin films are crack-free and homogeneous and exhibit excellent adhesion to the respective substrates.

Instead of a pure cubic phase, a rhombohedral distortion was evidenced by X-ray diffraction. This indicates a slight Sr deficiency and entails Co precipitations in the range of a few nanometers because of the depletion on the A-site of the ABO_3 crystal. Due to their small size, these secondary phases do not affect the functionality of the cathode. However, an interface reaction between the LSC thin film and the YSZ substrate leads to the precipitation of zirconates, which cause a massive deterioration of the chemical LSC phase. This interface reaction is predicted by thermodynamic simulations for the whole investigated temperature regime of 500 °C $\leq T \leq$ 850 °C – yet the kinetics of this reaction are unknown. The formation of zirconates at the LSC / YSZ interface has been reported for $T \geq$ 900 °C and long annealing times in literature. This work evidences the precipitation of strontium zirconate (SZO) microstructurally already at 700 °C. Electrical measurements prove the insulating SZO phase between the nanoscaled LSC cathode and the YSZ electrolyte for $T >$ 500 °C after 100 h annealing. The LSC / GCO interface, however, is free of secondary phases until at least T_{min} = 1200 °C. The microstructure of the nanoscaled cathodes changes with temperature: until 800 °C, the grain growth is self-limiting, i.e. the grain size approaches a final value (d = 83 nm). For higher annealing temperatures, the grain growth shows a non-parabolic behavior resulting in microstructurally instable LSC thin films.

The polarization losses evolving from the oxygen reduction at the cathode are exceptionally low for nanoscaled, mixed conducting LSC cathodes. In symmetrical cell measurements at 600 °C the polarization resistances are determined to 146 mΩ·cm² (LSC / YSZ) and 130 mΩ·cm² (LSC / GCO). These polarization resistances are lower than any values reported for concepts based on MIEC cathode structures in the literature and demonstrate the superior electrochemical activity during oxygen reduction. Due to their different stability regimes (LSC / YSZ: $T \leq 500$ °C, LSC / GCO: $T \leq 700$ °C), different scopes of high-performance operation come into consideration. Micro SOFCs (μ-SOFC), which are developed as battery replacement for laptops, restrict themselves to a temperature of approximately 500 °C; therefore, here the LSC / YSZ design is promising. At higher operation temperatures, the LSC / GCO system is auspicious for application in automotive auxiliary power units (APUs).

The excellent properties of nanoscaled LSC thin-film cathodes regarding oxygen reduction rely on the MIEC material properties and on the high surface area of the cathodes. The surface-exchange reaction at the cathode surface is the rate-determining step during the oxygen-reduction reaction. The oxygen diffusion in the bulk and the charge transfer from the cathode into the electrolyte can be neglected in case of nanoscaled LSC cathodes. The model of Adler, which describes the polarization during oxygen reduction at the cathode, is validated by a comparison of the electrical data of different specimens with a nanoscaled microstructure. The model predicts an increase of the surface by a factor of eigth, as compared to a dense cathode structure. These results suggest a systematic optimization of the cathode microstructure, where particularly an increase of the film thickness will entail further enhancement of the performance of nanoscaled LSC cathodes.

The results of this work and their discussion show that grain-size effects in nanoscaled YSZ thin films increase the total resistance instead of lowering it. Rather large mean grain sizes should be aimed to minimize ohmic losses in the SOFC electrolyte. On the cathode-site, however, nanoscaled and nanoporous LSC thin films exhibit excellent oxygen-reduction properties. Prevailing benchmarks for the electrochemical efficiency of MIEC cathodes are outclassed. The high surface area of the nanoscaled cathodes decreases the polarization losses decisively. The perceptions on the microstructural, chemical and electrical stability of nanoscaled LSC thin-film cathodes and the insights into the electrochemical processes of the cathode lay the foundation for the application of nanoscaled, mixed ionic-electronic conducting cathodes in the field of mobile SOFCs.

7 Appendix

7.1 List of Samples

The following tables (Table 6 - Table 9) summarize the experiments conducted within this work. The first column „IWE-ID" contains the continuous number for each individual sample, mostly processed by the ISC („ISC-ID", 2nd column). Unless denoted otherwise 8YSZ or LSC thin films (3rd column) were deposited by spin- or dip-coating or tampon-printing (4th column) on YSZ or sapphire substrates (5th column). The next three columns account for the temperature treatment of the samples including rapid thermal annealing (6th column) and an additional annealing at T_{dwell} (7th column) and t_{dwell} (8th column). The remaining columns account for the measuring objective and the conducted experiments. The last column („remarks") states the cooperation, in which the experimental results were obtained, including 1: M. Bockmeyer, R. Krüger (ISC), 2: L. Dieterle, B. Butz (LEM), 3: B. Szöke (diploma thesis, IWE), 4: J. Joos (study project, IWE), 5: H. Götz (study project, IWE), 6: I. Netsch (study project, IWE), 7: U. Peters (study project, IWE), 8: Th. Knapp (study project, IWE).

Table 6 Overview about performed experiments

IWE-ID	ISC-ID	Thin film	Deposition technique	Substrate	RTA / °C	T_{dwell} / °C	t_{dwell} / h	Measuring objective	TA	SEM	(HR)TEM	AFM	(HT)XRD	EIS	Measuring ID	other exp.	Remarks
MOD001 - 002 (2 samples)		LSM	spin	YSZ	170 / 700	-	-	Deposition tests	√					√	Ab154 Ab155		
MOD003 - 006 (4 samples)		8YSZ	-	Si	500	550 - 1150	-	Thin film development	√							√	1
MOD007 - 022 (16 samples)		8YSZ	dip	Si	500	500 - 1250	1	Grain growth analysis	√			√				√	1
MOD023	13	LSC50	spin	3YSZ	170 / 700 / 900	700	8			√	√						2
MOD024	14	LSC50	spin	3YSZ	170 / 700 / 900	800	8			√							2
MOD025	15	LSC50	spin	3YSZ	170 / 700 / 900	900	8			√							2
MOD026	16	LSC50	spin	3YSZ	170 / 700 / 900	1000	8			√	√						2
MOD027	17	LSC50	spin	3YSZ	170 / 700 / 900	700	8			√							2
MOD028	18	LSC50	spin	3YSZ	170 / 700 / 900	800	8	Analyses of LSC micro-structure, grain growth and LSC / YSZ interface		√							2
MOD029	19	LSC50	spin	3YSZ	170 / 700 / 900	900	8			√							2
MOD030	20	LSC50	spin	3YSZ	170 / 700 / 900	1000	8			√							2
MOD031	21	LSC50	spin	3YSZ	170 / 700 / 900	700	8			√							2
MOD032	22	LSC50	spin	3YSZ	170 / 700 / 900	800	8			√							2
MOD033	23	LSC50	spin	3YSZ	170 / 700 / 900	900	8			√							2
MOD034	24	LSC50	spin	3YSZ	170 / 700 / 900	1000	8			√							2
MOD035	25	LSC50	spin	3YSZ	170 / 700 / 900	700	8			√							2
MOD036	26	LSC50	spin	3YSZ	170 / 700 / 900	800	8			√							2
MOD037	27	LSC50	spin	3YSZ	170 / 700 / 900	900	8			√							2
MOD038	28	LSC50	spin	3YSZ	170 / 700 / 900	1000	8			√							2
MOD039 - 044 (6 samples)		8YSZ	dip	sapphire	500	500 - 1700	24	Thin film development	√		√			√	"IWE-ID" + T		3
MOD045 - 054 (10 samples)		LSC50	spin	sapphire	170 / 700 / 900	900 - 1300	8	Deposition tests	√								
MOD055	-	8YSZ	dip	sapphire	500	500	24			√		√	√	√	ID + T		
MOD056	-	8YSZ	dip	sapphire	500	650	24			√	√	√	√	√	ID + T		
MOD057	-	8YSZ	dip	sapphire	500	850	24	Electrical conduction as a function of grain size; grain growth; micro-structure		√	√	√	√	√	ID + T		2 3 4
MOD058	-	8YSZ	dip	sapphire	500	1000	24			√	√	√	√	√	ID + T		
MOD059	-	8YSZ	dip	sapphire	500	1250	24			√	√	√	√	√	ID + T		
MOD060	-	8YSZ	dip	sapphire	500	1350	24			√	√	√	√	√	ID + T		
MOD061	-	8YSZ	dip	sapphire	500	1400	24			√		√	√	√	ID + T		
MOD062	-	8YSZ	dip	sapphire	500	1700	24			√	√						
MOD063 - 066 (4 samples)		8YSZ	dip	8YSZ	500	500 - 1000	24	Reprodu-cibility	√								
MOD067	-	LSC50	spin	3YSZ	170 / 700 / 900	-	-							√	IS2.046		
MOD068	-	LSC50	spin	3YSZ	170 / 700 / 900	-	-	Thin film development						√	IS2.045		
MOD069	-	LSC50	tampon	3YSZ	170 / 700 / 900	-	-							√	IS2.020		
MOD070 - 73 (4 samples)		-	-	GCO / YSZ		-	-	ASR_{Pol}						√	IS2.055 - IS2.057		
MOD074	164	LSC50	spin	8YSZ	170 / 700 / 900	-	-										
MOD075a	165	LSC50	spin	8YSZ	170 / 700 / 900	-	-							√	IS2.069		
MOD075b	165	LSC50	spin	8YSZ	170 / 700 / 900	-	-							√	IS2.072		
MOD076a	166	LSC50	spin	8YSZ	170 / 700 / 900	-	-							√	IS2.078		
MOD076b	166	LSC50	spin	8YSZ	170 / 700 / 900	-	-			√							
MOD077	167	LSC50	spin	8YSZ	170 / 700 / 900	-	-										
MOD078	168	LSC50	spin	8YSZ	170 / 700 / 900	-	-										
MOD079a	169	LSC50	spin	8YSZ	170 / 700 / 900	-	-			√				√	IS2.066		
MOD079b	169	LSC50	spin	8YSZ	170 / 700 / 900	-	-							√	IS2.077		
MOD079c1	169	LSC50	spin	8YSZ	170 / 700 / 900	700	8	Dependency of polarization losses from thin film morphology		√							
MOD079c2	169	LSC50	spin	8YSZ	170 / 700 / 900	800	8			√							
MOD079c3	169	LSC50	spin	8YSZ	170 / 700 / 900	900	8			√							
MOD079c4	169	LSC50	spin	8YSZ	170 / 700 / 900	1000	8			√							
MOD080	170	LSC50	spin	8YSZ	170 / 700 / 900	-	-										
MOD081a	171	LSC50	spin	8YSZ	170 / 700 / 900	-	-							√	IS2.070		
MOD081b	171	LSC50	spin	8YSZ	170 / 700 / 900	-	-			√				√	IS2.071		
MOD082	172	LSC50	spin	8YSZ	170 / 700 / 900	-	-										
MOD083a	173	LSC50	spin	8YSZ	170 / 700 / 900	-	-							√	IS2.068		
MOD083b	173	LSC50	spin	8YSZ	170 / 700 / 900	-	-										
MOD084a	174	LSC50	spin	8YSZ	170 / 700 / 900	-	-							√	IS2.079		
MOD084b	174	LSC50	spin	8YSZ	170 / 700 / 900	-	-			√							
MOD084c	174	LSC50	spin	8YSZ	170 / 700 / 900	-	-										
MOD085a	175	LSC50	spin	8YSZ	170 / 700 / 900	700	8			√							

Table 7 (continued)

IWE-ID	ISC-ID	Thin film	Deposition technique	Substrate	RTA / °C	T_{dwell} / °C	t_{dwell} / h	Measuring objective	TA	SEM	(HR)TEM	AFM	(HT)XRD	EIS	Measuring ID	other exp.	Remarks
MOD085b	175	LSC50	spin	8YSZ	170 / 700 / 900	800	8	Parameter variation		√							
MOD085c	175	LSC50	spin	8YSZ	170 / 700 / 900	900	8			√							
MOD085d	175	LSC50	spin	8YSZ	170 / 700 / 900	1000	8			√							
MOD085e	175	LSC50	spin	8YSZ	170 / 700 / 900	-	-										
MOD086	147	LSC50	dip	GCO / 3YSZ	170 / 700 / 900	-	-							√	IS2.054		
MOD087	-	LSC50 precursor powder			170 / 700 / 900	700	8	Crystallization of LSC phase from precursor powder	√								
MOD088	-	LSC50 precursor powder			170 / 700 / 900	-	-		√								
MOD089	-	LSC50 precursor powder			170 / 700 / 900	700 850	8		√								
MOD090a	-	LSC50 precursor powder			170 / 700 / 900	1000	20		√								
MOD090b	-	LSC50 precursor powder			170 / 700 / 900	1350	20		√								
MOD091	-	LSC50 precursor powder			170 / 700 / 900	850	20		√								
MOD092	218	LSC50 precursor powder			170 / 700 / 900	-	-	Thin film development with emphasis on high catalytic activity									
MOD093a	216	LSC50	spin	8YSZ	170 / 700 / 900	-	-							√	IS2.074		
MOD093b	216	LSC50	spin	8YSZ	170 / 700 / 900	-	-							√	IS2.073		
MOD093c1	216	LSC50	spin	8YSZ	170 / 700 / 900	700	8										
MOD093c2	216	LSC50	spin	8YSZ	170 / 700 / 900	1000	8										
MOD093d1	216	LSC50	spin	8YSZ	170 / 700 / 900	700	8										
MOD093d2	216	LSC50	spin	8YSZ	170 / 700 / 900	1000	8										
MOD094a	217	LSC50	spin	8YSZ	170 / 700 / 900	-	-							√	IS2.080		
MOD094b	217	LSC50	spin	8YSZ	170 / 700 / 900	-	-			√				√	Z3.016		
MOD094c	217	LSC50	spin	8YSZ	170 / 700 / 900	-	-							√	Z3.013		
MOD094d	217	LSC50	spin	8YSZ	170 / 700 / 900	-	-							√	Z3.016		
MOD095a	-	LSC50	-	8YSZ		-	-							√	IS2.076		
MOD095b	-	LSC50	-	8YSZ		-	-							√	IS2.075		
MOD095c	-	LSC50	-	8YSZ		-	-							√	IS2.081		
MOD095d	-	LSC50	-	8YSZ		-	-			√							
MOD096	-	LSC50	-	8YSZ		-	-										
MOD097	144	LSC50	dip	GCO / 3YSZ	170 / 700 / 900	-	-							√	IS2.058		
MOD097a	151	LSC50	dip	GCO / 3YSZ	170 / 700 / 900	-	-							√	IS2.065		
MOD097b	146	LSC50	dip	GCO / 3YSZ	170 / 700 / 900	-	-							√	IS2.051		
MOD097c	147	LSC50	dip	GCO / 3YSZ	170 / 700 / 900	-	-							√	IS2.052		
MOD097d	150	LSC50	dip	GCO / 3YSZ	170 / 700 / 900	-	-							√	IS2.053		
MOD097e	152	LSC50	dip	GCO / 3YSZ	170 / 700 / 900	-	-							√	IS2.063		
MOD097f	181	LSC50	dip	GCO / 3YSZ	170 / 700 / 900	-	-			√				√	IS2.059		
MOD097g	184	LSC50	dip	GCO / 3YSZ	170 / 700	-	-			√				√	IS2.062		
MOD097h	183	LSC50	dip	GCO / 3YSZ	170 / 700	-	-							√	IS2.060		
MOD098a	221	LSC50	spin	8YSZ	170 / 700 / 900	500	2	Influence of thin film morphology on polarization losses						√	Z3.001		5
MOD098b	221	LSC50	spin	8YSZ	170 / 700 / 900	600	2			√				√	Z3.001		5
MOD098c	221	LSC50	spin	8YSZ	170 / 700 / 900	700	2							√	Z3.002		5
MOD098d	221	LSC50	spin	8YSZ	170 / 700 / 900	800	2							√	Z3.002		5
MOD099a	222	LSC50	spin	8YSZ	170 / 700 / 900	900	2							√	Z3.003		5
MOD099b	222	LSC50	spin	8YSZ	170 / 700 / 900	1000	2							√	Z3.003		5
MOD099c	222	LSC50	spin	8YSZ	170 / 700 / 900	500	10							√	Z3.004		5
MOD099d	222	LSC50	spin	8YSZ	170 / 700 / 900	600	10							√	Z3.004		5
MOD100a	223	LSC50	spin	8YSZ	170 / 700 / 900	700	10							√	Z3.005		5
MOD100b	223	LSC50	spin	8YSZ	170 / 700 / 900	800	10							√	Z3.005		5
MOD100c	223	LSC50	spin	8YSZ	170 / 700 / 900	900	10							√	Z3.006		5
MOD100d	224	LSC50	spin	8YSZ	170 / 700 / 900	1000	10			√				√	Z3.006		5
MOD101a	224	LSC50	spin	8YSZ	170 / 700 / 900	500	100							√	Z3.009		5
MOD101b	224	LSC50	spin	8YSZ	170 / 700 / 900	600	100							√	Z3.009		5
MOD101c	224	LSC50	spin	8YSZ	170 / 700 / 900	700	100							√	Z3.010		5
MOD101d	224	LSC50	spin	8YSZ	170 / 700 / 900	800	100							√	Z3.010		5
MOD102a	225	LSC50	spin	8YSZ	170 / 700 / 900	900	100							√	Z3.011		5
MOD102b	225	LSC50	spin	8YSZ	170 / 700 / 900	1000	100							√	Z3.011		5
MOD102c	225	LSC50	spin	8YSZ	170 / 700 / 900	800	10							√	Z3.012		5

Table 8 (continued)

IWE-ID	ISC-ID	Thin film	Deposition technique	Substrate	RTA / °C	T_{dwell} / °C	t_{dwell} / h	Measuring objective	TA	SEM	(HR)TEM	AFM	(HT)XRD	EIS	Measuring ID	other exp.	Remarks
MOD102d	225	LSC50	spin	8YSZ	170 / 700 / 900	-	-			√			√				6
MOD103a	226	LSC50	spin	8YSZ	170 / 700 / 900	-	-							√	LF2.055		5
MOD103b	226	LSC50	spin	8YSZ	170 / 700 / 900	500	2							√	Z3.008		5
MOD103c	226	LSC50	spin	8YSZ	170 / 700 / 900	600	2							√	Z3.008		5
MOD103d	226	LSC50	spin	8YSZ	170 / 700 / 900	-	-										5
MOD104	-	-	-	-	-	-	-										
MOD104a	227	LSC50	spin	8YSZ	170 / 700 / 900	700	10							√	Z3.012		5
MOD104b	227	LSC50	spin	8YSZ	170 / 700 / 900	-	-							√	Z3.018		5
MOD104c	227	LSC50	spin	8YSZ	170 / 700 / 900	-	-							√	Z3.007		5
MOD104d	227	LSC50	spin	8YSZ	170 / 700 / 900	-	-			√				√	Z3.007		5
MOD105a	228	LSC50	spin	8YSZ	170 / 700 / 900	500	2			√			√				6
MOD105b	228	LSC50	spin	8YSZ	170 / 700 / 900	600	2			√				√	LF2.061		5
MOD105c	228	LSC50	spin	8YSZ	170 / 700 / 900	700	2			√			√				6
MOD105d	228	LSC50	spin	8YSZ	170 / 700 / 900	800	2			√			√				6
MOD106a	229	LSC50	spin	8YSZ	170 / 700 / 900	900	2			√			√	√	LF2.060		5,6
MOD106b	229	LSC50	spin	8YSZ	170 / 700 / 900	1000	2			√			√				6
MOD106c	229	LSC50	spin	8YSZ	170 / 700 / 900	500	10			√			√	√	LF2.064		5,6
MOD106d	229	LSC50	spin	8YSZ	170 / 700 / 900	600	10			√			√				6
MOD107a	230	LSC50	spin	8YSZ	170 / 700 / 900	700	10			√			√				6
MOD107b	230	LSC50	spin	8YSZ	170 / 700 / 900	800	10			√			√				6
MOD107c	230	LSC50	spin	8YSZ	170 / 700 / 900	900	10			√			√				6
MOD107d	230	LSC50	spin	8YSZ	170 / 700 / 900	1000	10			√			√				6
MOD108a	231	LSC50	spin	8YSZ	170 / 700 / 900	500	100			√			√	√	LF2.065		5,6
MOD108b	231	LSC50	spin	8YSZ	170 / 700 / 900	600	100			√			√				6
MOD108c	231	LSC50	spin	8YSZ	170 / 700 / 900	700	100			√			√				6
MOD108d	231	LSC50	spin	8YSZ	170 / 700 / 900	800	100			√			√				6
MOD109a	232	LSC50	spin	8YSZ	170 / 700 / 900	900	100	Influence of thin film morphology on polarization losses		√			√				6
MOD109b	232	LSC50	spin	8YSZ	170 / 700 / 900	1000	100			√			√				6
MOD109c1	232	LSC50	spin	8YSZ	170 / 700 / 900	-	-							√	LF2.062		5
MOD109c2	232	LSC50	spin	8YSZ	170 / 700 / 900	-	-							√	LF2.066		5
MOD109d	232	LSC50	spin	8YSZ	170 / 700 / 900	600	2			√			√				6
MOD110abcd	243	LSC50	spin	8YSZ	170 / 700 / 900	-	-			√							
MOD111	244	LSC50	spin	8YSZ	170 / 700 / 900	700	8										
MOD111b	244	LSC50	spin	8YSZ	170 / 700 / 900	800	8										
MOD112abcd	245	LSC50	spin	8YSZ	170 / 700 / 900	-	-										
MOD113abcd	246	LSC50	spin	8YSZ	170 / 700 / 900	-	-										
MOD114a	238	LSC50	spin	8YSZ	170 / 700 / 900	-	-							√	IS2.082		
MOD114b	238	LSC50	spin	8YSZ	170 / 700 / 900	-	-							√	IS2.083		
MOD114c	238	LSC50	spin	8YSZ	170 / 700 / 900	-	-			√							
MOD114d - 117d (13 samples)		LSC50	spin	8YSZ	170 / 700 / 900	-	-										
MOD118a	242	LSC50	spin	8YSZ	170 / 700 / 900	-	-							√	Z3.028		
MOD118b	242	LSC50	spin	8YSZ	170 / 700 / 900	-	-							√	Z3.029		
MOD118c	242	LSC50	spin	8YSZ	170 / 700 / 900	-	-			√							
MOD119a	247	LSC50	spin	8YSZ	170 / 700 / 900	-	-							√	IS2.085		
MOD119b	247	LSC50	spin	8YSZ	170 / 700 / 900	-	-							√	IS2.084		
MOD119c	247	LSC50	spin	8YSZ	170 / 700 / 900	-	-							√	IS2.086		
MOD119d	247	LSC50	spin	8YSZ	170 / 700 / 900	-	-										
MOD120abcd	248	LSC50	spin	8YSZ	170 / 700 / 900	-	-			√							
MOD121a	249	LSC50	spin	8YSZ	170 / 700 / 900	-	-							√	Z3.013		5
MOD121b	249	LSC50	spin	8YSZ	170 / 700 / 900	-	-										5
MOD121c1	249	LSC50	spin	8YSZ	170 / 700 / 900	-	-							√	Z3.015		5
MOD121c2	249	LSC50	spin	8YSZ	170 / 700 / 900	-	-							√	Z3.015		5
MOD121d	249	LSC50	spin	8YSZ	170 / 700 / 900	-	-			√							5
MOD122abcd	250	LSC50	spin	8YSZ	170 / 700 / 900	-	-										5
MOD123a - 124 (3 samples)		GCO	tampon	8YSZ	400 / 1080	-	-			√							
MOD125a	276	LSC50	spin(LSC)	GCO / 8YSZ	170 / 700	-	-	Development of GCO buffer-layer									
MOD125b	276	LSC50	spin(LSC)	GCO / 8YSZ	170 / 700	-	-							√	Z3.017		
MOD126a	277	LSC50	spin(LSC)	GCO / 8YSZ	170 / 700 / 900	-	-										

Table 9 (continued)

IWE-ID	ISC-ID	Thin film	Deposition technique	Substrate	RTA / °C	T_{dwell} / °C	t_{dwell} / h	Measuring objective	TA	SEM	(HR)TEM	AFM	(HT)XRD	EIS	Measuring ID	other exp.	Remarks
MOD126b	277	LSC50	dip (LSC)	GCO / 8YSZ	170 / 700 / 900	-	-	Development of GCO buffer-layer						√	Z3.017		
MOD126c	277	LSC50	dip (LSC)	GCO / 8YSZ	170 / 700 / 900	-	-			√							
MOD127	278	LSC50	dip (LSC)	GCO / 8YSZ	170 / 700 / 900	-	-										
MOD128 - 133 (6 samples)		LSM	spray pyrolysis	8YSZ	-	750	1 / 2	CFN cooperation							Z3.019-1/2		
MOD134 (58 samples)		LSC microel.	various techn.	8YSZ	170 / 700 / 900	-	-	Characterization by micro-electrodes		√				√	"IWE-ID" + No.		7
MOD135	-	LSC microel.	various techn.	8YSZ	170 / 700 / 900	-	-			√				√			7
MOD135_a	171	LSC50	spin	8YSZ	170 / 700 / 900	-	-							√	IS2.071		
MOD136	-	LSC50	dip	GCO	170 / 700 / 900	-	-			√							
MOD137	-	LSC50	dip	GCO	170 / 700 / 900	-	-			√							
MOD138	287	LSC precursor powder			-	-	-	Crystallization of LSC phase									
MOD139	285	LSC precursor powder			-	850	16		√								
MOD140	286	LSC precursor powder			-	-	-										
MOD141a-f	-	sintering aids (LSC50_CP3)			-	-	-										
MOD142	ISC 296	LSC precursor powder			-	-	-	Interface reaction between LSC and YSZ / GCO									
MOD143	-	mixture: LSC50 + 8YSZ (Tosoh)			-	-	-										
MOD144	ISC 296	LSC precursor powder			-		-		√				√				
MOD145	-	mixture: MOD144 + 8YSZ			-		-						√				
MOD146	-	mixtues: MOD144 + GCO			-		-						√				
MOD147	-	GCO powder (Treibacher)			-	-	-										
MOD148	-	mixture: MOD142 + 8YSZ			-	-	-										
MOD149	-	-	-	GCO	-	-	-	Optimization of processing parameters		√							8
MOD150	-	-	-	GCO	-	-	-			√							8
MOD151	-	GCO powder (DKKK)			-	-	-			√							8
MOD151_1 - 151_14 (14 samples)		-	-	GCO	-	-	-			√							8
MOD151_15	1-372	LSC50	dip	GCO	170 / 700 / 900	800	10	Influence of thin film morphology on polarization losses		√				√	Z3.036		8
MOD151_16	2-372	LSC50	dip	GCO	170 / 700 / 900	900	10			√							8
MOD151_17	3-372	LSC50	dip	GCO	-	-	-			√				√	Z3.037		8
MOD151_18	4-372	LSC50	dip	GCO	170 / 700 / 900	900	10			√				√	Z3.050		8
MOD151_19 - 22 (4 samples)		-	-	GCO	-	-	-							√	Z3.035		8
MOD151_23	1-376	LSC50	dip	GCO	170 / 700 / 900	800	10			√				√	Z3.044		8
MOD151_24	2-376	LSC50	dip	GCO	170 / 700 / 900	-	-							√	Z3.038		8
MOD151_25	3-376	LSC50	dip	GCO	170 / 700 / 900	-	-							√	Z3.040		8
MOD151_26	4-376	LSC50	dip	GCO	170 / 700 / 900	800	10							√	Z3.043		8
MOD151_27	1-380	LSC50	dip	GCO	170 / 700 / 900	800	2							√	Z3.045		8
MOD151_28	2-380	LSC50	dip	GCO	170 / 700 / 900	-	-							√	Z3.041		8
MOD151_29	3-380	LSC50	dip	GCO	170 / 700 / 900	-	-							√	Z3.042		8
MOD151_30	4-380	LSC50	dip	GCO	170 / 700 / 900	800	2			√				√	Z3.047		8
MOD151_31	5-380	LSC50	dip	GCO	170 / 700 / 900	-	-			√							8
MOD151_32	6-380	LSC50	dip	GCO	170 / 700 / 900	900	10			√				√	Z3.046		8
MOD151_33	7-380	LSC50	dip	GCO	170 / 700 / 900	900	2			√				√	Z3.048		8
MOD151_34	8-380	LSC50	dip	GCO	170 / 700 / 900	900	2							√	Z3.049		8
MOD152 - 163 (12 samples)		8YSZ + Zr/Y-sol	dip	sapphire	500	1250 1350	24	Doping of YSZ gb.		√							
MOD164a	1-310	LSC50	tampon	8YSZ	170 / 700	-	-	ASR_{Pol} in nanoscaled LSC thin films						√	Z3.028		5
MOD164b	1-310	LSC50	tampon	8YSZ	170 / 700	-	-							√	Z3.029		5
MOD164c,d	1-310	LSC50	tampon	8YSZ	170 / 700	-	-			√							5

7.2 Indices

7.2.1 Symbols

α	polarizability
β	transference number
γ	temperature and geometry dependent scaling factor
δ	oxygen nonstoichiometry
δ_{gb}	"electrical" grain-boundary thickness [m]
Δ	full width at half maximum [°]
ε	porosity [%]
ε_0	permittivity of free space [$\varepsilon_0 = 8.85 \cdot 10^{-12}$ As/Vm]
ε_g	permittivity of the bulk
ε_{gb}	permittivity of the grain boundary
ε_r	relative permittivity
η	polarization loss [V]
λ	Debye length [m]
η	sol viscosity [m²/s]
ρ	density [kg/m³]
σ	electrical conductivity [S/m]
σ_{el}	electronic conductivity [S/m]
σ_g	bulk conductivity [S/m]
σ_{gb}	grain-boundary conductivity [S/m]
σ_{ion}	ionic conductivity [S/m]
σ_{tf}	electrical conductivity of the thin film [S/m]
τ	relaxation time [s]
θ	XRD grazing angle [°]
a	inner surface area [m^{-1}]
A	cross-section of thin film [m²]
c	concentration [1/m³]
C	capacitance [F]

d	mean grain size [m]
d_0	initial grain size at t_0 [m]
d_{gb}	microstructural grain-boundary thickness [m]
d_{crys}	distance between atomic layers in a crystal [m]
D	oxygen-diffusion coefficient [m²/s]
D_{chem} (D^δ, $\tilde{D}$)	oxygen-diffusion rate with respect to a "chemical" experiment [m²/s]
D_{tr} (D^0, D^*)	oxygen-diffusion rate with respect to a "tracer" experiment [m²/s]
D^q	oxygen-diffusion rate with respect to an "electrical" experiment [m/s]
e	strain [%]
E_A	activation energy [eV], [kJ/mol]
f	frequency [1/s]
F	Faraday constant [$F = 9.649 \cdot 10^4$ C/mol]
g	gravimetric constant [$g = 9.81$ m/s²]
I	current [A]
H_A	association enthalpy [eV]
H_M	migration enthalpy [eV]
j	current density [A/m²]
k	a) Boltzmann constant [$k = 8.617 \cdot 10^{-5}$ eV/K]
	b) surface-exchange rate [m/s]
k_{chem} (k^δ, $\tilde{k}$)	surface-exchange rate with respect to a "chemical" experiment [m/s]
k_{tr} (k^0, k^*, k_{ex})	surface-exchange rate with respect to a "tracer" experiment [m/s]
k^q	surface-exchange rate with respect to an "electrical" experiment [m/s]
k_p	parabolic rate constant [cm²/s]
l_δ	utilization range [m]
l_{cl}	electrode clearance [m]
l_{el}	electrode length [m]
l_g	particle dimension [m]
L_c	critical length of a dense cathode [m]
n	a) exponent in Q-C relation characterizing the deviation of Q from an "ideal" capacitance
	b) concentration of electrons [m⁻³]

OCV	open circuit voltage [V]
pO_2	oxygen partial pressure [bar]
Q	constant phase element
r_{ion}	ion radius [Å]
R	a) gas constant [R = 8.314 J/(mol·K)]
	b) resistance [Ω]
R_a	average surface roughness
R_g	bulk resistance [Ω]
R_{gb}	grain-boundary resistance [Ω]
R_{tf}	thin-film resistance [Ω]
RT	room temperature
t	film thickness [m]
t_{dwell}	dwell time [s]
t_{ion}	oxygen transference number
t_{RTA}	calcination time during rapid thermal annealing [s]
T	absolute temperature [K]
T_{cal}	calcination temperature [K]
T_{cell}	cell temperature [K]
U	voltage [V]
U_0	open circuit voltage (OCV) [V]
U_C	cell voltage [V]
U_N	Nernst voltage [V]
v_0	withdrawal rate in dip-coating process [m/s]
V	volume of unit cell [m³]
Z	complex impedance [Ω]
Z′	real part of the complex impedance [Ω]
Z′′	imaginary part of the complex impedance [Ω]

7.2.2 Abbreviations

AFM	atomic force microscopy
APU	auxiliary power unit
ASR	area specific resistance

ASR$_{chem}$	*ASR* caused by oxygen-reduction mechanism except charge-transfer (Adler's model)
ASR$_{gas}$	*ASR* caused by diffusion of oxygen molecules in the gas phase
ASR$_{ct}$	*ASR* caused by the incorporation of oxygen ions into the electrolyte (charge transfer)
ASR$_d$	*ASR* caused by diffusion of oxygen ions through the MIEC to the MIEC / electrolyte interface
ASR$_{ex}$	*ASR* caused by oxygen exchange at the MIEC surface
ASR$_{pol}$	area specific polarization resistance [$\Omega \cdot m^2$]
DSC	differential scanning calorimetry
EIS	electrochemical impedance spectroscopy
FEM	finite element method
FIB	focused ion beam
FRA	frequency response analyzer
FSZ	fully stabilized zirconia
FWHM	full width at half maximum
FWHM$_c$	full width at half maximum regarding the sample related peak broadening
FWHM$_i$	full width at half-maximum regarding instrumental peak broadening
GCO	gadolinium cerium oxide $(Gd,Ce)O_{2-\delta}$
HAADF	high-angle annular dark-field
HRTEM	high-resolution TEM
IT-SOFC	intermediate-temperature SOFC (500 °C ≤ *T* ≤ 750 °C)
ICP-AES	inductively coupled plasma atomic emission spectroscopy
ISC	Fraunhofer Institut für Silicatforschung, Würzburg
IWE	Institut für Werkstoffe der Elektrotechnik, Universität Karlsruhe (TH)
JCPDS	Joint Committee on Powder Diffraction Standards
LEM	Laboratorium für Elektronenmikroskopie, Universität Karlsruhe (TH)
LSC	lanthanum strontium cobaltite $(La_{1-x}Sr_x)CoO_{3-\delta}$
LSCF	lanthanum strontium cobalt ferrite $(La_{1-x}Sr_x)(Co_{1-y}Fe_y)O_{3-\delta}$
LZO	lanthanum zirconate $La_2Zr_2O_7$
MALT	materials oriented little thermodynamic database
MIEC	mixed ionic-electronic conductor

MOD	metallorganic deposition
OCV	open circuit voltage
ORR	oxygen-reduction reaction
PLD	pulsed laser deposition
rds	rate-determining step
rpm	rotations per minute
SEM	scanning electron microscopy
SIMS	secondary ion mass spectroscopy
SOFC	solid oxide fuel cell
STEM	scanning transmission electron microscope
SZO	strontium zirconate $SrZrO_3$
TA	thermal analysis
TG	thermogravimetry
TEC	thermal expansion coefficient
TEM	transmission electron microscope
tpb	triple-phase boundary
TZP	tetragonal zirconia polycrystal
XRD	X-ray diffraction
YSZ	general: yttria-stabilized zirconia (Y_2O_3-doped ZrO_2)
	here: 8 mol% Y_2O_3 stabilized ZrO_2 (8YSZ)
	here: 3.5 mol% Y_2O_3 stabilized ZrO_2 (3.5YSZ)

7.3 List of Figures

7.4 List of Tables

7.5 Supervised Diploma Theses and Study Projects

- Barbara Szöke, "Elektrische Charakterisierung von Nanoschichten" *(Electrical Characterization of Nanoscaled Thin Films)*, Diploma Thesis, IWE, Universität Karlsruhe (TH), 2006.

- Irene Netsch, "Mikrostrukturanalyse nanoskaliger Dünnschichtkathoden" *(Microstructural Analysis of nanoscaled Thin-Film Cathodes)*, Study Project, IWE, Universität Karlsruhe (TH), 2007.

- Holger Götz, "Einfluss der Mikrostruktur auf den Polarisationswiderstand einer LSC-Nanokathode" *(Influence of the Microstructure on the Polarization Losses of a nanoscaled LSC Thin-Film Cathode)*, Study Project, IWE, Universität Karlsruhe (TH), 2007.

- Ulrich Peters, "Mikroelektroden für die Kathodenentwicklung" *(Microelectrodes for Cathode Development)*, Study Project, IWE, Universität Karlsruhe (TH), 2007.

- Thassilo Knapp, "Nanoskalige LSC-Dünnschichten – Einfluss der Mikrostruktur auf die Kathodenverluste einer SOFC" *(Nanoscaled LSC Thin Films – Influence of the*

Microstructure on the Cathode Losses of an SOFC), Study Project, IWE, Universität Karlsruhe (TH), 2007.

7.6 Own Publications

Reviewed Contributions

(1)   C. Peters, A. Weber, B. Butz, D. Gerthsen, E. Ivers-Tiffée, "Grain Size Effects in 8YSZ Thin Film Electrolytes", submitted to the Journal of the American Ceramic Society (2008).

(2)   C. Peters, A. Weber, E. Ivers-Tiffée, "Nanoscaled $(La_{0.5}Sr_{0.5})CoO_{3-\delta}$ (LSC) Thin-film Cathodes for SOFC Application at 500 °C < T < 700 °C", Journal of The Electrochemical Society **155** (7), B730 – B737, (2008).

(3)   C. Peters, A. Weber, E. Ivers-Tiffée, "Grain size effects in nanoscaled 8YSZ thin-film electrolytes", Proceedings of the International Conference on Advanced Processing for Novel Functional Materials (APNFM), accepted for publication (2008).

(4)   L. Dieterle, D. Bach, R. Schneider, H. Störmer, D. Gerthsen, U. Guntow, E. Ivers-Tiffée, A. Weber, C. Peters, H. Yokokawa, "Structural and chemical properties of nanocrystalline $La_{0.5}Sr_{0.5}CoO_{3-\delta}$ layers on yttria-stabilized zirconia analyzed by transmission electron microscopy", Journal of Material Science, **43** (9), 3135 – 3143 (2008).

(5)   C. Peters, M. Bockmeyer, R. Krüger, A. Weber, E. Ivers-Tiffée, „Processing of Dense Nanocrystalline Zirconia Thin Films by Sol-Gel Method", in D. Kumar et al. (Eds.), Materials Research Society Symposium Proceedings - Current and Future Trends of Functional Oxide Films, Warrendale: Materials Research Society, Volume 928E, p. GG16-01 (2006).

(6)   T. Schneider, C. Peters, S. Wagner, W. Menesklou, E. Ivers-Tiffée, "$Sr(Ti,Fe)O_{3-\delta}$ exhaust gas sensors", Mater. Res. Soc. Symp. Proc. Vol. **828**, A3.7 (2005).

Conference Contributions

(7)   C. Peters, A. Weber, E. Ivers-Tiffée, Grain size effects in nanoscaled 8YSZ thin-film electrolytes, Advanced Processing for Novel Functional Materials – APNFM 2008, Dresden, Germany, 01/23/2008 – 01/25/2008.

(8)   B. Butz, H. Störmer, D. Gerthsen, C. Peters, A. Weber, E. Ivers-Tiffée, M. Bockmeyer, R. Krüger, "Microstructural and electrical investigations of sol-gel derived 8YSZ films", Bunsen Colloquium "Diffusion and Reactions in Advanced Materials", Clausthal-Zellerfeld, Germany, 09/27/2007 – 09/28/2007.

(9)   L. Dieterle, D. Bach, R. Schneider, H. Störmer, D. Gerthsen, U. Guntow, C. Peters, A. Weber, E. Ivers-Tiffée, "Chemical Stability and Structural Properties of Nanocrystalline $La_{0.5}Sr_{0.5}CoO_{3-\delta}$ Layers on Yttria-stabilized Zirconia", Euromat, Nürnberg, Germany, 09/10/2007 – 09/13/2007.

(10)   B. Butz, H. Störmer, M. Bockmeyer, R. Krüger, C. Peters, A. Weber, E. Ivers-Tiffée, D. Gerthsen, "Microstructural investigations of thin sol-gel fabricated 8YSZ films", Euromat, Nürnberg, Germany, 09/10/2007 – 09/13/2007.

(11)   C. Peters, A. Weber, W. Menesklou, E. Ivers-Tiffée, et al., "Interaction between grain size and electrical conductivity in YSZ thin films", International Conference on Electroceramics – ICE2007, Arusha, Tanzania, 07/31/2007 – 08/03/2007.

(12)   L. Dieterle, D. Gerthsen, E. Ivers-Tiffée, C. Peters, A. Weber, U. Guntow, H. Yokokawa, "Structural Characterization and Chemical Stability of nanocrystalline $La_{0.5}Sr_{0.5}CoO_{3-\delta}$ cathode layers on YSZ obtained by Sol-Gel processing", International Conference on Electroceramics – ICE2007, Arusha, Tanzania, 07/31/2007 – 08/03/2007.

(13)   E. Ivers-Tiffée, C. Peters, A. Weber, H. Störmer, D. Gerthsen, M. Bockmeyer, R. Krüger, "Ionic Conductivity in Nanoscaled Y-doped Zirconia (YSZ) Thin Films", 10th International Conference and Exhibition of the European Ceramic Society – ECERS2007, Berlin, Germany, 06/17/2007 – 06/21/2007.

(14)   C. Peters, A. Weber, E. Ivers-Tiffée, U. Guntow, "Nanoscaled (La,Sr)CoO₃ (LSC) Thin-film Cathodes for Solid Oxide Fuel Cells (SOFC)", Solid State Ionics 16, Shanghai, China, 07/02/2007 – 07/06/2007.

(15)   B. Butz, C. Peters, H. Störmer, A. Weber, E. Ivers-Tiffée, D. Gerthsen, „Mikrostrukturelle und elektrische Charakterisierung von nanokristallinen 8YSZ-Dünnfilmen", DGM-Tag of the Deutschen Gesellschaft der Materialkunde e.V., Karlsruhe, Germany, 06/21/2007 – 06/22/2007.

(16)   C. Peters, L. Dieterle, D. Gerthsen, A. Weber, E. Ivers-Tiffée, „Nanoskalige $La_{0.5}Sr_{0.5}CoO_3$ -Dünnschichtkathoden für Hochtemperaturbrennstoffzellen",DGM-Tag of the Deutschen Gesellschaft der Materialkunde e.V., Karlsruhe, Germany, 06/21/2007 – 06/22/2007.

(17)   C. Peters, H. Götz, I. Netsch, U. Guntow, A. Weber, E. Ivers-Tiffée, "Processing and structural characterization of nanoscaled $La_{1-x}Sr_xCoO_3$ (LSC) thin-film cathodes", Materials Research Society (MRS), Spring Meeting 2007, San Francisco, USA, 04/09/2007 – 04/13/2007.

(18)   C. Peters, A. Weber, E. Ivers-Tiffée, H. Störmer, D. Gerthsen, M. Bockmeyer, R. Krüger, "Interaction between grain size and electrical conductivity in YSZ thin films", Materials Research Society (MRS), Fall Meeting 2006, Boston, USA, 11/27/2006 – 12/01/2006.

(19)   L. Dieterle, D. Gerthsen, C. Peters, A. Weber, U. Guntow, „Structural Characterization and Chemical Stability of Nanoscale $La_{0.5}Sr_{0.5}CoO_{3-d}$ Cathodes on YSZ", Materials Research Society (MRS), Fall Meeting 2006, Boston, USA, 11/27/2006 – 12/01/2006.

(20)   C. Peters, A. Weber, E. Ivers-Tiffée, U. Guntow, L. Dieterle, D. Gerthsen, "Nanoscale MIEC Cathode for Solid Oxide Fuel Cells", European Materials Research Society (E-MRS), Spring Meeting 2006, Nice, France, 05/29/2006 – 06/02/2006.

(21)   C. Peters, M. Bockmeyer, R. Krüger, A. Weber, E. Ivers-Tiffée, "Processing of Dense Nanocrystalline Zirconia Thin Films by Sol-Gel Method", Materials Research Society (MRS), Spring Meeting 2006, San Francisco, USA, 04/18/2006 – 04/21/2006.

(22)   T. Schneider, C. Peters, C. Endler, B. Szöke, W. Menesklou, E. Ivers-Tiffée, "Stability limitations of $Sr(Ti,Fe)O_{3-\delta}$ for exhaust gas sensors", 15th International Conference on Solid State Ionics (SSI-15), Baden-Baden, Germany, 07/17/2005 – 07/22/2005.

(23)   T. Schneider, C. Peters, S. Wagner, W. Menesklou, E. Ivers-Tiffée, "$Sr(Ti,Fe)O_{3-\delta}$ exhaust gas sensors", Materials Research Society (MRS), Fall Meeting 2004, Boston, USA, 11/29/2004 – 12/03/2004.

(24)   T. Schneider, C. Peters, W. Menesklou, H. Yokokawa, E. Ivers-Tiffée, "Degradation processes in new type resistive oxygen sensors", Materials Research Society (MRS), Fall Meeting 2003, Boston, USA, 12/01/2003 – 12/05/2003.

8 Reference List

[1] K. R. Berge, "An Oil Crises is Probably Imminent", Association for the Study of Peak Oil and Gas (ASPO), www.peakoil.net, (4-2-2008).

[2] Members of the IPCC, "Climate Change 2007", Intergovernmental Panel on Climate Change (IPCC), www.ipcc.ch, (31-3-2008).

[3] N. Stern, "Stern Review on the Economics of Climate Change", Office of Climate Change (OCC), UK, www.hm-treasury.gov.uk , (31-3-2008).

[4] R. Witoelar, "The Bali Roadmap", United Nations Framework Convention on Climate Change (UNFCCC), http://unfccc.int/meetings/cop_13/items/4049.php, (26-5-2008).

[5] J. L. Morgan, "Towards a new global climate deal", E3G, www.e3g.org , (31-3-2008).

[6] P. Holtappels and U. Stimming, "Solid Oxide Fuel Cells (SOFC)", in W. Vielstich et al. (Eds.), Handbook of Fuel Cells: Fundamentals, Technology and Applications, Vol. 1, Chichester, England: John Wiley & Sons Ltd., p. 335-354, 2003.

[7] S. C. Singhal and K. Kendall, "High Temperature Solid Oxide Fuel Cells", New York: Elsevier Ltd., 2003.

[8] M. J. Heneka, "Alterung Der Festelektrolyt-Brennstoffzelle Unter Thermischen Und Elektrischen Lastwechseln", Aachen: Mainz GmbH, 2006.

[9] T. Lipman and D. Sperling, "Market Concepts, Competing Technologies and Cost Challenges for Automotive and Stationary Applications", in W. Vielstich et al. (Eds.), Handbook of Fuel Cells - Vol. 4, Chichester, England: John Wiley & Sons Ltd., p. 1318-1328, 2003.

[10] P. Lamp, J. Tachtler, O. Finkenwirth, P. Mukerjee and S. Shaffer, "Development of an Auxiliary Power Unit With Solid Oxide Fuel Cells for Automotive Applications", Fuel Cells, Volume 3, Issue 3, p. 1-7, 2003.

[11] D. Nikbin, "Micro SOFCs: Why Small Is Beautiful", The Fuel Cell Review, Volume 3, Issue 2, p. 21-24, 2006.

[12] L. Blum, W. A. Meulenberg, H. Nabielek and R. Steinberger-Wilckens, "Worldwide SOFC Technology Overview and Benchmark", International Journal of Applied Ceramic Technology, Volume 2, Issue 6, p. 482-492, 2005.

[13] T. Ishihara, N. M. Sammes and O. Yamamoto, "Electrolytes", in S. C. Singhal and K. Kendall (Eds.), High Temperature Solid Oxide Fuel Cells, New York: Elsevier Ltd., p. 83-117, 2003.

[14] O. Yamamoto, "Low Temperature Electrolytes and Catalysts", in W. Vielstich et al. (Eds.), Handbook of Fuel Cells - Vol. 4, Chichester, England: John Wiley & Sons Ltd., p. 1002, 2003.

[15] M. Gödickemeier, K. Sasaki, L. J. Gauckler and I. Riess, "Electrochemical Characteristics of Cathodes in Solid Oxide Fuel Cells Based on Ceria Electrolytes", Journal of the Electrochemical Society, Volume 144, Issue 5, p. 1635-1646, 1997.

[16] J. M. Bae and B. C. H. Steele, "Properties of $La_{0.6}Sr_{0.4}Co_{0.2}Fe_{0.8}O_{3-\delta}$ (LSCF) Double Layer Cathodes on Gadolinium-Doped Cerium Oxide (CGO) Electrolytes - I. Role of SiO_2", Solid State Ionics, Volume 106, Issue 3-4, p. 247-253, 1998.

[17] B. C. H. Steele and J. M. Bae, "Properties of $La_{0.6}Sr_{0.4}Co_{0.2}Fe_{0.8}O_{3-x}$ (LSCF) Double Layer Cathodes on Gadolinium-Doped Cerium Oxide (CGO) Electrolytes - II. Role of Oxygen Exchange and Diffusion", Solid State Ionics, Volume 106, Issue 3-4, p. 255-261, 1998.

[18] V. Dusastre and J. A. Kilner, "Optimisation of Composite Cathodes for Intermediate Temperature SOFC Applications", Solid State Ionics, Volume 126, Issue 1-2, p. 163-174, 1999.

[19] A. Mai, V. A. C. Haanappel, S. Uhlenbruck, F. Tietz and D. Stöver, "Ferrite-Based Perovskites As Cathode Materials for Anode-Supported Solid Oxide Fuel Cells Part I. Variation of Composition", Solid State Ionics, Volume 176, Issue 15-16, p. 1341-1350, 2005.

[20] C. C. Chen, M. M. Nasrallah and H. U. Anderson, "Cathode/Electrolyte Interactions and Their Expected Impact on SOFC Performance", in S. C. Singhal et al. (Eds.), Proceedings of the Third International Symposium on Solid Oxide Fuel Cells, Volume 1, p. 598-612, 1993.

[21] B. C. H. Steele, "Oxygen-Transport and Exchange in Oxide Ceramics", Journal of Power Sources, Volume 49, Issue 1-3, p. 1-14, 1994.

[22] H. L. Tuller, "Solid State Electrochemical Systems-Opportunities for Nanofabricated or Nanostructured Materials", Journal of Electroceramics, Volume 1, Issue 3, p. 211-218, 1997.

[23] H. L. Tuller, "Ionic Conduction in Nanocrystalline Materials", Solid State Ionics, Volume 131, Issue 1-2, p. 143-157, 2000.

[24] J. Maier, "Defect Chemistry and Ion Transport in Nanostructured Materials. Part II. Aspects of Nanoionics", Solid State Ionics, Volume 157, Issue 1-4, p. 327-334, 2003.

[25] J. Maier, "Nano-Sized Mixed Conductors (Aspects of Nano-Ionics. Part III)", Solid State Ionics, Volume 148, Issue 3-4, p. 367-374, 2002.

[26] S. B. Adler, J. A. Lane and B. C. H. Steele, "Electrode Kinetics of Porous Mixed-Conducting Oxygen Electrodes", Journal of the Electrochemical Society, Volume 143, Issue 11, p. 3554-3564, 1996.

[27] E. Ivers-Tiffée, "Basics: Electrolytes: Solid Oxygen", in J. Garche (Eds.), Encyclopedia of Electrochemical Power Sources, Amsterdam, Netherlands: Elsevier, p. to be announced, 2008.

[28] W. Nernst, "Über Die Elektrolytische Leitung Fester Körper Bei Sehr Hohen Temperaturen", Zeitschrift für Elektrochemie, Volume 6, p. 41-43, 1899.

[29] F. A. Kröger and H. J. Vink, "Relations Between the Concentrations of Imperfections in Crystalline Solids", Solid State Physics-Advances in Research and Applications, Volume 3, p. 307-435, 1956.

[30] W. Weppner, "Electronic Transport Properties and Electrically Induced P-N-Junction in ZrO_2+10m/o Y_2O_3", Journal of Solid State Chemistry, Volume 20, Issue 3, p. 305-314, 1977.

[31] S. P. S. Badwal and M. V. Swain, "ZrO$_2$-Y$_2$O$_3$: Electrical Conductivity of Some Fully and Partially Stabilized Single Grains", Journal of Materials Science Letters, Volume 4, Issue 4, p. 487-489, 1985.

[32] J. F. Baumard and P. Abelard, "Defect Structure and Transport Properties of ZrO$_2$-Based Solid Electrolytes", in N. Claussen et al. (Eds.), Advances in Ceramics - Science and Technology of Zirconia II, Columbus, OH, USA: American Ceramic Society Inc, Volume 12, p. 555-571, 1984.

[33] J. A. Kilner and C. D. Waters, "The Effects of Dopant Cation-Oxygen Vacancy Complexes on the Anion Transport Properties of Non-Stoichiometric Fluorite Oxides", Solid State Ionics, Volume 6, Issue 3, p. 253-259, 1982.

[34] J. A. Kilner, "Fast Oxygen Transport in Acceptor Doped Oxides", Solid State Ionics, Volume 129, Issue 1-4, p. 13-23, 2000.

[35] A. Nakamura and J. B. Wagner, "Defect Structure, Ionic-Conductivity, and Diffusion in Yttria Stabilized Zirconia and Related Oxide Electrolytes With Fluorite Structure", Journal of the Electrochemical Society, Volume 133, Issue 8, p. 1542-1548, 1986.

[36] J. Luo, D. P. Almond and R. Stevens, "Ionic Mobilities and Association Energies From an Analysis of Electrical Impedance of ZrO$_2$-Y$_2$O$_3$ Alloys", Journal of the American Ceramic Society, Volume 83, Issue 7, p. 1703-1708, 2000.

[37] Y. Arachi, H. Sakai, O. Yamamoto, Y. Takeda and N. Imanishai, "Electrical Conductivity of the ZrO$_2$-Ln$_2$O$_3$ (Ln = Lanthanides) System", Solid State Ionics, Volume 121, Issue 1-4, p. 133-139, 1999.

[38] J. Simonin, "Das elektrische Betriebsverhalten der Hochtemperatur-Festelektrolyt-Brennstoffzelle (SOFC) bei Temperaturen deutlich unterhalb der Betriebstemperatur", Diploma Thesis, Universität Karlsruhe (TH), Karlsruhe, Germany, 2006.

[39] O. Yamamoto, "Solid Oxide Fuel Cells: Fundamental Aspects and Prospects", Electrochimica Acta, Volume 45, Issue 15-16, p. 2423-2435, 2000.

[40] T. Hilpert, "Elektrische Charakterisierung von Wärmedämmschichten mittels Impedanzspektroskopie", Dissertation, Universität Karlsruhe (TH), Karlsruhe, Germany, 2006.

[41] X. Guo and J. Maier, "Grain Boundary Blocking Effect in Zirconia: A Schottky Barrier Analysis", Journal of the Electrochemical Society, Volume 148, Issue 3, p. E121-E126, 2001.

[42] P. Abelard and J. F. Baumard, "The Electrical Conductivity of Cubic Stabilized Zirconia", Pure and Applied Chemistry, Volume 67, Issue 11, p. 1891-1904, 1995.

[43] I. R. Gibson, G. P. Dransfield and J. T. S. Irvine, "Influence of Yttria Concentration Upon Electrical Properties and Susceptibility to Ageing of Yttria-Stabilised Zirconias", Journal of the European Ceramic Society, Volume 18, Issue 6, p. 661-667, 1998.

[44] F. T. Ciacchi and S. P. S. Badwal, "The System Y$_2$O$_3$-Sc$_2$O$_3$-ZrO$_2$: Phase Stability and Ionic Conductivity Studies", Journal of the European Ceramic Society, Volume 7, Issue 3, p. 197-206, 1991.

[45] M. J. Verkerk, B. J. Middelhuis and A. J. Burggraaf, "Effect of Grain Boundaries on the Conductivity of High-Purity ZrO$_2$ · Y$_2$O$_3$ Ceramics", Solid State Ionics, Volume 6, Issue 2, p. 159-170, 1982.

[46] S. P. S. Badwal, "Effect of Dopant Concentration on the Grain Boundary and Volume Resistivity of Yttria-Zirconia", Journal of Materials Science Letters, Volume 6, Issue 12, p. 1419-1421, 1987.

[47] J. Kondoh, T. Kawashima, S. Kikuchi, Y. Tomii and Y. Ito, "Effect of Aging on Yttria-Stabilized Zirconia. I. A Study of Its Electrochemical Properties", Journal of the Electrochemical Society, Volume 145, Issue 5, p. 1527-1536, 1998.

[48] A. I. Ioffe, D. S. Rutman and S. V. Karpachov, "On the Nature of the Conductivity Maximum in Zirconia-Based Solid Electrolytes", Electrochimica Acta, Volume 23, Issue 2, p. 141-142, 1978.

[49] T. H. Etsell and S. N. Flengas, "Electrical Properties of Solid Oxide Electrolytes", Chemical Reviews, Volume 70, Issue 3, p. 339-376, 1970.

[50] T. Ishihara, H. Matsuda and Y. Takita, "Doped Lagao3 Perovskite-Type Oxide As A New Oxide Ionic Conductor", Journal of the American Chemical Society, Volume 116, Issue 9, p. 3801-3803, 1994.

[51] B. Cales and J. F. Baumard, "Transport Properties and Defect Structure of Nonstoichiometric Yttria Doped Ceria", Journal of Physics & Chemistry of Solids, Volume 45, Issue 8-9, p. 929-935, 1984.

[52] T. Kudo and H. Obayashi, "Oxygen Ion Conduction of the Fluorite-Type $Ce_{1-x}Ln_xO_{2-x/2}$ (Ln=Lanthanoid Element)", Journal of the Electrochemical Society, Volume 122, Issue 1, p. 142-147, 1975.

[53] K. Yamaji, H. Negishi, T. Horita, N. Sakai and H. Yokokawa, "Vaporization Process of Ga From Doped $LaGaO_3$ Electrolytes in Reducing Atmospheres", Solid State Ionics, Volume 135, Issue 1-4, p. 389-396, 2000.

[54] M. Yashima, M. Kakihana and M. Yoshimura, "Metastable-Stable Phase Diagrams in the Zirconia-Containing Systems Utilized in Solid-Oxide Fuel Cell Application", Solid State Ionics, Volume 86-88, Issue 2, p. 1131-1149, 1996.

[55] B. Butz, P. Kruse, H. Störmer, D. Gerthsen, A. C. Müller, A. Weber and E. Ivers-Tiffée, "Correlation Between Microstructure and Degradation in Conductivity for Cubic Y_2O_3-Doped ZrO_2", Solid State Ionics, Volume 177, Issue 37-38, p. 3275-3284, 2006.

[56] D. P. Thompson, A. M. Dickins and J. S. Thorp, "The Dielectric Properties of Zirconia", Journal of Materials Science, Volume 27, Issue 8, p. 2267-2271, 1992.

[57] M. G. H. M. Hendriks, J. E. ten Elshof, H. J. M. Bouwmeester and H. Verweij, "The Electrochemical Double-Layer Capacitance of Yttria-Stabilised Zirconia", Solid State Ionics, Volume 146, Issue 3-4, p. 211-217, 2002.

[58] M. A. Subramanian and R. D. Shannon, "Dielectric Constant of Y-Stabilized Zirconia, the Polarizability of Zirconia and the Oxide Additivity Rule", Materials Research Bulletin, Volume 24, Issue 12, p. 1477-1483, 1989.

[59] J. S. Thorp and H. P. Buckley, "The Dielectric Constants of Current-Blackened Single Crystal Yttria-Stabilized Zirconia", Journal of Materials Science, Volume 8, Issue 10, p. 1401-1408, 1973.

[60] M. C. Steil, F. Thevenot and M. Kleitz, "Densification of Yttria-Stabilized Zirconia. Impedance Spectroscopy Analysis", Journal of the Electrochemical Society, Volume 144, Issue 1, p. 390-398, 1997.

[61] A. P. Santos, R. Z. Domingues and M. Kleitz, "Grain Boundary Blocking Effect in Tetragonal Yttria Stabilized Zirconia", Journal of the European Ceramic Society, Volume 18, Issue 11, p. 1571-1578, 1998.

[62] J. Maier, "Nano-Ionics: Trivial and Non-Trivial Size Effects on Ion Conduction in Solids", Zeitschrift für Physikalische Chemie, Volume 217, Issue 4, p. 415-436, 2003.

[63] J. Maier, "On the Conductivity of Polycrystalline Materials", Berichte der Bunsen-Gesellschaft-Physical Chemistry Chemical Physics, Volume 90, Issue 1, p. 26-33, 1986.

[64] I. Lubomirsky, J. Fleig and J. Maier, "Modeling of Space-Charge Effects in Nanocrystalline Ceramics: The Influence of Geometry", Journal of Applied Physics, Volume 92, Issue 11, p. 6819-6827, 2002.

[65] J. Maier, "Nanoionics: Ion Transport and Electrochemical Storage in Confined Systems", nature materials, Volume 4, p. 805-815, 2006.

[66] I. Kosacki, T. Suzuki, V. Petrovsky and H. U. Anderson, "Electrical Conductivity of Nanocrystalline Ceria and Zirconia Thin Films", Solid State Ionics, Volume 136-137, p. 1225-1233, 2000.

[67] I. Kosacki, C. M. Rouleau, P. F. Becher, J. Bentley and D. H. Lowndes, "Nanoscale Effects on the Ionic Conductivity in Highly Textured YSZ Thin Films", Solid State Ionics, Volume 176, Issue 13-14, p. 1319-1326, 2005.

[68] A. Cheikh, A. Madani, A. Touati, H. Boussetta and C. Monty, "Ionic Conductivity of Zirconia Based Ceramics From Single Crystals to Nanostructured Polycrystals", Journal of the European Ceramic Society, Volume 21, Issue 10-11, p. 1837-1841, 2001.

[69] U. Brossmann, G. Knöner, H.-E. Schaefer and R. Würschum, "Oxygen Diffusion in Nanocrystalline ZrO_2", Reviews on Advanced Material Science, Volume 6, p. 7-11, 2004.

[70] G. Knöner, K. Reimann, R. Röwer, U. Södervall and H. E. Schäfer, "Enhanced Oxygen Diffusivity in Interfaces of Nanocrystalline $ZrO_2 \cdot Y_2O_3$", in J. Halpern et al. (Eds.), Proceedings of the National Academy of Sciences of the United States of America, Washington, DC, USA: National Academy of Sciences, Volume 100, Issue 7, p. 3870-3873, 2003.

[71] P. Mondal, A. Klein, W. Jaegermann and H. Hahn, "Enhanced Specific Grain Boundary Conductivity in Nanocrystalline Y_2O_3-Stabilized Zirconia", Solid State Ionics, Volume 118, Issue 3-4, p. 331-339, 1999.

[72] S. Y. Chun and N. Mizutani, "The Transport Mechanism of YSZ Thin Films Prepared by MOCVD", Applied Surface Science, Volume 171, Issue 1-2, p. 82-88, 2001.

[73] X.-J. Ning, C.-X. Li, C.-L. Li and G.-J. Yang, "Modification of Microstructure and Electrical Conductivity of Plasma-Sprayed YSZ Deposit Through Post-Densification Process", Materials Science and Engineering A, Volume 428, Issue 1-2, p. 98-105, 2006.

[74] T. Nakakawa, I. Sakaguchi, N. Shibata, K. Matsunaga, T. Yamamoto, H. Haneda and Y. Ikuhara, "Oxygen Diffusion Blocking of Single Grain Boundary in Yttria-Doped Zirconia Bicrystals", Journal of Materials Science, Volume 40, p. 3185-3190, 2005.

[75] X. Guo and Z. Zhang, "Grain Size Dependent Grain Boundary Defect Structure: Case of Doped Zirconia", Acta Materialia, Volume 51, Issue 9, p. 2539-2547, 2003.

[76] X. Guo and Y. Ding, "Grain Boundary Space Charge Effect in Zirconia", Journal of the Electrochemical Society, Volume 151, Issue 1, p. J1-J7, 2004.

[77] F. Boulc'h, E. Djurado and L. Dessemond, "Dopant Segregation and Space Charge Effect in Nanostructured Tetragonal Zirconia", Journal of the Electrochemical Society, Volume 151, Issue 8, p. A1210-A1215, 2004.

[78] Y. Park, P. Chen Su, S. Cha Won, Y. Saito and F. B. Prinz, "Thin-Film SOFCs Using Gastight YSZ Thin Films on Nanoporous Substrates", Journal of the Electrochemical Society, Volume 153, Issue 2, p. A431-A436, 2006.

[79] E. Wanzenberg, F. Tietz, D. Stöver, D. Kek and L. M. Panjan, "Influence of Electrode Contacts on Conductivity Measurements of Thin YSZ Electrolyte Films and the Impact on Solid Oxide Fuel Cells", Solid State Ionics, Volume 164, Issue 3-4, p. 121-129, 2003.

[80] M. Aoki, Y. M. Chiang, I. Kosacki, L. J. R. Lee, H. L. Tuller and Y. Liu, "Solute Segregation and Grain-Boundary Impedance in High-Purity Stabilized Zirconia", Journal of the American Ceramic Society, Volume 79, Issue 5, p. 1169-1180, 1996.

[81] J.-H. Lee, T. Mori, J.-G. Li, T. Ikegami, M. Komatsu and H. Haneda, "Improvement of Grain-Boundary Conductivity of 8 Mol % Yttria-Stabilized Zirconia by Precursor Scavenging of Siliceous Phase", Journal of the Electrochemical Society, Volume 147, Issue 7, p. 2822-2829, 2000.

[82] M. Gödickemeier, B. Michel, A. Orliukas, P. Bohac, K. Sasaki, L. J. Gauckler, H. Heinrich, P. Schwander, G. Kostorz, H. Hofmann and O. Frei, "Effect of Intergranular Glass Films on the Electrical Conductivity of 3Y-TZP", Journal of Materials Research, Volume 9, Issue 5, p. 1228-1240, 1994.

[83] T. van Dijk and A. J. Burggraaf, "Grain Boundary Effects on Ionic Conductivity in Ceramic $Gd_xZr_{1-x}O_{2-(x/2)}$ Solid Solutions", Physica Status Solidi A, Volume 63, Issue 1, p. 229-240, 1981.

[84] J. Fleig, P. Pham, P. Sztulzaft and J. Maier, "Inhomogeneous Current Distributions at Grain Boundaries and Electrodes and Their Impact on the Impedance", Solid State Ionics, Volume 113-115, p. 739-747, 1998.

[85] J. Fleig and J. Maier, "A Finite Element Study on the Grain Boundary Impedance of Different Microstructures", Journal of the Electrochemical Society, Volume 145, Issue 6, p. 2081-2089, 1998.

[86] J. Fleig, "The Grain Boundary Impedance of Random Microstructures: Numerical Simulations and Implications for the Analysis of Experimental Data", Solid State Ionics, Volume 150, Issue 1-2, p. 181-193, 2002.

[87] X. Guo, W. Sigle, J. Fleig and J. Maier, "Role of Space Charge in the Grain Boundary Blocking Effect in Doped Zirconia", Solid State Ionics, Volume 154-155, p. 555-561, 2002.

[88] E. Ivers-Tiffée and A. V. Virkar, "Electrode Polarisations", in S. C. Singhal and K. Kendall (Eds.), High Temperature Solid Oxide Fuel Cells - Fundamentals, Design and Applications, Oxford, UK: Elsevier Ltd, p. 229-260, 2003.

[89] M. Mogensen and P. V. Hendriksen, "Testing of Electrodes, Cells and Short Stacks", in S. C. Singhal and K. Kendall (Eds.), High Temperature Solid Oxide Fuel Cells, Oxford, UK: Elsevier Ltd, p. 261, 2003.

[90] A. Weber, "Entwicklung und Charakterisierung von Werkstoffen und Komponenten für die Hochtemperatur-Brennstoffzelle SOFC", Dissertation, Universität Karlsruhe (TH), Karlsruhe, Germany, 2002.

[91] B. Rüger, A. Weber and E. Ivers-Tiffée, "3D-Modelling and Performance Evaluation of Mixed Conducting (MIEC) Cathodes", ECS Transactions, Volume 7, p. 2065-2074, 2007.

[92] Y. Ohno, S. Nagata and H. Sato, "Effect of Electrode Materials on the Properties of High-Temperature Solid Electrolyte Fuel Cells", Solid State Ionics, Volume 3-4, p. 439-442, 1980.

[93] Y. Takeda, R. Kanno, M. Noda, Y. Tomida and O. Yamamoto, "Cathodic Polarization Phenomena of Perovskite Oxide Electrodes With Stabilized Zirconia", Journal of the Electrochemical Society, Volume 134, Issue 11, p. 2656-2661, 1987.

[94] S. B. Adler, "Factors Governing Oxygen Reduction in Solid Oxide Fuel Cell Cathodes", Chemical Reviews, Volume 104, Issue 10, p. 4791-4843, 2004.

[95] S. C. Singhal, "Recent Progress in Tubular Solid Oxide Fuel Cell Technology", in U. Stimming (Eds.), Proceedings of the Fifth International Symposium on Solid Oxide Fuel Cells (SOFC-V), Pennington, NJ, USA: The Electrochemical Society, p. 37-50, 1997.

[96] H. Yokokawa and T. Horita, "Cathodes", in S. C. Singhal and K. Kendall (Eds.), High Temperature Solid Oxide Fuel Cells: Fundamentals, Design and Applications, New York, NJ, USA: Elsevier, p. 119-147, 2003.

[97] D. Beckel, U. P. Muecke, T. Gyger, G. Florey, A. Infortuna and L. J. Gauckler, "Electrochemical Performance of LSCF Based Thin Film Cathodes Prepared by Spray Pyrolysis", Solid State Ionics, Volume 178, Issue 5-6, p. 407-415, 2007.

[98] E. Ivers-Tiffée, A. Weber and D. Herbstritt, "Materials and Technologies for SOFC-Components", Journal of the European Ceramic Society, Volume 21, Issue 10-11, p. 1805-1811, 2001.

[99] D. Herbstritt, U. Guntow, A. Weber, A. C. Müller and E. Ivers-Tiffée, "Increased Cathode Performance Using a Thin Film LSM Layer on a Structured 8YSZ Electrolyte Surface", in K. Hilpert et al. (Eds.), Proceedings of the 10th International IUPAC Conference, Jülich, Germany: Research Center Jülich, Volume 2, p. 683-686, 2000.

[100] D. Herbstritt, A. Weber, U. Guntow, G. Müller and E. Ivers-Tiffée, "Cathode-Performance: Influence of MOD-Intermediate Layer and Electrolyte Surface Enlargement", in A. J. McEvoy (Eds.), Proceedings of the 4th European Solid Oxide Fuel Cell Forum, Oberrohrdorf, Switzerland: European Fuel Cell Forum, Volume 2, p. 697-706, 2000.

[101] D. Herbstritt, "Entwicklung Und Modellierung Einer Leistungsfähigen Kathodenstruktur Für Die Hochtemperatur-Brennstoffzelle SOFC", Aachen: Mainz GmbH, 2003.

[102] Y. Teraoka, H. M. Zhang, S. Furukawa and N. Yamazoe, "Oxygen Permeation Through Perovskite-Type Oxides", Chemistry Letters, Issue 11, p. 1743-1746, 1985.

[103] L. Qiu, T. H. Lee, L.-M. Liu, Y. L. Yang and A. J. Jacobson, "Oxygen Permeation Studies of $SrCo_{0.8}Fe_{0.2}O_{3-\delta}$", Solid State Ionics, Volume 76, p. 321-329, 1995.

[104] J. E. ten Elshof, H. J. M. Bouwmeester and H. Verweij, "Oxygen Transport Through $La_{1-x}Sr_xFeO_{3-d}$ Membranes. 1. Permeation in Air/He Gradients", Solid State Ionics, Volume 81, Issue 1-2, p. 97-109, 1995.

[105] H. M. Zhang, Y. Shimizu, Y. Teraoka, N. Miura and N. Yamazoe, "Oxygen Sorption and Catalytic Properties of $La_{1-x}Sr_xCo_{1-Y}Fe_yO_3$ Perovskite-Type Oxides", Journal of Catalysis, Volume 121, Issue 2, p. 432-440, 1990.

[106] H. J. M. Bouwmeester and A. J. Burggraaf, "Dense Ceramic Membranes for Oxygen Separation", in P. J. Gellings and H. J. M. Bouwmeester (Eds.), CRC Handbook of Solid State Electrochemistry, Boca Raton, FL, USA: CRC Press, p. 481-553, 1996.

[107] R. D. Shannon, "Revised Effective Ionic Radii and Systematic Studies of Interatomie Distances in Halides and Chaleogenides", Acta Crystallographica, Volume A32, p. 751-767, 1976.

[108] A. N. Petrov, O. F. Kononchuk, A. V. Andreev, V. A. Cherepanov and P. Kofstad, "Crystal Structure, Electrical and Magnetic Properties of $La_{1-x}Sr_xCoO_{3-y}$", Solid State Ionics, Volume 80, Issue 3-4, p. 189-199, 1995.

[109] J. Mizusaki, J. Tabuchi, T. Matsuura, S. Yamauchi and K. Fueki, "Electrical Conductivity and Seebeck Coefficient of Nonstoichiometric $La_{1-x}Sr_xCoO_{3-\delta}$", Journal of the Electrochemical Society, Volume 136, Issue 7, p. 2082-2088, 1989.

[110] M. Sogaard, P. V. Hendriksen, M. Mogensen, F. W. Poulsen and E. Skou, "Oxygen Nonstoichiometry and Transport Properties of Strontium Substituted Lanthanum Cobaltite", Solid State Ionics, Volume 177, Issue 37-38, p. 3285-3296, 2006.

[111] S. R. Wang, M. Katsuki, M. Dokiya and T. Hashimoto, "High Temperature Properties of $La_{0.6}Sr_{0.4}Co_{0.8}Fe_{0.2}O_{3-\delta}$ Phase Structure and Electrical Conductivity", Solid State Ionics, Volume 159, Issue 1-2, p. 71-78, 2003.

[112] R. P. Haggerty and R. Seshadri, "Oxygen Stoichiometry, Crystal Structure, and Magnetism of $La_{0.5}Sr_{0.5}CoO_{3-\delta}$", Journal of Physics: Condensed Matter, Volume 16, Issue 36, p. 6477-6484, 2004.

[113] S. B. Adler, "Chemical Expansivity of Electrochemical Ceramics", Journal of the American Ceramic Society, Volume 84, Issue 9, p. 2117-2119, 2001.

[114] L. W. Tai, M. M. Nasrallah, H. U. Anderson, D. M. Sparlin and S. R. Sehlin, "Structure and Electrical-Properties of $La_{1-x}Sr_xCo_{1-Y}Fe_yO_3$ 1. the System $La_{0.8}Sr_{0.2}Co_{1-Y}Fe_yO_3$", Solid State Ionics, Volume 76, Issue 3-4, p. 259-271, 1995.

[115] N. Q. Minh, "Ceramic Fuel-Cells", Journal of the American Ceramic Society, Volume 76, Issue 3, p. 563-588, 1993.

[116] A. Petric, P. Huang and F. Tietz, "Evaluation of La-Sr-Co-Fe-O Perovskites for Solid Oxide Fuel Cells and Gas Separation Membranes", Solid State Ionics, Volume 135, Issue 1-4, p. 719-725, 2000.

[117] F. M. Figueiredo, F. M. B. Marques and J. R. Frade, "Electrical Properties and Thermal Expansion of $LaCoO_3$ / $La_2(Zr,Y)_2O_7$ Composites", Solid State Ionics, Volume 138, Issue 3-4, p. 173-182, 2001.

[118] F. Morin, G. Trudel and Y. Denos, "The Phase Stability of $La_{0.5}Sr_{0.5}CoO_{3-\delta}$", Solid State Ionics, Volume 96, Issue 3-4, p. 129-139, 1997.

[119] S. Wang, A. Verma, Y. L. Yang, A. J. Jacobson and B. Abeles, "The Effect of the Magnitude of the Oxygen Partial Pressure Change in Electrical Conductivity Relaxation Measurements: Oxygen Transport Kinetics in $La_{0.5}Sr_{0.5}CoO_{3-\delta}$", Solid State Ionics, Volume 140, Issue 1-2, p. 125-133, 2001.

[120] W. Sitte, E. Bucher, W. Preis, I. Papst, W. Grogger and F. Hofer, "Microstructural Aspects of the Ionic Transport Properties of Strontium-Substituted Lanthanum Cobaltites", in P. Knauth et al. (Eds.), Proceeding of the MRS Fall Meeting 2002, Boston, MA, USA: Materials Research Society, Volume 756, p. EE1.7.1-EE1.7.6, 2003.

[121] R. H. E. van Doorn and A. J. Burggraaf, "Structural Aspects of the Ionic Conductivity of $La_{1-x}Sr_xCoO_{3-\delta}$", Solid State Ionics, Volume 128, Issue 1-4, p. 65-78, 2000.

[122] S. Stemmer, A. Sane, N. D. Browning and T. J. Mazanec, "Characterization of Oxygen-Deficient $SrCoO_{3-\delta}$ by Electron Energy-Loss Spectroscopy and Z-Contrast Imaging", Solid State Ionics, Volume 130, Issue 1-2, p. 71-80, 2000.

[123] S. Stemmer, A. J. Jacobson, X. Chen and A. Ignatiev, "Oxygen Vacancy Ordering in Epitaxial $La_{0.5}Sr_{0.5}CoO_{3-\delta}$ Thin Films on (001) $LaAlO_3$", Journal of Applied Physics, Volume 90, Issue 7, p. 3319-3324, 2001.

[124] J. Hadermann, G. van Tendeloo and A. M. Abakumov, "Transmission Electron Microscopy and Structural Phase Transitions in Anion-Deficient Perovskite-Based Oxides", Acta Crystallographica - Section A - Foundations of Crystallography, Volume A61, p. 77-92, 2005.

[125] Z. L. Wang and J. Zhang, "Microstructure of Conductive $La_{1-x}Sr_xCoO_3$ Grown on MgO(001)", Philosophical Magazine A, Volume 72, Issue 6, p. 1513-1529, 1995.

[126] Z. L. Wang and J. Zhang, "Tetragonal Domain Structure and Magnetoresistance of $La_{1-x}Sr_xCoO_3$", Physical Review B, Volume 54, Issue 2, p. 1153-1158, 1996.

[127] Z. L. Wang and J. S. Yin, "Cobalt Valence and Crystal Structure of $La_{0.5}Sr_{0.5}CoO_{2.25}$", Philosophical Magazine B, Volume 77, Issue 1, p. 49-65, 1998.

[128] J. Mizusaki, Y. Mima, S. Yamauchi, K. Fueki and H. Tagawa, "Nonstoichiometry of the Perovskite-Type Oxides $La_{1-x}Sr_xCoO_{3-\delta}$", Journal of Solid State Chemistry, Volume 80, Issue 1, p. 102-111, 1989.

[129] A. N. Petrov, V. A. Cherepanov, O. F. Kononchuk and L. Y. A. Gavrilowa, "Oxygen Nonstoichiometry of $La_{1-x}Sr_xCoO_{3-\delta}$ (0 < x < 0.6)", Journal of Solid State Chemistry, Volume 87, Issue 1, p. 69-76, 1990.

[130] M. Schießl, "Entwicklung einer keramischen Kathode für die Hochtemperaturbrennstoffzelle SOFC (Solid Oxide Fuel Cell)", Dissertation, Universität Erlangen-Nürnberg, Erlangen-Nürnberg, Germany, 1993.

[131] M. H. R. Lankhorst and J. E. tenElshof, "Thermodynamic Quantities and Defect Structure of $La_{0.6}Sr_{0.4}Co_{1-y}Fe_yO_{3-\delta}$ (y=0-0.6) From High-Temperature Coulometric Titration Experiments", Journal of Solid State Chemistry, Volume 130, Issue 2, p. 302-310, 1997.

[132] R. A. de Souza and J. A. Kilner, "Oxygen Transport in $La_{1-X}Sr_XMn_{1-Y}Co_YO_{3-\delta}$ Perovskites - Part I. Oxygen Tracer Diffusion", Solid State Ionics, Volume 106, Issue 3-4, p. 175-187, 1998.

[133] E. Bucher, W. Jantscher, A. Benisek, W. Sitte, W. Preis, I. Rom and F. Hofer, "Transport Properties of $La_{0.4}Sr_{0.6}CoO_{3-\delta}$", Solid State Ionics, Volume 141-142, p. 375-380, 2001.

[134] W. Sitte, E. Bucher and W. Preis, "Nonstoichiometry and Transport Properties of Strontium-Substituted Lanthanum Cobaltites", Solid State Ionics, Volume 154-155, p. 517-522, 2002.

[135] F. S. Baumann, "Oxygen reduction kinetics on mixed conducting SOFC model cathodes", Dissertation, Universität Stuttgart, Stuttgart, Germany, 2006.

[136] W. Zipprich, S. Waschilewski, F. Rocholl and H. D. Wiemhofer, "Improved Preparation of $La_{1-x}Me_xCoO_{3-\delta}$ (Me = Sr, Ca) and Analysis of Oxide Ion Conductivity With Ion Conducting Microcontacts", Solid State Ionics, Volume 101, Issue 2, p. 1015-1023, 1997.

[137] M. H. R. Lankhorst, H. J. M. Bouwmeester and H. Verweij, "High-Temperature Coulometric Titration of $La_{1-x}Sr_xCoO_{3-\delta}$: Evidence for the Effect of Electronic Band Structure on Nonstoichiometry Behavior", Journal of Solid State Chemistry, Volume 133, Issue 2, p. 555-567, 1997.

[138] G. Watterud, "Determination of oxygen transport coefficients in perovskites and perovskite related materials with mixed conductivity", Dissertation, Norwegian University of Science and Technology, Trondheim, Norway, 2005.

[139] L. W. Tai, M. M. Nasrallah, H. U. Anderson, D. M. Sparlin and S. R. Sehlin, "Structure and Electrical-Properties of $La_{1-x}Sr_xCo_{1-Y}Fe_YO_3$ 2. the System $La_{1-x}Sr_xCo_{0.2}Fe_{0.8}O_3$", Solid State Ionics, Volume 76, Issue 3-4, p. 273-283, 1995.

[140] Y. Teraoka, H. M. Zhang, K. Okamoto and N. Yamazoe, "Mixed Ionic-Electronic Conductivity of $La_{1-x}Sr_xCo_{1-Y}Fe_YO_{3-\delta}$ Perovskite-Type Oxides", Materials Research Bulletin, Volume 23, Issue 1, p. 51-58, 1988.

[141] J. A. Lane, S. J. Benson, D. Waller and J. A. Kilner, "Oxygen Transport in $La_{0.6}Sr_{0.4}Co_{0.2}Fe_{0.8}O_{3-\delta}$", Solid State Ionics, Volume 121, Issue 1-4, p. 201-208, 1999.

[142] Y. Teraoka, T. Nobunaga, K. Okamoto, N. Miura and N. Yamazoe, "Influence of Constituent Metal Cations in Substituted $LaCoO_3$ on Mixed Conductivity and Oxygen Permeability", Solid State Ionics, Volume 48, Issue 3-4, p. 207-212, 1991.

[143] H. D. Wiemhöfer, H. G. Bremes, U. Nigge and W. Zipprich, "Studies of Ionic Transport and Oxygen Exchange on Oxide Materials for Electrochemical Gas Sensors", Solid State Ionics, Volume 150, Issue 1-2, p. 63-77, 2002.

[144] E. Bucher, W. Sitte, I. Rom, I. Papst, W. Grogger and F. Hofer, "Microstructure and Ionic Conductivity of Strontium-Substituted Lanthanum Cobaltites", Solid State Ionics, Volume 152-153, p. 417-421, 2002.

[145] E. Bucher, A. Benisek and W. Sitte, "Electrochemical Polarization Measurements on Mixed Conducting Oxides", Solid State Ionics, Volume 157, Issue 1-4, p. 39-44, 2003.

[146] D. O. Klenov, W. Donner, B. Foran and S. Stemmer, "Impact of Stress on Oxygen Vacancy Ordering in Epitaxial $(La_{0.5}Sr_{0.5})CoO_{3-\delta}$ Thin Films", Applied Physics Letters, Volume 82, Issue 20, p. 3427-3429, 2003.

[147] L. M. van der Haar, M. W. den Otter, M. Morskate, H. J. M. Bouwmeester and H. Verweij, "Chemical Diffusion and Oxygen Surface Transfer of $La_{1-x}Sr_xCoO_{3-\delta}$ Studied With Electrical Conductivity Relaxation", Journal of the Electrochemical Society, Volume 149, Issue 3, p. J41-J46, 2002.

[148] S. B. Adler, "Mechanism and Kinetics of Oxygen Reduction on Porous $La_{1-x}Sr_xCoO_{3-\delta}$ Electrodes", Solid State Ionics, Volume 111, Issue 1-2, p. 125-134, 1998.

[149] J. A. Kilner, R. A. de Souza and I. C. Fullarton, "Surface Exchange of Oxygen in Mixed Conducting Perovskite Oxides", Solid State Ionics, Volume 86-88, Issue 2, p. 703-709, 1996.

[150] T. Kawada, K. Masuda, J. Suzuki, A. Kaimai, K. Kawamura, Y. Nigara, J. Mizusaki, H. Yugami, H. Arashi, N. Sakai and H. Yokokawa, "Oxygen Isotope Exchange With a Dense $La_{0.6}Sr_{0.4}CoO_{3-\delta}$ Electrode on a $Ce_{0.9}Ca_{0.1}O_{1.9}$ Electrolyte", Solid State Ionics, Volume 121, Issue 1-4, p. 271-279, 1999.

[151] R. H. E. van Doorn, I. C. Fullarton, R. A. de Souza, J. A. Kilner, H. J. M. Bouwmeester and A. J. Burggraaf, "Surface Oxygen Exchange of $La_{0.3}Sr_{0.7}CoO_{3-\delta}$", Solid State Ionics, Volume 96, Issue 1-2, p. 1-7, 1997.

[152] J. Maier, "Physical Chemistry of Ionic Materials: Ions and Electrons in Solids", San Francisco, CA, USA: John Wiley & Sons Inc., 2004.

[153] H. J. M. Bouwmeester, H. Kruidhof and A. J. Burggraaf, "Importance of the Surface Exchange Kinetics As Rate Limiting Step in Oxygen Permeation Through Mixed-Coducting Oxides", Solid State Ionics, Volume 72, Issue 2, p. 185-194, 1994.

[154] F. S. Baumann, J. Fleig and J. Maier, "Comparison of the Surface Exchange Resistance of Mixed Conducting SOFC Cathode Materials", in J. A. Kilner et al. (Eds.), Proceedings of the 7th European Solid Oxide Fuel Cell Forum, Oberrohrdorf, Switzerland: European Fuel Cell Forum, p. 1-4, 2006.

[155] F. S. Baumann, J. Fleig, H. U. Habermeier and J. Maier, "Impedance Spectroscopic Study on Well-Defined $(La,Sr)(Co,Fe)O_{3-\delta}$ Model Electrodes", Solid State Ionics, Volume 177, Issue 11-12, p. 1071-1081, 2006.

[156] O. Yamamoto, Y. Takeda, R. Kanno and M. Noda, "Perovskite-Type Oxides As Oxygen Electrodes for High Temperature Oxide Fuel Cells", Solid State Ionics, Volume 22, Issue 2-3, p. 241-246, 1987.

[157] E. Ivers-Tiffée, M. Schießl, H. J. Oel and W. Wersing, "SOFC Cathodes With Mixed Conduction: Advantages and Limitations of Co Containing Perovskites", in F. W. Poulsen et al. (Eds.), Proceedings of the 14th Risø International Symposium on Materials Science: High Temperature Electrochemical Behaviour of Fast Ion and Mixed Conductors, Roskilde, Denmark: Risø National Laboratory, p. 69-88, 1993.

[158] H. Y. Tu, Y. Takeda, N. Imanishi and O. Yamamoto, "$Ln_{0.4}Sr_{0.6}Co_{0.8}Fe_{0.2}O_{3-\delta}$ (Ln = La, Pr, Nd, Sm, Gd) for the Electrode in Solid Oxide Fuel Cells", Solid State Ionics, Volume 117, Issue 3-4, p. 277-281, 1999.

[159] W. H. Kim, H. S. Song, J. Moon and H. W. Lee, "Intermediate Temperature Solid Oxide Fuel Cell Using $(La,Sr)(Co,Fe)O_3$-Based Cathodes", Solid State Ionics, Volume 177, Issue 35-36, p. 3211-3216, 2006.

[160] J. A. Labrincha, J. R. Frade and F. M. B. Marques, "$La_2Zr_2O_7$ Formed at Ceramic Electrode/YSZ Contacts", Journal of Materials Science, Volume 28, Issue 14, p. 3809-3815, 1993.

[161] J. A. Labrincha, J. R. Frade and F. M. B. Marques, "Reaction Between Cobaltate Cathodes and YSZ", in F. Grosz et al. (Eds.), Proceedings of the 2nd International Symposium on SOFCs, Brussels, Belgium: Commission of European Communities, p. 689-696, 1991.

[162] M. Sase, D. Ueno, K. Yashiro, A. Kaimai, T. Kawada and J. Mizusaki, "Interfacial Reaction and Electrochemical Properties of Dense (La,Sr)CoO$_{3-\delta}$ Cathode on YSZ (100)", Journal of Physics & Chemistry of Solids, Volume 66, Issue 2-4, p. 343-348, 2005.

[163] V. A. Cherepanov, L. Y. Barkhatova, A. N. Petrov and V. I. Voronin, "Phase Equilibria in the La-Sr-Co-O System and Thermodynamic Stability of the Single Phases", in M. Dokiya et al. (Eds.), Proceedings of the Fourth International Symposium on Solid Oxide Fuel Cells (SOFC-IV), Pennington, NJ, USA: The Electrochemical Society, p. 434-443, 1995.

[164] F. W. Poulsen and N. van der Puil, "Phase Relations and Conductivity of Sr- and La-Zirconates", Solid State Ionics, Volume 53-56, Issue 2, p. 777-783, 1991.

[165] J. A. Labrincha, F. M. B. Marques and J. R. Frade, "Protonic and Oxygen-Ion Conduction in SrZrO$_3$-Based Materials", Journal of Materials Science, Volume 30, Issue 11, p. 2785-2792, 1995.

[166] M. Shiono, K. Kobayashi, T. L. Nguyen, K. Hosoda, T. Kato, K. Ota and M. Dokiya, "Effect of CeO$_2$ Interlayer on ZrO$_2$ Electrolyte/La(Sr)CoO$_3$ Cathode for Low-Temperature SOFCs", Solid State Ionics, Volume 170, Issue 1-2, p. 1-7, 2004.

[167] T. L. Nguyen, K. Kobayashi, T. Honda, Y. Iimura, K. Kato, A. Neghisi, K. Nozaki, F. Tappero, K. Sasaki, H. Shirahama, K. Ota, M. Dokiya and T. Kato, "Preparation and Evaluation of Doped Ceria Interlayer on Supported Stabilized Zirconia Electrolyte SOFCs by Wet Ceramic Processes", Solid State Ionics, Volume 174, Issue 1-4, p. 163-174, 2004.

[168] M. Hrovat, J. Holc and S. Bernik, "Subsolidus Phase Equilibria in the La$_2$O$_3$-CeO$_2$-Co$_2$O$_3$ System", Journal of Materials Research, Volume 14, Issue 5, p. 1692-1694, 1999.

[169] M. Gödickemeier and L. J. Gauckler, "Engineering of Solid Oxide Fuel Cells With Ceria-Based Electrolytes", Journal of the Electrochemical Society, Volume 145, Issue 2, p. 414-421, 1998.

[170] H. Uchida, S. Arisaka and M. Watanabe, "High Performance Electrodes for Medium-Temperature Solid Oxide Fuel Cells: Activation of La(Sr)CoO$_3$ Cathode With Highly Dispersed Pt Metal Electrocatalysts", Solid State Ionics, Volume 135, Issue 1-4, p. 347-351, 2000.

[171] T. Kawada, J. Suzuki, M. Sase, A. Kaimai, K. Yashiro, Y. Nigara, J. Mizusaki, K. Kawamura and H. Yugami, "Determination of Oxygen Vacancy Concentration in a Thin Film of La$_{0.6}$Sr$_{0.4}$CoO$_{3-\delta}$ by an Electrochemical Method", Journal of the Electrochemical Society, Volume 149, Issue 7, p. E252-E259, 2002.

[172] C. C. Chen, M. M. Nasrallah and H. U. Anderson, "Synthesis and Characterization of (CeO$_2$)$_{0.8}$(SmO$_{1.5}$)$_{0.2}$ Thin-Films From Polymeric Precursors", Journal of the Electrochemical Society, Volume 140, Issue 12, p. 3555-3560, 1993.

[173] M. Liu and D. Y. Wang, "Preparation of La$_{1-z}$Sr$_z$Co$_{1-y}$Fe$_y$O$_{3-x}$ Thin Films, Membranes, and Coatings on Dense and Porous Substrates", Journal of Materials Research, Volume 10, Issue 12, p. 3210-3221, 1995.

[174] I. Zergioti, A. W. M. de Laat, U. Guntow, F. Hutter and O. Maerten, "Laser Sintering of Perovskite-Oxide and Metal Coatings by the Sol Gel Process", Applied Physics A, Volume 69, p. S433-S436, 1999.

[175] A. Bieberle-Hütter and H. L. Tuller, "Fabrication and Structural Characterization of Interdigitated Thin Film $La_{1-x}Sr_xCoO_3$ (LSCO) Electrodes", Journal of Electroceramics, Volume 16, Issue 2, p. 151-157, 2006.

[176] A. Bieberle-Hütter, M. Sogaard and H. L. Tuller, "Electrical and Electrochemical Characterization of Microstructured Thin Film $La_{1-x}Sr_xCoO_3$ Electrodes", Solid State Ionics, Volume 177, Issue 19-25, p. 1969-1975, 2006.

[177] E. Koep, C. Jin, M. Haluska, R. Das, R. Narayan, K. Sandhage, R. Snyder and M. Liu, "Microstructure and Electrochemical Properties of Cathode Materials for SOFCs Prepared Via Pulsed Laser Deposition", Journal of Power Sources, Volume 161, Issue 1, p. 250-255, 2006.

[178] M. Prestat, A. Infortuna, S. Korrodi, S. Rey-Mermet, P. Muralt and L. J. Gauckler, "Oxygen Reduction at Thin Dense $La_{0.52}Sr_{0.48}Co_{0.18}Fe_{0.82}O_{3-\delta}$ Electrodes", Journal of Electroceramics, Volume 18, Issue 1-2, p. 111-120, 2007.

[179] J. Fleig, F. S. Baumann, V. Brichzin, H. R. Kim, J. Jamnik, G. Cristiani, H. U. Habermeier and J. Maier, "Thin Film Microelectrodes in SOFC Electrode Research", Fuel Cells, Volume 6, Issue 3-4, p. 284-292, 2006.

[180] K. W. Chour, J. Chen and R. Xu, "Metal-Organic Vapor Deposition of YSZ Electrolyte Layers for Solid Oxide Fuel Cell Applications", Thin Solid Films, Volume 304, Issue 1-2, p. 106-112, 1997.

[181] G. Soyez, J. A. Eastman, L. J. Thompson, G. R. Bai, P. M. Baldo, A. W. McCormick, R. J. DiMelfi, A. A. Elmustafa, M. F. Tambwe and D. S. Stone, "Grain-Size-Dependent Thermal Conductivity of Nanocrystalline Yttria-Stabilized Zirconia Films Grown by Metal-Organic Chemical Vapor Deposition", Applied Physics Letters, Volume 77, Issue 8, p. 1155-1157, 2000.

[182] Y. Y. Chen and W. C. J. Wei, "Processing and Characterization of Ultra-Thin Yttria-Stabilized Zirconia (YSZ) Electrolytic Films for SOFC", Solid State Ionics, Volume 177, Issue 3-4, p. 351-357, 2006.

[183] R. Chiba, F. Yoshimura, J. Yamaki, T. Ishii, T. Yonezawa and K. Endou, "Ionic Conductivity and Morphology in Sc_2O_3 and Al_2O_3 Doped ZrO_2 Films Prepared by the Sol-Gel Method", Solid State Ionics, Volume 104, Issue 3-4, p. 259-266, 1997.

[184] I. Kosacki, B. Gorman and U. Anderson, "Microstructure and Electrical Conductivity in Nanocrystalline Oxide Thin Films", in T. A. Ramanarayanan (Eds.), Proceedings of the Third International Symposium on Solid Oxide Fuel Cells (SOFC-III), Pennington, NJ, USA: The Electrochemical Society, Volume III, p. 631-642, 1998.

[185] Y. H. Lee, C. W. Kuo, C. J. Shih, I. M. Hung, K. Z. Fung, S. B. Wen and M. C. Wang, "Characterization on the Electrophoretic Deposition of the 8 Mol% Yttria-Stabilized Zirconia Nanocrystallites Prepared by a Sol-Gel Process", Materials Science and Engineering A-Structural Materials Properties Microstructure and Processing, Volume 445-446, p. 347-354, 2007.

[186] B. J. Kim, J. Lee and J. B. Yoo, "Sol-Gel Derived (La,Sr)CoO_3 Thin Films on Silica Glass", Thin Solid Films, Volume 341, Issue 1-2, p. 13-17, 1999.

[187] J. Pagnaer, A. Hardy, D. Mondelaers, G. Vanhoyland, J. D'Haen, M. K. Van Bael, H. Van den Rul, J. Mullens and L. C. Van Poucke, "Preparation of $La_{0.5}Sr_{0.5}CoO_3$ Powders and Thin Film From a New Aqueous Solution-Gel Precursor", Materials Science and Engineering B-Solid State Materials for Advanced Technology, Volume 118, Issue 1-3, p. 79-83, 2005.

[188] H. J. Hwang, J. Moon, M. Awano and K. Maeda, "Sol-Gel Route to Porous Lanthanum Cobaltite ($LaCoO_3$) Thin Films", Journal of the American Ceramic Society, Volume 83, Issue 11, p. 2852-2854, 2000.

[189] C. Argirusis, M. Kilo, P. Fielitz, G. Borchardt, U. Guntow, A. Weber, A. C. Müller and E. Ivers-Tiffée, "Chemical Diffusion of Cobalt in the System $La_{0.9}Sr_{0.1}Ga_{0.8}Mg_{0.2}O_{3-d}$/$La_{1-X}Sr_XCoO_{3-d}$ (x=0.3 to 0.4)", in H. Yokokawa et al. (Eds.), Proceedings of the Seventh International Symposium on Solid Oxide Fuel Cells (SOFC-VII), Pennington, USA: The Electrochemical Society, p. 914-921, 2001.

[190] P. Charpentier, P. Fragnaud, D. M. Schleich, Y. Denos and E. Gehain, "Preparation of Thin Film SOFCs Working at Reduced Temperature", Ionics, Volume 4, Issue 1-2, p. 118-123, 1998.

[191] O. Wilhelm, S. E. Pratsinis, D. Perednis and L. J. Gauckler, "Electrospray and Pressurized Spray Deposition of Yttria-Stabilized Zirconia Films", Thin Solid Films, Volume 479, Issue 1-2, p. 121-129, 2005.

[192] D. Perednis, O. Wilhelm, S. E. Pratsinis and L. J. Gauckler, "Morphology and Deposition of Thin Yttria-Stabilized Zirconia Films Using Spray Pyrolysis", Thin Solid Films, Volume 474, Issue 1-2, p. 84-95, 2005.

[193] M. F. Garcia-Sanchez, J. Pena, A. Ortiz, G. Santana, J. Fandino, M. Bizarro, F. Cruz-Gandarilla and J. C. Alonso, "Nanostructured YSZ Thin Films for Solid Oxide Fuel Cells Deposited by Ultrasonic Spray Pyrolysis", Solid State Ionics, Volume 179, Issue 7-8, p. 243-249, 2008.

[194] D. Beckel, "Thin Film Cathodes for Micro Solid Oxide Fuel Cells", Dissertation, Swiss Federal Institute of Technology Zürich, Zürich, Switzerland, 2007.

[195] J. Will, A. Mitterdorfer, C. Kleinlogel, D. Perednis and L. J. Gauckler, "Fabrication of Thin Electrolytes for Second-Generation Solid Oxide Fuel Cells", Solid State Ionics, Volume 131, Issue 1-2, p. 79-96, 2000.

[196] H. Chen and C. X. Ding, "Nanostructured Zirconia Coating Prepared by Atmospheric Plasma Spraying", Surface & Coatings Technology, Volume 150, Issue 1, p. 31-36, 2002.

[197] G. Witz, V. Shklover, W. Steurer, S. Bachegowda and H. P. Bossmann, "Phase Evolution in Yttria-Stabilized Zirconia Thermal Barrier Coatings Studied by Rietveld Refinement of X-Ray Powder Diffraction Patterns", Journal of the American Ceramic Society, Volume 90, Issue 9, p. 2935-2940, 2007.

[198] J. H. Joo and G. M. Choi, "Electrical Conductivity of YSZ Film Grown by Pulsed Laser Deposition", Solid State Ionics, Volume 177, Issue 11-12, p. 1053-1057, 2006.

[199] K. Rodrigo, J. Knudsen, N. Pryds, J. Schou and S. Linderoth, "Characterization of Yttria-Stabilized Zirconia Thin Films Grown by Pulsed Laser Deposition (PLD) on Various Substrates", Applied Surface Science, Volume 254, Issue 4, p. 1338-1342, 2007.

[200] X. Chen, N. J. Wu, D. L. Ritums and A. Ignatiev, "Pulsed Laser Deposition of Conducting Porous La-Sr-Co-O Films", Thin Solid Films, Volume 342, Issue 1-2, p. 61-66, 1999.

[201] N. Imanishi, Y. Sumiya, K. Yoshimura, T. Matsumura, A. Hirano, Y. Takeda, D. Mori and R. Kanno, "Impedance Study and TEM Characterization of a PLD Perovskite Air Electrode", Solid State Ionics, Volume 177, Issue 19-25, p. 2165-2173, 2006.

[202] D. Mori, H. Oka, Y. Suzuki, N. Sonoyama, A. Yamada, R. Kanno, Y. Sumiya, N. Imanishi and Y. Takeda, "Synthesis, Structure, and Electrochemical Properties of Epitaxial Perovskite $La_{0.8}Sr_{0.2}CoO_3$ Film on YSZ Substrate", Solid State Ionics, Volume 177, Issue 5-6, p. 535-540, 2006.

[203] F. S. Baumann, J. Fleig, M. Konuma, U. Starke, H. U. Habermeier and J. Maier, "Strong Performance Improvement of $La_{0.6}Sr_{0.4}Co_{0.8}Fe_{0.2}O_{3-d}$ SOFC Cathodes by Electrochemical Activation", Journal of the Electrochemical Society, Volume 152, Issue 10, p. A2074-A2079, 2005.

[204] B. W. Busch, W. H. Schulte, E. Garfunkel, T. Gustafsson, W. Qi, R. Nieh and J. Lee, "Oxygen Exchange and Transport in Thin Zirconia Films on Si(100)", Physical Review B, Volume 62, Issue 20, p. R13290-R13293, 2000.

[205] D. O. Klenov, W. Donner, L. Chen, A. J. Jacobson and S. Stemmer, "Composition Control of Radio-Frequency Magnetron Sputter-Deposited $La_{0.5}Sr_{0.5}CoO_{3-\delta}$ Thin Films", Journal of Materials Research, Volume 18, Issue 1, p. 188-194, 2003.

[206] M. Bockmeyer and P. Löbmann, "Densification and Microstructural Evolution of TiO_2 Films Prepared by Sol-Gel Processing", Chemistry of Materials, Volume 18, Issue 18, p. 4478-4485, 2006.

[207] M. Bockmeyer and P. Löbmann, "Crack Formation in TiO_2 Films Prepared by Sol-Gel Processing: Quantification and Characterization", Thin Solid Films, Volume 515, Issue 13, p. 5212-5219, 2007.

[208] P. Löbmann, R. Jahn, S. Seifert and D. Sporn, "Inorganic Thin Films Prepared From Soluble Powders and Their Applications", Journal of Sol-Gel Science and Technology, Volume 19, p. 473-477, 2000.

[209] M. Mallak, M. Bockmeyer and P. Loebmann, "Liquid Phase Deposition of TiO_2 on Glass: Systematic Comparison to Films Prepared by Sol-Gel Processing", Thin Solid Films, Volume 515, Issue 20-21, p. 8072-8077, 2007.

[210] R. C. Jaeger, "Introduction to Microelectronic Fabrication", Upper Saddle River, NJ, USA: Prentice Hall Inc., 2002.

[211] R. Krüger, M. J. Bockmeyer, A. Dutschke and P. C. Löbmann, "Continuous Sol-Gel Coating of Ceramic Multifilaments: Evaluation of Fiber Bridging by Three-Point Bending Test", Journal of the American Ceramic Society, Volume 89, Issue 7, p. 2080-2088, 2006.

[212] M. Bockmeyer, "Stucture and Densification of Thin Films Prepared from Soluble Precursor Powders by Sol-Gel Processing", Dissertation, Universität Würzburg, Würzburg, Germany, 2007.

[213] D. Herbstritt, A. Weber and E. Ivers-Tiffée, "Increased Cathode Performance Using a Structured Electrolyte Surface", in S. C. Singhal et al. (Eds.), Proceedings of the Sixth International Symposium on Solid Oxide Fuel Cells (SOFC-VI), Pennington, NJ, USA: The Electrochemical Society, p. 972-980, 1999.

[214] L. Dieterle, D. Bach, R. Schneider, H. Störmer, D. Gerthsen, U. Guntow, E. Ivers-Tiffée, A. Weber, C. Peters and H. Yokokawa, "Structural and Chemical Properties of Nanocrystalline $La_{0.5}Sr_{0.5}CoO_{3-\delta}$ Layers on Yttria-Stabilized Zirconia Analyzed by Transmission Electron Microscopy", Journal of Materials Science, Volume 43, Issue 9, p. 3135-3143, 2008.

[215] B. Butz, H. Störmer, D. Gerthsen, M. Bockmeyer, R. Krüger, E. Ivers-Tiffée and M. Luysberg, "Microstructure of Nanocrystalline Y-Doped Zirconia Thin Films Obtained by Sol-Gel Processing", Journal of the American Ceramic Society, Volume 91, Issue 7, p. 2281-2289, 2008.

[216] L. Reimer, "Transmission Electron Microscopy: Physics of Image Formation and Microanalysis", New York: Springer series in optical sciences, 1993.

[217] L. Jian, T. Malis and S. Dionne, "Recent Advances in FIB-TEM Specimen Preparation Techniques", Materials Characterization, Volume 57, Issue 1, p. 64-70, 2006.

[218] D. Fuchs, M. Adam, P. Schweiss, S. Gerhold, S. Schuppler, R. Schneider and B. Obst, "Structural Properties of Slightly Off-Stoichiometric Homoepitaxial SrTixO3-Delta Thin Films", Journal of Applied Physics, Volume 88, Issue 4, p. 1844-1850, 2000.

[219] J. L. M. Rupp, A. Infortuna and L. J. Gauckler, "Microstrain and Self-Limited Grain Growth in Nanocrystalline Ceria Ceramics", Acta Materialia, Volume 54, Issue 7, p. 1721-1730, 2006.

[220] J. R. Macdonald, "Impedance Spectroscopy", New York, USA: John Wiley & Sons, 1987.

[221] C. Peters, A. Weber and E. Ivers-Tiffée, "Grain Size Effects in 8YSZ Thin Film Electrolytes", in Y. Grin et al. (Eds.), Proceedings of the International Conference on Advanced Processing for Novel Functional Materials (APNFM), Dresden, Germany: APNFM, p. in print, 2008.

[222] O. T. Özkan and A. J. Moulson, "The Electrical Conductivity of Single-Crystal and Polycrystalline Aluminium Oxide", Journal of Physics D: Applied Physics, Volume 3, p. 983-987, 1970.

[223] A. Weber, A. C. Müller, D. Herbstritt and E. Ivers-Tiffée, "Characterization of SOFC Single Cells", in H. Yokokawa et al. (Eds.), Proceedings of the Seventh International Symposium on Solid Oxide Fuel Cells (SOFC-VII), Pennington, NJ, USA: The Electrochemical Society, p. 952-962, 2001.

[224] S. Primdahl and M. Mogensen, "Gas Diffusion Impedance in Characterization of Solid Oxide Fuel Cell Anodes", Journal of the Electrochemical Society, Volume 146, Issue 8, p. 2827-2833, 1999.

[225] H. Schichlein, M. Feuerstein, A. C. Müller, A. Weber, A. Krügel and E. Ivers-Tiffée, "System Identification: a New Modelling Approach for SOFC Single Cells", in S. C. Singhal et al. (Eds.), Proceedings of the Sixth International Symposium on Solid Oxide Fuel Cells, p. 1069-1077, 1999.

[226] H. Schichlein, A. C. Müller, M. Voigts, A. Krügel and E. Ivers-Tiffée, "Deconvolution of Electrochemical Impedance Spectra for the Identification of Electrode Reaction Mechanisms in Solid Oxide Fuel Cells", Journal of Applied Electrochemistry, Volume 32, Issue 8, p. 875-882, 2002.

[227] Service group Scientific Data Processing at Freiburg Materials Research Center, "User Manual FTIKREG: A program for the solution of Fredholm integral equations of the first kind", 2008.

[228] Z. Lei and Q. Zhu, "Low Temperature Processing of Dense Nanocrystalline Scandia-Doped Zirconia (ScSZ) Ceramics", Solid State Ionics, Volume 176, Issue 37-38, p. 2791-2797, 2005.

[229] C. Peters, M. Bockmeyer, R. Krüger, A. Weber and E. Ivers-Tiffée, "Processing of Dense Nanocrystalline Zirconia Thin Films by Sol-Gel Method", in D. Kumar et al. (Eds.), Materials Research Society Symposium Proceedings - Current and Future Trends of Functional Oxide Films, Warrendale: Materials Research Society, Volume 928E, p. GG16-01, 2006.

[230] J. Seydel, "Nanokristallines Zirkondioxid für Hochtemperatur-Brennstoffzellen", Dissertation, Technische Universität Darmstadt, Darmstadt, Germany, 2003.

[231] A. Díaz-Parralejo, R. Caruso, A. Ortiz and F. Guiberteau, "Densification and Porosity Evaluation of $ZrO_2 - 3$ Mol.% Y_2O_3 Sol–Gel Thin Films", Thin Solid Films, Volume 458, Issue 1-2, p. 92-97, 2004.

[232] B. Gorman and H. U. Anderson, "Microstructure Development in Unsupported Thin Films", Journal of the American Ceramic Society, Volume 85, Issue 4, p. 981-985, 2002.

[233] C. Sakurai, T. Fukui and M. Okuyama, "Preparation of Zirconia Coatings by Hydrolysis of Zirconium Alkoxide With Hydrogen Peroxide", Journal of the American Ceramic Society, Volume 76, Issue 4, p. 1061-1064, 1993.

[234] K. T. Miller and F. F. Lange, "Highly Oriented Thin Films of Cubic Zirconia on Sapphire Through Grain Growth Seeding", Journal of Materials Research, Volume 6, Issue 11, p. 2387-2392, 1991.

[235] F. C. M. Woudenberg, W. F. C. Sager, J. E. ten Elshof and H. Verweij, "Nanostructured Dense ZrO_2 Thin Films From Nanoparticles Obtained by Emulsion Precipitation", Journal of the American Ceramic Society, Volume 87, Issue 8, p. 1430-1435, 2004.

[236] R. Neagu, E. Djurado, L. Ortega and T. Pagnier, "ZrO_2-Based Thin Films Synthesized by Electrostatic Spray Deposition: Effect of Post-Deposition Thermal Treatments", Solid State Ionics, Volume 177, Issue 17-18, p. 1443-1449, 2005.

[237] Q. Zhu and B. Fan, "Low Temperature Sintering of 8YSZ Electrolyte Films for Intermediate Temperature Solid Oxide Fuel Cells", Solid State Ionics, Volume 176, Issue 9-10, p. 889-894, 2005.

[238] M. N. Rahaman, "Sintering of Ceramics", Boca Raton, FL, USA: Taylor & Francis Group, CRC Press, p. 105-176, 2008.

[239] H. Yokokawa, "Thermodynamic Database MALT for Windows", Kagaku Gijutsu-Sha, http://www.kagaku.com/malt/index.html, (31-5-2008).

[240] H. Yokokawa, "Generalized Chemical Potential Diagram and Its Applications to Chemical Reactions at Interfaces Between Dissimilar Materials", Journal of Phase Equilibria, Volume 20, Issue 3, p. 258-287, 1999.

[241] H. Yokokawa, "Understanding Materials Compatibility", Annual review of materials research, Volume 33, p. 581-610, 2003.

[242] H. Yokokawa, N. Sakai, T. Kawada and M. Dokiya, "Thermodynamic Stabilities of Perovskite Oxides for Electrodes and Other Electrochemical Materials", Solid State Ionics, Volume 52, Issue 1-3, p. 43-56, 1992.

[243] D. D. Wagman, W. H. Evans, V. B. Parker, R. H. Schumm, I. Halow, S. M. Bailey, K. I. Churney and R. I. Nuttall, "The NBS Tables of Chemical Thermodynamic Properties: Selected Values for Inorganic and C_1 and C_2 Organic Substances in SI Units", Journal of Physical and Chemical Reference Data, Volume 11, Issue 2, p. 392, 1982.

[244] H. Yokokawa, N. Sakai, T. Kawada and M. Dokiya, "Thermodynamic Analysis of Reaction Profiles Between $LaMO_3$ (M=Ni,Co,Mn) and ZrO_2", Journal of the Electrochemical Society, Volume 138, Issue 9, p. 2719-2727, 1991.

[245] H. Yokokawa, N. Sakai, T. Kawada and M. Dokiya, "Chemical Thermodynamic Considerations on Reactivity of Perovskite Oxide Electrodes With Zirconia (in Japanese)", Denki Kagaku, Volume 57, Issue 8, p. 821-828, 1989.

[246] H. Yokokawa, N. Sakai, T. Kawada and M. Dokiya, "Thermodynamic Analysis on Relation Between Nonstoichiometry of $LaMnO_3$ Perovskites and Their Reactivity With ZrO_2 (in Japanese)", Denki Kagaku, Volume 57, Issue 8, p. 829-836, 1989.

[247] H. Yokokawa, N. Sakaki, T. Kawada and M. Dokiya, "Chemical Thermodynamic Considerations on Chemical-Stability of $(La_{1-x}Sr_x)_YMnO_3$ Perovskite Air Electrode Against Reaction With ZrO_2 Electrolyte in Sofc", Denki Kagaku, Volume 58, Issue 2, p. 162-171, 1990.

[248] H. Yokokawa, N. Sakai, T. Kawada and M. Dokiya, "Chemical-Potential Diagrams for La-M-Zr-O (M=V, Cr, Mn, Fe, Co, Ni) Systems - Reactivity of Perovskites With Zirconia As A Function of Oxygen Potential", Denki Kagaku, Volume 58, Issue 6, p. 489-497, 1990.

[249] V. V. Vashook, M. V. Zinkevich, H. Ullmann, J. Paulsen, N. Trofimenko and K. Teske, "Oxygen Non-Stoichiometry and Electrical Conductivity of the Binary Strontium Cobalt Oxide $SrCoO_x$", Solid State Ionics, Volume 99, Issue 1-2, p. 23-32, 1997.

[250] V. A. Cherepanov, L. Y. A. Gavrilova, L. Yu. Barkhatova, V. I. Voronin, M. V. Trifonova and O. A. Bukhner, "Phase Equilibria in the La-Me-Co-O (Me=Ca, Sr, Ba) Systems", Ionics, Volume 4, Issue 3-4, p. 309-315, 1998.

[251] H. Yokokawa, N. Sakai, T. Kawada and M. Dokiya, "Thermodynamic Analysis on Interface Between Perovskite Electrode and YSZ Electrolyte", Solid State Ionics, Volume 40-41, Issue 1, p. 398-401, 1990.

[252] M. Rühle, N. Claussen and A. H. Heuer, "Microstructural Studies of Y_2O_3-Containing Tetragonal ZrO_2 Polycrystals (Y-TZP)", in M. Rühle et al. (Eds.), Advances in Ceramics: Science and Technology of Zirconia II, Chapter 12, Columbus, OH: American Ceramics Society, p. 352-370, 1984.

[253] H. Schubert, N. Claussen and M. Rühle, "Preparation of Y_2O_3-Stabilized Tetragonal ZrO_2 Polycrystals (Y-TZP) From Different Powders", in M. Rühle et al. (Eds.), Advances in Ceramics: Science and Technology of Zirconia II, Chapter 12, Columbus, OH: American Ceramics Society, p. 766-773, 1984.

[254] M. F. Yan, "Microstructural Control in the Processing of Electronic Ceramics", Material Science Engineering, Volume 48, Issue 1, p. 53-72, 1981.

[255] B. C. H. Steele and E. P. Butler, "Electrical Behaviour of Grain Boundaries in Zirconia and Related Ceramic Electrolytes", in B. C. H. Steele (Eds.), British Ceramic Proceedings, London, England: British Ceramic Society, Volume 36, p. 45-55, 1985.

[256] S. Boulfrad, L. Dessemond and E. Djurado, "Grain Size Dependence of Ionic Conductivity in 8YSZ Nanostructured Ceramics for IT-SOFC", in J. A. Kilner et al. (Eds.), Proceedings of the 7th European Solid Oxide Fuel Cell Forum, Oberrohrdorf, Switzerland: European Fuel Cell Forum, p. 1-11, 2006.

[257] R. A. de Souza, M. J. Pietrowski, U. Anselmi Tamburini, S. Kim, Z. A. Munir and M. Martin, "Oxygen Diffusion in Nanocrystalline Yttria-Stabilized Zirconia: the Effect of Grain Boundaries", Physical Chemistry Chemical Physics, Volume 10, p. 2067-2072, 2008.

[258] H. J. Kweon, S. T. Kuk, H. B. Park, D. G. Park and K. Kim, "Synthesis of $La_{0.8}Sr_{0.2}CoO_3$ by Sol-Gel Type Reaction Modified by Poly(Vinyl Alcohol)", Journal of Materials Science Letters, Volume 15, Issue 5, p. 428-430, 1996.

[259] Y. L. Yang, C. L. Chen, S. Y. Chen, C. W. Chu and A. J. Jacobson, "Impedance Studies of Oxygen Exchange on Dense Thin Film Electrodes of $La_{0.5}Sr_{0.5}CoO_{3-\delta}$", Journal of the Electrochemical Society, Volume 147, Issue 11, p. 4001-4007, 2000.

[260] M. J. Jorgensen and M. Mogensen, "Impedance of Solid Oxide Fuel Cell LSM/YSZ Composite Cathodes", Journal of the Electrochemical Society, Volume 148, Issue 5, p. A433-A442, 2001.

[261] A. Esquirol, N. P. Brandon, J. A. Kilner and M. Mogensen, "Electrochemical Characterization of $La_{0.6}Sr_{0.4}Co_{0.2}Fe_{0.8}O_3$ Cathodes for Intermediate-Temperature SOFCs", Journal of the Electrochemical Society, Volume 151, Issue 11, p. A1847-A1855, 2004.

[262] A. Leonide, V. Sonn, A. Weber and E. Ivers-Tiffée, "Evaluation and Modeling of the Cell Resistance in Anode-Supported Solid Oxide Fuel Cells", Journal of the Electrochemical Society, Volume 155, Issue 1, p. B36-B41, 2008.

[263] M. M. Seabaugh, S. L. Swartz, K. Hasinska and C. T. Holt, "Low Temperature Composite Cathodes for SOFC Application", in S. C. Singhal et al. (Eds.), Proceedings of the Eigth International Symposium on Solid Oxide Fuel Cells (SOFC-VIII), Pennington, NJ, USA: The Electrochemical Society, p. 451-457, 2003.

[264] M. Cassidy, C. Bagger, N. Brandon and M. Day, "Improved Cathode Performance Using Graded Structures", in S. C. Singhal et al. (Eds.), Proceedings of the 4th European Solid Oxide Fuel Cell Forum, Oberrohrdorf, Switzerland: European Fuel Cell Forum, p. 637-646, 2000.

Ionic and mixed ionic-electronic conductors (MIEC) are of strategic interest for applications related to energy conversion and environmental monitoring including batteries, fuel cells, permeation membranes and sensors. Due to their high energy conversion efficiencies and low emissions, Solid Oxide Fuel Cells (SOFCs) show promise as a replacement for combustion-based electrical generators at all sizes. Further increase of SOFC efficiency is aimed by microstructural optimization of the electrolyte and the electrodes. At the nanoscale, grain-size effects potentially lead to substantially enhanced electrical conductivity. Improved charge-transport properties in turn reduce the ohmic losses in the electrolyte and the polarization of the electrodes.

However, an increased grain-boundary density at the nanoscale affects the charge transport in electrolytes and electrodes in different ways: whereas ionic transport is decreased in nanoscaled yttria-doped zirconia (YSZ) thin film electrolytes, nanoscaled and nanoporous $(La_{0.5}Sr_{0.5})CoO_{3-\delta}$ (LSC) thin film electrodes exhibit excellent oxygen-reduction properties. Due to the beneficial material properties of LSC and the high active surface area of the nanostructured cathode, prevailing benchmarks for the electrochemical efficiency of MIEC cathodes are outclassed. The research results are based on microstructural, chemical and electrical measurements of nanoscaled LSC thin-film cathodes and give insights into the electrochemical processes of the cathode. Thus, this work lays the foundation for the application of nanoscaled, mixed ionic-electronic conducting cathodes in the field of mobile SOFCs with operating temperatures of 500 °C $\leq$ T $\leq$ 750 °C.